Simulations of Axisymmetric Stepped Surfaces with a Facet

by

Pak-Wing Fok

MSci., Imperial College London, 2001

Submitted to the Department of Mathematics
in partial fulfillment of the requirements for the degree of

DOCTOR OF PHILOSOPHY

at the

MASSACHUSETTS INSTITUTE OF TECHNOLOGY

June 2006

Author .....
Department of Mathematics
May 5th, 2006

Certified by .....
Rodolfo Ruben Rosales
Professor of Applied Mathematics
Thesis Supervisor

Certified by .....
Dionisios Margetis
Lecturer, Department of Mathematics
Thesis Supervisor

Accepted by .....
Rodolfo Ruben Rosales
Chairman, Applied Mathematics Committee

Accepted by .....
Pavel I. Etingof
Chairman, Department Committee on Graduate Students

Simulations of Axisymmetric Stepped Surfaces with a Facet

by

Pak-Wing Fok

Submitted to the Department of Mathematics
on May 5th, 2006, in partial fulfillment of the
requirements for the degree of
DOCTOR OF PHILOSOPHY

Abstract

A crystal lattice with a small miscut from the plane of symmetry has a surface which consists of a series of atomic height steps separated by terraces. If the surface of this crystal is not in equilibrium with the surrounding medium, then its evolution is strongly mediated by the presence of these steps, which act as sites for attachment and detachment of diffusing adsorbed atoms ('adatoms'). In the absence of material deposition and evaporation, steps move in response to two main physical effects: line tension, which is caused by curvature of the step edge, and step-step interactions which can arise because of thermal step fluctuations, or elastic effects. This thesis focuses on axisymmetric crystals, with the result that the position of a step is uniquely described by a single scalar variable, and the step positions obey a coupled system of "step-flow" Ordinary Differential Equations (step flow ODEs). Chapter 2 of this thesis concentrates on the derivation and numerical solution of these equations, and their properties in the limits of slow adatom terrace diffusion and slow adatom attachment-detachment.

Chapter 3 focuses on the analysis carried out by Margetis, Aziz and Stone ('MAS') [78] on a Partial Differential Equation (PDE) description of surface evolution. Here, the crystal is also axisymmetric and has a single macroscopically flat region, a facet. It is discovered that the boundary condition of Step Chemical Potential Continuity, first suggested by Spohn [109] yields results that are inconsistent with the scalings predicted by the MAS analysis and with results from the step flow ODEs. The 'step drop' condition suggested by Israeli and Kandel [50] is implemented instead, and is shown to give good agreement with the results from the step flow ODEs.

Chapters 4 and 5 explore the evolution of algebraic profiles: instead of starting with steps that are equally spaced, the step radii are initialized as a more general algebraic function of the height. In these two chapters, results are presented which involve approximate self-similarity of the profiles, a stability analysis of small perturbations, and quantification of decay rates.

Chapter 6 of this thesis details the numerical procedure used to integrate the step flow equations. A 'multi-adaptive' time integrator is used where different time steps are taken for different components of the solution. This procedure has benefits over

a standard integrator, because when a few steps cluster tightly together, these steps (and these steps only) become very stiff to integrate. Whereas the inner most steps in the structure undergo a rapid motion, the majority of steps which are sufficiently far away from the facet, move relatively slowly and exhibit smooth behaviour in time. Using the same time step for all components in the solution is therefore quite inefficient. This chapter discusses the concept of "local stiffness", and how the motion of the inner most steps is handled.

Thesis Supervisor: Rodolfo Ruben Rosales
Title: Professor of Applied Mathematics

Thesis Supervisor: Dionisios Margetis
Title: Lecturer, Department of Mathematics

Acknowledgments

I now come to the easiest section of the thesis to write: the acknowledgements. This part is easy, because it is very clear to me which people have been instrumental in helping me achieve all that I have done within the last four years.

The person to whom I owe the most thanks is Dio. One of the main reasons I was able to finish the PhD program here at MIT in four years is because Dio introduced me to the previous work that he had done with Howard Stone and Mike Aziz on Steps. I hear that one of the main reasons for PhDs taking a long time is that it is quite hard to find a suitable problem to work on. In my case, the problem was basically handed to me on a plate by Dio. Dio has also supported me by writing many letters of recommendation, and using the opportunities he had at his job interviews to "spread the word" about me and the work that we were doing. I am very grateful to Dio for all this free publicity, and I am sure that I would not be in such a comfortable position today, jobwise, if it was not for his support. He has also read many drafts of this thesis, meticulously (sometimes, too meticulously!), and recommended many helpful corrections.

Graduate Students often wonder if they would be better off with a young Assistant Professor as an Advisor, or an older tenured Prof. Probably there are advantages and disadvantages to each, but in my case, I think I managed to benefit both from Dio's energy and Ruben's wisdom. Ruben is a very busy man, and it might easy for people to think that he has only been my Advisor on paper, but not in practice. In fact, this is far from the truth. He has been there for me when I needed him, and his advice on job related matters has always been sensible and unbiased. Ruben has also been very supportive in the letters that he wrote for me when I was job hunting, and I benefitted from his advice before and after interviewing for positions. Last, but certainly not least, he helped me to write the step flow code (described in Chapter 6): the results from this code blossomed into the research on which this whole thesis is based.

I would also like to thank Petri Fast, at the Center for Applied Scientific Comput-

ing, at Lawrence Livermore National Lab for taking a chance on my application two years ago, in the Summer 2004, and bringing me to Livermore again subsequently in Summer 2005. Like Ruben and Dio, he supported my numerous job applications, sending off many letters, and even taking the time to personalize a few of them. I learnt a lot from Petri over the two summers at LLNL, including a hands on, practical approach to Scientific Computation. He also introduced me to a quote, the details of which I can't remember exactly, but it boils down to this: in research, you should try to be involved in problems which really excite you, otherwise "nothing can be expected to happen". I think Petri will be happy to find out that I did actually follow this advice in deciding where I will be spending my postdoc years. I would also like to express my gratitude to Christine Orme, also at LLNL, for the two incredibly helpful meetings we had while I was visiting in Summer 2005. I really learnt a lot about the experimental and practical side of Steps from talking to her, and this knowledge was very useful when giving job talks and defending my thesis.

Of course, no acknowledgements section would be complete without a mention of parents. Although I am certain that my Mum probably has no idea about the contents of this thesis, I am even more certain that she has always done her best to provide for me the best education possible, from an early age. It was really during my 5 years at St. Paul's School, in London, that I learnt "how to learn". She also instilled into me a disciplined work ethic and a perfectionist attitude to my studies. Of course, there are many other things that she has done for me, which I am grateful for, but if written out in full, these things would probably extend this thesis by another Chapter...

My Dad has often been the source of sound advice throughout the course of my academic life so far. He has sometimes been reluctant to give advice, in order not to interfere, and to let me make my own decisions. This, I am grateful for, but at the same time, having been an Academic himself, he is probably in one of the best positions to give advice on matters academically related. In particular, after I enjoyed a blissful Mathematics-free gap year in Toyama, Japan, he essentially told me to get my act together and apply to graduate school. Had I stayed in Japan any longer,

I might well have ended up at the Kanazawa Institute of Technology, instead of its more prestigious American counterpart.

I am also grateful in particular to two of my Mathematics teachers from St. Paul's School. These two people are Michael Bradley and Matthew Harvey whose lessons I still remember, nearly a decade after leaving SPS. They taught me ways to approach and think about Mathematical problems which I still use to this day, to a certain extent. They are also directly responsible for me gaining confidence in Mathematics at a relatively early age. Michael Bradley, in particular, encouraged all his students to ask questions when they did not understand something he said in his lessons. I made sure I followed his advice, and this has put me in good stead ever since.

Finally, I would like to thank fellow grad and ex-grad students Chris Rycroft, Eng-Sew Aw, Brian Ross, John Lee, Sabri Kilic, King-Yeung Yick, Ken Kamrin, Boguk Kim, Jaehyuk Choi, David Hu and Kevin Chu for making life at MIT enjoyable and, dare I say it, even fun sometimes. I enjoyed many interesting discussions with Kevin Chu in particular on everything from the Fluid Dynamics of Smoothies to Pseudospectral Numerical Methods. He deserves special credit for writing the code (detailed in Appendix C) to solve the MAS Universal ODE. When all these people are either top CEOs or tenured Professors, hopefully, they will still remember a time when all that mattered to us grad students was passing our quals and the free food available after seminars.

Pak-Wing Fok,

May 2006

THIS PAGE INTENTIONALLY LEFT BLANK

Contents

List of Figures

THIS PAGE INTENTIONALLY LEFT BLANK

List of Tables

Chapter 1

Introduction

1.1 Chapter Overview

In this short chapter, we will first introduce the notion of a step in the context of crystal surfaces. We will discuss why researchers studied steps in the past, and why steps are studied today. Finally, a summary of this thesis is presented, outlining the main results and how the results build on previous work.

1.2 Description of Surfaces at the Nanoscale

Recent advances in the fabrication of nanoscale electronic devices have led to active research into the fundamentals of surface evolution and kinetics at this lengthscale [55]. With quantum dots [2], and other "low-dimensional" structures becoming ever more widespread, it becomes increasingly important to understand the basic properties of these structures – for example, the lifetime of surface features, and how these features decay. It is thought that the phenomenon of *step-bunching*, which will be described extensively in Chapter 2, can be used as a means to manufacture quantum wires [72], and experimentalists have successfully used vicinal surfaces as a substrate on which to grow quantum dots [60]. We will discuss vicinal surfaces shortly.

For temperatures below the roughening transition temperature ("below roughening"), a crystal lattice with a small miscut from a plane of symmetry consists of a

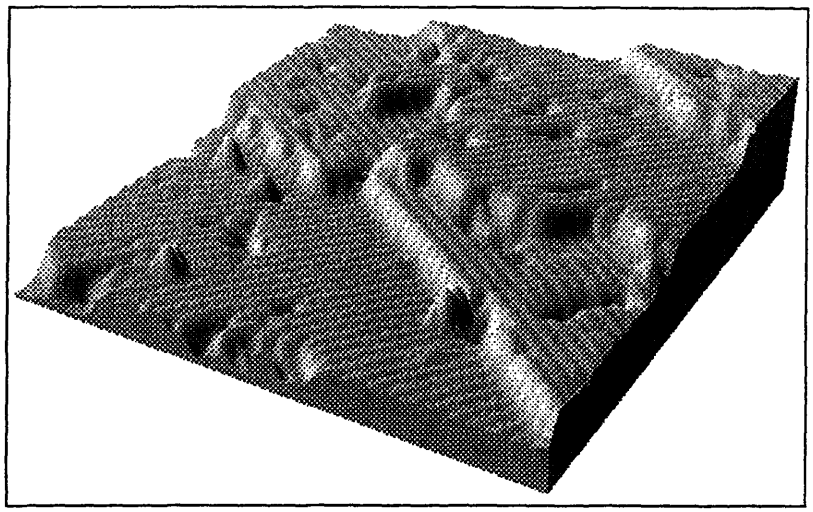

Figure 1-1: Image from a Scanning Tunneling Microscope of a Step on Si(001), used with permission from B. Swartzentruber and taken from [6].

series of *steps*. The roughening temperature, T_R, is that temperature well below which steps are thermally stable: essentially, the steps have a lifetime that is long enough so that they can be directly observed. Figure 1-1 shows an image from a Scanning Tunneling Microscope of a step on Si(001) [†]. The height of the step is of the order of a few angstroms. When the temperature is raised above T_R, it is thought that the surface undergoes a *Kosterlitz-Thouless* phase transition [23], and it becomes statistically "rough". In this case the height-height correlation function has been shown to diverge [95], [118], [120], through theoretical arguments in statistical mechanics.

These steps, having a height of about one lattice constant, are separated by terraces, whose widths are typically hundreds or thousands of lattice constants. Surfaces like these are often referred to as being 'vicinal' because they can be thought of as being 'in the vicinity' of, or being close to, one of the planes of symmetry of the crystal lattice. Two main physical processes can occur on stepped surfaces: the diffusion of adsorbed atoms ('adatoms') on the terraces, and the attachment and detachment of adatoms at step edges. When adatoms detach from step edges, steps retreat; when they attach to step edges, the steps advance. Figure 1-2 shows a di-

[†]Material scientists allocate a *Miller Index* to a surface's orientation. In the case of a cubic lattice, it consists of 3 integers which describes the direction of the vector normal to the surface, for example (001), or (110).

agram of a series of "single signed" steps with diffusion of adatoms on terraces and attachment-detachment at step edges.

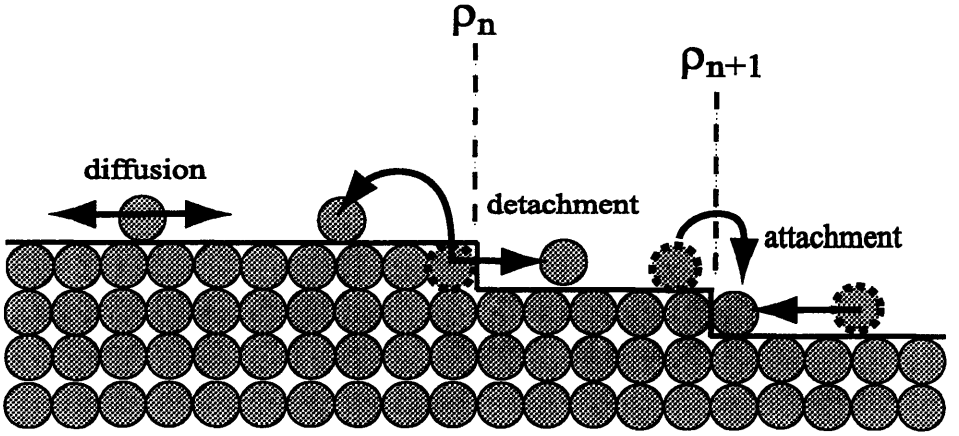

Figure 1-2: Diagram of single signed steps illustrating diffusion on terraces and attachment-detachment at step edges. The step at ρ_n will retreat to the left as atoms detach, while the step at ρ_{n+1} will advance to the right as atoms attach from above and below.

The steps are assumed to be straight, and infinite in length: in 1-2, the step edges come out of the page. Steps are said to be *single signed* when they all face the same direction, i.e. the profile is monotone. When two steps face toward or away from each other, they have opposite/different signs.

Figure 1-2 is an oversimplification in many ways. The first is that steps in general are not straight and infinite in length. Second, there can be "empty pockets" (voids) and other defects on terraces that are not shown. Finally, in 1-2, the atoms on the surface of the crystal are identical to those in the bulk. In reality, when the surface of a crystal is exposed, the atoms on the surface can "reconstruct": surface atoms with free bonds can form additional bonds with neighbors. This can give rise to some unexpected properties on the surface – for example, the diffusivity can vary over the terrace width.

A more realistic picture of a step is shown in Figure 1-3. The kinks shown in this picture can act as sites for preferential attachment of adatoms and edge atoms, leading to a local advance of the step. This picture emphasizes the discrete nature of the crystal lattice, and shows that 2D steps move through the *propagation* of kinks

along the step. When an atom attaches to a kink, the kink effectively moves along the step by one lattice constant. When a 2D step advances, it does so because kinks 'zig-zag' along the step edge. With each pass, kinks successively nucleate, adding more mass is added to the step edge.

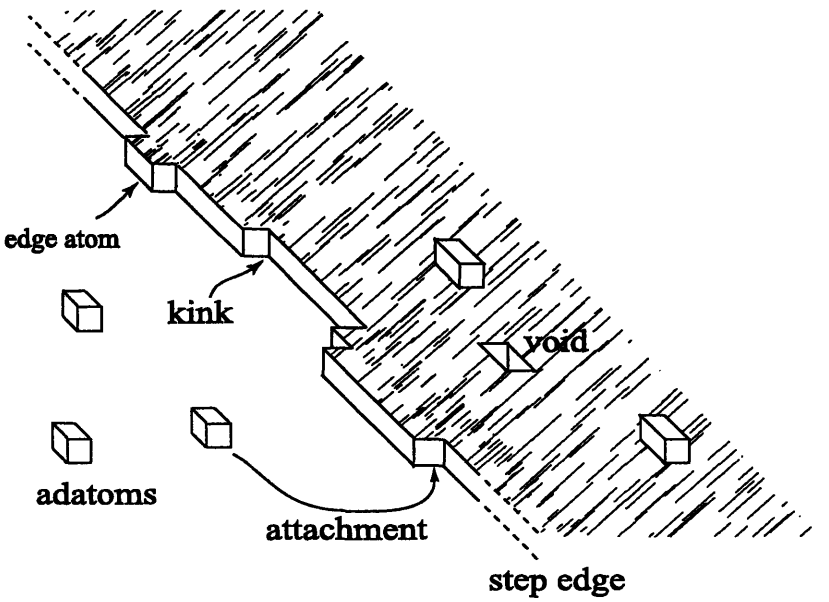

Figure 1-3: Steps are not straight, but consist of many kinks which act as sites for preferential attachment of diffusing adatoms. A void on the terrace is also shown.

In the situation we just described, steps advanced because there was an excess of adatoms. Now consider the opposite situation, where we have a single island (a closed, 2D step) on an infinite substrate, and assume that there are no adatoms on the substrate. The island will evolve in a way that minimizes the number of unbonded atoms on the edge – that is, the step will shrink by emitting adatoms. This is the effect of *step line tension.* This decay of single islands has been demonstrated experimentally in by Ichimaya and coworkers in [48].

If what we have said about steps so far is true, then their behavior is completely passive: islands on a substrate will respond to deposition[1] by growing or, if the surface is isolated from the vapor above, it shrinks under the effect of line tension (if the deposition rate is high enough, *new* islands can also be created on the substrate).

[1]This increases the adatom concentration on the substrate.

However, steps are *not* completely passive: the presence of a step can actually affect the attachment-detachment rate, and hence the motion, of nearby steps. This phenomenon is a result of *step-step interactions*. The propensity of a step edge for accepting a diffusing adatom from a terrace (or an atom from the surrounding medium) is quantified through the notion of a *step chemical potential* [55]. When steps interact with each other, they do so by affecting the chemical potentials of each other: the step chemical potential governs the transport of adatoms from one step edge to the next, and in turn, the transport of adatoms governs the motion of steps. The interactions of steps is still an active area of research [24], [54] and there are still many unresolved issues. We will discuss why step interactions should arise physically in Chapter 2.

Much more will be said about step interactions in Chapter 2.

1.3 Motivation for Studying Steps

Steps provide a mesoscale description of a crystal surface below the roughening transition temperature. Essentially, the evolution of a surface can be accurately predicted if one can understand how steps interact with each other and move on the surface. Understanding how surfaces evolve on a fundamental level is important is many applications: e.g. the fabrication of quantum devices, epitaxial growth[2] and sintering. Epitaxy is probably one of the most important motivations for studying steps. The first stage of manufacturing any semiconductor device is to grow extremely pure, defect free wafers of silicon. This growth proceeds through the nucleation and advance of silicon steps on the surface. Ensuring the right conditions for steps to advance as quickly as possible, without creating defects and *step bunches* (see Chapter 2) is an important part of the manufacturing process.

As another modern day example of crystal growth, researchers at The National Ignition Facility (NIF) [4] at Lawrence Livermore National Laboratory have grown huge Potassium DiPhosphate (KDP) crystals, weighing hundreds of pounds. These

[2]Epitaxy is a process by which features such as thin films are grown by deposition onto a substrate so that crystal properties of the feature are close to that of the substrate.

crystals are grown [28] through screw dislocations (which is essentially a single step wound around itself in a screw-like manner), and are used in frequency conversion and polarization rotation in the lasers at the NIF. The method used to grow these massive crystals in record times (2 months, when normally, 2 years would be the normal growth time) has been one of the more publicized pieces of technology at the Lab.

1.4 Background and History of Steps

In 1951, Burton, Cabrera and Frank ("BCF") [17] considered a problem in crystal morphological evolution. Specifically, their problem involved the growth of crystals in solution. One way to grow crystals is through *supersaturated* solutions. At a given temperature and pressure, there is a maximum amount of solute that a fixed volume of solvent can dissolve. If this maximum is reached, the resulting solution is said to be saturated. However, the solution can hold more solute if its temperature, for instance, is increased. When the temperature is lowered back to its original value, the excess solute will actually stay dissolved, but now, this *supersaturated solution* is unstable in the sense that even small scratches on the side of the container, or the addition of small particles ('seeds') can cause the excess solute to crystallize out of solution. BCF [17] noted that in most experimental situations, crystals could grow in supersaturations of about 1%. This observation seemed to contradict the contemporary theory at that time, which stipulated that growth conditions required much higher supersaturations, typically 50% or so, because of the large nucleation energies involved in creating islands on a perfect, atomically flat, crystal surface. They concluded that in real experiments, even the most carefully prepared crystal surfaces are not atomically flat, and in fact, consist of steps which act as sites for attachment and detachment of atoms on the surface, and from the solution.

One of the model problems studied by BCF [17] was an infinite series of uniformly spaced steps of the same sign, and one of their central results was to derive an expression for the step velocity in terms of (i) the solution's supersaturation, (ii) the

mean displacement of adatoms[3], (iii) the spacing between steps and (iv) the 'hopping frequency' of diffusing adatoms. As Jeong and Williams [55] point out, the major insight of the BCF model was that the growth of crystals is mediated by the presence of steps, and this model provides a starting point for studying the surfaces of crystals which are not at equilibrium. In part II of their paper [17] , BCF studied the growth of crystalline pyramids via screw dislocations. The pyramid essentially consists of a single step, wound around in a screw. With the paradigm of attachment-detachment through steps already established in part I, adatoms can attach themselves to any part of the step, which results in the screw 'unwinding' as the crystal grows.

However, the BCF model [17] is limited in several ways. The three most basic ones are that (i) the result for the step velocities is derived under the assumption that the *only* transport process on the surface is diffusion, (ii) it does not model interactions between steps, and (iii) BCF do not include the effects of kinks and edge atoms. Most of these limitations have been remedied since the inception of the BCF model. It is a fairly simple matter to include first order effects of finite attachment-detachment rates, at the step edges – see [50], for example – and a variety of step interactions can be included in today's step models: in Section 2.2, we will use 'dipolar' interactions[4]. Descriptions for how steps interact were developed in [39], [53] and [64], and a more complete kinetic model accounting for the presence of kinks and edge atoms is given in [18]. The most important drawback of the BCF model, however, is that their model of a *step* is strictly 1D. Although BCF do consider the growth of screw dislocations, they do not account for step curvature.

Rettori and Villain [99] considered a 2D array of circular mounds, and so incorporated the effects of step line tension into the BCF model. Geometrically, these *nanostructures* consist of a finite number of concentric circular layers, in a 'wedding cake' configuration (see Figure 1-4). The radius, at time t of each step in the structure is assumed to be a continuous quantity, and is assigned a value, $\rho_i(t)$.

[3]This is the typical distance that an adatom travels on a terrace before being desorbed into the vapor.

[4]This amounts to modeling the force between two neighboring steps by placing dipoles at the step edges.

By considering the flux of adatoms in and out of step edges, and relating them to attachment-detachment rates, one can write down a set of locally coupled ODEs for $\rho_i(t)$. The ODEs for the step positions are called *step flow equations* and they can be solved to obtain quantitative information on the motion of steps. These step models are powerful because they can account for the discreteness of the surface, imposed by the structure of the crystal lattice. Furthermore, simulations of step motion can take place over much longer periods of time compared to atomistic Monte-Carlo models; they can model larger length scales; and they require much fewer computational resources.

Remark 1.4.1 *A facet is a macroscopically flat region on a crystal. For an isolated, axisymmetric nanostructure, which is the focus of this thesis, we will assume that there is only a single facet. This circular facet grows as the inner most steps in Figure 1-4 successively shrink and annihilate under the effect of line tension. This particular type of surface evolution, in the absence of deposition and evaporation, is called* ***Relaxation****. The role of facets in this thesis is very important: in particular, how they evolve and how they can be modeled are all questions we will seek to address in the next three chapters.*

Much progress has been made on understanding the evolution of surfaces through steps, since Burton, Cabrera and Frank developed the BCF model. Today, research on steps is performed at almost every level of application, from detailed calculations at the atomic level on how steps move [18], understanding fundamentally how steps interact [64], to modeling the growth of arbitrarily shaped islands [98], describing step bunching as a chaotic phenomenon [102], to using stepped surfaces as substrates for the growth of Quantum Dots [60]. As chip manufacturers squeeze increasingly large number of transistors onto their silicon wafers, it becomes increasingly important for us to establish, as a resource, a body of basic research on steps and surface physics at the atomic scale.

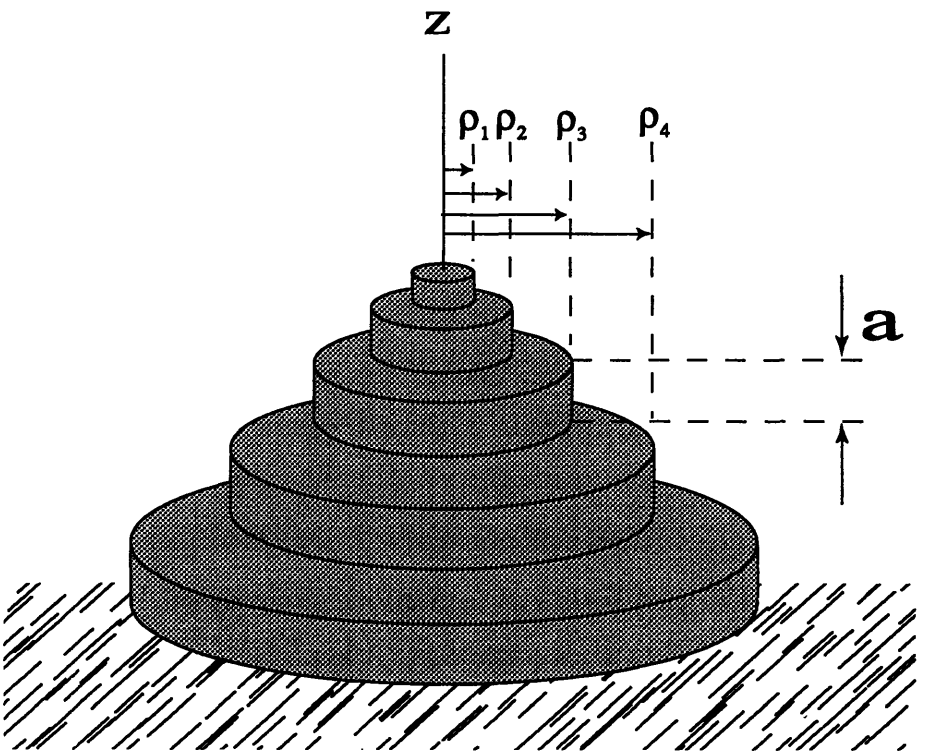

Figure 1-4: The 'Wedding Cake' step configuration for an axisymmetric nanostructure, consisting of a finite number of concentric, circular steps. The step height is a, which is of the order of the lattice constant of the crystal. The number of steps used in the simulations is much larger than what is shown in this picture, but still finite.

1.5 Overview of this Thesis

This thesis is mainly the result of extending the work from two papers: the research done on discrete step simulations by Israeli and Kandel [50], and the continuum theory of Margetis, Aziz and Stone [78].

Israeli and Kandel [50] performed their simulations for two limiting cases: when diffusion on terraces was much faster than attachment-detachment, and vice versa. In all their simulations, they used a value for the step-interaction parameter that was very small. We will call this parameter g. Furthermore, they considered a very specific geometry for their simulations: an axisymmetric structure (as in Figure 1-4) with an *infinite* number of steps, which are all, initially, uniformly spaced: this will be refered to from now on as a 'conical' or 'linear' initial condition. Their paper contains many important results on step bunching, and facet evolution. They showed that the surface was basically self-similar in time: the nanostructure's profile at a later time can simply be obtained by stretching the profile from an earlier time. Israeli and Kandel also propose a particular boundary condition for a *continuum* model of relaxation. The form of this boundary condition is motivated by their simulation results and it involves discrete steps. However, it appears that they did not directly implement this condition.

The work by Margetis, Aziz and Stone [78] is complementary to Israeli and Kandel's: the geometry used in [78] is identical, and the modeling considerations only differ slightly. However, a PDE (the 'MAS PDE') is used to study surface relaxation[5]. The paper concerns itself mainly with finding solutions of the MAS PDE in the limit of small g, deriving boundary conditions, and implementing them. Again, there are many important results: some confirm the predictions by Israeli and Kandel (e.g., an analytic derivation for the facet evolution), and others are completely new (e.g. scaling results for the maximum step density). The authors also compare the scaling results predicted by their PDE solution with the simulation results of Israeli and Kandel [50].

[5]This PDE is actually derived from a similar step model to Israeli and Kandel's

The work in this thesis extends [50] in many ways and also uses the MAS PDE in [78] to make new predictions. There is never a restriction on g having to be small. In Chapter 2, new results where both Diffusion and Attachment-Detachment are comparable are given. The width of step bunches is analyzed and the effect of finite height on facet evolution is quantified. In Chapter 4, we will see results for non-conical profiles. For these algebraic profiles, there is still similarity in time for certain cases, and the results for facet evolution are also extended for non-conical shapes. These similarity solutions are confirmed by using the MAS PDE. Chapter 5 focuses on perturbations of algebraic profiles. This chapter is concerned with how these perturbations decay, and how the decay rate is affected by the material's properties and the wavenumber of the perturbation. Again, the MAS PDE is used to correctly predict these dependencies.

In Chapter 3, results from step simulations and ideas from the MAS PDE are brought together to put relaxation and facet evolution in the context of multiscale problems. Israeli and Kandel's 'discrete' boundary condition in [50] is implemented on the MAS PDE and the results give good agreement with the step simulations. However, implementation of the condition requires knowing a parameter which involves discrete steps. The theme for this chapter is that although relaxation away from the facet can be modeled using a PDE, modeling the *facet evolution* must take into account the discrete nature of individual steps near the facet.

Finally, Chapter 6 gives details on how the discrete step equations were solved, and the reason why a particular integration algorithm is used for the set of step flow ODEs, namely: (i) step bunches are very *stiff* to integrate; and (ii) in some cases, most of the steps in the structure move very slowly compared to those close to the facet, and therefore it is inefficient to take the same time step for all components in the ODE system.

THIS PAGE INTENTIONALLY LEFT BLANK

Chapter 2

Step Flow Models

2.1 Chapter Overview

In this chapter, we will derive a set of 'step flow' equations to describe the morphology of an axisymmetric crystal which consists of a *finite number of discrete steps.* The crystal rests on a flat substrate which is infinite in extent, and it has a single, circular facet which expands as time progresses. The two main physical effects incorporated into the equations are *step line tension* and *step-step interactions*, characterized by the step-step interaction parameter g.

We will then study two limiting cases of these equations ('TDL' and 'ADL') before proceeding to study the generic, 'mixed' case. Under TDL kinetics, we will quantify how the presence of a substrate affects the facet expansion. In the ADL case, the results center around the *step bunching* instability. We will show that step bunching can occur for any value of g providing initial conditions are chosen appropriately and one waits for long enough times. Step bunching is induced only through the effects of step line tension. A scaling law for the step bunch width with g is also presented. In the mixed case, we show that the system exhibits features characteristic of ADL kinetics provided g or the initial step spacing is made sufficiently small.

2.2 Derivation of the Axisymmetric Step Flow Model

Many different types of step flow model have been studied in the past, e.g. [102], [50], [58], , [63] and the equations which arise in each case vary depending on what kind of physical effects are incorporated into the model. The derivation presented here is very similar to the one by Israeli and Kandel's [50] and Margetis et al. [78]. In these two cases, the modeling considerations are fairly similar to each other[1]: nearest-neighbor, dipolar step interactions, curvature effects arising from circular steps, isotropic diffusivity on terraces, finite attachment-detachment rates at step edges, and axisymmetric nanostructures consisting of an infinite number of concentric, circular steps.

The derivation of the equations of motion for a multi-layered nanostructure comes essentially from a steady-state diffusion equation with boundary conditions for attachment-detachment at step edges, and enforcing conservation of mass to give the step velocity. The justification for only considering steady-state solutions of the diffusion equation comes about through the "quasi-steady" approximation [17], which assumes a priori that the motion of the steps occurs over a much longer time scale than the time taken for the adatom concentrations to equilibrate. This approach amounts to neglecting the time derivative in the diffusion equation; the time dependence of the adatom density stems from the moving step edges alone.

For the sake of clarity and completeness, we re-derive the step flow equations in this section. For comparisons, the reader may refer to [50] or [78].

Consider an axisymmetric nanostructure with N steps, in a so-called 'wedding cake' configuration (Figure 1-4). By assuming axisymmetry, all quantities considered in our model will be independent of the azimuthal angle. We label the time-dependent radius of each step $r_i(t)$, $i = 1, 2, ..., N$ with the understanding that $r_i(t)$ is a continuous variable, not necessarily an integer multiple of the lattice constant [2]

Remark 2.2.1 *In our model, we consider structures consisting of a finite number*

[1] Although one of the main distinctions between the two is that the authors in [78] use a different form for the step chemical potential.

[2] The justification for this is that $r_i(t)$ is interpreted as a space-averaged step position: a real step is not perfectly circular, but will have imperfections which are "coarse grained" – see [55] for more details.

of concentric, circular steps. In the absence of material deposition from above, the 'relaxation' of the surface causes it to become flatter as time goes on. As we will see, the surface flattening is a result of the step line tension which causes the inner most step to shrink and finally annihilate, at which point the number of steps in the structure reduces by one. This process repeats itself so that the number of layers in the system constantly decreases over time.

The notion of perfectly circular steps is, of course, an idealization. However, this geometric description of steps proves to be an excellent approximation in some cases. The experiments of Thürmer et al. on Lead crystallites are done on a configuration of steps that *are* in the 'wedding cake' configuration shown in Figure 1-4. Their results show that when the typical length scale of a layer is about 100 nm, the steps really do look circular, despite the fact that Lead has a cubic crystal structure. Furthermore, as the inner most step shrinks, the step stays circular for a large part of the collapse period[3]. The relaxation experiments by Tanaka et al. [114] were performed on biperiodic gratings on Silicon. Here, a 2D periodic corrugation was forced onto a high symmetry plane of Silicon. The result is an array of uniformly spaced minima and maxima. In this experimental situation, the local topology around a maximum can be viewed as being approximately axisymmetric, and the subsequent step motion is shown [114] to be well predicted by axisymmetric models such as the one discussed in this chapter.

We assume that two types of transport processes occur on the surface: Diffusion and Attachment-Detachment. Diffusion of adatoms occurs on terraces, and on the ith terrace, the adatoms are represented through a concentration field $c_i(r,t)$. At step edges, adatoms can either attach onto the step edge, or detach from it. The associated attachment-detachment rate is characterized by the constants k_u and k_d, and steps advance (retreat) by attachment (detachment) of adatoms. Our step flow model is a mesoscopic one because it describes a surface in terms of its steps, and not through individual atoms. The motion of adatoms on terraces and at step edges is "coarse-grained" so that adatoms are represented through a concentration field, and

[3]'Period' here is used in the loose sense to refer to the length of time between step collapses

their attachment-detachment at step edges is represented as a flux. Furthermore, we assume that the nanostructure is isolated, so that there is no mass transport between the surface and the surrounding medium. In practice, preventing mass transport to and from the surface can be achieved by immersing the crystal in an inert medium.

At various stages of the following derivation, some of the modeling assumptions will be put into question. We will postpone a discussion of the model's validity to Section 2.2.2.

The starting point for our derivation is a mass conservation statement. This relates the velocity of a step edge to an influx and outflux of adatoms (adatom current). The adatom current is proportional to the adatom concentration gradient, so that $J = -D_s \frac{\partial c}{\partial r}$ where D_s is the terrace diffusivity, c is the adatom concentration and r is the radial coordinate. Throughout this thesis, D_s will be treated as a constant: we will neglect any anisotropy which may arise from reconstruction effects on terraces, for example.

Applying mass conservation to step i, which is assumed to have at least two neighbors on either side, yields:

$$\frac{dr_i}{dt} = \frac{\Omega}{a}\left[J_{i-1}(r_i) - J_i(r_i)\right] \tag{2.1}$$

$$= \frac{\Omega}{a}\left[-D_s \frac{\partial c_{i-1}}{\partial r}\bigg|_{r_i} + D_s \frac{\partial c_i}{\partial r}\bigg|_{r_i}\right]. \tag{2.2}$$

Here, Ω is the atomic volume, a is the lattice constant for the crystal and t is time. Typically, $\Omega = O(a^3)$. The goal now is to find the concentrations c_i in terms of step radii in order to close the above system. The adatom concentrations satisfy the diffusion equation between step edges:

$$D_s \Delta c_i = \frac{\partial c_i}{\partial t}, \quad r_i < r < r_{i+1}. \tag{2.3}$$

At this stage, the quasi-steady approximation is invoked in order to make progress analytically. This approximation states that the rate at which adatom concentrations relax to their steady-state distributions on the terraces is much faster than the rate at

which the steps move. Therefore, it is a reasonable approximation to always replace the (explicitly time dependent) adatom concentration by its steady-state distribution. Then, the time dependence enters implicitly through the boundary conditions at the moving boundaries, $r_i(t)$ and $r_{i+1}(t)$. Mathematically, this approximation means that the time dependent term in the diffusion can be neglected, with the result that the adatom concentration satisfies Laplace's equation on each terrace:

$$\Delta c_i = 0, \quad r_i < r < r_{i+1}, \tag{2.4}$$

$$\Rightarrow c_i(r) = A_i \ln r + B_i, \tag{2.5}$$

where A_i and B_i are constants. These constants are chosen in order to satisfy boundary conditions at step edges, which state that the adatom concentrations obey the *linear* kinetic rate equations[4]

$$D_s \frac{\partial c_i}{\partial r}\bigg|_{r_i} = k_u(c_i|_{r_i} - C_i^{eq}), \tag{2.6}$$

$$-D_s \frac{\partial c_i}{\partial r}\bigg|_{r_{i+1}} = k_d(c_i|_{r_{i+1}} - C_{i+1}^{eq}). \tag{2.7}$$

Here, C_i^{eq} is the equilibrium concentration at the i^{th} step and k_u and k_d are attachment-detachment rate coefficents for atoms to attach to/detach from a step edge, from below and above respectively. Experimental evidence [32], and statistical calculations [104], [105] suggest that in many materials, $k_u > k_d$. This inequality in the rate coefficients is informally called the "Schwoebel Effect" or an "Ehrlich-Schwoebel" ("ES") barrier. If $k_u > k_d$, then the ES barrier is "positive". If $k_d > k_u$, then the ES barrier is "negative".

Application of boundary conditions (2.6) and (2.7) yields an expression for A_i:

$$A_i = \frac{C_{i+1}^{eq} - C_i^{eq}}{\frac{D_s}{k_u r_i} + \frac{D_s}{k_d r_{i+1}} + \ln \frac{r_{i+1}}{r_i}}. \tag{2.8}$$

[4]This assumption is valid providing the adatom concentration at a step edge does not deviate too far from the equilibrium value.

The coefficients B_i do not have to be explicitly computed because (2.2) only contains derivatives of c_i. Hence, from (2.2),

$$\frac{dr_i}{dt} = \frac{D_s\Omega}{ar_i}(A_i - A_{i-1}), \tag{2.9}$$

$$\Rightarrow \frac{dr_i}{dt} = -\frac{D_s\Omega}{ar_i}\left[\frac{C_i^{eq} - C_{i+1}^{eq}}{\ln\frac{r_{i+1}}{r_i} + \frac{D_s}{k_u}\left(\frac{1}{r_i} + \frac{\alpha}{r_{i+1}}\right)} - \frac{C_{i-1}^{eq} - C_i^{eq}}{\ln\frac{r_i}{r_{i-1}} + \frac{D_s}{k_u}\left(\frac{1}{r_{i-1}} + \frac{\alpha}{r_i}\right)}\right], \tag{2.10}$$

where $\alpha = k_u/k_d$ and $\alpha > 1$ for a positive ES barrier. Now, the equilibrium concentration of atoms, C_i^{eq} is related to the step chemical potential (μ_i) through the Gibbs-Thomson relation [45]:

$$C_i^{eq} = c_s e^{\frac{\mu_i}{k_B T}} \tag{2.11}$$

$$\sim c_s\left(1 + \frac{\mu_i}{k_B T}\right) \tag{2.12}$$

because $\left|\frac{\mu_i}{k_B T}\right| \ll 1$ for most experimental situations [115]. Here, c_s is the atom equilibrium concentration at an isolated step, T is the absolute temperature, and k_B is the Boltzmann constant. The step chemical potential, μ_i, defined as the change in free energy of the step when an atom is removed or added, is given by [78]

$$\mu_i = \frac{\Omega g_1}{r_i} + \frac{\Omega}{2\pi a r_i}\frac{\partial[V(r_i, r_{i+1}) + V(r_{i-1}, r_i)]}{\partial r_i}. \tag{2.13}$$

The chemical potential potential at a step edge consists of two terms: the first represents the Step Line Tension, and the second is a result of Step-Step Interactions. Both of these terms will be explain shortly.

Remark 2.2.2 *When $r_i \to 0$ in (2.13), the step chemical potential $\mu_i \to \infty$, which violates the approximation made in (2.12). Nevertheless, we will continue to use (2.12) . When the inner most step collapses, we will see later on that although some of the approximations made in deriving the governing equations break down, the predicted results still, surprisingly, give good agreement with results from experiments.*

In (2.13), Ω is the atomic volume, and a is the lattice constant. The parameter g_1 is called the step stiffness. An isolated, closed step is stiff because there is an energy cost associated with each 'free' unbonded atom on the step edge. Therefore, the step will evolve in such a way to minimize its perimeter. A closed, perfectly circular step will stay circular and reduce its radius by emitting adatoms. A closed, non-circular step will gradually *become* circular as it minimizes its perimeter, providing it does not split into two or more smaller islands [9]. Step stiffness is, therefore, intimately related to step line tension. This behavior is the result of Step Line Tension. The potential V in (2.13) represents the interaction between two steps. It takes the form [114]

$$V(r_i, r_{i+1}) = \frac{4\pi a^3 g_3}{3} \frac{r_i r_{i+1}}{(r_i + r_{i+1})(r_{i+1} - r_i)^2}, \tag{2.14}$$

where g_3 is the step-step interaction coefficient. Why should steps interact with each other? The two main ways of explaining step interactions are through Statistical Mechanics [55], [62], and Elasticity Theory [76], [64], [66].

A *statistical* description of a step treats the step's position $x(y)$ (at a particular instance in time) as a random walk in the space variable y. It is not energetically favorable for steps to cross, and there can be "collisions" between two neighboring steps at different values of y. In particular, one can define a *collision length* for a step, trapped between two straight walls[5], spaced w apart. The collision length is the average distance that one must go in the y direction to have one collision between the step and the wall. From the statistical properties of random walks, one can show [55] that the collision length scales like w^2, and this gives rise to "entropic" step repulsions. As a result, entropic repulsions give rise to a force between steps which is inversely proportional to the square of the inter step spacing.

From the solid mechanical viewpoint, a step is treated as a line defect [93] on the surface of a crystal, which gives rise to a stress field affecting atoms both on the surface and in the bulk. The stress field can be represented with monopoles, dipoles and higher order poles [64], [66]. The most commonly used representation is the

[5]Which can be thought of as being straight, infinitely long steps

one first adopted by Marchenko and Parshin [76], who model the step interactions as arising from stress fields generated by a force dipole. In their model, the stress fields of two opposite signed steps interact, resulting in "dipolar" step repulsions. Consistent with the entropic approach, the dipolar repulsions also scale inversely with the square of the inter step spacing.

In our model, we consider only *nearest-neighbor* interations, that is, the chemical potential of a step edge in (2.13) is only affected by the presence of *immediately neighboring* step edges. Also, the potential used only accounts for step repulsions. As a result of (2.13) and (2.14), (2.12) becomes

$$C_i^{eq} \sim c_s \left(1 + \frac{\Omega g_1}{r_i k_B T} + \frac{2a^2 \Omega g_3}{3 k_B T} \frac{1}{r_i} \frac{\partial}{\partial r_i} \left[\frac{r_i r_{i+1}}{(r_i + r_{i+1})(r_{i+1} - r_i)^2} + \frac{r_{i-1} r_i}{(r_{i-1} + r_i)(r_i - r_{i-1})^2} \right] \right). \tag{2.15}$$

Accordingly,

$$C_i^{eq} - C_{i+1}^{eq} = \frac{\Omega g_1 c_s}{k_B T} \left(\frac{1}{r_i} - \frac{1}{r_{i+1}} + \frac{2a^2 g_3}{3 g_1} \left[\frac{1}{r_i} \frac{\partial W_i}{\partial r_i} - \frac{1}{r_{i+1}} \frac{\partial W_{i+1}}{\partial r_{i+1}} \right] \right) \tag{2.16}$$

where

$$W_i(r_{i-1}, r_i, r_{i+1}) = \frac{r_i r_{i+1}}{(r_i + r_{i+1})(r_{i+1} - r_i)^2} + \frac{r_{i-1} r_i}{(r_{i-1} + r_i)(r_i - r_{i-1})^2} \tag{2.17}$$

The equations are now non-dimensionalized with

$$\tau = \frac{t}{(L/U)}, \tag{2.18}$$

$$\rho_i = \frac{r_i}{L}, \tag{2.19}$$

where L is the characteristic separation length between steps and U is a characteristic step velocity. L can range from $\sim 10\mathring{A}$ [90] to $10^4\mathring{A}$ [46]. Experiments on lead crystallites [116] suggest that a representative step velocity is $\sim 5\mathring{A}$/min. This is the characteristic velocity of $r_2(t)$: as we will see later on, the inner most step moves much more quickly than a typical step in the bulk and, in fact, does not have a single

characteristic velocity. We now have

$$\frac{d\rho_i}{d\tau} = -\frac{\Phi}{\rho_i}\left\{\frac{\frac{1}{\rho_i}-\frac{1}{\rho_{i+1}}+g[\Lambda(\rho_{i-1},\rho_i,\rho_{i+1})-\Lambda(\rho_i,\rho_{i+1},\rho_{i+2})]}{\ln\frac{\rho_{i+1}}{\rho_i}+m\left(\frac{1}{\rho_i}+\frac{\alpha}{\rho_{i+1}}\right)} - \frac{\frac{1}{\rho_{i-1}}-\frac{1}{\rho_i}+g[\Lambda(\rho_{i-2},\rho_{i-1},\rho_i)-\Lambda(\rho_{i-1},\rho_i,\rho_{i+1})]}{\ln\frac{\rho_i}{\rho_{i-1}}+m\left(\frac{1}{\rho_{i-1}}+\frac{\alpha}{\rho_i}\right)}\right\} \tag{2.20}$$

where

$$g = \frac{2g_3}{3g_1}\left(\frac{a}{L}\right)^2, \tag{2.21}$$

$$\Phi = \frac{\Omega_s^2 g_1 c_s}{k_B T}\left(\frac{aD_s}{L^2 U}\right), \quad \text{where} \quad \Omega_s = \frac{\Omega}{a} \tag{2.22}$$

$$\alpha = \frac{k_u}{k_d} = 1, \tag{2.23}$$

$$m = \frac{D_s}{k_u L}, \tag{2.24}$$

$$\begin{aligned}\Lambda(\rho_{i-1},\rho_i,\rho_{i+1}) = {} & \frac{2\rho_{i+1}}{\rho_{i+1}+\rho_i}\frac{1}{(\rho_{i+1}-\rho_i)^3} - \frac{2\rho_{i-1}}{\rho_i+\rho_{i-1}}\frac{1}{(\rho_i-\rho_{i-1})^3} \\ & + \frac{1}{\rho_i}\left[\left(\frac{\rho_{i+1}}{\rho_{i+1}+\rho_i}\right)^2\frac{1}{(\rho_{i+1}-\rho_i)^2}\right. \\ & \left. + \left(\frac{\rho_{i-1}}{\rho_i+\rho_{i-1}}\right)^2\frac{1}{(\rho_i-\rho_{i-1})^2}\right].\end{aligned} \tag{2.25}$$

We have introduced the parameter g as a measure of the strength of the step-step interactions relative to the step line tension [78]. We have taken $\alpha = 1$ because we will not be considering Ehrlich-Schwoebel Effects in this thesis. However, in experiments, α can range from about 6×10^{-2} to 4×10^2, assuming that the frequency of attempts to attach onto/detach from the step are equal on either side of the step [6]. The dimensionless constant m measures how fast diffusion takes place along the terraces, compared to the attachment and detachment of adatoms at step edges.

The first two steps and last two steps in the structure are special in the sense that they do not have two neighboring steps on either side. Therefore the derivation

[6] Tabulated values for energy barriers at step edges are given for a wide variety of materials in [55], Table 6.

of their equations of motion differ slightly from the above. For the first step, $r_1(t)$, there is no step on the inside to supply an adatom current, so $J_0(r) \equiv 0$. Hence, (2.2) becomes

$$\frac{dr_1}{dt} = \frac{D_s\Omega}{a}\left.\frac{\partial c_1}{\partial r}\right|_{r_1} \tag{2.26}$$

$$= \frac{D_s\Omega A_1}{ar} \tag{2.27}$$

$$= -\frac{D_s\Omega}{ar}\left(\frac{C_1^{eq} - C_2^{eq}}{\frac{D_s}{k_u r_1} + \frac{D_s}{k_d r_2} + \ln\frac{r_2}{r_1}}\right), \tag{2.28}$$

using (2.5 and (2.8) with $i = 1$. Now, C_1^{eq} takes a slightly different form because the chemical potential at the first step is only affected by the one step on the outside. Instead of (2.13), for the first step, we have

$$\mu_1 = \frac{\Omega g_1}{r_1} + \frac{\Omega}{2\pi a r_1}\frac{\partial V(r_1, r_2)}{\partial r_1}, \tag{2.29}$$

and in contrast to (2.15),

$$C_1^{eq} \sim c_s\left(1 + \frac{\Omega g_1}{r_1 k_B T} + \frac{2a^2\Omega g_3}{3k_B T}\frac{1}{r_1}\frac{\partial}{\partial r_1}\left[\frac{r_1 r_2}{(r_1 + r_2)(r_2 - r_1)^2}\right]\right). \tag{2.30}$$

Hence,

$$C_1^{eq} - C_2^{eq} = \frac{\Omega g_1 c_s}{k_B T}\left(\frac{1}{r_1} - \frac{1}{r_2} + \frac{2a^2 g_3}{3g_1}\left[\frac{1}{r_1}\frac{\partial \tilde{W}_1}{\partial r_1} - \frac{1}{r_2}\frac{\partial W_2}{\partial r_{i+1}}\right]\right), \tag{2.31}$$

where

$$\tilde{W}_1(r_1, r_2) \equiv W_1(0, r_1, r_2). \tag{2.32}$$

Thus, the equation of motion for the first step is

$$\frac{d\rho_1}{d\tau} = -\frac{\Phi}{\rho_1}\left\{\frac{\frac{1}{\rho_1} - \frac{1}{\rho_2} + g[\Lambda(0, \rho_1, \rho_2) - \Lambda(\rho_1, \rho_2, \rho_3)]}{\ln\frac{\rho_2}{\rho_1} + m\left(\frac{1}{\rho_1} + \frac{\alpha}{\rho_2}\right)}\right\} \tag{2.33}$$

A similar process will yield an equation for $\dot{\rho}_2(t)$ of the form (2.20), but taking $i = 2$, and $\rho_0 = 0$. The equation of motion for the penultimate step is obtained by taking the general equation of motion (2.20) for $i = (N-1)$, and letting $\rho_{N+1} \to \infty$. The equation of motion for the step at the base is obtained by taking $i = N$ in (2.20), then letting $\rho_{N+2} \to \infty$, and then $\rho_{N+1} \to \infty$.

We now discuss three possible forms for (2.20), depending on whether diffusion or attachment-detachment is the rate limiting process:

Terrace Diffusion Limited (TDL) Kinetics

For $m \ll \dfrac{\ln \frac{\rho_{i+1}}{\rho_i}}{\frac{1}{\rho_i} + \frac{1}{\rho_{i+1}}}$ (where $\rho_{i+1} > \rho_i$), diffusion across the terraces is very slow compared attachment-detachment, in which case the equations of motion become

$$\frac{d\rho_i}{d\tau'} = -\frac{1}{\rho_i}\left\{ \frac{\frac{1}{\rho_i} - \frac{1}{\rho_{i+1}} + g[\Lambda(\rho_{i-1},\rho_i,\rho_{i+1}) - \Lambda(\rho_i,\rho_{i+1},\rho_{i+2})]}{\ln \frac{\rho_{i+1}}{\rho_i}} - \frac{\frac{1}{\rho_{i-1}} - \frac{1}{\rho_i} + g[\Lambda(\rho_{i-2},\rho_{i-1},\rho_i) - \Lambda(\rho_{i-1},\rho_i,\rho_{i+1})]}{\ln \frac{\rho_i}{\rho_{i-1}}} \right\} \tag{2.34}$$

where $\tau' \equiv \Phi\tau$.

Attachment-Detachment Limited (ADL) Kinetics

For $m \gg \dfrac{\ln \frac{\rho_{i+1}}{\rho_i}}{\frac{1}{\rho_i} + \frac{1}{\rho_{i+1}}}$, attachment-detachment at step edges is much slower than diffusion across the terraces. In this case, we have

$$\frac{d\rho_i}{d\tau'} = -\frac{1}{\rho_i}\left\{ \frac{\frac{1}{\rho_i} - \frac{1}{\rho_{i+1}} + g[\Lambda(\rho_{i-1},\rho_i,\rho_{i+1}) - \Lambda(\rho_i,\rho_{i+1},\rho_{i+2})]}{\left(\frac{1}{\rho_i} + \frac{1}{\rho_{i+1}}\right)} - \frac{\frac{1}{\rho_{i-1}} - \frac{1}{\rho_i} + g[\Lambda(\rho_{i-2},\rho_{i-1},\rho_i) - \Lambda(\rho_{i-1},\rho_i,\rho_{i+1})]}{\left(\frac{1}{\rho_{i-1}} + \frac{1}{\rho_i}\right)} \right\} \tag{2.35}$$

where $\tau' \equiv \frac{\Phi}{m}\tau$.

Mixed Kinetics

For $\frac{\ln \frac{\rho_{i+1}}{\rho_i}}{\frac{1}{\rho_i}+\frac{1}{\rho_{i+1}}} = O(m)$, both processes are comparable to one another, and the full set of equations is

$$\frac{d\rho_i}{d\tau'} = -\frac{1}{\rho_i}\left\{\frac{\frac{1}{\rho_i}-\frac{1}{\rho_{i+1}}+g[\Lambda(\rho_{i-1},\rho_i,\rho_{i+1})-\Lambda(\rho_i,\rho_{i+1},\rho_{i+2})]}{\ln\frac{\rho_{i+1}}{\rho_i}+\left(\frac{1}{\rho_i}+\frac{1}{\rho_{i+1}}\right)} - \frac{\frac{1}{\rho_{i-1}}-\frac{1}{\rho_i}+g[\Lambda(\rho_{i-2},\rho_{i-1},\rho_i)-\Lambda(\rho_{i-1},\rho_i,\rho_{i+1})]}{\ln\frac{\rho_i}{\rho_{i-1}}+\left(\frac{1}{\rho_{i-1}}+\frac{1}{\rho_i}\right)}\right\} \tag{2.36}$$

where $\tau' = \Phi\tau$. We have taken $m = 1$ in (2.36), and this can be done without loss of generality because the $m \neq 1$ case is equivalent to the $m = 1$ case, but with redefined variables and parameters $\rho_i \to \rho_i/m$, $\tau' \to \tau'/m^3$ and $g \to g/m^2$.

Numerical Evaluation of Material Parameters

In order to make quantitative predictions with the step flow equations, one needs the numerical values of the terrace diffusivities, attachment-detachment rates, and other material parameters. Values for a Si(111) system are shown in Table A.1. These numbers are taken from various experiments, simulations and calculations [94], [68], [48], [55], and by using these, along with estimates for $U \sim 5\mathring{A}/\text{min}$ [116] and $L \sim 100\mathring{A}$, we obtain that the dimensionless parameters Φ and m have the approximate values

$$\Phi = \frac{\Omega_s^2 g_1 c_s}{k_B T}\left(\frac{aD_s}{L^2 U}\right) \simeq 4 \times 10^6 \tag{2.37}$$

$$m = \frac{D_s}{kL} \simeq 6 \times 10^6. \tag{2.38}$$

In the above, we used $c_s = 10^{-3}s^{-1}$, $k_d = k = 150\mathring{A}/s$, $\Omega_s = 25\mathring{A}^2$

Qualitative features of TDL, ADL and Mixed Kinetics

The results in this chapter are divided broadly into 3 categories: those from Terrace Diffusion Limited (TDL) systems, Attachment-Detachment Limited (ADL) systems, and Mixed systems with $m = 1$. There is good reason to make the distinction between these three cases, because the results from each display very different characteristics. Generally speaking, in TDL systems, the steps in the bulk are close to being uniformly spaced and the profile of the structure appears smooth at the macroscale, making it amenable to continuum descriptions such as Partial Differential Equations (PDEs). In this thesis, when we refer to steps being 'in the bulk', this simply means that the index of the step is much greater than the index of the inner most step, and much less than the index of the outer most step (providing there are a sufficiently large number of steps in the structure). ADL systems display opposite characteristics, the most striking being the step bunching phenomenon. When this happens, steps cluster together in bunches, separated by relatively wide terraces. Step bunching is an instability that can be made to occur in the step flow simulations when step configurations, interaction parameters and length of integration are appropriately chosen. Continuum descriptions in this case usually have to be more sophisticated – see [81], for example. Studying the two limiting cases of TDL and ADL kinetics is useful before embarking upon a study of the full, mixed case. The results from this last case can exhibit features which are common to both TDL and ADL systems.

2.2.1 Equations of Motion

The equations of motion which we have derived relate step velocities to the step positions and the positions of neighboring steps. From the derivation, one can see, at first, that the motion of the n^{th} step is coupled to the motion of its immediate neighbors because the diffusion equation is solved on terraces which are on either side of the step, $[\rho_{n-1}(t), \rho_n(t)]$ and $[\rho_n(t), \rho_{n+1}(t)]$. Mixed boundary conditions are imposed at $\rho_{n-1}(t)$ and $\rho_{n+1}(t)$ and these conditions involve C^{eq}_{n-1} and C^{eq}_{n+1}, the adatom equilibrium concentrations at these step edges. Since adatom equilibrium

concentrations at step edges are determined by step chemical potentials, and the chemical potential at the n^{th} step is locally coupled to the positions of the $(n-1)$st and $(n+1)$st step through the local interaction potential, the coupling of a given step in the bulk extends to its two neighbors immediately on either side.

For reference, the complete set of equations for an N-layered structure are now given, in the general case of mixed kinetics. Dropping the primed time variables, if $\rho_n(t)$ denotes the radius of the n^{th} step (counting from the inner most step) measured from the axis of symmetry, then for ρ_1, we have

$$\dot{\rho_1} = -\frac{1}{\rho_1}\frac{\frac{1}{\rho_1} - \frac{1}{\rho_2} + g\left[\Lambda(0,\rho_1,\rho_2) - \Lambda(\rho_1,\rho_2,\rho_3)\right]}{\ln\frac{\rho_2}{\rho_1} + \left(\frac{1}{\rho_1} + \frac{1}{\rho_2}\right)}, \tag{2.39}$$

because the inner most step only 'sees' its two neighbors directly on the outside, which have radii $\rho_2(\tau)$, $\rho_3(\tau)$ respectively. Now, the equation for ρ_2 will be locally coupled to ρ_1, ρ_3 and ρ_4, because it has one neighbor on the inside and two neighbors on the outside:

$$\dot{\rho_2} = -\frac{1}{\rho_2}\left\{\frac{\frac{1}{\rho_2} - \frac{1}{\rho_3} + g[\Lambda(\rho_1,\rho_2,\rho_3) - \Lambda(\rho_2,\rho_3,\rho_4)]}{\ln\frac{\rho_3}{\rho_2} + \left(\frac{1}{\rho_2} + \frac{1}{\rho_3}\right)} - \right. \tag{2.40}$$

$$\left. \frac{\frac{1}{\rho_1} - \frac{1}{\rho_2} + g[\Lambda(0,\rho_1,\rho_2) - \Lambda(\rho_1,\rho_2,\rho_3)]}{\ln\frac{\rho_2}{\rho_1} + \left(\frac{1}{\rho_1} + \frac{1}{\rho_2}\right)}\right\}.$$

For the general n^{th} step,

$$\dot{\rho_n} = -\frac{1}{\rho_n}\left\{\frac{\frac{1}{\rho_n} - \frac{1}{\rho_{n+1}} + g[\Lambda(\rho_{n-1},\rho_n,\rho_{n+1}) - \Lambda(\rho_n,\rho_{n+1},\rho_{n+2})]}{\ln\frac{\rho_{n+1}}{\rho_n} + \left(\frac{1}{\rho_n} + \frac{1}{\rho_{n+1}}\right)} - \right. \tag{2.41}$$

$$\left. \frac{\frac{1}{\rho_{n-1}} - \frac{1}{\rho_n} + g[\Lambda(\rho_{n-2},\rho_{n-1},\rho_n) - \Lambda(\rho_{n-1},\rho_n,\rho_{n+1})]}{\ln\frac{\rho_n}{\rho_{n-1}} + \left(\frac{1}{\rho_{n-1}} + \frac{1}{\rho_n}\right)}\right\},$$

where $n = 3, 4, ..., N-2$. The penultimate step obeys the equation

$$\dot{\rho}_{N-1} = -\frac{1}{\rho_{N-1}} \left\{ \frac{\frac{1}{\rho_{N-1}} - \frac{1}{\rho_N} + g[\Lambda(\rho_{N-2}, \rho_{N-1}, \rho_N) - \tilde{\Lambda}(\rho_{N-1}, \rho_N)]}{\ln \frac{\rho_N}{\rho_{N-1}} + \left(\frac{1}{\rho_{N-1}} + \frac{1}{\rho_N}\right)} - \right.$$

$$\left. \frac{\frac{1}{\rho_{N-2}} - \frac{1}{\rho_{N-1}} + g[\Lambda(\rho_{N-3}, \rho_{N-2}, \rho_{N-1}) - \Lambda(\rho_{N-2}, \rho_{N-1}, \rho_N)]}{\ln \frac{\rho_{N-1}}{\rho_{N-2}} + \left(\frac{1}{\rho_{N-2}} + \frac{1}{\rho_{N-1}}\right)} \right\}, \tag{2.42}$$

and the base step is governed by

$$\dot{\rho_N} = +\frac{1}{\rho_N} \frac{\frac{1}{\rho_{N-1}} - \frac{1}{\rho_N} + g\left[\Lambda(\rho_{N-2}, \rho_{N-1}, \rho_N) - \tilde{\Lambda}(\rho_{N-1}, \rho_N)\right]}{\ln \frac{\rho_N}{\rho_{N-1}} + \left(\frac{1}{\rho_{N-1}} + \frac{1}{\rho_N}\right)}, \tag{2.43}$$

where

$$\begin{aligned} \tilde{\Lambda}(\rho_{N-1}, \rho_N) &\equiv \lim_{\rho_{N+1} \to \infty} \Lambda(\rho_{N-1}, \rho_N, \rho_{N+1}) \\ &= -\frac{2\rho_{N-1}}{\rho_N + \rho_{N-1}} \frac{1}{(\rho_N - \rho_{N-1})^3} + \frac{1}{\rho_N} \left(\frac{\rho_{N-1}}{\rho_N + \rho_{N-1}}\right)^2 \frac{1}{(\rho_N - \rho_{N-1})^2}. \end{aligned} \tag{2.44}$$

This is a system of N locally coupled Ordinary Differential Equations (ODEs), with the motion of a step in the bulk dependent on the the radius of the step itself, the radii of the two steps on the outside, and the two steps on the inside. Integration of this set of equations gives a description for the relaxation of a nanostructure with N layers, sitting on an infinite substrate.

The $\frac{1}{\rho_n}$ terms in the numerators of (2.41) represent the line tension in the step. The overall effect of line tension is to shrink the radius of the step. Furthermore, steps with a higher curvature are more strongly affected by line tension. As a result, the system of ODEs has a very important property. The radius of the inner most step annihilates at a finite time, τ_1, at which point, the second step becomes the inner most step (and would obey an equation similar in form to (2.39) but with $\rho_1 \to \rho_2, \rho_2 \to \rho_3$ and $\rho_3 \to \rho_4$. This second step then annihilates at a later time τ_2 and so on. Note

that steps are *not* relabeled when collapses occur: after ρ_1 collapses, ρ_2 becomes the new inner most step. Strictly, equations (2.39) - (2.43) apply when $\tau < \tau_1$.

Remark 2.2.3 (Collapse Times) *The system of equations (2.39)-(2.43) has the property that at a finite time τ_1, the radius of the inner most step will have shrunk to zero: $\rho_1(\tau) \to 0$ as $\tau \to \tau_1$. When this happens, ρ_1 is removed from the system of equations and ρ_2 takes the place of ρ_1 as the inner most step. Then, ρ_2 will shrink to zero at some finite time τ_2, in which case ρ_3 will ρ_2 as the inner most step etc. This means that an integration of the system of equations (2.39)-(2.43) will yield a sequence of* ***collapse times****, τ_n, where $0 < \tau_1 < \tau_2 < ....$*

The $g\Lambda$ terms represent the step-step interaction terms, which essentially scale like the reciprocal of the cube of the distance between the steps. These singular terms ensure that steps never cross each other providing $g \neq 0$.

Conservation of Mass

The system (2.39)-(2.43) conserves the mass of the N-layer nanostructure. Multiplying each equation for $\dot{\rho}_i$ by ρ_i for each i, and adding all N equations in the system gives

$$\sum_{i=1}^{N} \rho_i \dot{\rho}_i = 0 \tag{2.45}$$

$$\Rightarrow \frac{d}{dt}\left(\sum_{i=1}^{N} \frac{1}{2}\rho_i^2\right) = 0 \tag{2.46}$$

and $\sum_{i=1}^{N} \frac{1}{2}\rho_i^2$ is proportional to the nanostructure's total volume. It should be noted that the nature of these equations is such that all diffusing adatoms will eventually end up attached to the outermost step, which expands as the radii of inner most steps sequentially shrink to zero. In theory, at $t = \infty$, the nanostructure will have flattened into a single step, consisting of a monolayer of atoms.[7].

[7]However, this is not actually predicted by (2.39)-(2.43) because this system of equations requires the existence of at least 5 steps with non-zero radius at any given time.

2.2.2 Criticisms of the Step Flow Model

In our derivation of the equations of motion (2.39)-(2.43), we made certain a priori assumptions which may not always be justified. In this section, we will highlight the main criticisms of the model and argue that although the equations may not always be valid uniformly in time and in step number, they are still useful in providing quantitative information on the behavior of steps.

1. **Quasi-steadiness assumption:** The diffusion equation (2.3) can be written as

$$U\frac{\partial c_i}{\partial t} = \frac{D_s}{L}\Delta c_i \tag{2.47}$$

$$\Rightarrow \beta\frac{\partial c_i}{\partial t} = \Delta c_i \tag{2.48}$$

where L is the characteristic terrace width, U is the typical velocity of a step and D_s/L is the velocity associated with the equilibration of the adatom density c_i to its steady state. The terms Δc_i and $\frac{\partial c_i}{\partial t}$ are both dimensionless and $O(1)$. The dimensionless parameter

$$\beta \equiv \frac{U}{D_s/L} \tag{2.49}$$

is the ratio of the step velocity to the equilibration velocity. The quasi-steady approximation assumes a priori that since the equilibration velocity is much faster than the velocity of a step ($\beta \ll 1$), one can simply replace (2.48) with the Laplace equation $\Delta c_i = 0$. Is it always possible to assume $\beta \ll 1$? Consider the mass conservation equation for a typical bulk step

$$U\frac{\partial \rho_i}{\partial t} = \left(\frac{D_s}{L}\right)\left(\frac{\Omega}{a^3}\right)\left[-\frac{\partial c_{i-1}}{\partial \rho} + \frac{\partial c_i}{\partial \rho}\right] \tag{2.50}$$

$$\Rightarrow \beta\frac{\partial \rho_i}{\partial t} = O\left(\left[-\frac{\partial c_{i-1}}{\partial \rho} + \frac{\partial c_i}{\partial \rho}\right]\right) \tag{2.51}$$

where we have used the fact that $\frac{\partial c_i}{\partial \rho} = O((a^2L)^{-1})$ near a step edge and $\Omega = O(a^3)$. The term $\frac{\partial \rho_i}{\partial t} = O(1)$. Hence, the quasi-steady approximation holds for

a bulk step if and only if the difference in fluxes at a step edge is very small, i.e.

$$\left[-\frac{\partial c_{i-1}}{\partial \rho}+\frac{\partial c_i}{\partial \rho}\right] \ll 1 \tag{2.52}$$

Note that c_i and c_{i-1} in this inequality satisfy the full diffusion equation (2.48) and are *not* the same as the adatom densities in equation (2.5).

Things are slightly different for the inner most step in the nanostructure. We will see later on that near the collapse times, the velocity of the inner most step can become arbitrarily large, and in fact goes to infinity *at* the collapse time itself. Clearly, in this case, it is not possible for $\beta \ll 1$ to hold uniformly up to the time of collapse: the quasi-steady approximation will break down when the radius of the inner most step is sufficiently small.

2. **Singular Nature of Collapsing Steps:** The linear approximation for C_i^{eq} in equation (2.12) is only valid if $|\mu_i/k_BT| \ll 1$. However, the chemical potential of step i can become arbitrarily large if it is the inner most step and its radius shrinks to zero, because of (2.13). In fact, many of our modeling assumptions break down when steps collapse. Because of the nature of cylindrical coordinates, we will also have singularities in quantities such as the equilibrium step density (2.30). These singularities manifest themselves in the equation of motion for the inner most step (2.33) through the $1/\rho_1$ and $\ln(\rho_2/\rho_1)$ terms. The assumption of circular steps for $\rho_1 \ll 1$ also breaks down.

Despite the apparent shortcomings of axisymmetric step flow equations, they are still powerful tools which can provide quantitative information about the evolution of crystal surfaces at the nanoscale. Step flow equations for axisymmetric structures have been used by previous researchers, and the generated results (over many collapses) have been validated by experiments. For example, in [116] and [114], predictions of step motion from step models are fitted to data points from experiments; also see [48] and [29] for more experimental results which show that the motion of individual steps is, qualitatively, very

similar to the plots which we will subsequently discuss in this chapter. While the equations in these papers are not exactly the same as (2.39)-(2.43), the researchers still assume a chemical potential which diverges as the step radius goes to zero, and they also use the quasi-steady approximation. Although some of our modeling assumptions are violated near the times of collapse, axisymmetric step flow models generally do seem to yield results which are in agreement with experiments.

3. **Far-field assumption for interaction potential:** The form of the interaction potential (2.14) is valid only when the distance between the steps is very large compared to a, the step height. When steps get close to each other, equation (2.14) may not be a good approximation to the actual interaction potential. In fact, Kukta et al. [65] showed theoretically that the potential between steps is more complicated than (2.14), and should contain terms which cause steps to attract each other. However, these attractive interactions only become important when steps are fairly close to each other. In particular, they showed that a step "bunch" containing N steps will attract a single step if they are $3 - 5a$ and $20 - 30a$ apart for $N = 10$; otherwise they will repel each other. Later on in this chapter, results on step bunching will be presented. Incorporating the effects of attractive interactions is not difficult, and is likely to cause step bunching to occur sooner. The qualitative nature of our results would probably be unchanged if we were to use the more realistic potential described in [65].

2.2.3 Other Modeling Considerations

1. **Arbitrarily shaped 2D steps:** Since 1951, much progress has been made on improving the BCF theory. One of the most natural generalizations is to relax the assumption of axisymmetry and consider closed steps of an arbitrary shape. The evolution of steps and island boundaries in this case is nicely formulated in terms of a Stefan problem, and many Stefan problems have been solved numerically using the level-set method [22], [37].

However, a (full) 2D analogue of the step model considered in this chapter is difficult to implement because: (i) the diffusion equation on each terrace has to be solved numerically in general; and (ii) analytic descriptions for the interactions between neighboring steps are not currently available[8]. As a result of (i), the number of steps that one can solve for is limited, and because of (ii), current level set simulations for 2D steps have been restricted to single-layer island dynamics [19], [98]. Recently, Margetis and Kohn [80] have developed a continuum theory for nanostructures where the steps have a slowly varying curvature, and in particular, they are able to solve (asymptotically) the diffusion equation between step edges.

The main phenomenon which is not seen when simulating perfectly circular steps is the step-meandering instability, as observed in experiments [121] and analyzed by Kandel and Weeks [58], and Bales and Zangwill [8]. When the instability happens, straight steps start to meander and develop extrema, giving the steps a "wavy" look. The steps, however, do not cross and meander roughly in phase with each other.

2. **Anisotropic Diffusion** Experiments [32] have shown that diffusion of terrace adatoms *along* step boundaries may compete with diffusion transverse to steps. Margetis [77] used this fact to explain different decay rates observed in experiments involving corrugated surfaces. For 1D corrugations, where transverse currents *across* steps are dominant, an exponential decay rate was observed [59]. However, in 2D corrugations, he argued that transverse currents along steps play an important role. These currents are responsible for the "inverse linear" decay seen in experiments [91], [34].

3. **Ehrlich-Schwoebel Barriers:** Our model takes $k_u/k_d = \alpha = 1$ in (2.20), so that the attachment-detachment barriers are symmetric on the boundaries of each terrace. Experiments using Field-Ion Microscopy on Tungsten [32] have shown, however, that adatoms are often 'reflected' at step boundaries. This

[8] Although information can be inferred from Atomistic Simulations: see [101] or [61], for example.

resulting inequality in k_u and k_d was modeled by Schwoebel and Shipsey [105] in terms of attachment-detachment probabilities. Since then, many models have taken this effect into account, see for instance [46], [103], but the actual activation energy barriers associated with k_u and k_d have only been estimated in experiments for a small number of materials – see Table 6 in [55] for example.

4. **Desorption and Deposition:** The derivation of equations (2.39)-(2.43) assumes that adatom transport is only restricted to the terraces, and that there is no mass exchange between the crystallite and the surrounding medium[9]. However, studies have been carried out where the effects of Desorption and Deposition *are* taken into account, dating as far back as the 50s: for example, see [85]; and [80], [49] and [46] for more recent work. To account for desorption and deposition effects, equation (2.4) is replaced with

$$D_s \Delta c = \frac{c}{T} - R \tag{2.53}$$

where the desorption process has associated with it a time constant T and the deposition of adatoms has a flux R. Step flow equations can then be derived in the same fashion, using the solution of this *forced* diffusion equation. In practice, to completely exclude desorption and deposition, one can immerse the crystallites in an inert medium such as hexane.

5. **General Step Interactions:** Step interactions were modeled mathematically over 20 years ago by Marchenko and Parshin [76]. These researchers used force dipoles to represent the stress field generated by an isolated, straight step edge: it is this stress field that is responsible for step interactions. Since then, the idea of using high order poles to represent stress fields has been developed by other researchers [64], [66], [100].

   In particular, Kukta et al. [65] show that step interactions can be attractive or repulsive depending on how far apart the steps are: for Tungsten, they predict

[9]Note: these conditions are relevant for experiments involving *relaxation* of surface profiles.

that steps steps of opposite sign attract when they are about 3 – 5 and 15 – 20 lattice constants apart, but otherwise, they repel (see Figure 3 of [65]).

Experiments by Pai et al. [90] for *same-signed* steps on Ag(110) show that steps do not interact at all when they are about 5 lattice constants apart, but repel when the inter step distance is about 7 lattice constants and attract when the distance is about 10 lattice constants.

6. **Step Permeability:** As well as attachment-detachment at step edges and diffusion on terraces, some researchers [89], [50] have also accounted for adatoms crossing, or "hopping over" step edges without being incorporated into the step first. This phenomenon is accounted for by introducing the notion of *permeable steps.* The experiments of Tanaka et al. [114] suggest that steps on Silicon can be remarkably permeable. The authors actually conclude from their experiments that the probability of an adatom hopping *over* a step is much greater than the step-incorporation probability. However, it should be noted that step permeability is *not* generally well understood and current theories for permeable steps are based on phenomenology.

7. **Effect of Direct Currents** Applying a Direct Current to a crystal surface is a very common way to induce motion in the steps. The resulting electric field causes a preferential drift in the adatoms. The experiments of Yagi et al. [121] show that in silicon, this drift is always toward the cathode. This drift has been incorporated into the BCF model by many researchers, see for example [111], [102], by including a $\mathbf{v} \cdot \nabla c_i$ term on the left hand side of (2.4) where the drift velocity $\mathbf{v}$ is induced by the electric field. The effect of Direct Current on steps will be discussed much more in the context of step bunching, in Section 2.4.1.

2.3 Terrace-Diffusion Limited (TDL) Kinetics

One of the most important features of Terrace Diffusion Limited structures is the *regular collapse of the inner most step.* Under TDL kinetics, for an initial conical

profile, this result is true for a wide range of values for g[10] A log-log plot of the collapse τ_n against n is shown in Figure B-26, indicating a strong n^4 scaling for τ_n as n gets large. In contrast, for ADL kinetics, "step bunches" can form and the inner most steps can collapse almost simultaneously, resulting in erratically spaced τ_n.

Remark 2.3.1 (Algebraic law for collapse times under TDL kinetics) *When diffusion across terraces is the dominant transport process on the surface of an infinite,* ***conical*** *nanostructure, the inner most step collapses according to*

$$\tau_n \sim \tau^* n^4 \tag{2.54}$$

as $n \to \infty$, where τ_n are the collapse times, and for a given initial step spacing, $\tau^*(g)$ is a function of g only. This empirical result was also demonstrated by Israeli and Kandel [50].

For non-conical initial shapes of the form $\rho_n = n^{1+s}$ where $|s| <\sim 0.3$[†] , (2.54) can be generalized to

$$\tau_n \sim \tau^* n^{\gamma(s)} \tag{2.55}$$

where $\gamma(s) = 4 + 3s$ if step line tension is dominant, or $\gamma(s) = 4 + 5s$ if step-step interactions are dominant. See Chapter 4.4.5 for more details on how these relations are derived.

Figures B-1, B-2, B-3 and B-4 show the results of integrating the step flow equations in the TDL case. Four different values of g were used. One can see immediately that, broadly speaking, the region in (ρ_i, τ) space can be separated into two subregions: one subregion where the steps are more or less uniformly spaced and do not move very much, and another that contains mainly the trajectory of the inner most step, collapsing regularly to zero. Separating the two regions, is a front consisting of cusps (most clearly visible in B-2). The approximate location of the front is indicated

[10]This has been tested for $g \sim 10^{-6} - 10$.

[†]There seems to be a critical value for s, s_{crit}, where for $s < s_{crit}$, there are only a finite number of collapses, no matter how many initial steps there are, and no matter how long the simulation is run. Empirically, s_{crit} was determined to lie somewhere between -0.425 and -0.45.

with a dashed line. We will be studying these results a lot more in Chapter 3, but for now, notice that:

1. For Figures B-1 and B-2, in the region which only contains the inner most step, the distance between the two inner most steps can become very large, relative to the spacing in the bulk. At the time of collapse, the distance between the two inner most steps can be as much as $30L$, (where L is the macroscopic length scale set by the initial step configuration) for $\tau = 2 \times 10^5$.

2. In Figures B-3 and B-4, the maximum distance between the first two steps is somewhat reduced. In B-3, this distance is about $20L$, and in B-4, it is about $8L$. The subregion underneath the dashed line occupies a much smaller region of the (ρ_i, τ) plot in B-3 and B-4, compared to Figure B-2.

3. If we label the steps $(\rho_1(\tau), \rho_2(\tau), ...\rho_N(\tau))$, then we see that ρ_1 collapses to zero after a finite time, then ρ_2 collapses after that, etc. The cusps which are most clearly visible in B-2 arise because at the time of collapse, what was originally the second step becomes the new first step and hence obeys a different equation of motion: instead of being governed by (2.40), it is now governed by (2.39). This accounts for the sudden change of sign in the $\dot{\rho}_i$. Steps which are only a few steps outside the first step also suffer discontinuities because of the local coupling in the equations. Although in reality, the acceleration of steps cannot be infinite[11], there can be very sudden changes in their velocities: see the experimental results in Figure 2 (c) of [116], for example.

We will study the properties of nanostructures under TDL kinetics extensively in this thesis. Chapters 3, 4 and 5 all concern the relaxation of nanostructures in the TDL case. For now, we only focus on the effects of finite-height, and for TDL kinetics, we can quantify these effects quite precisely.

[11]The discontinuities are a mathematical consequence of the equations and should not be taken literally.

2.3.1 Substrate Effects: the effect of finite-height

Before we begin our study of Substrate Effects, we note the following important assumption:

Remark 2.3.2 *The substrate effects considered here do not account for strain effects arising due to lattice mismatches between the crystal and the substrate, or the detailed energetics of the interface and adhesion mechanism. Therefore, bulk stress is not accounted for in the following analysis.*

Consider two axisymmetric crystalline structures, identical in every respect, except that one has an infinite number of concentric steps, and the other has only a finite number, and rests upon an infinite substrate (which can be regarded as being a step of infinite radius). When both crystals undergo relaxation, the differences in their subsequent morphologies can be attributed to the finite-height of the second crystal. We will refer to these differences as a 'Finite-Height Effect', or a 'Substrate Effect'. With regards to the choice of nomenclature, we will not use the term 'Finite-Size Effect', because this term is already used to describe a wide variety of other physical phenomena: for example, in [55] the term is used to refer to any effects that that are not accounted for by coarse-graining the motion of atoms in formulating continuum models, and in [27] a finite-size effect describes non-negligible curvature effects arising from finite, closed steps. Unrelated to the physics of surfaces, it is also used in the theory of phase transitions [70] and Computational Fluid Dynamics [108].

Many theoretical approaches to the evolution of crystal nanostructures below roughening have involved either semi-infinite, monotonic structures, i.e. structures with an infinite number of descending steps with a single facet [50], [109], [78], infinite monotonic structures with periodic boundary conditions, [102], or periodic, non-monotonic corrugations in 1D and 2D [99], [33]. In all these cases, the effect that the substrate has (if any) on the dynamics of the steps is either irrelevant (in the case of the periodic corrugations), or regarded as being unimportant because only the motion of steps far from the substrate are considered. Some work, however, has been done on substrate effects for crystals in equilibrium; for example, Kaishew's

theorem (see [83] and references therein) predicts how the presence of a substrate affects the shape of the Wulff plot and, hence, the Equilibrium Crystal Shape (ECS). The researchers in [27] also explore finite-height and interface effects in the context of the ECS and Meta-stable shapes [12].

In our approach, we account for finite-height effects under *near-equilibrium*[13] conditions simply by taking the infinite set of step flow equations in [78], and truncating the set after the N^{th} equation. Then, ρ_{N+1} and ρ_{N+2} are removed from the system by first taking $\rho_{N+2} \to \infty$, and then $\rho_{N+1} \to \infty$. This process leads to the definition of $\tilde{\Lambda}$ in (2.43).

There are many possible ways to measure how the substrate affects the morphology of the crystallite. One way would be to start two simulations: one with M_1 steps, and the other with $M_2 \gg M_1$ steps. We let the two structures relax, and then, for some $m \leq M_1$, sum the absolute differences in step radii for the m inner most steps. This would be a global measure of the finite-height effect. Another way would be just to see how the last few steps at the base of the finite crystallite evolve, and how their evolution differs from the infinite case.

What we will see in this section is that the growth of the facet can be affected by the presence of the substrate, and adopt the following procedure: for a structure with a finite number of initial steps (N say), measure the collapse times $\tau_n(g, N)$ where n denotes the collapse number, and g is the step-step interaction parameter in (2.21). Then, for an infinite structure with $N \to \infty$, repeat the procedure to obtain $\tau_n(g, \infty)$. The *difference* in the two sets of collapse times will be our measure of the finite-height effect:

$$\underbrace{E_n(g, N)}_{\text{Finite-Height Effect}} \equiv \tau_n(g, \infty) - \tau_n(g, N). \tag{2.56}$$

For sufficiently large N, we expect the collapse times to be very close to the infinite case, and thus $|E_n|$ will be small. With the onset of finite-height effects, E_n will devi-

[12] Meta-stable shapes are those which attain a local, but not global minimum in the surface free energy.

[13] "Near-equilibirum" means that we can apply linear kinetics equations (2.6) and (2.7) at step edges: for modifications to allow for non-equilibrium conditions, see [18].

ate from zero. This is fairly intuitive because one would expect finite-height effects to become important only when the facet can 'see' the substrate, i.e. when enough steps have collapsed so that the distance between the facet and the substrate is sufficiently small. Finite-Height Effects defined through (2.56) will provide quantification of what "sufficiently small" really means in this context.

There are several advantages for using E_n as a measure of the finite-height effect:

1. The E_n form a scalar sequence, and are therefore easier to study than the entire height profile as a function of space and time.

2. The time when finite-height effects become important can be easily quantified: it is that collapse time τ_n such that the corresponding value of $|E_n|$ is significantly greater than some pre-determined tolerance. Finite-height effects become important as soon as the motion of the inner most step is significantly affected by the presence of the substrate.

3. How strongly the finite-height effects manifest themselves can easily be quantified by calculating $|Min(E_n)|$ (it will turn out that E_n will have a local minimum in n). Here, we have made a particular choice of "norm", or measure, for E_n, but other choices are possible as well. We will discuss this point further later on in this section.

4. The algorithm used to integrate the step flow equations was specially designed to extract the collapse times accurately. Also, taking the difference of collapse times to obtain E_n is easier than making a pointwise comparison between two height profiles.

5. The concept of using E_n as a measure of the finite-height effects can be generalized to structures composed of layers of concentric steps of a fixed 2D shape, e.g. ellipses and triangles instead of circles. Even for non-circular steps, there are regular collapses of the inner most step, and $\tau_n(g, \infty)$ and $\tau_n(g, N)$ can still be computed[14]. However, one should note that in these cases, the steps do not

[14]This assumes that as steps gets smaller, they do not split into two or more islands, by "pinching off" in the middle.

evolve in a shape-preserving manner: as they shrink, they may become more circular as step line tension dominates.

Numerical Details on Evaluating $E_n(g, N)$

E_n is plotted as a function of n in two cases. In the first, we vary g (which is kept small) but keep N fixed, and in the second, we vary N but keep g fixed. The $\tau_n(g, \infty)$ are approximated with $\tau_n(g, 2000)$. The results are shown in Figure B-21, and B-22. In each case, we have a non-monotonic E_n. The curves all have a very similar shape, staying at zero for the first few n (as expected), and then rising up to a small local maximum, before dropping down to a local minimum and then finally rising up again. The feature which distinguishes one curve from the next is the location of the minimum – call this n^* – and also the magnitude of the minimum, which decreases as g decreases in B-21 and increases as N increases in B-22. The minimizer n^* indicates the step collapse number at which the facet starts to be most affected by the finite-height, τ_{n*} gives the *time* at which the inner most step is affected, and E_{n^*} quantifies the strength of the finite-height effect. The fact that E_n becomes positive, then negative, then positive again means that compared to an infinite cone with the same material properties (i.e. same value of g), the inner most steps are initially collapsing at the same rate, and then those for the finite cone collapse earlier, then later, then earlier again. These plots of E_n all look self similar, and it is natural to wonder if all these curves are simply stretched versions of each other. This motivates us to try to investigate how the geometric dimensions of each curve – characterized by n^* and $Min(E_n)$ – scale with N and g.

The results of this investigation are shown in Figure B-23: for the two plots on the right, a log-log plot of $Min(E_n)$ against $\log(N)$ indicates a $Min(E_n) \sim N^4$ scaling law, and plotting n^* against N yields a simple linear relation[15]. However, the plots on the left show results that are a lot less conclusive. There seems to be a linear relation between $\log g$ and n^*, and perhaps one between $Min(E_n)$ and $\log g$. The constant of proportionality in the latter, however, is very large ($\simeq -96$) and does not seem to

[15]To compute n^*, cubic splines were used to interpolate the data (n, E_n).

have any physical relevance. Any potential relation between $Min(E_n)$ and g we leave as future research, and we focus now on the relation between $Min(E_n)$ and N, where the scaling law is a lot more concrete. The scalings suggest that E_n has the similarity form

$$E_n = N^4 G\left(\frac{n}{N}\right) \tag{2.57}$$

for some function G. This form of similarity is verified in Figure B-24, which shows the expected data collapse. The interpretation of these results is that, for fixed g and N, finite-height effects become most significant after a certain fraction $f \equiv \frac{n^*}{N}$ of the steps have collapsed. When $g = 0.01$, this fraction is about $f \approx 0.43$ and when $g = 0.02$, $f \approx 0.40$. The lag in the collapse times of the finite crystal (compared to the infinite case) also becomes more pronounced as N increases, with the lag scaling as N^4. Whether a similarity collapse of the form $E_n(g) = f_1(g)F\left(\frac{n}{f_2(g)}\right)$ (for some functions f_1, f_2 and F) also exists for the data in Figure B-21 is a question we hope to answer in future work.

Remark 2.3.3 *Our quantification of Finite-Height Effects does not assume that n is large, or that we have waited for sufficiently long times. In computing E_n, it would be quite natural to measure deviations, not from $\tau_n(g, \infty)$, but from $\tau^*(g)n^4$ (see Remark 2.3.1) because this asymptotic power law is a relatively well known result [50]. However, the law is only valid for long times and with this formulation, one could only draw limited conclusions about the effect of Finite-Height for large n, as a result. Furthermore, it is very likely that the similarity form (2.57) can be extended to algebraic shapes, (see Chapter 5) as in the collapse times of Remark 2.3.1. However, it remains to be seen whether the N^4 behavior is characteristic of the conical initial condition, or a fundamental property of the step flow equations which is shape-independent.*

We end this section on a note about the choice of norm used to measure E_n. It is likely that the scaling relation (2.57) will still be valid for any choice of norm. The 'size' of the E_n in Figure B-22 could also be captured, for example, by considering its integral: $\int E_n dn$, in which case the areas under each of the curves in B-22 would still scale as N^4.

2.4 Attachment-Detachment Limited (ADL) Kinetics

When diffusion across terraces is much faster than the attachment-detachment at step edges, we can take $m \to \infty$ in equation (2.20), resulting in (2.34). In this limiting case, diffusion across the terraces is modeled as being instantaneous, and the motion of the steps is controlled only by the attachment-detachment of adatoms at the step edges. Although all surfaces have a finite terrace diffusivity, it is still useful to develop a good understanding of ADL systems because more realistic *mixed systems* (see Section 2.5) can exhibit qualitative features which are characteristic of ADL systems. Intuitively, one would expect ADL-like behavior if and when steps get very close to each other ("bunch") because the time taken for an adatom to diffuse from one step edge to the next would be very small compared to the time it would take to attach onto the step edge. A more quantitative analysis of step bunching is presented in Section 2.5.

Step bunching is a phenomenon particular to ADL and mixed kinetics: when it occurs, steps cluster tightly together, leaving widely spaced terraces between the step bunches. This complicated phenomenon is characteristic of ADL systems in the sense that the step bunching instability never occurs in the TDL case [50]. In TDL systems, mass transport happens much more slowly between steps because it is mediated by the diffusion on the terraces, and the steps generally tend to be uniformly spaced.

Researchers have also tried to formulate continuum models for ADL systems in much the same way as for TDL systems: to write down PDEs governing surface evolution where the dynamics is governed by attachment-detachment of adatoms at step edges; for instance, see [78] or [86]. However, generally speaking, surfaces under ADL kinetics have very non-uniformly spaced terraces. In the presence of line tension and a single facet, steps with smaller radii have a tendency to bunch together. This means that the width of a general terrace defined by steps ρ_m and ρ_{m+1} can change drastically depending on whether the ρ_m and ρ_{m+1} are inside a single step bunch, or whether they belong to the edges of two separate bunches. In particular, the

step spacing *within* a step bunch is much smaller than the spacing *between* step bunches. Margetis et al. [78] point out that this phenomenon calls into question the assumptions made when approximating the stepped surface with continuum models such as PDEs. In particular, they state that a necessary consequence of a continuum description holding (for monotonic axisymmetric nanostructures) is:

$$r_{n+1} - r_n \ll r_n \tag{2.58}$$

$$\Rightarrow \frac{a}{F_n} \ll r_n \tag{2.59}$$

$$\Rightarrow \frac{a}{r_n F_n} \ll 1 \tag{2.60}$$

where a is the height of a single step, r_n is the radius of the n^{th} step and F_n is a local approximation to the slope at step r_n. Sufficient conditions for the PDE to hold are not known at present, but one possibility could center around the concept of step radii ρ_n varying sufficiently slowly as n increases.

This breakdown of continuum models is particular to ADL kinetics, in contrast to the TDL case (see Chapter 3) where continuum descriptions of steps are generally well understood and fairly common. However, there *are* current efforts to model ADL systems and step bunching instabilities with PDEs [81], [63].

2.4.1 Step Bunching Instabilities

The step bunching phenomenon has motivated much theoretical and experimental research [71], [121], [57]. Step bunching has applications to nanotemplates for the fabrication of quantum wires [1], [72], and potential applications for biological antifreeze agents [87] [3]: certain fish in the Antarctic and insects can survive even though their body temperatures are below the freezing point of water [92], and it is thought that this may be due to the presence of "biological" antifreeze proteins [38], [87] in their blood. These proteins are adsorbed onto the surface of the seeds of ice crystals. As the ice crystal grows via step flow, if enough of these proteins are present, they can 'pin' an advancing step of ice, and stop it from advancing any further. This

step pinning phenomenon has been studied using Atomistic Monte Carlo Simulations by Zepeda-Ruiz and co-workers [124] in Potassium Diphosphate (KDP) crystals. The step behind the pinned step advances and is pushed up against the pinned step, because interacting steps cannot cross. More and more steps are subsequently pinned, resulting in step bunching. This type of step bunching, however, is induced by deposition of metal impurities onto the crystal surface, and is not taken into account in the step flow model being considered in this thesis. In the majority of cases, however, step bunching is a phenomenon that workers in industry try to avoid, particularly in epitaxial applications. For example, in the manufacture of integrated circuits, where it is desirable to grow very pure wafers of silicon layer by layer, step *flow* is always preferred to step *bunching*, as the former results in a more homogeneous silicon, with better electrical properties. In all these cases, it is important to be able to understand the properties of step bunches and the fundamental mechanisms that can give rise to step bunching. In most experimental situations, step bunching is made to occur either through material deposition or through application of a Direct Current (see below). In this section, we will show that the effects of step line tension can also induce a step bunching instability.

The most common way to induce step bunching in straight steps is by application of a Direct Current [69]. This effect is not modeled in our equations of motion (2.39)-(2.43), but here we review some previous experimental work to show that step bunching is, in general, not well understood at a fundamental level. Details on how the equations of motion can be modified to account for electromigration effects were given in Section 2.2.3, Item 7.

Although it has been known since the early 90s that the presence of an electric field causes a bias in the diffusion of adatoms on terraces [110], how and whether the field affects step bunching is not well understood. In 1989, Latyshev et al. [69] reported the results of their experiments on Silicon wafers. They observed that the configuration of steps on the surface depended on the direction along which the Direct Current was applied, and also on the temperature. In particular, they found [69] that for temperatures in the range $1050°C - 1250°C$, application of a current in the step-up

direction caused step bunching, and application of a current in the step-down direction resulted in uniformly spaced steps. In the temperature range 1250°C – 1350°C, the behavior was reversed: a *step-down* current direction promoted step bunching, and a step-up current prevented it, thus having a stabilizing effect. In the range 1350°C – 1400°C, the behavior switched yet again. Kandel and Kaxiras [56] proposed that this switch in behavior was due to a competition between electromigration of adatoms and an "electron wind". However, this theory was later shown to be inaccurate by the experiments of Yagi and co-workers [121]. These authors show that between 830°C and 1300°C, the drift in adatoms is always in the same direction *regardless of whether the steps bunch up or stay uniformly spaced.* Hence, an explanation of the *temperature dependent* switch in stability must clearly take other factors into account, in addition to a drift effect. The paper by Yagi et al. [121] also reports many interesting phenomena related to step bunching and electromigration. For example, they observed that the step bunches can align at different angles with respect to the direction of the applied current: in some instances, the steps in the bunch orient themselves *along* the direction of the current, and in other instances, the step bunches are *perpendicular* to the current direction: see the pictures on page 90 of [121].

Step bunching can also be induced by depositing onto the surface from above. Hong et al. [46] grew thin films of $SrRuO_3$ on $SiTiO_3$ using Pulsed Laser Deposition [74]. Their experimental results suggest that for a fixed deposition rate, step bunching occurs if the vicinal surface is prepared with sufficiently wide terraces. Although our step flow equations (2.39)-(2.43) do not model deposition, or strain effects arising from a lattice mismatch, we will confirm that more widely spaced initial steps *do* result in a step bunching instability.

The theoretical understanding of step bunches has more or less progressed with the aid of Step Flow models [72]. Monte Carlo Simulations are generally too computationally expensive to provide quantitative results [71]. In the numerical experiments of Liu, Tersoff and Lagally [72], step bunching was induced by deposition onto the surface from above. Their straight-step flow model did not include the effects of line tension, but did include strain effects and attractive step interactions (recall that the

potential we used in (2.14) only accounts for repulsive interactions). Each of the step bunches in their simulations always had roughly the same number of steps as time progressed. They also found that the step bunches were relatively static in comparison with the individual steps, and that step bunches containing a larger number of steps moved more slowly compared to those with fewer steps. Lastly, as well as step bunching, they also noticed step *debunching*: that is, terraces within a step bunch could grow, resulting in a 'break up' of the step bunch. Although our model confirms some of the results mentioned above, the general qualitative behavior of relaxing circular steps is very different to the results in [72] where straight steps are forced to bunch and debunch because of deposition. The number of steps in our step bunches grows with time because the bunches tend to coalesce, forming larger bunches. It is rare (but not impossible) to find individual steps 'passing' between step bunches. We confirm that step bunches with more steps move more slowly (under the effects of line tension) compared to those with fewer steps. However, because we do not incorporate the effects of deposition, we do not see step debunching: our step bunching is an irreversible process.

Krug and co-workers [63] used continuum equations, derived from a step flow model with an infinite number of straight steps, to describe step bunches. The step bunching in their equations is induced by the addition of a drift in the terrace diffusion to account for electromigration effects. Their investigations focused on structure *within* the bunch. They found that the local slope of the surface varies as one traverses the step bunch: outside, on the terraces, the slope is zero. As one enters the bunch, the slope increases, developing a maximum roughly in the middle, before decreasing to zero again: see Figure 3 in [63]. We notice a similar profile our step bunches, but have not analyzed the step bunch structure quantitatively.

Sato and Uwaha [102] used a step flow model, without step line tension effects, to obtain a scaling for the step bunch interstep spacing with the step-step interaction parameter. Their step flow model used periodic boundary conditions, and so did not account for substrate effects or facets, but they did incorporate the effects of evaporation, and adatom drift. We will present a similar result for how the step

bunch *width* scales with the interaction parameter[16]: in our model, it is difficult to control the number of steps within a bunch.

Finally, the step simulations (for relaxation) of Israeli and Kandel [50] must be mentioned, because a lot of the work in this thesis builds directly on their research. Our step model uses an identical geometry to theirs, modeling the step line tension in the same way, but has a finite number of steps. Their main result for step bunching was to show that, for a unit initial step spacing, step bunching occurred for sufficiently small values of g, the interaction parameter which measures the strength of step-step interactions relative to the step line tension (see (2.21)). We will show that step bunching can be made to occur for any value of g providing the initial terrace width is sufficiently large and integration is performed for sufficiently long times.

This survey of the models for step bunching reveals that, in general, (with the exception of [50]) the effects of step line tension are not included. The reasons for this are geometric and computational in nature: for step line tension to be correctly modeled, steps must be closed, and models for arbitrarily shaped 2D steps are, in general, difficult to implement, as we have already mentioned in Section 2.2.3, Item 1.

Although the ADL results in Figures B-7 – B-10 seem to exhibit a very complex behavior, there are some features that are consistent in all three plots, and are likely to be robust features of step bunching under line tension – robust in the sense that they probably still hold in many non-axisymmetric geometries. A summary of observations on Figures B-7 – B-10 now follows:

1. Individual step bunches which are on the outside of a *collapsing* step bunch tend to merge shortly after the collapse occurs.

2. The step bunches contain more and more steps as time progresses because step bunches keep merging with one another and form larger bunches.

3. Step bunching starts near the facet, and propagates into the bulk. As time

[16]The width of the step bunch is simply the radial distance between the inner most and outer most step in the bunch

increases, more and more steps in the bulk bunch up. There is clearly a region where steps are uniformly spaced, a region where step bunching has occurred, and a (relatively thin) region where there is a transition between the two states. Since the step bunching starts at the inner most steps, and gradually spreads outwards, we infer that the step bunching instability in the simulations is due to step line tension, as emphasized in Remark 2.4.1, below.

4. The step bunch closest to the facet changes its width with time as it collapses. In particular, the width seems to be practically zero at the actual time of collapse. This effect is not seen in the simulations by Sato and Uwaha [102] where straight steps were used and facets were absent.

We shall now address each of these points separately, and in more detail. As the inner most step bunch collapses, there is a gradual emission of adatoms produced from the layer decay. When g takes very small values, step bunches only experience weak interactions with one another, and any kind of small perturbation to their positions is liable to make them merge. This steady current of adatoms provides this perturbation, and the step bunches immediately outside of the collapsing step bunch go through a complex transient motion before forming larger step bunches. This proposed mechanism for step bunches bunching up can also be applied to individual steps.

The merging of step bunches into larger step bunches was already observed by Sato and Uwaha and shown clearly in their numerical results: see Fig 1 in [102]. In the initial stages of step bunching, steps usually pair up, and these pairs then combine with other pairs to form bunches of four. Some of the steps however, cluster together in bunches of three, initially. Probably, the details of the initial clustering process are very sensitive to step positions, and are not a robust feature of step bunching: this sensitivity is shown in Figures B-13 and B-7. The two plots use the same simulation parameters and initial conditions, but B-13 had a smlla perturbation added to the initial step positions. Both plots show step bunching, but the way that steps bunch together in each plot is very different.

Remark 2.4.1 *Figures B-7 – B-10 show a feature that is not present in the step bunching of straight steps [102]: the step bunching starts at the inner most steps and slowly propagates outwards, causing more and more steps to bunch up as time progresses, thus confirming the step bunching plots in [50]. This behavior strongly suggests that step bunching in the simulations is a direct effect of the step line tension: providing the system admits the step bunching instability, steps with high curvature are more likely to bunch up than steps with lower curvature.*

Wth regards to Item 3 above, it is interesting to compare the region in which step bunching occurs in Figure B-7 to the region under the dashed line in B-2 which approximately defines the location of the facet in TDL kinetics. In the TDL case, under the dashed line, individual steps rapidly collapse. In the ADL case, it is not individual steps that collapse, but rather, step bunches.

The steepening of step bunches mentioned in Item 4 above is characteristic of step line tension effects: this phenomenon is not observed in the straight-step numerical experiments of Sato and Uwaha [102], but *is* present in the results of Israeli and Kandel [50]. This steepening is started by the motion of the two outer-most steps in Figure B-12, which clearly shows the effect of having an ADL structure rest on an infinite substrate. The 29th step shrinks monotonically, forcing all steps inside of it to bunch up. The outer-most step in the structure grows monotonically and disappears off the plot: this outer-most step acts as a sink for all the emitted adatoms from the shrinking step bunch. The width of the step bunch goes to zero as the steps shrink because the line tension becomes increasingly dominant over step-step interactions as the bunch radius goes to zero. Hence, step repulsions are overcome in the limit of small radius, and the steps are all squeezed together, resulting in bunch steepening. This situation is also illustrated in in Figure B-10 for the inner most step bunches: since the distance between bunches is usually very large, the outer-most step in the bunch 'sees' a large terrace and behaves as though this terrace were the substrate.

2.4.2 Invariance of the Equations

The simulation results of Israeli and Kandel [50] for an initial cone show that for ADL surfaces, where the initial step spacing is unity (so the physical distance between steps is about $1000\mathring{A} \sim L$), step bunching occurs for sufficiently small values of the parameter g, which is proportional to the ratio of step interaction strength to step line tension (see equation (2.21)). Typically, step bunching is predicted to occur when $g <\sim 10^{-4}$. The actual values of g vary from material to material, and also depends on the orientation of the surface as characterized by the Miller Index – see Table 7 of [55]. In fact, from this table, the value of g_3 for Silicon can range over several orders of magnitude (from 10^{-3} – 10^{2}) depending on the Miller index. The important point to note in the case of ADL systems initialized with equally spaced steps is that it is not g which has to be 'small' for step bunching to occur, but rather, it is the value $g/(\text{step-spacing})^2$ which must be small compared to unity. We will now show this result.

Although the ODE system (2.39) – (2.43) is very complicated we can consider scaling transformations which leave the equations invariant. Instead of treating the full set of equations, it is sufficient just to consider the simplified 'pseudo-equation'

$$\frac{d\rho}{dt} \sim -\frac{1}{\rho}\frac{\frac{1}{\rho}+g\frac{1}{\rho^3}}{\frac{1}{\rho}}, \tag{2.61}$$

$$= -\left(\frac{1}{\rho}+g\frac{1}{\rho^3}\right), \tag{2.62}$$

Equation (2.62) should be compared with equation (2.35). We simplified equation (2.35) in this way because we only want to see if the equation is invariant under certain stretching transformations of the "representative" variables and parameters ρ, t and g. In essence, the first term on the right of (2.62) represents the step line tension, and the second term represents the step-step interactions. If g is taken to be 0, we are left with $\dot{\rho} = 1/\rho$, which is the evolution equation of a single circular island shrinking under the effects of curvature.

The pseudo-equation (2.62) is invariant under the transformation

$$\begin{aligned} \rho &\rightarrow M\rho' \\ g &\rightarrow M^2 g' \\ t &\rightarrow M^2 t' \end{aligned} \tag{2.63}$$

As a consequence of this invariance, a step bunching instability for a certain (small) value of g and a given step spacing, can also occur with a larger value of g, but by starting with a configuration of more widely spaced steps, and waiting for longer times (or equivalently using higher temperatures). For example, in the simulations by Israeli and Kandel [50], step bunching for an initial step train with a spacing of unity was observed when $g = 10^{-6}$ (see Figure B-7), but when g was larger at 5×10^{-4}, no such instability occurred (Figure B-6). The invariance of the equations predicts that in fact step bunching can be made to occur when $g = 5 \times 10^{-4}$ as long as a step spacing greater than $\sqrt{500}$ is used in the initial configuration of steps, and thus one would have to wait 500 times longer to see an identical (ρ_n, t) plot with a stretched ρ_n variable. This prediction is confirmed in Figure B-8, and the invariance property is also illustrated by Figure B-9.

It should be noted that although the results in B-7 and B-8 exhibit many features which are qualitatively similar, they are not identical. Mathematically, because of (2.63), one plot should simply be a scaled version of the other – providing the integration of (2.39)-(2.43) was carried out exactly. Numerical integration of ODEs is never done with perfect accuracy, of course, and there are always local truncation errors associated with any given numerical scheme. When step bunching occurs, the behavior of the governing equations is *very sensitive* to small changes in the spacing within step bunches because of the presence of terms which behave as $(\rho_{i+1} - \rho_i)^{-3}$. Figure B-13 shows that the exact details of how steps come together in the bunch are very sensitive to small perturbations in the initial conditions (compare this Figure with Figure B-7, which does not have a perturbation in the initial condition). Small errors made in calculating $(\rho_{i+1} - \rho_i)$ can result in large changes in the velocity of the step. This is confirmed by the work currently in progress by Margetis and Rosales

[81] who use continuum Lagrangian coordinates to derive a PDE governing surface evolution in ADL systems. The resulting PDE in this case resembles a Kuramoto-Sivasinky ('KS') equation [67], [107], and the solutions of this PDE are very sensitive to changes in the initial conditions.

What is interesting about results like B-7 and B-8 is that step bunching occurs spontaneously, when the simulations are initialized with uniformly spaced steps, providing $g/(\text{step-spacing})^2$ is made small enough. In most experimental situations, step bunching is usually forced to occur through application of a direct current, addition of impurities or initializing with a highly non-uniform step train. In general, step bunching instabilities have not been observed in clean samples with regularly spaced steps, in the absence of deposition/condensation, and without some sort of bias in the adatom diffusion; there does not seem to be any experimental evidence to confirm our step simulations. There are three possible reasons for this lack of evidence:

1. Actual values of $g = O((g_3/g_1)(a/L)^2)$ used in experiments are too large because the samples have been prepared with an initial terrace spacing (L) that is not large enough compared to the step height a. In our simulations, step bunching occurs for values of g less than about 10^{-4}. For Ag(110) at 210K, the ratio g_3/g_1 was calculated to be between 10^{-1} and 1 [77], and so for this system, the initial terrace width must be at least 100 times greater than the step height in order for step bunching to occur. The critical initial step spacing required to see step bunching is obviously material dependent because different materials have different values of g_3/g_1: for example, Si(111) which has a value of $g_3/g_1 \sim 50$ (see Appendix A) will require $L/a \sim 10^3$.

2. The times required for step bunching to occur are much greater than the duration of typical experiments. In the simulations, step bunching occured in a substantial number of steps[17] after about $\tau \sim 10^4$ ($\Phi/m \sim O(1)$, according to (2.37) and (2.38)). From (2.18), with $U \sim 5\mathring{A}$ / min, and $L \sim 100\mathring{A}$, these estimates amount to physical times of about 2×10^5 minutes which is nearly

[17] About 30-40 steps.

5 months. This time can be shortened by performing experiments at higher temperatures because this decreases the value of Φ in (2.37). Hong et al [46] also predict that for a fixed initial terrace spacing and deposition flux, step bunching will occur if the temperature is sufficiently high.

3. We have seen that the step line tension plays an important role in the step bunching mechanism observed in our simulations. However, our circular steps are highly idealized; if steps under normal experimental conditions are close to being straight, step bunching may be suppressed in the absence of material deposition from above, because curvature effects are not so important.

Nevertheless, these step bunching results are still useful. In particular, they may help us understand the basic mechanism of step bunching, purely in terms of step line tension and step interactions. Furthermore, our results provide a reference for the recent, ongoing work on step bunching in the generic framework of continuum Lagrangian coordinates [81].

2.4.3 Scaling of Step Bunch Widths

In this section, we investigate how step bunch widths scale with g, the interaction parameter. We define the *width* of a step bunch to be the radial distance between the inner-most step in the bunch and the outer-most step. Intuitively, one would expect the widths to decrease as the strength of the step-step interaction is decreased. However, we noted in point 4 of Section 2.4.1 that the widths of the inner most step bunches decreased with time, with the width going to zero at the time of collapse. Hence, we have to be careful about how we measure the step bunch widths.

Referring to Figure B-10 we see that although g has spanned 3 orders of magnitude, the qualitative nature of the results is not that different. In particular, the way the inner most steps bunch up is quite similar for all the plots. We choose to focus on the step bunch indicated by the arrows, and see if we can try to extract a scaling for the widths. The plots in B-10 show that the step bunching is well developed, and it is quite clear where the step bunches are, and how many steps are in a bunch. For

larger values of g, this is not usually so clear. For example, for the steps within the box in Figure B-9 a), step bunching is only starting to develop.

With the step bunch width depending on time, when should we measure the width? Since line tension clearly affects the widths, and the line tension of a step depends only on its radius in the axisymmetric case, we can delineate line tension effects by choosing to make our measurement at times when the step bunch radius takes certain values, r_0. In this investigation, we take r_0 to be the width of the inner most step in the step bunch [18] and study only the inner most step bunches, which are indicated by the arrows in Figure B-10. Only plots for three values of g are shown in B-10, but we will also measure the step bunch widths for other values of g, the results of which are very similar to those in B-10. Note that these inner most step bunches do *not* contain the same number of steps. The number of individual steps in each step bunch are given in the caption of Figure B-19.

The results in Figures B-19 and B-20 show that the scaling for the average widths and spacings within the bunch take the form

$$\text{step bunch width} \sim g^a \tag{2.64}$$

$$\text{spacing between steps} \sim g^b \tag{2.65}$$

where $a \simeq 0.33$ and $b \simeq 0.38$. Changing r_0 in each case does not significantly affect the value of either exponent. If there are N steps in a bunch, then the average inter step spacing is simply (Total step bunch width)$/(N-1)$. The small discrepency in the value of the exponents is caused by the number of steps in the step bunch increasing slightly as g decreases by orders of magnitude.

These results are very suggestive of the scaling

$$\text{spacing between steps, step bunch width} \propto g^{1/3} \tag{2.66}$$

when step bunching occurs, in agreement with [102]. This means that for a fixed initial

[18] Then r_0 will be a good approximation to the radius of the step bunch because $r_0 \gg$ the step bunch width.

step spacing, terms like $\frac{g}{(\rho_{i+1}-\rho_i)^3}$ in equations (2.39)-(2.43) are always $\sim O(1)$, and never vanish, no matter how small g is made. This type of singular limit, of course, is often seen in many *continuum* settings, the most well known probably being the inviscid limit in Fluid Mechanics: here terms like "$\nu\Delta u$" (where ν is the kinematic viscosity and u is the velocity field) always remain bounded away from zero because of the development of a spatially rapidly varying velocity, u, near boundaries, with the consequence that viscosity is non-negligible if one is sufficiently close to the boundary. Similarly, when describing step bunches, the step interaction term is always important and is $O(1)$ even as $g \to 0$, resulting in a 'discrete' singular limit. In fact, when g is set to zero, the equations governing step motion in the bulk reduce to

$$\dot{\rho}_i = -\frac{1}{\rho_i}\left(\frac{\rho_{i+1}-\rho_i}{\rho_{i+1}+\rho_i} - \frac{\rho_i-\rho_{i-1}}{\rho_i+\rho_{i-1}}\right). \tag{2.67}$$

Note the absence of terms which repel steps from one another. Steps are therefore free to pass through each other when g is actually set to be zero in the integration code. This situation is illustrated in Figure B-11. The crossing of trajectories corresponds to an overhang in the nanostructure: this is something which is never observed in realistic situations.

Finally, we end this subsection with the observation that step bunches in general do have some kind of internal structure: see the close up in Figure B-10. Typically, the steps which are right in the middle of the bunch have terraces which are narrower than those on the fringes. Krug [63] makes predictions on the structure within bunches in using a continuum theory, and his numerical experiments also suggest a 'diffuse' structure with tighter bunching/steepness in the middle. It would be interesting to compare our results with those in [63] quantitatively, but for now, we leave this possibility as a future potential research direction.

2.5 The General Case: Mixed Kinetics

When both the diffusion across terraces and the rate of attachment-detachment at step edges are comparable to one another, we take (2.36) as our governing equation in the bulk. Numerical simulations of step flow models in the general case, without the effects of line tension being incorporated, were carried out in [111] and [102]. Israeli and Kandel's [50] results on axisymmetric structures (with line tension effects included) concentrated exclusively on the limiting cases of ADL and TDL kinetics. Here, we go beyond [50] by considering the more realistic case of mixed kinetics.

Unlike the TDL and ADL cases, in mixed kinetics, the equations are not invariant under simple stretching transformations of the dependent and independent variables; in other words, one cannot apply arguments based on (2.63). Unlike the ADL case, where decreasing g is equivalent to increasing the initial step spacing and integrating for longer times, in the mixed case the initial step spacing and g are two truly independent parameters. Two step flow plots initialized with ($g = g_1$, initial spacing $= \delta\rho_1$) and ($g = g_2$, initial spacing $= \delta\rho_2$) for different g_1, g_2 and $\delta\rho_1, \delta\rho_2$ can never be mapped onto one another using linear stretches, no matter how long/short the integration is done for.

Two sets of results for mixed kinetics are shown in Figure B-14, for $g = 10^{-5}$ and $g = 10^{-3}$. Similar to the ADL results, a step bunching instability is seen when g is made sufficiently small. The plots in B-14 a) differ qualitatively from the previous ADL results, however, because one can see that the inner most step of the inner most bunch regularly separates away and rapidly shrinks. There are features in B-14 a) which are common to *both* the TDL result in B-2 *and* the step bunching ADL result in B-7.

Remark 2.5.1 *In the mixed case, we assume that the properties of the material are such that the rate of diffusion on the terraces matches the rate of attachment-detachment at step edges. This situation is characterized by taking* $m = D_s/(kL) = O(1)$ *in (2.36). However, we also have to bear in mind that the (physical) terrace widths will determine how fast a diffusing adatom will travel from one step to the*

next. From now on, in mixed systems, when we speak of regions of the structure being "dominated by diffusion" or "dominated by attachment-detachment", we do so with the understanding that this classification is based only on the ***local*** *geometry of the nanocrystal, and not on global properties of its steps (like the value of the kinetic parameter m, for example).*

In the following subsections, we will explore how ADL and TDL dominated regions on the surface of the crystalline structure compete with each other, and how these regions vary as the two parameters g and (initial step spacing) are changed. To see whether attachment-detachment or diffusion is prevalent locally at a given ρ_n on the structure, we use the following criteria, in reference to equation (2.41):

$$\ln \frac{\rho_{n+1}}{\rho_n} \ll \left(\frac{1}{\rho_n} + \frac{1}{\rho_{n+1}} \right) \tag{2.68}$$

$$\text{and} \quad \ln \frac{\rho_n}{\rho_{n-1}} \ll \left(\frac{1}{\rho_{n-1}} + \frac{1}{\rho_n} \right) \tag{2.69}$$

if attachment and detachment are dominant,

$$\ln \frac{\rho_{n+1}}{\rho_n} \gg \left(\frac{1}{\rho_n} + \frac{1}{\rho_{n+1}} \right) \tag{2.70}$$

$$\text{and} \quad \ln \frac{\rho_n}{\rho_{n-1}} \gg \left(\frac{1}{\rho_{n-1}} + \frac{1}{\rho_n} \right) \tag{2.71}$$

if terrace diffusion is dominant, and

$$\ln \frac{\rho_{n+1}}{\rho_n} = O\left(\frac{1}{\rho_n} + \frac{1}{\rho_{n+1}} \right) \tag{2.72}$$

$$\text{and} \quad \ln \frac{\rho_n}{\rho_{n-1}} = O\left(\frac{1}{\rho_{n-1}} + \frac{1}{\rho_n} \right) \tag{2.73}$$

if both diffusion *and* attachment-detachment are equally important.

Notice that these conditions depend on the radii of three consecutive steps. Figure B-18 shows the level curves of the function

$$F(\rho_n, \delta\rho_n) \equiv \ln \left[\frac{\ln(1 + \delta\rho/\rho_n)}{\frac{1}{\rho_n} + \frac{1}{\rho_n + \delta\rho_n}} \right] \tag{2.74}$$

where $\delta\rho_n \equiv \rho_{n+1} - \rho_n$ is the terrace width at ρ_n. The value of F indicates the relative magnitude of the logarithmic and fractional terms in (2.70) and (2.71) Thus, depending on whether $F > 0$ or $F < 0$ for two consecutive pairs of steps, (ρ_{n-1}, ρ_n) and (ρ_n, ρ_{n+1}), we can classify step n as either being ADL dominated, TDL dominated, or neither (which is the mixed case). In the following investigations, if $F > 1.38$, we classify the step as being Terrace Diffusion Limited, and if $F < -1.38$, we classify the step as being Attachment-Detachment Limited. This corresponds to the logarithmic terms in (2.68) - (2.71) being about 4 times greater than the fractional terms for TDL classification, and about 4 times smaller for an ADL classification.

In Figure B-18, if the n^{th} step is in the bulk, then we must stay on the right of the dashed line: clearly, $\delta\rho_n < \rho_n$ because otherwise $\rho_{n-1} < 0$ which is unphysical. The inner most and outer most steps are special because they only have one neighbor, and so it suffices to look at $F(\rho_1, \delta\rho_1)$ and $F(\rho_{N-1}, \delta\rho_{N-1})$ where N is the index of the last step. For the case of the inner most step, $\delta\rho_1 > \rho_1$ is allowed, and the whole region in $(\rho_n, \delta\rho_n)$ space in Figure B-18 can be used to determine whether the behavior is ADL/TDL/mixed.

Classification of Step Kinetic Behavior

From Figure B-18, we predict that a necessary condition for TDL dominance is that $\rho_n > 2$. For an infinite number of uniformly spaced steps, and a given fixed step width, providing we go far enough into the bulk steps ($\rho_n \to \infty$), terrace diffusion will be dominant. One would think that physically, the distinction between ADL and TDL behavior would stem from the positions of steps relative to one another. This is indeed the case for straight, parallel steps in the absence of line tension: repeating the derivation of the step flow model in Cartesian coordinates gives

$$A_i = \frac{C_{i+1}^{eq} - C_i^{eq}}{\frac{D_s}{k_d} + \frac{D_s}{k_u} + (x_{i+1} - x_i)} \tag{2.75}$$

instead of equation (2.8), where the positions of the steps are denoted by r_i instead of x_i. From (2.75), we see that classification of ADL/TDL at step x_i now will depend on

the relative magnitude of $\frac{D_s}{k_u} + \frac{D_s}{k_d}$ compared to $(x_{i+1} - x_i)$, and $(x_i - x_{i-1})$, i.e. only on the *relative* positions of steps. The dependence on absolute position in cylindrical geometry arises because of the presence of line tension which affects steps with a smaller radius more strongly.

Conversely, for a fixed distance from the axis of symmetry, shrinking the terraces on either side of the step eventually leads to ADL dominance, which (as we have seen) is characterized by the step bunching instability. Also, we can always get ADL behavior (for a fixed terrace width) by bringing the terrace closer to the axis of symmetry, providing the terrace width is small enough ($<\sim 2$).

When considering the inner most step, since we can now be on either side of the dotted line in figure B-18, in addition to the predictions above, the inner most step in the structure will be in the ADL case if its radius < 2.

2.5.1 Kinetic Dependence on Step-Step Interaction Parameter

The sequence of plots in Figure B-15 shows the eventual dominance of ADL over TDL as $g \rightarrow 0$ for a fixed step spacing. Step trajectories highlighted with a solid dot indicate that diffusion is dominant, and those highlighted with an empty circle indicate that attachment-detachment is dominant. As g becomes smaller, the TDL region retreats, and step bunching (and hence ADL behavior) is more prevalent. A trajectory was classified as being ADL if the log terms in (2.70) and (2.71) were 4 times smaller than the fractional terms, and TDL if the log term was four times greater – this same criterion was used in the next section when the step spacing approaches ∞.

This result makes intuitive sense because, as the strength of step interactions is decreased, steps are able to get closer to each other, meaning that transport through diffusion across terraces is faster, resulting in adatom attachment-detachment being the limiting rate process.

2.5.2 Kinetic Dependence on Initial Terrace Width

Figures B-16 and B-17 show a sequence of plots where g is kept fixed at 10^{-3} and the initial step spacing is decreased from 8.3 to 0.5. The system moves towards an ADL-like behavior as this happens. Again, this observation is consistent with our intuition because as we force the step spacing to be smaller and smaller, diffusion of adatoms from one step edge to the next becomes quicker, and attachment- detachment becomes rate limiting. Conversely, diffusion will be rate limiting as we make the initial terrace widths larger. Contrast this situation to the pure ADL case where increasing the spacing for a fixed g only makes step bunching more severe.

Chapter 3

Continuum Models: Multiscale Modeling of Facet Expansion

3.1 Chapter Overview

This chapter is concerned mainly with a Partial Differential Equation (PDE) model of surface relaxation[1]. The focus of the chapter is to test two different boundary conditions for the PDE, and see which resulting solution gives better agreement with data from simulation results. The two boundary conditions are called 'Continuity of Chemical Potential', and the 'Step Drop Condition'. Continuity of Chemical Potential only performs well when the value of the step-step interaction parameter (called ε in this chapter) is large. The Step Drop condition performs well for all values of ε, but implementing it requires the knowledge of a parameter involving *discrete steps*. We obtain this parameter from the step flow simulations.

3.2 Multiscale Modeling of Surfaces

All physical problems have multiple length and time scales: for example, a fluid has many levels of description, each one providing a different amount of detail. Consider

[1]Relaxation is the term used to describe surfaces which evolve in the absence of material deposition, evaporation and sublimation

a gas under conditions of room temperature and pressure. On length scales of the order of centimeters, or greater, the Navier-Stokes equations provide information on a fluid's velocity and pressure. When the length scales are comparable to a molecule's mean free path, the Navier-Stokes description becomes inadequate[2], and one can try to solve the Boltzmann Equation to obtain statistical information on, say, the number of molecules whose velocities lie within a certain range. At length scales of the order of nanometers, one can run Molecular Dynamics Simulations where individual particles collide with each other, and their interactions are explicitly modeled. Note that for a given length scale more than one of the models mentioned above could certainly be used because each of these models are valid over a different range of length scales and these ranges can overlap. The reference [30] elaborates on many of the points made here and later on.

Multiscale models describe physical problems across more than one length and time scale and they often involve different physical laws at each scale. There are various multiscale paradigms. For example, one can run a microscale and macroscale simulation concurrently in different physical regions of the problem, use the results from the microscale simulation as the "boundary conditions" for the macroscale one, and vice versa. An alternative is to first run a microscale simulation to deduce some material properties, constitutive relations, or parameters, and then use them as input to a macroscale model. It is common, especially in the derivation of PDEs, to start with a conservation law relating the density of the conserved quantity with its flux. The next step is to "close" the PDE, i.e. relate the fluxes back to the density. One typically uses empiricism or phenomenology in this case. The second multiscale paradigm can be seen as replacing this "closure step" with a less ad hoc process which is governed by the underlying physics of the problem.

Why should one use multiscale methods? Two reasons are presented here, and of course, they are not the only ones. The first reason is simply that one may be forced to consider modeling at more than one length scale in order to obtain satisfactory

[2]For example it no longer makes sense to talk about fluid 'packets' advecting with the flow, which means that concepts like a material derivative are not well defined

answers. There may be regions where microscale effects are always significant, and can never be just "averaged out". Keeping with examples in fluids, a well known example is the contact-line problem for two-fluid flow in a pipe [40]. Here, the idealized no-slip boundary condition resulting from a Navier-Stokes treatment conflicts with the condition of zero mass flux through the contact line. This problem can be resolved by introducing fluid slip at the wall: one way (and not the only way, but this was done in [40]) is to run Direct Simulation Monte Carlo (DSMC) [11] near the pipe wall to quantify the slip. The second reason to use multiscale methods is specific to materials engineering. Today, the design and fabrication of new materials has advanced to such a point that it is possible to physically engineer a material's atomic structure in order to increase, for example, its strength, ductility or electrical conductivity. However, deducing the properties of a material for a given microstructure through experiment and testing alone can be very expensive. On the other hand, running atomistic simulations *along with* performing experiments, and using the results in, say, a Finite Element Code, can make the design process less costly. It can also be very instructive to see how exactly the microstructure affects macroscale properties through simulations. For example, a lot of work has been done to study the dynamics of dislocations in crystals, and their effects on plasticity [123], [113].

There are many other examples of multiscale modeling. The method of Car and Parrinello [20] involves running a Molecular Dynamics simulation, but instead of using the empirical Lennard-Jones potential, it computes the interactions during run time using the Schrödinger equation, and assuming that the nuclei of the atoms are much more massive than the electrons [16]. Complex Fluids[3] also provide a rich source of multiscale problems. In [12], the viscosity of simple, dumbbell-shaped polymers immersed in a solvent, is modeled by considering Brownian forces acting on individual molecules. The Quasicontinuum method [112] blends together a finite element code with atomistic calculations to solve problems in nonlinear elasticity.

As a prototypical case of multiscale methods, we now focus on a two-scale problem

[3]Complex Fluids are fluids whose properties (for example, viscosity) are strongly influenced by the presence of a mesoscopic length scale [36]. Examples of Complex Fluids are colloidal suspensions and polymer solutions.

in the context of the axisymmetric step models derived in Chapter 2. By using an identical geometry, Margetis, Aziz and Stone [78] (referred to as 'MAS' from now on) derived a continuum theory for surface relaxation, incorporating the same physical effects, and then assuming that steps were close enough together that discrete steps could be replaced with a continuous *slope*. They arrived at a fourth-order nonlinear Partial Differential Equation (PDE) governing the evolution of the slope, thus providing a macroscopic scale description of the surface. The step flow model and the MAS PDE complement each other in their approach to describe surface relaxation. Continuum models have been criticized [52], [21] for not taking into account the effects of discrete steps of finite height, especially at facets. However, they provide a description of the surface in terms of only a few parameters, and continuum solutions can often be obtained using relatively modest computational resources. On the other hand, step flow models can provide the element of discreteness that is required when modeling the evolution of facets, for example, but are computationally much more expensive to implement.

The focus of this chapter is to combine both models to set up and solve the two scale problem for surface relaxation when the kinetics is limited by diffusion on terraces (TDL). The discrete model involves the coupled ODEs for steps derived in Chapter 2, and the continuum model involves the MAS PDE. The idea is to use the PDE on the parts of the surface where the slope profile can be well approximated with a continuous function, and to use the step model to help evolve the surface in places where the continuum fails: namely on facets. In this two-scale problem, our two, widely separated, length scales are: the microscopic length scale, which is determined by the height of a single step; and the macroscopic length scale, which is determined by the radius of a typical bulk step within a finite nanostructure.

Other Continuum Models

We have already discussed some features of the MAS theory, and how we plan to combine it with a step model to accurately capture the step dynamics on the facet. Now, we shall make a brief survey of a few other treatments of crystal surface evolution, to

put the MAS theory in perspective.

The most common way to model surface evolution is through a PDE. In the 1950s, Mullins [85], [84] derived an equation governing relaxation of a surface $h(x,y,t)$ *above* the roughening temperature, when surface diffusion was dominant. A key part of the derivation is to introduce the continuum concepts of surface free energy and surface chemical potential. The surface free energy functional, $F[h(x,y,t)]$, is defined as

$$F[h(x,y,t)] = \int \gamma(\nabla h) dA, \tag{3.1}$$

where the integral is taken over the entire surface. The quantity γ is called the *surface tension* and is assumed to depend only on the local normal. It takes two different forms, depending on whether the surface is above, or below roughening [53]:

$$\gamma(\nabla h) = \begin{cases} g_0 + \frac{1}{2} g_2 (h_x^2 + h_y^2) + \ldots & \text{above roughening} \\ g_0 + g_1 (h_x^2 + h_y^2)^{1/2} + \frac{1}{3} g_3 (h_x^2 + h_y^2)^{3/2} + \ldots & \text{below roughening} \end{cases} \tag{3.2}$$

where higher order terms depend on the precise physical assumptions. The coefficient g_0 is the surface tension for a reference flat surface, g_2 is the surface stiffness [55], g_1 is the energy to create an isolated step, and g_3 accounts for pairwise step interactions [78]. Note that γ is only an analytic function of $\nabla h = (h_x, h_y)$ above the roughening temperature. With F defined, the surface chemical potential is proportional to the change in F with respect to infinitesimal changes in the height profile $h(x,y,t)$, i.e.

$$\mu(x,y,t) \propto -\frac{\delta F}{\delta h} = -\frac{\partial}{\partial x}\left(\frac{\partial \gamma}{\partial h_x}\right) - \frac{\partial}{\partial y}\left(\frac{\partial \gamma}{\partial h_y}\right) \tag{3.3}$$

$$\propto \begin{cases} -g_2 \Delta h & \text{above roughening,} \\ -g_1 \nabla \cdot \left(\frac{\nabla h}{|\nabla h|}\right) - g_3 \nabla \cdot (|\nabla h| \nabla h) & \text{below roughening.} \end{cases} \tag{3.4}$$

Now, a PDE for the height profile comes from using a conservation law relating the height h to the surface current, J:

$$h_t + \Omega \nabla \cdot J = 0. \tag{3.5}$$

where Ω is the atomic volume. When surface diffusion is the dominant transport process,

$$J \propto -\nabla\mu. \tag{3.6}$$

Hence,

$$h_t \propto -\Delta^2 h \tag{3.7}$$

above the roughening temperature, but

$$h_t \propto -\Delta\left(g_1\nabla\cdot\left(\frac{\nabla h}{|\nabla h|}\right)+g_3\nabla\cdot(|\nabla h|\nabla h)\right) \tag{3.8}$$

below roughening. Since Mullins derived (3.7), researchers have directed their research efforts towards relaxation below roughening [86], [99], obtaining PDEs similar to (3.8). The main difficulty with (3.8) (apart from its nonlinearity) is that it is singular at $\nabla h = 0$. The singularity is associated the existence of a facet and is a direct consequence of the non-analyticity of $\gamma(\nabla h)$ below roughening.

The formation of facets has been observed experimentally [122] when a periodic corrugation is forced onto a high symmetry plane of the crystal. Above roughening, the corrugation maintains its sinusoidal shape as it decays, as predicted by (3.7). However, below roughening, flat facets appear at the extrema, giving the corrugations a trapezoidal shape (see [99] for an illustration). As the corrugation decays according to (3.8), the facets expand. It is worth pointing out at this stage that regularization methods do exist [97], which effectively "smooth out" the corners of the trapezoids, and replace the flat facet with a slightly curved surface. However, this method has been criticized because the regulator [4] has no physical meaning [51], and more importantly, the results from this method seem to differ from those generated through discrete simulations [52].

Spohn [109] pioneered the treatment of facet evolution as a free boundary problem. One of the geometries which he considered was a periodic corrugation on a high symmetry plane. He used a phenomenological, continuum framework and treated

[4] In the case of [97], the regulator is a small parameter added to $|\nabla h|$ to remove singularities in (3.8), so that $|\nabla h| \to \sqrt{|\nabla h|^2+\varepsilon^2}$.

the position of the facet edge as an unknown function of time. Therefore, he had to supplement his PDE with additional boundary conditions. One of these boundary conditions involved extending the concept of a chemical potential from the sides of the corrugation up to and onto the facet. In his paper, the solutions of the PDE were not checked against experiments or simulations. Hence, at the time, it was impossible to tell if his formulation of a free boundary problem was correct.

Following Spohn's [109] treatment, Margetis, Aziz and Stone [78] also formulated surface relaxation in terms of a free boundary problem. They also extended the chemical potential onto the facet, but their treatment was different in that their PDE was not phenomenologically motivated, but was derived by considering the continuum limit of a discrete set of step flow equations. The authors in [78] were also able to obtain limited results from the kinetic simulations of Israeli and Kandel [50], to validate their solutions. These results came in the form of *scaling laws*, and Margetis et al. [78] were able to confirm that (for example), the maximum step density in their solution scaled correctly as a power of the step-step interaction parameter. However, later on, it was found that the agreement with the simulation results was due to a small programming error. A correctly implemented version of the MAS PDE, along with the boundary condition enforcing continuity of step chemical potential actually resulted in the following: the slope profiles generated by the program were sometimes unphysical, and the resulting scaling laws *disagreed* with the results of Israeli and Kandel. Nevertheless, as we will see in the next section, there are many aspects of MAS which remain valid and are independent of the programming error. Their *analytical* scaling predictions for the boundary layer width is confirmed by the results of Israeli and Kandel [50], as is their $t^{1/4}$ prediction for the expansion of the facet radius with time.

In this chapter, we go beyond using scaling laws to test the continuum solutions: with the correct boundary conditions, we will see *pointwise* agreement between continuum solutions of the MAS PDE and step simulation results from Chapter 2.

3.3 The MAS Analysis, for $\varepsilon \ll 1$

The MAS PDE for surface relaxation describes the evolution of an axisymmetric nanostructure with a semi-infinite number of steps[5]. The structure has a single circular facet that continually expands with time. In a continuum description, the facet is usually idealized as being completely flat, and not containing any steps. In this case, the slope changes *discontinuously* at the facet edge, and the growth of the facet corresponds to the flat region translating vertically down, while expanding its width at the same time. This expansion is unknown apriori, and it is therefore natural to formulate the problem in terms of a free boundary [109].

In the MAS analysis, both the edge of the facet, denoted by $r = w(t)$, and the height of the structure at the facet edge, $h_f(t)$, are regarded as unknown functions of time (see Figure 3-1).

Remark 3.3.1 *In general, the notion of a* ***facet*** *really only applies in a continuum description of surface evolution. In the results of Figure B-2, B-3 and B-4, dashed lines indicate possible locations for the facet edge, but these choices are not unique. However, as* $\varepsilon \to 0$*, the notion of a facet in the context of the discrete simulations becomes more concrete. We will see later, that the region of high step density in B-1 shrinks to a curve* $w(t) \propto t^{1/4}$*, in the limit as* $\varepsilon \to 0$*. In this limiting case only, the facet becomes well defined. In the MAS description, the position of the facet,* $w(t)$ *is* ***always*** *well defined: it is that region such that for* $0 < r < w(t)$*, there are no steps, and therefore the step density is zero.*

Since the MAS PDE is of fourth order, a necessary condition for well-posedness is the inclusion of 6 boundary conditions. These conditions enforce: continuity of height, slope and adatom current at $r = w(t)$, and fix the two far field conditions for the slope. The sixth boundary condition used by MAS was the one first introduced by Spohn[109]. This involves extending the concept of a continuous step chemical potential up to the facet edge, and onto the facet itself. In this thesis, this boundary

[5]So that physically, the situation is the same as the one described by equations (2.39) - (2.43), but with $N \to \infty$.

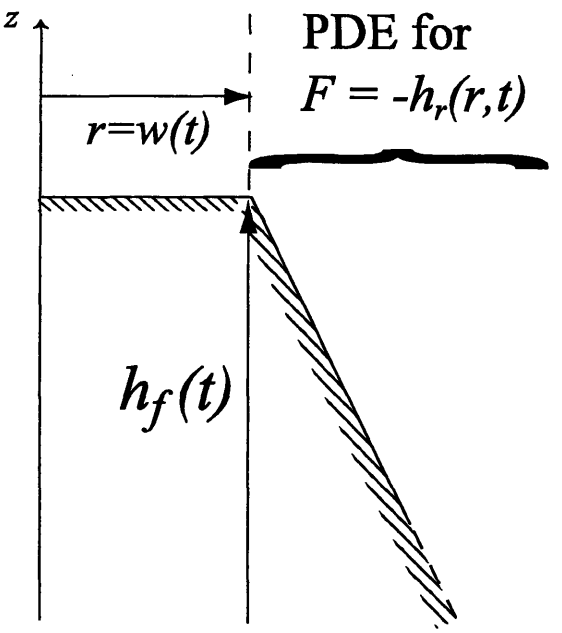

Figure 3-1: Side view of the axisymmetric nanostructure considered by MAS [78]. The structure has infinite height, $r = w(t)$ is the radius of the facet, considered as a free boundary, and $h_f(t) \equiv h(r = w(t), t)$ is the height at the facet edge.

condition will simply be referred to as "continuity of step chemical potential". For each step in the structure, one defines a local step chemical potential by considering changes in step free energy when a single adatom is added to or removed from that step. Step chemical potentials are only defined *at step edges*, r_i and r_{i+1}, say, and their role is to induce adatom currents on terraces between the edges, $r_i < r < r_{i+1}$. In the case of TDL kinetics, we have [78]

$$J_i(r) = -\frac{D_s c_s}{k_B T} \frac{1}{r} \frac{\mu_{i+1} - \mu_i}{\ln\left(\frac{r_{i+1}}{r_i}\right)}, \tag{3.9}$$

where J_i is the adatom current on the ith terrace, between steps i and $(i+1)$, D_s is the diffusivity on each terrace, c_s is the equilibrium adatom concentration at a straight step edge, k_B is the Boltzmann constant, and T is the absolute temperature. The step chemical potential at the ith steps is denoted by μ_i. However, when taking the continuum limit, so that step spacings become very small compared to the local step radius, the step chemical potential also generalizes to become a continuous function

of the radial coordinate (outside the edge of the facet) in which case, $r_{i+1} = r_i + \delta r$, $\delta r \ll r_i$, and $\ln \frac{r_{i+1}}{r_i} \sim \frac{\delta r}{r_i}$:

$$J(r,t) = -\frac{D_s c_s}{k_B T} \frac{\partial \mu}{\partial r}. \tag{3.10}$$

Enforcing continuity of chemical potential at the facet edge assumes that (3.10) also holds for $r < w(t)$, and therefore, an adatom current J_f can be defined through the conservation equation $\dot{h}_f + \Omega \nabla \cdot J_f = 0$ where h_f is the height at the facet, and Ω is the atomic volume. Then, $\nabla \cdot J_f$ can be integrated to obtain an 'extended' chemical potential on the facet: setting the chemical potentials to be equal inside and outside the facet leads to the sixth and final boundary condition for the PDE.

With regards to notation, MAS use ε to denote the strength of the step-step interactions relative to the step line tension. Because MAS assume that the nanostructure has unit slope in the far field as $r \to \infty$, they effectively set $L = a$ in (2.21), and so $\varepsilon = O(g)$ (see Appendix D.4.3). In this chapter, we will use both g and ε so that references to their paper are clear. We saw in Section 2.4.1 that in the case of ADL kinetics, $g \to 0$ is a singular limit. This is also the case in TDL kinetics. Figure B-5 shows that, similar to the ADL case, when step interactions are switched off, steps can cross. Because ε multiplies the highest derivative in the MAS PDE, the authors obtain a solution by using singular perturbation theory for $\varepsilon \ll 1$. Results from TDL step flow simulations [50] show that for small ε, steps cluster together locally near the facet, with the result that the slope there is maximal, and in fact grows as ε gets smaller. This behavior signifies the presence of a boundary layer near the facet, and we will see later on that quantitative aspects of this boundary layer are correctly predicted by MAS.

Probably the strongest criticism of the MAS analysis is the use of the boundary condition involving continuity of chemical potential. For small values of ε, the results in Chapter 2 suggest that as the top step is collapsing, the radial distance between the top step and the second step can be macroscopic: it is essentially comparable to the facet radius. One can therefore question the definition of a chemical potential through a relation like $J \propto -\nabla \mu$. On the other hand, if the facet radius is somehow forced to

become sufficiently small, then the step chemical potential boundary condition can probably be justified.

The key result in this chapter is to show that application of the step chemical potential boundary condition leads to results that disagree with those produced by the discrete step simulations when $g \ll 1$. However, the PDE produces the *correct* solution for all values of g when a 'Step Drop'[6] boundary condition first suggested by Israeli and Kandel [50] is applied instead. This condition is unusual in that its implementation requires knowledge of a parameter external to the PDE formulation, and involves the motion of the inner most step. Israeli and Kandel [50] call this parameter θ_0. This normally unknown external parameter is the cause of the 'uniqueness problem' which they faced when tackling this problem. Although they first suggested the Step Drop boundary condition, it appears that they did not actually implement it. Instead, what they did was to use the Step Drop condition to relate θ_0 to x_0^*, a scaled facet position, which is a constant. Then, they tuned x_0^* in order to make their continuum solutions resemble as closely as possible those predicted by their step flow model. to obtain a value for θ_0. It appears that they did not check this value of θ_0 with their simulation results. Hence, by implementing one fewer boundary condition than what was required, they were left with a free parameter, x_0^*, which led to a *family* of solutions and thus the uniqueness problem [50].

We shall take the opposite viewpoint, and accept that an accurate solution of the PDE for $g \ll 1$ must take into account the microscale step motion on the facet, the dynamics of which are normally invisible to any continuum formulation (and not just the MAS PDE). Therefore, the external parameter will come in the form of extra input from the discrete step flow equations.

At the heart of the MAS analysis is the fourth order nonlinear PDE:

$$\frac{1}{B}\frac{\partial F}{\partial t} = \frac{3}{r^4} - \varepsilon \frac{\partial}{\partial r}\nabla^2\left[\frac{1}{r}\frac{\partial}{\partial r}(rF^2)\right] \tag{3.11}$$

$$= \frac{3}{r^4} - \varepsilon\left(\frac{\partial^4 F^2}{\partial r^4} + \frac{2}{r}\frac{\partial^3 F^2}{\partial r^3} - \frac{3}{r^2}\frac{\partial^2 F^2}{\partial r^2} + \frac{3}{r^3}\frac{\partial F^2}{\partial r} - \frac{3F^2}{r^4}\right) \tag{3.12}$$

[6] A step on the facet does not really 'drop': rather, its radius decreases until it annihilates, at which point the height of the structure drops by an amount equal to the step height, a.

The goal is to take advantage of the size of $\varepsilon \equiv g_3/g_1$ and apply ideas from boundary layer theory to solve (3.11). Here, $F \equiv -\dfrac{\partial h}{\partial r}$ is the physical slope, r is the physical radial distance from the axis of symmetry, t is time and B is a material parameter defined as $B = \dfrac{c_s D_s \Omega^2 g_1}{k_B T}$ (see Appendix D for definitions of constants). In addition to this PDE being nonlinear, another problem arises due to the fact that this PDE is valid on the domain $(w(t), \infty)$ where $w(t)$ is the (currently unknown) radius of the facet (see Figure (3-1)).

Remark 3.3.2 (Step Density and Slope) *The quantity $F(r,t) = -\frac{\partial h}{\partial r}$ is the magnitude of the physical slope, but it will also be referred to as the "Step Density" (keeping with the terminology in [78]) frequently in this thesis. Strictly, this is not quite correct because the slope is dimensionless, whereas the step density has units of (length)$^{-1}$. The two quantities are proportional to each other, and related through*

$$a \times (\textit{Step Density}) = (\textit{Magnitude of Slope}) = -\frac{\partial h}{\partial r} \tag{3.13}$$

where a is the height of a single step.

We now review the derivation of the similarity solution for the MAS PDE when $\varepsilon \ll 1$. As a reminder, a particularly useful form of similarity solution is

$$F(r,t) = t^a f(\eta), \tag{3.14}$$

$$\text{where} \quad \eta = \frac{r}{t^b}. \tag{3.15}$$

Thus, $F(r,t)$ at any time t can simply be obtained by stretching an original 'template function' $f(\eta)$ horizontally by a amount t^b, and vertically by an amount t^a. We will use similarity solutions as a 'probe' into the MAS PDE, to test the two competing conditions: continuity of chemical potential, and condition of step drop. As a note for the remainder of this chapter, all of the plots for the continuum step density in this chapter will be made using the similarity variable as the independent one.

In the MAS Analysis, the boundary conditions corresponding to an initial *linear*

profile with unit slope (i.e. $h(r,0) = h_0 - r$ for some constant h_0) are:

$$\begin{aligned}
\text{Continuity of Slope } F(w,t) &= 0, && (3.16)\\
\text{Continuity of Height at } r &= w, && (3.17)\\
\text{Continuity of Adatom Current at } r &= w, && (3.18)\\
\text{Continuity of Chemical Potential at } r &= w, && (3.19)\\
F(\infty,t) &= 1, && (3.20)\\
\text{and } \frac{\partial F}{\partial r}(\infty,t) &= 0. && (3.21)
\end{aligned}$$

An 'outer' solution to (3.12) is obtained by setting $\varepsilon = 0$ and integrating:

$$\begin{aligned}
F_{outer} &= \frac{3Bt}{r^4} + 1 && (3.22)\\
&= \frac{3}{x^4} + 1, && (3.23)
\end{aligned}$$

where

$$x = \frac{r}{(Bt)^{1/4}} \tag{3.24}$$

is the similarity variable. To obtain the inner solution, for $\varepsilon \ll 1$, we balance the $\dfrac{\partial F}{\partial t}$ term on the left in (3.12) with the highest derivative on the right because we expect these two terms to be the dominant ones when ε becomes small:

$$\frac{1}{B}\frac{\partial F}{\partial t} \sim -\varepsilon \frac{\partial^4 F^2}{\partial r^4}. \tag{3.25}$$

Note that since r is bounded away from zero by $w(t) \neq 0$, the $\dfrac{3}{r^4}$ term in (3.12) will not contribute to the balance. We now need to obtain a similarity variable, η, for the inner solution. This variable must have a scaling with r and t similar to (3.24), but it must also account for a boundary layer which travels along with the expanding facet radius. The boundary layer width should scale as some power of ε. This motivates the form

$$F_{inner} = a_0 t^a f_0 \left(\frac{A(r - w(t))}{\varepsilon^m (Bt)^{1/4}} \right), \tag{3.26}$$

for some constant a_0 and some exponents a and m. The constant A has been introduced so that later on we can choose its value to simplify algebra, and $w(t)$ is the unknown facet width. Equation (3.26) iinplies that the characteristic boundary layer width $= O(\varepsilon^m)$. Furthermore, we assume that $w(t)$ takes the form

$$w(t) = w_0 t^c, \tag{3.27}$$

for some exponent c that will be determined. Substituting (3.26) into (3.25) gives

$$\begin{aligned}\left(\frac{at^{a-1}}{B}\right) a_0 f_0(\eta) + \left(\frac{At^a}{B^{5/4}\varepsilon^m}\right)\left(-\frac{rt^{-5/4}}{4} - \dot{w}t^{-1/4} + \frac{w(t)t^{-5/4}}{4}\right) a_0 f_0'(\eta) = \\ -\varepsilon^{1-4m}\left(\frac{A^4}{Bt}\right) a_0^2 f_0^{2''''}(\eta).\end{aligned} \tag{3.28}$$

For $r \approx w$, this reduces to

$$\left(\frac{at^{a-1}}{B}\right) a_0 f_0(\eta) - \left(\frac{At^a c w_0}{B^{5/4}\varepsilon^m}\right) t^{c-5/4} a_0 f_0'(\eta) = -\varepsilon^{1-4m}\left(\frac{A^4}{Bt}\right) a_0^2 f_0^{2''''}(\eta). \tag{3.29}$$

In order for the terms to balance for all time t, we need to take

$$a = 0, \tag{3.30}$$

$$m = 1/3, \tag{3.31}$$

$$c = 1/4. \tag{3.32}$$

Hence the expansion of the facet radius satisfies

$$w(t) = w_0 t^{1/4}, \tag{3.33}$$

as predicted by MAS, the boundary layer width $= O(\varepsilon^{1/3})$, and the inner solution is

$$F_{inner} = a_0 f_0(\eta), \tag{3.34}$$

where

$$\eta = \frac{A(x-x_0)}{\varepsilon^{1/3}}, \tag{3.35}$$

$$x_0 = \frac{w(t)}{(Bt)^{1/4}} = \frac{w_0}{B^{1/4}}. \tag{3.36}$$

Equation (3.29) simplifies to

$$f_0' = \left(\frac{4A^3 a_0 B^{1/4}}{w_0}\right) f_0^{2''''}, \tag{3.37}$$

in which case we choose the constant A so that

$$\left(\frac{4A^3 a_0 B^{1/4}}{w_0}\right) = 1, \tag{3.38}$$

$$\Rightarrow A = \left(\frac{w_0}{4B^{1/4}a_0}\right)^{1/3} = \left(\frac{x_0}{4a_0}\right)^{1/3}, \tag{3.39}$$

in order to obtain the Universal ODE

$$\frac{d^3 f_0^2}{d\eta^3} = f_0 - 1. \tag{3.40}$$

Equation (3.40) is the result of integrating (3.37) and using $f_0 \to 1$ as $\eta \to \infty$. We will solve this equation numerically, later on. Now, we match the inner (3.34)and outer (3.26) solutions in the 'overlap' region $O(\varepsilon^{1/3}) \ll r - w \ll 1$:

$$a_0 = \frac{3}{x_0^4} + 1, \tag{3.41}$$

in which case, the full solution is given by Equation (91) in [78]:

$$F(r,t) \sim \left[\frac{3Bt}{w^4} + 1\right](f_0(\eta) - 1) + \frac{3Bt}{r^4} + 1, \tag{3.42}$$

$$\text{or} \quad F(r,t) \sim \left[\frac{3}{x_0^4} + 1\right](f_0(\eta) - 1) + \frac{3}{x^4} + 1. \tag{3.43}$$

Numerical Solution to the Universal ODE

Our solution is now complete, except for the numerical solution of (3.40). Let c_1 and c_3 be coefficients introduced into the expansion of f_0 as $\eta \to 0$ [78]:

$$f_0(\eta) \sim c_1\eta^{1/2} + c_3\eta^{3/2} \tag{3.44}$$

Each solution of (3.40) will be uniquely determined by a particular choice of (c_1, c_3). The aim of the numerical method will be to solve (3.40) for a given value of c_1, which is incorporated into the boundary condition, and from this solution, obtain a value for c_3. This procedure gives a relation between c_1 and c_3. First, however, we rewrite (3.44) as

$$f_0^2(\eta) \sim \underbrace{c_1^2}_{\alpha}\eta + \underbrace{2c_1c_3}_{\beta/2}\eta^2 + \ldots \tag{3.45}$$

Solving for f_0^2 with the (α, β) parameterization leads to more robust numerical procedures than solving with (c_1, c_3), because $f_0^{2\prime}$, $f_0^{2\prime\prime}$ and $f_0^{2\prime\prime\prime}$ are finite at $\eta = 0$. The boundary conditions used for f_0^2 are

$$f_0^2(0) = 0, \tag{3.46}$$

$$f_0^{2\prime}(0) = \alpha, \tag{3.47}$$

$$f_0^2(\infty) = 1. \tag{3.48}$$

For a particular value of α, a pseudospectral Newton iteration is used to solve this semi-infinite boundary value problem for f_0^2, and then the second derivative at $\eta = 0$ is numerically evaluated to obtain β through

$$\beta = \left.\frac{d^2 f_0^2}{d\eta^2}\right|_{\eta=0}. \tag{3.49}$$

This gives a relationship between α and β, and hence a relationship between $c_1 = \sqrt{\alpha}$ and $c_3 = \dfrac{\beta}{4\sqrt{\alpha}}$, which we shall call

$$c_1 = S(c_3). \tag{3.50}$$

Appendix C contains more details on the pseudospectral method.

3.3.1 Summary of the MAS Analysis

The solution to (3.11) for $\varepsilon \ll 1$ is

$$F(x) \sim \underbrace{\left[\frac{3}{x_0^4} + 1\right]}_{a_0}(f_0(\eta(x)) - 1) + \frac{3}{x^4} + 1, \tag{3.51}$$

valid on $x_0 < x < \infty$ where f_0 satisfies (3.40) and $\eta = \dfrac{A(x - x_0)}{\varepsilon^{1/3}}$, $x = \dfrac{r}{(Bt)^{1/4}}$ and $x_0 = \dfrac{w(t)}{(Bt)^{1/4}} = \dfrac{w_0}{(Bt)^{1/4}}$. The function $f_0(\eta)$ is parameterized by a pair (c_1, c_3), so the composite solution (3.51) contains 5 unknown constants, c_1, c_3, x_0, A and a_0. As a note for future reference, in the original MAS analysis, their $\tilde{w}$ is related to our constants through

$$\tilde{w} = \left(\frac{x_0^4}{4a_0}\right)^{1/3} = x_0 A. \tag{3.52}$$

Equation (3.12) is to be solved using the 5 conditions [78]:

$$\begin{aligned}
a_0^2 x_0 A(3\varepsilon^{2/3}c_1^2 + (x_0 A)^2) &= 3, \quad \text{(Height and Current)} && (3.53)\\
a_0^2 \varepsilon^{1/3} x_0 A(3\varepsilon^{1/3}c_1^2 - 4x_0 A c_1 c_3) &= 3, \quad \text{(Chemical Potential)} && (3.54)\\
4a_0 A^3 &= x_0, \quad \text{(from 3.39)} && (3.55)\\
\text{and } a_0 &= \frac{3}{x_0^4} + 1, \quad \text{('overlap condition')}, && (3.56)\\
c_1 &= S(c_3). \quad \text{(solution to (3.40))} && (3.57)
\end{aligned}$$

In order to obtain the full solution, the constants x_0, A, c_1, c_3 and a_0 must be obtained numerically by solving the five equations (3.53)-(3.57). Appendix C contains more

details on this.

3.3.2 Conclusions of the MAS analysis, with Continuity of Chemical Potential

If one solves the 5 equations (3.53)-(3.57) one obtains the following scalings numerically:

$$c_1 = O(1) \tag{3.58}$$

$$c_3 = O(1) \tag{3.59}$$

$$a_0 = O(\varepsilon^{-1/2}) \tag{3.60}$$

$$\tilde{w} = x_0 A = O(\varepsilon^{1/3}) \tag{3.61}$$

$$x_0 = O(\varepsilon^{1/8}) \tag{3.62}$$

The analytical predictions made by MAS conflict with these scalings and are in fact, the correct ones, agreeing with simulations from Israeli and Kandel [50].

The numerical scalings (3.58)–(3.61) predict that the magnitude of F is determined not by the inner solution $f_0(\eta)$, but by the size of $a_0 = O(\varepsilon^{-1/2})$. Figure B-33 a) shows that as a result of (c_1, c_3) not scaling with ε, the solutions to (3.40) do not vary much as ε changes (see also Figure B-34 b)). The lower plot B-33 b) shows the similarity solutions constructed using the composite formula (3.51). These curves are constructed from $f_0(\eta)$, the inner solution, using the constants x_0, A and a_0. Apart from generating solutions that are an order of magnitude too large compared to step flow simulations (see Figure B-34 a)), the boundary condition also generates values for a_0 that force the step density to become *negative* for sufficiently small ε, which is of course, unphysical.

Also, the width of the boundary layer, predicted as being

$$O\left(\frac{A}{\varepsilon^{1/3}}\right) = O(\varepsilon^{-1/8}) \tag{3.63}$$

is unphysical: as the strength of the step interactions decreases, one would expect the steps to bunch together more tightly at the facet edge, leading to a *decrease* in the width of the boundary layer. It should be stressed that all these unphysical results were obtained by imposing continuity of chemical potential at the facet and taking $\varepsilon \ll 1$.

3.3.3 The 'Step-Drop' Condition

In light of the huge discrepencies between the solutions generated by imposing continuity of chemical potential and the results from simulations, a natural next step is to try to use alternative boundary conditions. The new condition that we will implement was first suggested by Israeli and Kandel [50] and will be the focus of this chapter from now on. We will discuss the nature of this condition and its implications much more in Section 3.5 and in Chapter 4.

Recall from the simulation results of Chapter 2 that one of the main features of surface relaxation is the collapse of the inner most step under the effect of line tension. In its simplest form, the step drop condition states that between two consecutive collapse times the height of the structure must drop by an amount equal to the height of a single step:

$$h(w^+, t_{n+1}) - h(w^+, t_n) = -a. \tag{3.64}$$

Here, a is the height of a single step, $h(r,t)$ is the height of the structure, $r = w^+$ is the limiting value for the facet width taken from $r > w$, and t_n are the collapse times of the inner-most step.

Although Israeli and Kandel first suggested the step drop condition, it appears that they never directly implemented it. Instead, by rewriting (3.64), they related the scaled facet width, x_0^*, to a parameter involving the discrete collapse of steps, which they called θ_0. Since (3.64) was never implemented, they had one too few boundary conditions, and as a result, x_0 was left as a free parameter. They did, however, 'use' the step drop condition in the following sense: they tuned x_0^* to make their solutions match as closely as possible the data generated by their step flow

simulations, and then from this value of x_0^*, found the corresponding θ_0. Without resorting to results from their step flow simulations, they were left with a *family* of step density functions, parameterized by x_0^* or θ_0. This 'uniqueness problem' was left unresolved in their paper [50].

The step flow TDL results presented in Chapter 2 for $g \ll 1$ show the development of a macroscopically flat facet at the top of the crystal. The width between a collapsing top step and its neighbor can therefore also become macroscopically large. The motion of single steps on top of the facet greatly influences those steps which are immediately below it, and the microscale motion at/on the facet needs to be captured accurately in order to predict the morphology *away* from the facet. However, the MAS PDE is a coarse grained formulation of surface evolution and the *step*, as a discrete entity cannot, therefore, be represented within this framework. Hence, we expect that obtaining Israeli and Kandel's unknown constant will probably not be possible within the PDE theory: one must treat the motion of discrete steps [7] in order to obtain its value. In this chapter, we will compute this constant using discrete step simulations, and see if implementation of the boundary condition (3.64) can lead to an improvement over the poor results seen in the last section.

Derivation of Step Drop Condition

The step drop condition in its present form involves the height profile, h. It turns out that it is possible to write the step drop condition in many different ways. Equation (3.64) is probably the most intuitive. However, to use it in the MAS PDE, we need to convert it into a condition involving F (and when implementing it as a condition for the inner solution in (3.51), we need to rewrite it in terms of c_1 and c_3).

Equation (3.64) is equivalent to

$$\int_{t_n}^{t_{n+1}} \frac{dh_f}{dt} dt = -a. \tag{3.65}$$

[7] One method to make progress may be to analyze a small subset of the step flow equations (2.39)-(2.43)

The height of the structure at the facet, $h_f(t)$ obeys

$$h_f(t) = h(r,t) + \int_{w(t)}^{r} F(r',t)dr' \tag{3.66}$$

$$\Rightarrow \dot{h}_f = \frac{\partial h}{\partial t}(r,t) + \frac{d}{dt}\int_{w(t)}^{r} F(r',t)dr' \tag{3.67}$$

$$= \frac{\partial h}{\partial t}(r,t) + \int_{w(t)}^{r} F_t dr' - \underbrace{F(w,t)}_{=0\text{: see (3.16)}}\ \dot{w} \tag{3.68}$$

$$\Rightarrow \dot{h}_f = \int_{w(t)}^{\infty} F_t dr', \tag{3.69}$$

taking $r \to \infty$ and using the fact that $h(r,t)$ does not change in time in the far field. Therefore,

$$\int_{t_n}^{t_{n+1}} \int_{w(t)}^{\infty} \frac{\partial F}{\partial t}(r,t)dr\,dt = -a. \tag{3.70}$$

This is a very useful form of the step drop condition, written in terms of F. Notice that currently, (3.70) is a condition that is *non-local* in both time and space[8]! It involves integrating through the whole step density profile, from the facet edge to $r = \infty$ and a time integration from collapse time t_n to t_{n+1}. It is fortunate, therefore, that this condition can be hugely simplified if F, the step density, has some special properties. The two key properties that transform (3.70) into *local conditions in time and space* are:

1. If the PDE for $F(r,t)$ is a conservation law of the form $\dfrac{\partial F}{\partial t} + \dfrac{\partial Q}{\partial r} = 0$ for some flux Q, then the Step Drop Condition becomes local in *space.*

2. If F is self-similar, then the Step Drop Condition becomes local in *time.*

Both of these points will be discussed further in Section 3.5. The main purpose of the next few sections is to derive a usable form of the step drop condition, implement it, and show that it gives results which agree with simulation data.

[8]and hence is not a 'boundary' condition.

Here, we convert (3.64) into a condition which will replace equation (3.54).

$$\begin{aligned} \Rightarrow h_f(t_n) - h_f(t_{n+1}) = \int_{w_n}^{r} dr' F(r', t_n) \quad &- \quad \int_{w_{n+1}}^{r} dr' F(r', t_{n+1}) \\ &+ \quad h(r, t_n) - h(r, t_{n+1}) \end{aligned} \tag{3.71}$$

where $w_n \equiv w(t_n)$. Now, we proceed to calculate $\int_w^r dr' F(r', t)$ using the composite solution (3.51) and the Universal ODE (3.40):

$$\begin{aligned} \int_w^r dr' F(r', t) = \left(\frac{a_0 \varepsilon^{1/3}}{A}\right) \int_0^\eta d\eta' \underbrace{(f_0(\eta') - 1)}_{f_0^{2'''}} [(Bt)^{1/4}] \\ + \left[\frac{1}{x'^3} + x'\right]\Bigg|_{x_0}^{x} [(Bt)^{1/4}], \end{aligned} \tag{3.72}$$

where

$$\eta = \frac{A}{\varepsilon^{1/3}} \frac{(r - w)}{(Bt)^{1/4}}, \tag{3.73}$$

$$x = \frac{r}{(Bt)^{1/4}}. \tag{3.74}$$

Taking $r \to \infty$ in (3.71) gives

$$h_f(t_n) - h_f(t_{n+1}) = \int_{w_n}^{\infty} dr' F(r', t_n) - \int_{w_{n+1}}^{\infty} dr' F(r', t_{n+1}) \tag{3.75}$$

where we have used the fact that $h(r, t)$ does not change in time, as $r \to \infty$. This implies that

$$\begin{aligned} h_f(t_n) - h_f(t_{n+1}) = -\left(\frac{4 c_1 c_3 a_0 \varepsilon^{1/3}}{A}\right) [(Bt_n)^{1/4} - (Bt_{n+1})^{1/4}] \\ + \left[\frac{1}{x_0^3} - x_0\right] [(Bt_n)^{1/4} - (Bt_{n+1})^{1/4}] \end{aligned} \tag{3.76}$$

where we have used (3.72) and $f_0^{2''}(0) = 4c_1c_3$ from (3.45). Now, it is observed from step flow simulations that after a large [9] number of steps have collapsed, the collapse times obey a relation of the form

$$\tau_n \sim \tau^* n^4 \tag{3.77}$$

as $n \to \infty$, where n is the collapse number, and τ^* is a constant, and τ^*, τ_n are related to t^*, t_n through some multiplicative factors (details in Appendix D). Therefore, we have

$$(Bt_n)^{1/4} - (Bt_{n+1})^{1/4} = -(Bt^*)^{1/4} \tag{3.78}$$

and so with the step drop condition (3.64),

$$\left(\frac{4a_0c_1c_3\varepsilon^{1/3}}{A}\right) - \frac{1}{x_0^3} + x_0 = \frac{a}{(Bt^*)^{1/4}} \tag{3.79}$$

$$\Rightarrow \left(\frac{x_0}{A^4}\right) c_1c_3\varepsilon^{1/3} - \frac{1}{x_0^3} + x_0 = \frac{a}{(Bt^*)^{1/4}} \quad \text{(using (3.39))} \tag{3.80}$$

$$= \frac{1}{\tau^{*1/4}}. \tag{3.81}$$

Discrete step simulations typically yield a value of $\tau^* \sim 0.22 = O(1)$, for $\varepsilon \ll 1$ (see Appendix C for some tabulated values of τ^*).

Hence, as Israeli and Kandel [50] discovered, implementation of the step drop condition requires knowledge of an external parameter intrinsic to the step motion near the facet. We call this parameter τ^*. Rather than try to derive its value within a continuum framework, we will simply obtain its value from step flow simulations.

Remark 3.3.3 (Scaling of c_1 and c_3) *An important corollory of (3.81) is that providing x_0 and A are $O(1)$ when $\varepsilon \ll 1$, then we have $c_1c_3\varepsilon^{1/3} = O(1)$. The curve $c_1 = S(c_3)$ from (3.50) is unchanged, which implies that $c_1 = O(c_3)$. Hence, $c_1, c_3 = O(\varepsilon^{-1/6})$, which verifies the data for the maximum value of F provided by Israeli and Kandel [50] in [78] providing $a_0 = O(1)$.*

[9] Typically 30 or more steps for $\varepsilon \approx 10^{-2}$ and unit step spacing.

Comparison of results

We now implement the Step Drop boundary condition to find similarity solutions to (3.11) when $\varepsilon \ll 1$. Figures B-35 and B-36 show the result of using the composite formula (3.51) together with the Step-Drop condition, superimposed on results generated from numerical simulations. The agreement with data from the fully discrete simulations is now much better than when continuity of chemical potential was enforced. Four different values of ε are used, and the agreement is better for smaller values of ε, which is to be expected because the boundary layer theory in MAS becomes exact in the limit as $\varepsilon \to 0$. Numerical Step Densities were obtained using the Profile Sampling Algorithm in Chapter 4, and for M inner most step collapses, sampling was started halfway between τ_{M-6} and τ_{M-5}. The choice to consider only the last 6 collapses is an arbitrary one. Typical values of M which were used ranged from 25-35, with the only requirement on M being that enough collapses should occur (and so integration is carried out long enough) so that the step profile density takes on a similarity form: see Chapter 4 for more details on all aspects of obtaining the similarity solution numerically.

The parameter τ^* in equation (3.81) involves the motion of individual steps. Instead of trying to derive its value, we used the value of τ^* predicted by the step flow simulations to implement the boundary condition (3.64) and obtained significantly better agreement with simulation data, compared to results obtained from using continuity of chemical potential at the facet. One could also imagine obtaining τ^* from an asymptotic analysis of the discrete step flow equations of motion (this would be quite a formidable task). In either case, because τ^* is a parameter which comes from the micro-scale step dynamics at the facet, it is unlikely that its value can be derived within the context of the PDE framework. However, because of the weak dependence of τ^* on ε, one can imagine doing just *one* step flow simulation for a particular value of $\varepsilon \ll 1$, obtaining τ^*, and then using this value as input for the Step Drop condition in the MAS Model for other (small) values of ε.

Figure B-37 shows the numerical values of c_1, c_3 and F_{peak} and how they depend on

ε. There is good agreement with the theoretical $c_1, c_3 = O(\varepsilon^{-1/6})$, scaling predicted in [78] provided ε is sufficiently small, and since $F_{peak} = O(\varepsilon^{-1/6})$, we have $a_0 = O(1)$, independent of ε. It then follows that $x_0 = O(1)$ from (3.56) and $A = O(1)$ from (3.55). It should be noted that in generating these data points, a fixed value of $\tau^* = 0.22$ was always used and was *not* computed from step flow simulation data. This simplification is enabled by the weak dependence of τ^* on the step interaction parameter ε.

The MAS theory together with the Step-Drop condition (3.64) contains a constant, a which is a finite atomic length scale in the problem. This condition is unusual because it introduces an element of 'discreteness' into the PDE. In fact, attempting to improve a continuum model by taking into account finite, atomic-size effects is not new. In simulations of thin-film sputtering, O'Sullivan and co-workers [88] incorporated a finite, atomic length scale into their level set codes to enhance 'breadloafing' effects at convex corners, and obtained better qualitative agreement with results from experiments and Monte Carlo Simulations.

The current results and method of solution are, however, still rather unsatisfactory for two main reasons. First, the method of finding the constants associated with the composite formula (3.51) is unnecessarily complicated. The details have not been stated here for sake of clarity, but have been documented in Appendix C. Second, there is still some discrepancy between the simulation data and the solution of the PDE even when the step drop condition is imposed. Whether this is due to the boundary condition being only approximately correct, or the nature of the asymptotic solution, which is exact only in the limit $\varepsilon \to 0$, is not clear. This latter consideration motivates us to relax the condition that $\varepsilon \ll 1$, to test more rigorously the validity of the step drop boundary condition, and furthermore to numerically compute the continuum solutions in such a way that evaluation of all associated unknown constants (such as a_0 etc.) is done simultaneously. The pseudospectral method used to compute the inner solution in (3.51) is basically a Newton iteration for f_0. The solution is discretized as a vector, $\mathbf{f}$ say, and the Universal ODE (3.40) implies that the components of $\mathbf{f}$ satisfy a system of algebraic equations: the more finely discretized

$\mathbf{f}$ is, the larger the system of equations. It would not require much more computational effort to incorporate the unknown constants (c_1, c_3, x_0, A, a_0) into the Newton iteration, because we would only be increasing the number of unknown variables by five. We would also supplement the algebraic system for $\mathbf{f}$ by equations (3.53), (3.55), (3.56), (3.57) and the step drop condition (3.81). This is in contrast to the current method where we first compute the inner solution f_0, and then *afterwards*, calculate all the unknown stretch and shift factors a_0, x_0 etc. in order to construct the full F in (3.51).

3.4 Extension to Arbitrary ε

In this section, we set up and solve numerically the MAS PDE for arbitrary values of ε. The motivation for doing this is to test the 'competing' boundary conditions at the facet: i) Continuity of Chemical Potential, and ii) The Step Drop condition. As before, the performance of each boundary condition is evaluated by comparing with simulation data from the step flow model.

Focusing again on the case of initial conical profiles, a self-similar solution to (3.11) is sought. Since the PDE is invariant under the stretching transformations

$$r \quad \to \lambda r', \tag{3.82}$$

$$F \quad \to \lambda^{-1} F', \tag{3.83}$$

$$\varepsilon \quad \to \lambda^2 \varepsilon', \tag{3.84}$$

$$t \quad \to \lambda^3 t', \tag{3.85}$$

a similarity solution is

$$F(r,t) = \varepsilon^{-1/2} f(\xi) \quad \text{where} \quad \xi = \frac{r}{\varepsilon^{1/8} B^{1/4} t^{1/4}}. \tag{3.86}$$

As before, we set $x \equiv \dfrac{r}{(Bt)^{1/4}}$, and $x_0 \equiv \dfrac{w(t)}{(Bt)^{1/4}}$ where $w(t)$ is the facet radius. When comparing with simulation data, F will be plotted against $x = \varepsilon^{1/8}\xi$, with the scaled

facet widths related through

$$x_0 = \varepsilon^{1/8}\xi_0. \tag{3.87}$$

Substitution of this form into the PDE (3.11) results in the following fourth order, nonlinear ODE for $f(\xi)$:

$$\frac{d^4f^2}{d\xi^4} + \frac{2}{\xi}\frac{d^3f^2}{d\xi^3} - \frac{3}{\xi^2}\frac{d^2f^2}{d\xi^2} + \frac{3}{\xi^3}\frac{df^2}{d\xi} - \frac{\alpha_0}{4}\xi\frac{df}{d\xi} - \frac{3}{\xi^4}f^2 = \frac{3}{\xi^4}, \tag{3.88}$$

where α_0 has been artificially introduced for convenience. This constant takes the value 1 in all physically relevant cases, but when $\alpha_0 = 0$ the ODE is linear in f^2, and can solved exactly. Exact solutions for this latter case are presented in Appendix C and can be used as a check on the numerical solution. Appendix C also contains details on the numerical solution to (3.88). We aim to solve (3.88) in terms of $f^2(\xi)$, so the boundary conditions must also be formulated in terms of f^2. Furthermore, in the numerical method, we take the domain of solution to be $[\xi_0, E]$ where $E \gg 1$, and then make sure that the solution is insensitive to changes in E.

3.4.1 Boundary Conditions at the Facet

The fourth order Equation (3.11) is to be supplemented with 6 boundary conditions because there are two unknown functions of time. The height of the structure at the facet $h_f(t)$ and the facet radius $w(t)$ are both unknown a priori.

The 6 boundary conditions are, as before:

1. Continuity of slope at the facet:

$$F(w^+, t) = 0. \tag{3.89}$$

2. Continuity of height:

$$1 + \varepsilon\left[-r\frac{\partial F^2}{\partial r} + 2r^2\frac{\partial^2 F^2}{\partial r^2} + r^3\frac{\partial^3 F^2}{\partial r^3}\right]\Bigg|_{r=w^+} = \frac{\dot{h}_f w^3}{B}. \tag{3.90}$$

Here, dot denotes differentiation with respect to time, and $h_f(t) \equiv h(w^+, t)$.

3. Continuity of surface current at the facet:

$$1 - \varepsilon \left[r \frac{\partial F^2}{\partial r} + r^2 \frac{\partial^2 F^2}{\partial r^2} \right] \Bigg|_{r=w^+} = -\frac{\dot{h}_f w^3}{2B}. \tag{3.91}$$

4. Constant slope, independent of ε, at infinity (1):

$$F(r,t) \to k, \quad \text{as} \quad r \to \infty. \tag{3.92}$$

5. Constant slope at infinity (2):

$$\frac{\partial F}{\partial r} \to 0, \quad \text{as} \quad r \to \infty. \tag{3.93}$$

6. **EITHER** Continuity of chemical potential:

$$-1 + \varepsilon\, w \frac{\partial F^2}{\partial r} \Bigg|_{r=w} = \frac{\dot{h}_f w^3}{8B}, \tag{3.94}$$

OR Step Drop Condition:

$$h_f(t_n) - h_f(t_{n+1}) = a. \tag{3.95}$$

Step Drop Condition for full MAS PDE, with arbitrary ε

Here, we aim to turn (3.95) into a form which involves f so we can use it in (3.88). To do this, we take equation (3.70) and use the PDE to replace the integrand:

$$B \int_{t_n}^{t_{n+1}} \int_{w(t)}^{\infty} \left\{ \frac{3}{r^4} - \varepsilon \left[\frac{\partial^4 F^2}{\partial r^4} + \frac{2}{r} \frac{\partial^3 F^2}{\partial r^3} - \frac{3}{r^2} \frac{\partial^2 F^2}{\partial r^2} + \frac{3}{r^4} \frac{\partial F^2}{\partial r} - \frac{3F^2}{r^4} \right] \right\} dr\,dt = -a. \tag{3.96}$$

The inner integration can be carried explicitly, using repeated integration by parts to leave *only* boundary terms. Actually, the MAS PDE (3.12) stems more fundamentally from a relation like (3.8), so it is not surprising that this integration can be done

without leaving any terms like $\int \frac{F^2}{r^4} dr$. Upon performing this integration, we have

$$\Rightarrow B \int_{t_n}^{t_{n+1}} dt' \left\{ \frac{1}{r^3} + \varepsilon \left[\frac{\partial^3 F^2}{\partial r^3} + \frac{2}{r} \frac{\partial^2 F^2}{\partial r^2} - \frac{1}{r^2} \frac{\partial F^2}{\partial r} + \frac{F^2}{r^3} \right] \Big|_{r=w}^{\infty} \right\} = -a. \tag{3.97}$$

The value of the integrand in (3.97) goes to zero as $r \to \infty$ and the upper limit does not contribute to the integral's value. Upon substitution of the similarity form (3.86) for $F(r,t)$, and using

$$w(t) = \varepsilon^{1/8} \xi_0 (Bt)^{1/4}, \tag{3.98}$$

we have [79]

$$4[(Bt_{n+1})^{1/4} - (Bt_n)^{1/4}] \left[\frac{1}{\xi^3} + \frac{d^3 f^2}{d\xi^3} + \frac{2}{\xi} \frac{d^2 f^2}{d\xi^2} - \frac{1}{\xi^2} \frac{df^2}{d\xi} \right]_{\xi=\xi_0} = -a\varepsilon^{3/8} \tag{3.99}$$

$$\Rightarrow \left[\frac{1}{\xi^3} + \frac{d^3 f^2}{d\xi^3} + \frac{2}{\xi} \frac{d^2 f^2}{d\xi^2} - \frac{1}{\xi^2} \frac{df^2}{d\xi} \right]_{\xi=\xi_0} = -\frac{a\varepsilon^{3/8}}{4(Bt^*)^{1/4}}, \tag{3.100}$$

using $t_n \sim t^* n^4$, the asymptotic relation for collapse times.

Summary of Boundary Conditions

The boundary conditions for (3.88) must come from the PDE conditions. The scaled facet width is now independent of time so $\xi_0 = \frac{w(t)}{\varepsilon^{1/8} B^{1/4} t^{1/4}}$ is a constant:

$$f^2(\xi_0^+) = 0 \tag{3.101}$$

$$\left[3\xi \frac{df^2}{d\xi} - \xi^3 \frac{d^3 f^2}{d\xi^3} \right] \Big|_{\xi=\xi_0^+} = 3 \tag{3.102}$$

$$f^2(E) = k^2 \varepsilon \tag{3.103}$$

$$\frac{df^2}{d\xi}\Big|_{\xi=E} = 0 \tag{3.104}$$

$$\textbf{EITHER:} \left[3\xi \frac{df^2}{d\xi} - \xi^2 \frac{d^2 f^2}{d\xi^2} \right] \Big|_{\xi=\xi_0^+} = 3 \quad \text{(cont. chem. pot.)} \tag{3.105}$$

$$\textbf{OR:} \left[\frac{1}{\xi^3} + \frac{d^3 f^2}{d\xi^3} + \frac{2}{\xi} \frac{d^2 f^2}{d\xi^2} - \frac{1}{\xi^2} \frac{df^2}{d\xi} \right] \Big|_{\xi=\xi_0^+} = -\frac{\varepsilon^{3/8} a}{4(Bt^*)^{1/4}} \quad \text{(step drop)} \tag{3.106}$$

$$= -\frac{\varepsilon^{3/8}}{4\tau^{*1/4}} = O(\varepsilon^{3/8}). \tag{3.107}$$

The parameter τ^* seems to be only weakly dependent on ε in the $\varepsilon \ll 1$ limit and $= O(1)$ as $\varepsilon \to 0$. Note that (3.102) is obtained from (3.90) and (3.91), and (3.105) is obtained from (3.91) and (3.94). For details on how to obtain (3.107) from (3.106), see Appendix D, Section D.4.5.

3.4.2 Comparison of Boundary Conditions

In Figures B-38 and B-39, similarity solutions for the PDE (3.11) are shown corresponding to the step drop boundary condition (dashed) and the boundary condition corresponding to continuity of chemical potential (solid). The circles represent data from step-flow simulations.

Unlike the plots in Figure B-35 and B-36 where the curves disagree slightly with the simulation data, solving the full ODE (3.88) with the step drop condition produces results where the agreement is excellent for values of ε spanning four orders of magnitude. However, rather unexpectedly, the agreement with the solid curve and the simulation data also becomes better as ε becomes larger. As a reminder, in order to implement the step drop boundary condition, the constant τ^* in (3.107) needs to be known a priori. Its numerical value is obtained through a discrete step flow simulation of a large[10] number of steps by finding the best-fit straight line through

$$\log \tau_n = \log \tau^* + \gamma \log n \quad \text{for each } n \tag{3.108}$$

via least squares optimization, and obtaining τ^* and $\gamma \approx 4$ for a cone. Hence, although agreement between the dashed curves and the simulation data is always good, implementing the step drop boundary condition in each case required a separate step flow run to be done beforehand. The continuity of chemical potential boundary condition does not require this extra input, but can only give agreement for large values of ε. As ε becomes smaller, the disagreement becomes greater, confirming the scalings (3.58), (3.59) and (3.60) for the magnitude of $F = O(a_0 c_1) + O(a_0 c_3)$ in the

[10]The number of steps must be sufficiently large so that finite-height effects are negligible throughout the simulation.

$\varepsilon \ll 1$ limit.

Physical Interpretation

When $\varepsilon \ll 1$, results from the TDL step flow simulations (see Figures B-1 and B-2 for example), show the development of a macroscopic facet on the top of the crystal. When the top step collapses, the distance between this step and the step below it can therefore become also macroscopically large, and (3.9) is *not* well approximated by (3.10) on the facet. This discrepancy is probably the main reason why enforcing continuity of chemical potential at the facet edge yields such poor agreement with the simulation data.

On the other hand, when $\varepsilon \gg 1$, Figures B-3 and B-4 show that the facet width becomes rather small and the step density changes slowly as one approaches the facet edge. In the limit of $\varepsilon \to \infty$, the width of the facet shrinks to zero. When this happens, the radial separation of the top two steps has to stay microscopically small (i.e. of the order of the terrace width in the bulk), and the approximation for the current in terms of $\dfrac{\partial \mu}{\partial r}$ is valid almost everywhere. Therefore, applying continuity of chemical potential in this case produces results that agree very well with the data.

Since both the step drop and chemical potential boundary conditions give good agreement in the case where $\varepsilon \gg 1$, it is probably possible to show that (3.105) and (3.106) are equivalent, in some sense, in the $\varepsilon \to \infty$ limit. This task is left for future work.

3.4.3 Applications to Two-scale Modeling

The results in presented in the last two chapters provide the tools for what is a potentially powerful way of solving problems in surface evolution over several length scales.

Recall that in order to correctly implement the step drop boundary condition, the numerical value of τ^* had to be evaluated using the discrete step flow equations. In addition, because the PDE (3.88) describes the relaxation of *infinite* structures, the

computed value of τ^* must come from a simulation initialized with a sufficiently large number of steps (typically hundreds) so that finite-height effects are avoided. This simulation, which has to be done before solving the PDE, can be computationally expensive if there are a large number of steps involved.

We have, however, quantified finite-height effects in Chapter 2. The form of the E_n can probably be generalized to include the effects of step-step interactions, though the details of this inclusion are left for future work. In particular, let us assume that

$$E_n(g,N) = N^4 \tilde{G}\left(\frac{H(g)n}{N}\right) \tag{3.109}$$

is known from the very outset, for some function $H(g)$. The form of $\tilde{G}$ could be obtained by running some discrete step simulations for various structure sizes and step interaction strengths, finding scalings for the minima, and collapsing the data as we did in Section 2.3.1. What is important is that the function $\tilde{G}$ is known, and is saved for reference. Then, since

$$\underbrace{E_n(g,N)}_{known} = \tau_n(g,\infty) - \tau_n(g,N), \tag{3.110}$$

one only needs to compute the collapse times for $\tau_n(g,N)$ in order to evaluate $\tau_n(g,\infty)$ – this is the quantity which is expensive to compute because a large number of steps needs to be simulated. Hence, if one wanted to solve the PDE (3.88) for some g, one could imagine first doing a quick simulation, using only $N = 30$ steps (say) for that particular value of g, and use (3.110) to obtain $\tau_n(g,\infty)$ immediately. From $\tau_n(g,\infty) \sim \tau^*(g)n^4$, $\tau^*(g)$ is then evaluated through least squares, and the step drop boundary condition can be implemented much more cheaply.

3.5 More on the Step Drop Condition

3.5.1 Step Density as a Conserved Quantity

In this section, we discuss further the step drop condition, paying particular attention its physical interpretation. Although there will be no new results in this section, it is quite interesting to regard the MAS PDE as a conservation law for steps and to think about the step drop condition in this new context. Although the MAS PDE concerns itself with *step densities* as opposed to discrete steps, the step drop condition effectively amounts to specifying that the number of steps in structure should reduce by integer amounts between collapses.

We already mentioned in Section 3.3.3 that there are a few different ways of writing the step drop condition. We will derive two different forms in this last section, and use them to interpret the step drop condition within the framework of a Conservation Law.

Note that the MAS PDE (3.12) can be re-written as

$$\frac{\partial F}{\partial t} + \frac{\partial Q}{\partial r} = 0 \tag{3.111}$$

where

$$Q = \frac{1}{r^3} + \varepsilon \left[\frac{\partial^3 F^2}{\partial r^3} + \frac{2}{r}\frac{\partial^2 F^2}{\partial r^2} - \frac{1}{r^2}\frac{\partial F^2}{\partial r} + \frac{F^2}{r^3} \right] \tag{3.112}$$

so that F, the slope (which is proportional to the step density) can be interpreted as a conserved quantity, with flux Q.

Alternative Step Drop Condition (1)

From

$$h_f(t_{n+1}) - h_f(t_n) = -a, \tag{3.113}$$

we write

$$h_f(r,t) = h(r,t) + \int_w^r F(r',t)dr', \tag{3.114}$$

and therefore

$$h_f(r,t_{n+1}) - h_f(t_n) = h(r,t_{n+1}) - h(r,t_n) + \int_{w_{n+1}}^{r} F(r',t_{n+1})dr' - \int_{w_n}^{r} F(r',t_n)dr'. \tag{3.115}$$

Taking $r \to \infty$, and noting that $h(r,t)$ does not change with time in the far field, we obtain

$$\int_{w_{n+1}}^{\infty} F(r',t_{n+1})dr' - \int_{w_n}^{\infty} F(r',t_n)dr' = -a \tag{3.116}$$

The quantity $\int_w^\infty F(r,t)dr$ is the total integrated slope, which of course, is just the total height of the nanostructure. The total height in our problem is infinite, because $F \to 1$ as $r \to \infty$. From Remark 3.3.2, an alternative interpretation of (3.116) is that between two consecutive collapse times, the total number of steps in the nanostructure reduces by 1.

Alternative Step Drop Condition (2)

From equation (3.70),

$$\int_{t_n}^{t_{n+1}} \int_{w}^{\infty} F_t dr dt, \tag{3.117}$$

we use the fact that F obeys (3.111) and re-write this as

$$\int_{t_n}^{t_{n+1}} -Q\Big|_{r=w}^{\infty} dt = -a. \tag{3.118}$$

If we assume that $Q \to \infty$ as $r \to \infty$, then we have

$$\int_{t_n}^{t_{n+1}} Q\Big|_{r=w(t)} dt = -a. \tag{3.119}$$

This equation simply means that the time integrated out-flux of slope, between two collapses, at the facet, is equal to a. Equivalently, the out-flux of *step density* between two collapse times, at the facet, is equal to 1 (see Remark 3.3.2). Also, one could imagine writing down other conservative PDEs to describe the evolution of step density: perhaps these PDEs could incorporate other physical effects such as electromigration, or model the interaction potential between steps in a different way. For

these cases, (3.119) could still be used, but of course, with a different form for Q.

Condition (3.116) implies that there is a net loss in the total number of steps between two collapse times. In addition, if the step density is conserved away from the facet, then condition (3.119) specifies that the loss must occur at the facet, if there is no out-flux at the base of the structure. These conditions do not say that the loss in step density is continuous in time, however: only that the loss between two consecutive collapse times is equal to 1. Note that when applying the Step Drop boundary condition to the similarity solution in (3.106), the flux is normalized by a factor proportional to $t^{*1/4}$. Although the flux is not continuous in time, by imposing similarity, we have effectively 'smeared' the flux over a period of time equal to the difference in collapse times, i.e. replaced a on the right hand side of (3.119) with its time average. Much more will be said about this in Chapter 4.

Hence, when the step density obeys a conservation law like (3.111), the step flow condition describes how quickly step density must leave the nanostructure at the facet edge in order for the resulting continuum solution to agree with kinetic simulations. We can now understand why the *global* constraint (3.117) reduces to a local condition when the step density is conserved. When we implemented continuity of chemical potential at the facet, we found solutions whose maxima were far too large. One intuitive explanation for this is that the continuity of chemical potential condition (see (3.94)) results in an out-flux of step density that is too small: there are only first derivatives in (3.94) whereas (3.97) has *third* derivatives. When $\varepsilon \ll 1$, a rapidly varying boundary layer forms near the facet, making ${F^2}_r \ll {F^2}_{rrr}$. Hence there is a 'pile up' of step density near the facet, resulting in the over-sized peaks in Figure B-38 when $\varepsilon \ll 1$.

3.5.2 Step Drop and Similarity

In this final section, we will show that the step drop condition,

$$\int_{t_n}^{t_{n+1}} \int_{w}^{\infty} F_t dr dt = -a \tag{3.120}$$

which is a condition non-local-in-time, reduces to conventional local-in-time condition if F is assumed to be self-similar and if the collapse times obey $t_n \sim t^* n^4$. Furthermore, with these assumptions, (3.120) corresponds to a *smooth downward translation of the facet* as the nanostructure relaxes.

The Step Drop Condition (3.120) stated in this form is not a boundary condition, but really an integral constraint in time. Trying to implement the step drop condition in this form would require knowing F at future times in order to evolve the current $F(r,t)$: it seems that one needs to know the future to change the present. However, when we impose similarity, this condition does indeed becomes local-in-time. Intuitively, this makes sense because future versions of $F(r,t)$ will simply be stretches of the current F, and so "predicting the future" in this case is made a lot easier! Imagine that the solution at $F(r,t_n)$ is known and condition (3.120) had to be implemented. How do we obtain the value of t_{n+1}? This must come from the simulations: the similarity solution needs a bit of help in determining 'where' t_{n+1} is relative to t_n in order to satisfy (3.120). This is done in the form of extra input, through t^*. More will be said about the step drop condition in the context of similarity in Chapter 4.

We will now show that (3.120) becomes local in time when we assume similarity for $F(r,t)$. We will restrict ourselves to conical profiles with slope k. Let $F(r,t) = f(x)$ where $x = r(Bt)^{-1/4}$. We have included the material paramater B here to be consistent with the notation used in MAS. Then, (3.120) implies that

$$\int_{t_n}^{t_{n+1}} \int_w^\infty (F-k)_t dr dt = -a \tag{3.121}$$

$$\Rightarrow \int_{t_n}^{t_{n+1}} \frac{d}{dt}\left\{\int_w^\infty (F-k)dr - kw\right\} dt = -a \tag{3.122}$$

$$\Rightarrow \int_{t_n}^{t_{n+1}} \{H'(t) - kw'(t)\}\, dt = -a \tag{3.123}$$

where

$$H(t) \equiv \int_{w(t)}^\infty (F(r,t)-k)dr. \tag{3.124}$$

The quantity $H(t)$ is the total deviation of the step density from the the initial

condition. Now, we use $F(r,t) = f(x)$ so that

$$H(t) = (Bt)^{1/4} \int_{x_0}^{\infty} (f(\eta) - k) dx \tag{3.125}$$

$$= K(Bt)^{1/4}. \tag{3.126}$$

Here, we assumed that the facet radius evolves according to

$$w(t) = x_0 (Bt)^{1/4} \tag{3.127}$$

consistent with (3.24), where x_0 is a constant. We now substitute (3.126) and (3.127) into (3.123) to obtain

$$(K - kx_0)[(Bt_{n+1})^{1/4} - (Bt_n)^{1/4}] = -a, \tag{3.128}$$

and with $t_n \sim t^* n^4$,

$$H(t) = \left(kx_0 - \frac{a}{(Bt^*)^{1/4}} \right) (Bt)^{1/4} \tag{3.129}$$

The point of this calculation is to show that $H(t)$ is, in principle, a known function of time, providing t^* is available through step flow simulations. In this case, (3.129) is a local-in-time, evolution equation for $H(t)$. The equation imposes a global (spatial) constraint on the integrated step density deviation at a particular instance in time. Hence, we have shown that (3.120) reduces to being *local in time* when similarity for $F(r,t)$ is assumed, along with certain assumptions on the facet evolution, $w(t)$.

As a simple corollary, using (3.123) and (3.65), we have

$$\frac{dh_f}{dt} = H'(t) - kw'(t) \tag{3.130}$$

$$\Rightarrow h_f(t) = h_0 - a \left(\frac{t}{t^*} \right)^{1/4} \tag{3.131}$$

for some constant h_0. Hence, the height of the structure at the facet $r = w$ translates downward smoothly, according to (3.131), with a velocity proportional to $t^{*-1/4}$. This result is a little counter-intuitive because although the step drop condition in

the form (3.64) involves discrete drops in h_f, we have replaced this very sudden, impulsive motion of h_f with a smooth vertical translation. This apparent paradox will be resolved in Chapter 4.

Chapter 4

Similarity of Algebraic Profiles under TDL Kinetics

4.1 Chapter Overview

The focus of this chapter is on the evolution of non-conical initial profiles so that the initial shape of the crystal structure can have a non zero curvature with respect to the radial coordinate. For these *algebraic* profiles, we show analytically and empirically through simulations that there exist approximate similarity solutions to the PDE studied in Chapter 3.

4.2 Algebraic Profiles and Similarity

Looking for similarity solutions, or starting with some kind of similarity scaling ansatz, is a very common strategy used by researchers who want to apply continuum models like PDEs to problems in surface evolution, e.g. see [84], [49], [78], [50]. These treatments tend to be confined to cases where either evaporation-condensation or surface diffusion is the main mode of mass transport.

In the previous chapter, similarity solutions for a fourth-order PDE were presented under the assumption of TDL kinetics, which describe the relaxation of an infinite cone below the roughening temperature. These similarity solutions were compared

with data from step flow simulations. However, most of the data presented so far from step flow simulations has been in the form of solutions to the ODE system (2.39)-(2.43). A natural question to ask now is how one can interpret plots like Figures B-1, B-2, B-3 and B-4 in the context of similarity, i.e. how to map a plot like B-2 onto the top set of data points in Figures B-38 (both of these data sets use $g = 0.01$).

A conical profile consisting of an infinite number of steps, is the simplest case of an axisymmetric nanostructure: this kind of profile was the focus of study in Chapters 3 and 4. However, this geometry is very special, and not very relevant to actual physical situations. Keeping within the framework of axisymmetry, the two obvious generalizations to the infinite cone are to account for finite height effects (Section 2.3.1) and to consider shapes with non-zero curvature, which is done in this chapter. In Section 2.2, we discussed some situations where making the axisymmetry assumption was justified. However, in many experiments with axisymmetric crystallites, the initial step spacing is not constant[1]. For example, the lead crystallites in [116] and [29] seem to be convex and sinusoidal corrugations imposed on a high symmetry plane [114] have non-zero curvature almost everywhere.

In this chapter, we also resolve some conflicts between the similarity solutions used in Chapter 3 and the simulation data. We have been quite cavalier in using similarity solutions so far, without really questioning their validity. Consider one of the TDL simulation results from Chapter 2, say Figure B-2. Let us sample the step density at time $t = t_0$, say. Now let t increase continuously. How does the step density change with t? Can future step density profiles always be obtained by stretches of the original data set sampled at t_0? The TDL step flow results from Chapter 2 seem to exhibit a kind of periodic structure imposed by the collapse of the inner most step, and the step density at the facet appears to get smaller in between collapse times and larger *at* the times of collapse. A self-similar solution which is valid continuously in time should account for these oscillations in the step density. However, the similarity solutions proposed so far do not show this feature. In the final part of this chapter, we will discuss the solution of the MAS PDE [78] in light of these oscillations. The

[1]The Silicon mounds in [47] *do* appear to be linear, but are not axisymmetric.

step drop condition, again, is the key to understanding these 'similarity solutions'.

Hence, the four main points of this chapter are to:

1. Give details on how to look for 'similarity' in the numerical data; show that the data from the conical profiles exhibit a strong similarity structure; obtain numerical similarity functions for the step density from plots of $\rho_i(t)$.

2. Show that step flow numerical data for *algebraic* profiles also exhibit strong similarity structure, and use the MAS PDE (3.11) to make quantitative scaling predictions on the form of this similarity.

3. Use items 1. and 2. above to make quantitative predictions on collapse times for the inner most step.

4. Explain similarity in the context of step flow simulations in light of the discrepancies between step flow data and the similarity solutions predicted in Chapter 3.

4.3 Numerical Step Density Functions

4.3.1 Initializing Algebraic Profiles in the Step Flow Model

Chapters 2 and 3 focused on the evolution of profiles that were initially *linear* in n, i.e. $\rho_n \propto n$. In this chapter, however, we will study more general profiles of the form $\rho(n) \propto n^{1+s}$ where $|s| < 0.3$: these are profiles which are convex/concave for s negative/positive. The restriction on s is mainly due to two reasons. First, when the initial shape is highly convex, steps become very close together as ρ_n becomes large, making the integration of the step flow equations (2.39)-(2.43) extremely computationally expensive (see Chapter 6 for an explanation of this). Second, there exists a critical (negative) value of s, s_{crit} such that for $s < s_{crit}$, there are only a *finite* number of collapses, no matter how long the simulation is run for. As we will see in this chapter, determining the similarity solutions numerically relies crucially on the collapse times obeying an algebraic law of the form (2.55). There is no reason,

in principle, to disregard highly concave profiles, but the behavior for s large and positive is not expected to be qualitatively different to the positive, small s case.

Eulerian and Lagrangian Coordinates

In this chapter, step flow simulations based on (2.39)-(2.43) are started using the modified initial condition

$$\rho_n = n^{1+s} \tag{4.1}$$

where s is specified by the user and controls the convexity/concavity of the initial profile. We will refer to s, from now on, as the "shape parameter". The integer n labels each step, from the inner most ($n = 1$) to the outer most ($n = \infty$). However, n also acts like a vertical coordinate, with increasing n corresponding to positions further down the axis of symmetry in the nanostructure. If the integer assumption for n is relaxed, $\rho(n) = n^{1+s}$ can be regarded as a continuum description of the profile, for variables n and $\rho(n)$. Then, the step density F is obtained by differentiation and reciprocation:

$$F = \frac{1}{\rho'(n)} \tag{4.2}$$

$$F_L(n) = \frac{1}{(1+s)n^s} \tag{4.3}$$

Equation (4.3) is a *Lagrangian* description of the profile because it describes the step density as a function of the step number, n. In Fluid Mechanics, a Lagrangian description of the field variables amounts to knowing how these quantities change as one moves with the fluid. Similarly, in our step model, $F_L(n)$ is a Lagrangian description of the step density because it tells us how the density changes as one moves with the step. An *Eulerian* description, on the other hand, involves switching variables from n to the radial polar coordinate using the change of variable $\rho = n^{1+s}$:

$$F_E(\rho) = \frac{1}{1+s}\rho^{-\frac{s}{1+s}} \tag{4.4}$$

Equation (4.4) provides an Eulerian description of the profile because F_E is the step density for a given radial distance from the axis of symmetry. A fixed radial distance will correspond, in general, to *different* steps as the structure evolves. Going back to the analogy with Fluid Mechanics, this situation is akin to sitting at a fixed point[2] in the fluid and making measurements of the field variables.

4.3.2 Collapse times for the Inner Most Step

In Chapter 2, we saw from the results of solving the discrete step flow equations for an initial conical profile, that the inner most step would collapse at regular times τ_n, $n = 1, 2, 3, ...$, and this collapse was due to the Step Line Tension effect. The results from the TDL simulations (e.g. Figure B-1) appear to have a periodic[3] structure which is a direct consequence of the regular collapse of the inner most step. In particular, the plots in Figures B-1 suggest that the height profiles at any two consecutive collapse times look like stretched versions of one another.

Israeli and Kandel [50] noticed that although these collapses did not occur periodically in time for an initial cone, they did obey an asymptotic relation of the form

$$\tau_n \sim n^4 \tag{4.5}$$

as $n \to \infty$ (see Figure B-26). This behavior in the τ_n motivated them to define a new variable $\theta \equiv t^{1/4}$, and with this definition the inner most steps *would* collapse periodically - but periodically in θ. Following Israeli and Kandel's [50] notation, this period in 'stretched time' will be denoted Θ_0. Now it makes sense to generalize this relation for the case of algebraic profiles of the form (4.1), so we have

$$\tau_n \sim C n^{\gamma(s)}, \tag{4.6}$$

for $n \to \infty$, and we can expect $\gamma(0) = 4$. Numerical values for C and γ are obtained

[2]Fixed with respect to the lab frame.

[3]"Periodic" is used here loosely, simply to mean that there is always a finite amount of time in between collapses. However, $\tau_{n+1} - \tau_n$ is *not* constant in time.

through the discrete step flow equations by by performing a linear regression on the collapse times:

$$\ln(\tau_n) \approx \underbrace{\ln C}_{\beta} + \gamma \ln n \tag{4.7}$$

In practice, when performing this regression, the first few τ_n are ignored to obtain a more accurate estimate of γ because $\tau_n \sim Cn^\gamma$ is a long time asymptotic relation for $n \to \infty$. Note that these results for τ_n hold so long as finite height effects are not important. We have seen in Chapter 2 how (4.6) must be modified in this case.

4.3.3 Linear Profiles

The observations described in Section 4.3.2 motivated Israeli and Kandel [50] to look for similarity solutions, for the step density, in the form

$$D(\rho, \tau) = \theta^\alpha F(\rho/\tau^\beta, \theta), \tag{4.8}$$

and they deduced empirically *and* numerically that $\alpha = 0$, $\beta = \frac{1}{4}$. Here, D is the step density, ρ is the radius, τ is time, $\theta = \tau^{1/4}$ and F is some (unknown) similarity function. To verify these scalings, they used data from their step flow simulations: at some time τ_j, they would compute

$$\hat{\rho}_i = \frac{\rho_i + \rho_{i+1}}{2} \tag{4.9}$$

$$D_i = \frac{1}{\rho_{i+1} - \rho_i} \tag{4.10}$$

and attempt to collapse the data at each τ_j onto a single curve F by applying stretching transformations. The equation (4.8) has the following physical interpretation: since the function F is periodic in θ with some period Θ_0, step density profiles which are sampled at integer multiples of Θ_0 later can be obtained simply by stretching the horizontal dimensions of the original profile. However, two profiles sampled within one θ period (i.e. between two consecutive collapses of the inner most step) are not similar to each other. This means that an algorithm to generate numerical versions

of the similarity function F should sample the profile at different times τ_1 and τ_2 such that $|\tau_1^{1/4} - \tau_2^{1/4}| = m\Theta_0$ for some integer m. The times τ_1 and τ_2 must also be chosen sufficiently large[4] so that the similarity form (4.8) is established.

4.3.4 Algebraic Profiles

The ideas in 4.3.3 all generalize to the case of algebraic initial conditions of the form (4.1). The scaled variable is now defined as $\theta \equiv \tau^{1/\gamma(s)}$, with $\tau_n \sim n^{\gamma(s)}$ as $n \to \infty$. Sampling must be down at times τ_1 and τ_2 such that $|\tau_1^{1/\gamma} - \tau_2^{1/\gamma}| = m\Theta_0$. In this chapter, we will use as our scaling ansatz

$$D(\rho, \tau) = \tau^a F(\rho/\tau^b, \theta) \tag{4.11}$$

which is of the same form as (4.8). In addition, as an improvement to (4.10), we use the more accurate second-order, centered difference formula[5]

$$\hat{\rho}_i = \rho_i, \tag{4.12}$$

$$D_i = \frac{2}{\rho_{i+1}(t) - \rho_{i-1}(t)}. \tag{4.13}$$

For convenience, we will drop the hats and use an arrow to denote a vector of data points, e.g. $\vec{D} = (D_1, D_2, ..., D_n)$, and $\vec{\rho} = (\rho_1, \rho_2, ..., \rho_n)$.

4.3.5 Profile Sampling Algorithm

The algorithm to generate numerical similarity functions for the step density is now presented. The algorithm takes in as input γ, which is the exponent describing the collapse times (4.6), and M, the number of times to sample, and then computes the period in scaled time, Θ_0 using (4.7). Then, specific times are chosen to do the

[4]How large the sampling times should be is not known a priori.

[5]In Finite-ifference numerical schemes, $\frac{y_{i+1}-y_i}{\Delta x}$ is a 'one-sided' difference approximation for $\frac{dy}{dx}$ for some function $y(x)$, whereas $\frac{y_{i+1}-y_{i-1}}{2\Delta x}$ is called a 'centered difference' formula. Here, $y_i \equiv y(x_i)$ are function evaluations made at uniformly spaced grid points x_i.

sampling and data $(\vec{\rho}_i, \vec{D}_i)$ are obtained at each time. The algorithm then tries to "collapse" these data sets onto a single curve by applying horizontal and vertical stretches to $(\vec{\rho}_i, \vec{D}_i)$, by using an optimization routine. This routine, called G, takes two sets of data, $(\vec{\rho}_1, \vec{D}_1)$ and $(\vec{\rho}_2, \vec{D}_2)$, sampled at τ_1 and τ_2, and finds real exponents a and b such that $(\vec{\rho}_1/\tau_1^b, \vec{D}_1/\tau_1^a)$ and $(\vec{\rho}_2/\tau_2^b, \vec{D}_2/\tau_2^a)$ are as "close together" as possible, in some sense:

1. Decide on a time to start sampling, τ_s, say, and define $\bar{\theta} = \tau_s^{1/\gamma}$.

2. For each collapse time τ_n, define $\theta_n = \tau_n^{1/\gamma}$. The θ_n are now approximately equally spaced with respect to n.

3. Define $\Theta_0 = \dfrac{1}{N-1}\displaystyle\sum_{n=2}^{N}(\theta_n - \theta_{n-1})$ as an estimate of the period in stretched time. Since the relation $\tau_n \sim Cn^\gamma$ holds for *large* n, assuming that finite-height effects have not set in yet, a better estimate of this period would be $\Theta_0 = \dfrac{1}{N-m+1}\displaystyle\sum_{n=m}^{N}(\theta_n - \theta_{n-1})$ where the first $(m-1)$ times have been ignored. How large or small m should be depends on many factors such as the size of ε and the initial step configuration. In practice, the value of m is inputted by the user.

4. Sample the solution M times at times $\tau_n = (\bar{\theta} + n\Theta_0)^\gamma$ for $n = 0, 1, ..., M-1$, using (4.12) and (4.13). This yields M data sets $(\vec{\rho}_i, \vec{D}_i)$, $i = 1, 2, ..., M$.

5. For every pair of data sets, $X_i \equiv (\vec{\rho}_i, \vec{D}_i)$ and $X_j \equiv (\vec{\rho}_j, \vec{D}_j)$, compute a and b through $G(X_i, X_j)$ (see below). This yields $\binom{M}{2}$ values of a and b. Let a_{av} and b_{av} be the mean values. The standard deviations (ignoring outliers) are a measure of the quality of the collapse.

After the algorithm has terminated, we take $a = a_{av}$ and $b = b_{av}$ in (4.11). In practice, the quality of the data is better for longer times, so τ_s should (ideally) be chosen to be large, and so, if the last collapse to occur in the integration occurs at τ_N, one should take τ_s to be between τ_{N-M} and τ_{N-M+1}. In practice, M was taken to be 6.

Data Collapse via Optimization; Computing $G(X_i, X_j)$

The function G takes as input two data sets, $(\vec{\rho}_1, \vec{D}_1)$ and $(\vec{\rho}_2, \vec{D}_2)$, sampled at times τ_1 and τ_2, and then finds real exponents a and b such that $X_1 \equiv (\vec{\rho}_1/\tau_1^b, \vec{D}_1/\tau_1^a)$ and $X_2 \equiv (\vec{\rho}_2/\tau_2^b, \vec{D}_2/\tau_2^a)$ are as close as possible, in some sense. This is quantified by minimizing the Residual function, $g(a,b) \equiv ||X_1 - X_2||$, which measures, in some norm, how far apart X_1 and X_2 are for a given a and b. This norm is defined through the following procedure:

Given a and b and data sets $(\vec{\rho}_1, \vec{D}_1)$ and $(\vec{\rho}_2, \vec{D}_2)$:

1. Compute the stretched data sets $(\vec{\rho}_1/\tau_1^b, \vec{D}_1/\tau_1^a)$ and $(\vec{\rho}_2/\tau_2^b, \vec{D}_2/\tau_2^a)$. For convenience, we now label these two transformed data sets simply as $(\vec{\rho}_1, \vec{D}_1)$ and $(\vec{\rho}_2, \vec{D}_2)$.

2. Take the data set which has the *smaller* value of $min(\vec{\rho}_1)$ (without loss of generality, let's assume it's $(\vec{\rho}_1, \vec{D}_1)$) and interpolate these points[6] so that $D_{interp}(\rho)$ can be found for any $min(\vec{\rho}_1) < \rho < max(\vec{\rho}_1)$.

3. Compute the residual $g(a,b) \equiv ||\vec{D}_2 - D_{interp}(\vec{\rho}_2)||_2$ where $D_{interp}(\vec{\rho}_2)$ is simply the vector formed by evaluating D_{interp} for each component in $\vec{\rho}_2$.

The exponents a and b can now obtained numerically by minimising $g(a,b)$, using any standard minimization routine, for example the Nelder-Mead Algorithm in [96]. The routine for G is thus:

```
[a,b] = G(X_1,X_2)              % outputs exponents a and b, given X_1 and X_2
  [a,b] = Nelder_Mead(g(a,b))   % finds a and b which minimize g
```

Note that interpolation in Item 2 is done using the data set with the smaller $min(\vec{\rho}_1)$ so that extrapolation is always avoided.

Before collapsing the data, the step density functions must be truncated after a certain radial value, ρ_{trunc}, (say): in other words, all data points (ρ_i, D_i) are disgarded

[6] A natural cubic spline was used in practice.

for $\rho_i > \rho_{trunc}$. The reason for doing this is that the step flow model only simulates a finite number of steps. If finite-height effects are taken into account, the resulting step density functions will *not* show similarity: finite-height effects can also manifest themselves by making the steps near the base to expand more quickly than usual, in order to conserve mass in (2.57). The net effect of this is to cause the step density function near the outer most steps to decrease as ρ increases. In addition, more and more steps will be affected by the finite-height effect as time progresses. This phenomenon can be clearly seen in Figure B-27: the finite-height effect here manifests itself as an oscillation which slowly propagates into the bulk as time increases. Therefore, ρ_{trunc} must decrease as time increases, and this could potentially cause problems if the simulation is not initialized with a sufficiently large number of steps.

4.4 Similarity Solutions predicted by the MAS PDE

4.4.1 Far-Field Condition

The PDE (3.11) has the property where for certain classes of (infinite) initial shapes, the behaviour of the solution for $r \gg 1$ is simply dictated by the initial condition. In particular, initial shapes of the form

$$F(r,0) \propto r^p, \tag{4.14}$$

where $p = -\frac{s}{1+s}$, for $|s| < 0.3 \Rightarrow -\frac{3}{13} < p < \frac{3}{7}$ will have this property. To see this, one can substitute (4.14) directly into (3.11) to obtain

$$0 = \frac{3}{r^4} - O(r^{2p-4}), \tag{4.15}$$

and since $2p - 4 < 0$, the PDE is satisfied in the far-field, $r \to \infty$. Therefore,

$$F(r,t) \sim t^{\frac{-bs}{1+s}} \left(\frac{r}{t^b}\right)^{\frac{-s}{1+s}} \tag{4.16}$$

as $r \to \infty$. In (4.16), b is arbitrary, a reflection of the fact that there are infinitely many horizontal and vertical stretches that leave invariant a function of the form $y(x) = x^m$ for some constant m. Thus, for $F(r,t) = t^a f(\eta)$, where $\eta = rt^{-b}$, this far-field constraint fixes a relation between a and b (see 4.11 for the definition of a and b), namely,

$$a = -\frac{bs}{1+s}. \tag{4.17}$$

A simple corollary is that $f(\eta) \to \eta^{\frac{-s}{1+s}}$ as $\eta \to \infty$.

4.4.2 Exact Similarity for Linear Profiles

From [79], the PDE (3.11) only admits one (exact) similarity solution. We substitute $F(r,t) = t^a f(rt^{-b})$, using (4.8) but drop the θ dependence: accounting for the periodicity in 'stretched' time in the current theory is left for future work. We discuss the nature the resulting non-periodic solution in Section 4.7.1. We now have

$$\left(\frac{a}{B}\right) t^{a-1} f - \left(\frac{b}{B}\right) t^{a-1} \eta f' = \underbrace{\frac{3}{\eta^4} t^{-4b}}_{\text{A}} \underbrace{- \varepsilon t^{2a-4b} \left[f^{2''''} + \frac{2}{\eta} f^{2'''} - \frac{3}{\eta^2} f^{2''} + \frac{3}{\eta^3} f^{2'} - \frac{3}{\eta^4} f^2 \right]}_{\text{B}}. \tag{4.18}$$

Term A represents the effect of step line tension (note this quantity is *independent* of F), and term B represents the step-step interactions: this term becomes larger when the step densities are greater, i.e. steps become closer together. For all terms to contribute uniformly in time, we must have that $a - 1 = -4b = 2a - 4b$. In other words

$$a = 1/4, \tag{4.19}$$

$$b = 0, \tag{4.20}$$

which are exactly the exponents for a similarity solution in a linear profile, predicted in (4.8).

4.4.3 Approximate Self-Similarity for Algebraic Shapes

In this section, we will derive the exponents for similarity solutions for nanostructures which have algebraic initial conditions. Throughout this section, ε should be thought of as being arbitrary, and not necessarily much smaller than unity.

There are two other possibilities for equation (4.18). If we balance the terms containing t^{a-1} and t^{-4b}, then we have that

$$\left(\frac{a}{B}\right) f - \left(\frac{b}{B}\right) \eta f' \sim \frac{3}{\eta^4}, \tag{4.21}$$

providing that $a - 1 = -4b$. We will discuss when or whether the neglect of term B in (4.18) is justified in the next section. Along with the far-field constraint (4.17), we have

$$b_L(s) = \frac{1+s}{4+3s}, \tag{4.22}$$

$$a_L(s) = -\frac{s}{4+3s}, \tag{4.23}$$

where a_L and b_L denote the exponents for the similarity solution (4.11) when step line tension is dominant.

If we now balance the terms containing t^{a-1} and t^{2a-4b}, then

$$\left(\frac{a}{B}\right) f - \left(\frac{b}{B}\right) \eta f' \sim -\varepsilon \left[f^{2''''} + \frac{2}{\eta} f^{2'''} - \frac{3}{\eta^2} f^{2''} + \frac{3}{\eta^3} f^{2'} - \frac{3}{\eta^4} f^2 \right], \tag{4.24}$$

providing that $a-1 = 2a-4b$. Again, using the far-field constraint (4.17), we conclude that

$$b_S(s) = \frac{1+s}{4+5s}, \tag{4.25}$$

$$a_S(s) = -\frac{s}{4+5s}, \tag{4.26}$$

where b_S and a_S are the exponents for (4.11) when step-step interactions are dominant.

4.4.4 Validity of Similarity Solutions

Whether the Step-line tension or the Step-step interaction term in (4.18) dominates depends crucially on the size of

$$H \equiv \varepsilon t^{2a} \left(|f^2| + \eta^4 \left| \frac{d^4 f^2}{d\eta^4} \right| \right) \tag{4.27}$$

compared to unity. This term effectively represents the strength of step interactions relative to line tension at a point η in the algebraic profile. Furthermore, H must be $\ll 1$ or $\gg 1$ throughout the entire profile for the general similarity solutions to be valid. If $H \gg 1$, then we expect relations (4.25) and (4.26) to hold. If $H \ll 1$, then (4.22) and (4.23) will hold.

If $s < 0$, then this implies that f^2 is an *increasing* function of η. In both cases of (4.23) and (4.26), the theoretical exponent $a(s) > 0$, meaning that $|\varepsilon t^{2a} f^2|$ (and therefore H) grows with time. Providing ε is sufficiently large, then we can conclude that $H \gg 1$, and use the predicted forms of $a_S(s)$ and $b_S(s)$. These predicted values should become more accurate as time increases, and if larger values of $|s|$ are used, as this implies a larger value for $|a_S|$. One can also derive theoretical results for a time, t_c (in terms of f and ε), such that it is 'safe' to neglect step line tension in the PDE providing $t \gg t_c$ by using the inequality $H \gg 1$. In practice, however, because $|a_S|$ is typically very small (typically $\sim 0.01 - 0.04$), t^{2a} hardly has any effect on the magnitude of H: in theory, for $s < 0$ and sufficiently long times, step-step interactions eventually dominate, but in practice, t_c is too large to see this effect. Furthermore, equation (4.18) is a reduction of a PDE to an ODE, using a similarity solution ansatz which is valid for sufficiently long times. Since we have no a priori quantitative estimate of *when* (4.18) is even valid[7], having an estimate of a time at which we can negelect term A is not very helpful.

[7]Though the step flow simulations suggest that similarity is more quickly established for convex profiles ($s < 0$) and large values of g.

If $s > 0$, we would think that the opposite of the above is true: that since f^2 decreases with η, then providing ε is sufficiently small, term A would dominate in (4.18), leading us to conclude (incorrectly) that a_L and b_L could be used under these circumstances. However, we noted in Chapter 3 that $\varepsilon \to 0$ is a singular limit. As ε is made smaller, a boundary layer for $f(\eta)$ develops near the facet, making the derivatives in (4.18) very large. In fact, the $|\varepsilon\eta^4 f^{2''''}|$ term in H is never negligible near the facet, no matter how small ε becomes. This means that the predicted values for a_L and b_L are only useful for *really* long times, such that $t^{2a} \ll 1$ ($a < 0$ because $s > 0$ and $\varepsilon\eta^4 f^{2''''} = O(1)$). From the comments made in the previous paragraph, since $|a|$ is typically very small, this term is never really negligible in practice.

In summary, we only expect similarity solutions for $s < 0$, and these will take the form

$$D(r,t) = t^{a_S} f(r/t^{b_S}) \tag{4.28}$$

where a_S and b_S are given by (4.25) and (4.26).

4.4.5 Theoretical Predictions for Collapse Exponent

When steps undergo a collapse, the collapse times obey an asymptotic relation of the form

$$t_n \sim C n^{\gamma(s)}, \tag{4.29}$$

as $n \to \infty$, where the initial condition is $\rho(m) = m^{1+s}$. Consider the 'step drop' boundary condition first introduced in Chapter 3. This takes the form

$$h_f(t_n) - h_f(t_{n+1}) = a, \tag{4.30}$$

where a is the step height, h_f is the height of the structure at the facet edge, and t_n are the collapse times. Now, since

$$\begin{aligned} h(r,t) &= -\int^r F(r',t)dr', && (4.31)\\ &= -t^a \int^r f(r't^{-b})dr', && (4.32)\\ &= -t^{a+b} \int^\eta f(\eta')d\eta', && (4.33)\\ &= t^{a+b}G(\eta), && (4.34) \end{aligned}$$

we must have, via height continuity,

$$h(w,t_n) \equiv h_f(t_n) = t_n^{a+b}G(\eta_0) \tag{4.35}$$

where $\eta_0 \equiv w/t^b$ is the scaled facet width. Then, the step drop condition (4.30) becomes

$$\begin{aligned} (t_n^{a+b} - t_{n+1}^{a+b})G(\eta_0) &= a && (4.36)\\ \Rightarrow C[(n+1)^{(a+b)\gamma} - n^{(a+b)\gamma}]G(\eta_0) &= -a, && (4.37) \end{aligned}$$

and for long times $n \to \infty$, this relation reduces to

$$C(a+b)\gamma n^{(a+b)\gamma-1}G(\eta_0) = -a. \tag{4.38}$$

For the left hand side to be independent of n, we must have

$$\begin{aligned} \gamma(s) &= \frac{1}{a(s)+b(s)}\\ &= 4+3s \quad \text{for line tension dominated structures} && (4.39)\\ &= 4+5s \quad \text{for step-step interaction dominated structures} && (4.40) \end{aligned}$$

4.5 Comparison of Theoretical and Simulation Exponents

Tables A.2 – A.7 show the numerical values for a,b and γ obtained numerically, for a wide variety of initial algebraic shapes. To compare with theoretical predictions, the numerical values a_{num},b_{num} and γ_{num} are plotted along with theoretical forms $a_L(s), b_L(s), \gamma_L(s)$ and $a_S(s), b_S(s), \gamma_S(s)$ on Figures B-28 and B-29. Finally, some of the density functions for representative algebraic shapes are shown in B-30, B-31 and B-32.

Looking at Figures B-28 and B-29, one sees immediately, that comparing the exponent a_{num} to a_L and a_S will not be very useful in order to determine whether line tension or step-step interactions are dominant uniformly throughout the structure. Since the two curves $a_L(s)$ and $a_S(s)$ are nearly identical to each other, it is difficult to tell whether $a_{num} = a_L$ or a_S numerically. However, the curves for the b exponent in B-28 clearly show that simulation results and theoretical predictions agree, for $b = b_S(s)$ when $s < 0$ and sufficiently large values of $\varepsilon = \frac{3}{2}g$). When s becomes more positive however, this agreement breaks down, although b_S still performs better than b_L in predicting an approximate value. When $g = 0.01$ (see B-29), the agreement between b_{num} and the predicted values seems to be always poor, no matter whether b_S or b_L is used. These results validate the comments made in Section 4.4.4.

For the collapse times exponents γ, when $\varepsilon \gg 1$ and $s < 0$, we have step-step interactions dominating throughout the whole profile, and $\gamma = \gamma_S(s) = 4 + 5s$. Interestingly, although b_L does not agree so well with b_{num} for $s > 0$, γ_L does agree with γ_{num}, and it is interesting to note the switch in behaviour here from s negative to positive. This switch, however, does *not* occur for the $\varepsilon = 0.01$ case, with γ_{num} agreeing well with γ_L for a whole range of s values.

Finally, it should be mentioned here that although the numerical collapse exponents do not always agree with the theoretical predictions, nevertheless, the numerical values of a_{num} and b_{num} do still correspond to some kind of similarity solution, because the collapse of data is, in general, of a high quality (indicated by σ_a and σ_b

in the tables). However, one should check that collapsing data profiles from longer times do not adversely affect the similarity exponents.

4.6 Summary of Results

For initial conditions

$$r(n) = n^{1+s} \tag{4.41}$$

$$\Rightarrow F(r) = \frac{1}{1+s} r^{-\frac{s}{1+s}} \tag{4.42}$$

where the shape parameter $|s| < 0.3$, there exist *approximate* similarity solutions, valid for t sufficiently large, for the step density $D(r,t)$, of the form

$$D(r,t) = t^{a(s)} f(r/t^{b(s)}), \tag{4.43}$$

where

$$a(s) = -\frac{s}{\gamma(s)} \tag{4.44}$$

$$b(s) = \frac{1+s}{\gamma(s)} \tag{4.45}$$

and $\gamma(s)$ is the exponent for the collapse times relation

$$\gamma(s) = \begin{cases} 4+3s & \text{if step line tension is dominant uniformly throughout the profile} \\ 4+5s & \text{if step-step interactions are dominant throughout} \end{cases} \tag{4.46}$$

Step-step interactions are dominant throughout the structure if g is sufficiently large, and if $s < 0$, in which case the exponents $a(s)$ and $b(s)$ take on the forms

$$a(s) = a_S(s) = -\frac{s}{\gamma_S(s)}, \tag{4.47}$$

$$b(s) = b_S(s) = -\frac{1+s}{\gamma_S(s)} \tag{4.48}$$

These forms have been verified empirically from simulations. The case where step line tension is dominant throughout corresponds to

$$a(s) = a_L(s) = -\frac{s}{\gamma_L(s)}, \tag{4.49}$$

$$b(s) = b_L(s) = -\frac{1+s}{\gamma_L(s)} \tag{4.50}$$

but is seldom applicable in practice, because one has to wait for extremely long times for this similarity to establish. These exponents have *not* been verified numerically.

The case when $s = 0$, corresponding to that of a linear cone, is special in that both step line tension and step step interactions are equally important for all time. In this case, the similarity is 'exact' and the exponents are $a(0) = 0$, $b(0) = 1/4$, in agreement with the findings of Israeli and Kandel [50].

4.7 Discrepancies in Self-Similarity

Figure B-25 shows 5 step density profiles sampled at 5 different times between the 47th and 48th collapse of a step flow simulation of a linear profile. For clarity, the profiles have been translated horizontally to separate them from each other. The value of ε used is quite small ($\varepsilon = 1.7 \times 10^{-4}$) so the width of each peak is very narrow. The maximum step density seems to fluctuate greatly between the two collapses. Figure B-25 shows that the steps bunch up locally near the facet as the inner-most step collapses. What causes this behaviour?

When the inner-most step is just about to annihilate, it emits a burst of adatoms, meaning that the few steps just on the outside of it expand their radii very suddenly as they absorb the emitted adatoms and push out against those in the bulk. This causes the sudden increase in step density near the facet at the collapse times. These oscillations in the step density do not disappear, no matter how long the simulations are run. They are also greater for small ε than they are for more moderate values. For example, for $\varepsilon \approx 0.01$, the oscillations are hardly noticeable. However, the MAS boundary layer analysis [78] predicts similarity solutions in the $\varepsilon \ll 1$ limit, and does

not account for these fluctuations. Neither do the similarity solutions of Israeli and Kandel [50], although they do acknowledge the presence of these fluctuations through the θ variable in equation (4.8).

In Chapter 3, we used a parameter, τ^*, to construct similarity solutions that seemed to agree very well with simulation data. The external parameter τ^* is defined from the collapse times:

$$\tau_n \sim \tau^* n^4. \tag{4.51}$$

as $n \to \infty$. What is interesting about the resulting continuum solutions is that a particular set of simulation data produces one value of τ^*, resulting in a single similarity solution. However, we have empirical evidence in the form of Figure B-25 which suggests that the similarity function f can be very different depending on the value of τ_s in the Profile Sampling Algorithm in Section 4.3.5. The step drop condition as it currently stands seems to select a very specific form for f. In fact, when constructing empirical forms for f from simulation data, τ_s has to be chosen *away* from collapse times in order to obtain good agreement with the continuum solutions[8]. This suggests that the current form of the step drop condition is not general enough, because it cannot account for similarity solutions which result from choosing different values for τ_s.

4.7.1 The Generalized Step Drop Condition

The step drop condition (3.64) is actually very special. It imposes the restriction that the difference in height *at* two consecutive collapse times must be equal to $-a$. This restriction can be relaxed: instead of

$$\int_{t_n}^{t_{n+1}} \frac{dh_f}{dt} dt = -a, \tag{4.52}$$

[8]Optimal results seemed to come from selecting a τ_s which was about halfway between collapse times.

more generally, we write

$$\int_{T_1}^{T_2} \frac{dh_f}{dt} dt = \begin{cases} -a & \text{if } T_1 < t_n < T_2, \\ 0 & \text{if } t_n < T_1,\ T_2 < t_{n+1}. \end{cases} \tag{4.53}$$

Whenever $\dot{h}_f$ is integrated *through* a collapse time, the integral's value will be $-a$; otherwise it will be zero. This motivates us to write $\dot{h}_f$ as:

$$\dot{h}_f = \frac{dh(w(t),t)}{dt} = -a \sum_{n=1}^{\infty} \delta(t - t_n). \tag{4.54}$$

Equation (4.53), or equivalently, (4.54) is the *Generalized Step Drop* Condition. It states that the downward velocity of the flat facetted region is always zero, except when a collapse occurs, in which case, it moves impulsively, resulting in an infinite velocity. The t_n here are, as usual, the collapse times, which must come from a step flow simulation. With (4.54), one can actually write down the full set of boundary conditions for the MAS PDE [78]:

$$1 - \varepsilon w[(F^2)_r + w(F^2)_{rr}]|_{r=w} = -\frac{\dot{h}_f w^3}{2B} \tag{4.55}$$

$$1 + \varepsilon w[-(F^2)_r + 2w(F^2)_{rr} + w^2(F^2)_{rrr}]|_{r=w} = \frac{\dot{h}_f w^3}{B} \tag{4.56}$$

$$F(w,t) = 0 \tag{4.57}$$

$$F \sim -H'(r) \text{ as } r \to \infty \tag{4.58}$$

$$F_r \sim -H''(r) \text{ as } r \to \infty \tag{4.59}$$

$$\text{where } \dot{h}_f = -a \sum_{n=1}^{\infty} \delta(t - t_n) \tag{4.60}$$

The first three conditions impose, respectively, continuity of current, height, and slope. The fourth and fifth equations are the far-field conditions, where $H(r)$ is a specified initial height profile. Hence, with only $w(t)$ as an unknown, these five conditions can uniquely determine the solution of the PDE. Collapse times from the step flow simulations determine where the delta functions should be placed in time.

Note that by writing (4.60), we are still not taking into account the detailed motion

of the step collapses. The goal of this generalized condition is simply to imitate the *effect* of the inner most collapsing step while staying within the continuum framework. The actual motion of the collapsing step is still invisible to the PDE (3.12), even with (4.60) implemented. Equation (4.60) could be an improvement over (3.106), however in the sense that it may be able to account for the oscillations seen in Figure B-25. Whereas the original step drop condition corresponded to a uniform vertical translation of $h_f(t)$ (see (3.131)), the motion of $h_f(t)$ described by (4.60) is a sequence of step functions in time, with the jumps in h_f located at the collapse times. Hence, h_f has now truly become a "microscale" variable because changes in h_f are of the order of a step height, a. The discontinuities in $h_f(t)$ could give rise to the oscillations in (B-25), which are due to the microscale dynamics of individual steps on the facet. Note that the facet edge, $w(t)$ is still a macroscale variable: by Remark 3.3.1, $w(t)$ is *defined* by equation (4.57). The facet edge $w(t)$ is *not* the radius of the inner most step[9].

4.7.2 Interpretation of Similarity Solutions

With the Generalized Step Drop Condition established, we are now in a good position to understand how we can impose similarity solutions like (4.43) onto the PDE, despite conflicting numerical evidence such Figure B-25 and why the old Step Drop condition (3.64) produces only one of infinitely many "similarity solutions". For the rest of this section, we will refer to (3.106) as the "t^* condition" and the resulting similarity solutions to the MAS PDE (3.12) as "t^* solutions". The solution generated by (3.106) is very special, and corresponds to using a particular range of integration in (4.53). By choosing $T_1 = t_n^-$, $T_2 = t_{n+1}^-$ and imposing similarity, we are in fact replacing an impulsive out-flux of step density at the the facet with its time-average. The aim of this last section is to justify this statement.

First, we re-write equation (3.97), but use the scaled time variable $\theta \equiv t^{1/4}$, and $F(r,t) = f(x)$, where $x = r/\theta$ is the similarity variable, and $x_0 = w(t)/\theta$ is the facet

[9]Actually, for $\varepsilon \ll 1$, $w(t)$ will be well approximated by the radius of the *second* step.

width, a constant with respect to time:

$$B\left[\frac{1}{x^3}+\varepsilon\left(\frac{d^3f^2}{dx^3}+\frac{2}{x}\frac{d^2f^2}{dx^2}-\frac{1}{x^2}\frac{df^2}{dx}+\frac{f^2}{x^3}\right)\right]\Bigg|_{x=x_0}\int_{\theta_n}^{\theta_{n+1}}d\theta=a \tag{4.61}$$

The θ_n are the scaled collapse times $\theta_n \equiv t_n^{1/4}$. Therefore, we have

$$\underbrace{B\left[\frac{1}{x^3}+\varepsilon\left(\frac{d^3f^2}{dx^3}+\frac{2}{x}\frac{d^2f^2}{dx^2}-\frac{1}{x^2}\frac{df^2}{dx}+\frac{f^2}{x^3}\right)\right]\Bigg|_{x=x_0}}_{Q_0}\equiv\frac{a}{\Theta_0} \tag{4.62}$$

where $\Theta_0 \equiv \theta_{n+1}-\theta_n$. The term on the left hand side of (4.62) is the flux of step density at the facet, and it is constant ($= a/\Theta_0$), provided time is scaled properly. Note that equation (4.62) is basically identical to (3.106), but uses different similarity variables.

The actual evolution of F will react to sudden, impulsive fluxes resulting from the collapse of the inner most step. The generalized form of the step drop condition (3.88) from Section 3.5 is

$$\int_{T_1}^{T_2} dt\, Q|_{r=w(t)} = \begin{cases} a & \text{if } T_1 < t_n < T_2, \\ 0 & \text{if } t_n < T_1,\ T_2 < t_{n+1}. \end{cases} \tag{4.63}$$

$$\Rightarrow Q(w(t),t) = a\sum_{n=1}^{\infty}\delta(t-t_n). \tag{4.64}$$

Comparing (4.64) to (4.62), we see that when we force a similarity solution onto the generalized step drop condition (3.88) and choose $T_1 = t_n^-$ and $T_2 = t_{n+1}^-$, we are effectively 'smearing out' the delta functions uniformly over the θ period of the collapse. The impulsive fluxes at the facet are replaced with a constant Q_0 such that

$$\int_{\theta_n^-}^{\theta_{n+1}^-} Q_0 d\theta = \int_{t_n^-}^{t_{n+1}^-} Q(w(t),t)dt = a. \tag{4.65}$$

Although the outflux is constant with respect to θ, in actual time, the outflux must decrease gradually as $(t_{n+1}-t_n)$ increases with n (in contrast, $(\theta_{n+1}-\theta_n) \equiv \Theta_0$ is

a constant with respect to n for sufficiently long times). The integral $\int_{\theta_n^-}^{\theta_{n+1}^-} Q_0 d\theta$ is rewritten in terms of t as

$$\int_{\theta_n^-}^{\theta_{n+1}^-} Q_0 d\theta = \int_{t_n^-}^{t_{n+1}^-} Q_{av}(t) dt, \tag{4.66}$$

where

$$Q_{av}(t) = \left(\frac{a}{4t^{*1/4}}\right) t^{-3/4}. \tag{4.67}$$

Hence, with the definition of Q in (3.112), we have

$$Q(w(t), t) = Q_{av}(t), \tag{4.68}$$

which is the "smeared out" version of boundary condition (4.56), in the same way that (3.131) is the "smeared out" version of (4.60).

Summary

By imposing $T_1 = t_n$, $T_2 = t_{n+1}$ and similarity on the generalized flux condition

$$Q(w(t), t) = a \sum_{n=1}^{\infty} \delta(t - t_n), \tag{4.69}$$

we are effectively replacing the delta functions, located at the collapse times, t_n, with a smooth function

$$Q_{av}(t) = \left(\frac{a}{4t^{*1/4}}\right) t^{-3/4}. \tag{4.70}$$

where t^* is the parameter relating to the discrete step collapses. The functions $Q_{av}(t)$ and $a \sum_{n=1}^{\infty} \delta(t - t_n)$ are equivalent in an integrated sense:

$$\int_{t_m}^{t_{m+1}} Q_{av}(t) = \int_{t_m}^{t_{m+1}} a \sum_{n=1}^{\infty} \delta(t - t_n). \tag{4.71}$$

When $t \gg 1$ and $\neq t_n$, $n = 1, 2, 3, ...$, we have

$$Q_{av}(t) \approx a \sum_{n=1}^{\infty} \delta(t - t_n), \tag{4.72}$$

which provides an explanation for why sampling the step density profile in the simulations *away* from the collapse times results in agreement with the t^* similarity solution.

The computed continuum similarity solutions in Chapter 3 are only an approximation to the true solution of the MAS PDE with the boundary conditions (4.55)–(4.60), because the boundary condition (3.106) is only an approximation to the generalized step drop condition. One interpretation of the generalized step drop boundary condition is that step density leaves the nanostructure impulsively, and the flux can be described by a series of delta functions in time, whose locations coincide with collapse times. When we implement the t^* step drop condition, we are:

- Replacing the impulsive motion of h_f in (4.60) with a smooth downward translation of the facetted part of the crystal, through equation (3.131).

- Replacing the impulsive outfluxes of step density in (4.69) with an 'equivalent' (in an integrated sense) smooth outflux of density, through equation (4.67).

- Replacing the oscillating solutions (seen in B-25) with their time-averaged versions. These time-averaged solutions are obtained by solving the MAS PDE (3.12) using the "smeared out" boundary conditions described above. These are the similarity solutions which we solved for in Chapter 3.

Chapter 5

Stability of Algebraic Profiles under TDL kinetics

5.1 Chapter Overview

This short chapter focuses on the stability of the algebraic profiles that were studied in Chapter 4. We present results on the decay rates of perturbations to the base shape and quantify the decay rate dependence on the wavenumber of the perturbation and the value of the step-interaction parameter.

5.2 Relaxation of Periodic Corrugations

It has been quite common to study the decay of surface corrugations theoretically and experimentally: for example, see [106], [34], [41] and [14]. In these cases, the researchers considered sinusoidal perturbations of some given wavelength imposed onto a high symmetry plane of the crystal and then investigated the decay in time.

Above the roughening temperature, Mullins [85] showed that the height profile, $h(x,t)$ of a 1D corrugation obeyed a PDE of the form $h_t \propto -h_{xxxx}$, where x is distance along the symmetry plane and t is time. The two main consequences of the PDE are that: i) The corrugations decay exponentially, with the decay constant proportional to the fourth power of the wave number, and ii) sinusoidal perturbations remain si-

nusoidal as they decay. However, below the roughening temperature, the qualitative behavior of the decay is very different. Yamashita et al. [122] studied corrugations that were made on different crystallographic orientations of Ni. Depending on the orientation on which the corrugation was made, the researchers in [122] observed the following: on the (110) face, the corrugations maintained their sinusoidal shape as they decayed, but on the (100) and (111) surfaces, the corrugations became trapezoidal, developing facets at the extrema. Bonzel et al. [15] explained this by saying that different surface orientations had different roughening temperatures, so that that the roughening temperature was *not* just material dependent. They concluded that the (110) corrugations were relaxing above the roughening temperature, and obeyed the fourth order equation derived by Mullins [85]; the (100) and (111) corrugations, however, were faceting while they relaxed. From the results in Chapters 2 and 3, this is suggestive of the fact that these orientations are below the roughening temperature. Margetis [78] and Spohn [109] derived *nonlinear* diffusion PDEs governing relaxation for these cases, which are characterized by the growth of a facet as the corrugations decay.

Below the roughening temperature, both 1D [99] and 2D [51], [13] corrugations have been studied, and surprisingly, the time dependent nature of the decay varies according to whether 1D or 2D corrugations are used. Margetis [77] explained this by proposing a tensor form for the terrace diffusivity in a model where steps could be of an arbitrary shape. In this case, there are adatom currents both along step edges (longitudinal) and across step edges (transverse). Depending on which type of current is dominant (which in turn depends on whether the corrugation is 1D or 2D), and depending on whether the system is TDL or ADL, one obtains different types of decay which seem to agree with published experimental results. In particular, for ADL kinetics, the decay is exponential when transverse currents are dominant, but inverse linear when longitudinal currents are dominant. However, here we will focus only on decay in the TDL case.

In this chapter, the physical situation for the stability problem will be slightly different to what has been commonly used in experiments. Although our crystal

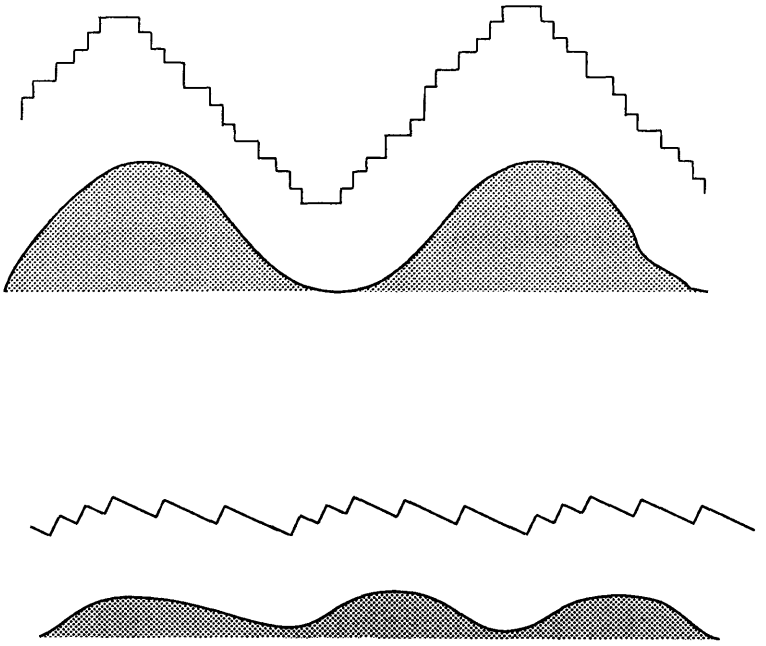

Figure 5-1: The top profile shows the type of perturbation that has been most commonly studied (see [51], for example): the perturbation consists of steps of opposite signs, and faceting is usually observed as the decay happens. The lower profile is not so often studied and will be the subject of investigation in this chapter: all the steps have the same sign and faceting will *not* occur.

is relaxing below the roughening temperature, instead of studying sinusoids which consist of steps of differing sign (see Figure 5-1), we will be considering a profile consisting of an infinite series of single signed, circular steps.

We will then introduce a periodic perturbation into the *terrace widths*. In a continuum description, if $F \equiv -\frac{\partial h}{\partial r}$ is the slope profile, the perturbation is now being introduced into the quantity F^{-1} as opposed to h itself. This situation has not been studied so often experimentally. However, Bonzel and Mullins [13] did analyze an analagous situation, but with straight steps, and some researchers have performed linear stability analysis (again with straight steps) on equally spaced step positions [46], [102] on a monotone, vicinal surface. In these cases, when perturbations decay, the steps space themselves out more evenly, in order to minimize their step free energies. In this chapter, we will show that there are other shapes (apart from linear profiles) which are also stable: small disturbances to the step positions decay, leaving behind a distribution of terrace widths which is determined by the shape of the

underlying base profile.

The focus of this chapter is the stability of algebraic profiles. We will show that there are classes of algebraic initial shapes which are stable with respect to small perturbations in the terrace widths, and we will quantify their decay rate dependence on wavenumber, and step-step interaction strength by linearizing the MAS PDE (3.12). Results concerning *large* perturbations in F from a base linear profile, will also be presented, but not analyzed. The initial stages of decay in this case can only be predicted by considering the full PDE.

5.3 PDE for the Perturbation

In this section, we derive a PDE governing the evolution of small perturbations $f(r,t)$ from a basic state $F_0(r,t)$, so that $f \ll F_0$. Let

$$F(r,t) = F_0(r,t) + f(r,t), \tag{5.1}$$

where $F_0(r,t)$ is an exact solution of the PDE (3.11). F_0 must also satisfy boundary conditions at the facet which were discussed in the Chapter 3. Substituting (5.1) into (3.11) and discarding high order terms of size $O(f^2)$, we obtain

$$\begin{aligned}\frac{1}{B}\frac{\partial f}{\partial t} =& \frac{3}{r^4} - 2\varepsilon\left(\frac{\partial^4}{\partial r^4} + \frac{2}{r}\frac{\partial^3}{\partial r^3}\right. \\ &\left. -\frac{3}{r^2}\frac{\partial^2}{\partial r^2} + \frac{3}{r^3}\frac{\partial}{\partial r} - \frac{3}{r^4}\right)(F_0 f).\end{aligned} \tag{5.2}$$

We now consider the behaviour of f in the far field $r \to \infty$, and therefore we drop terms which are multiplied by $\frac{1}{r^4}, \frac{1}{r^3}, \frac{1}{r^2}$ and $\frac{1}{r}$ to obtain the simplified equation

$$\frac{\partial f}{\partial t} = -2\varepsilon B\frac{\partial^4(F_0 f)}{\partial r^4} \tag{5.3}$$

In the far field, $F_0(r,t)$ resembles the initial condition (see Section 4.4.1). Hence we can replace $F_0(r,t)$ with $\frac{1}{1+s}r^{-s/(1+s)}$ (see (4.4)), expand the fourth derivative with

the product rule and keep only the largest term to obtain

$$\frac{\partial f}{\partial t} + \frac{2\varepsilon B}{1+s} r^{-\frac{s}{1+s}} \frac{\partial^4 f}{\partial r^4} = 0. \tag{5.4}$$

This is a linear PDE for $f(r,t)$, and f satisfies homogeneous boundary conditions which are obtained by substituting $F = F_0 + f$ into (3.89)-(3.93) and (3.101), and keeping terms of $O(f)$ only. Ideally, we would now want to substitute in normal modes like $e^{i(kx-\omega t)}$ into (5.4) and investigate their resulting behavior, but our domain is not $(-\infty, \infty)$, and very specific boundary conditions have to be satisfied at $r = w(t)$, the facet edge. Instead of proceeding with a rather involved eigen-analysis, we shall subsitute in normal mode solutions anyway far from the facet, and then set $f \equiv 0$ for $r < r_1$, for some constant $r_1 > w(t)$. This crude approximation for f will break down as soon as the radius of the facet exceeds r_1. We shall also assume that the effects of forcing $f \equiv 0$ at $r = r_1$ propagate sufficiently slowly into the bulk so as not to adversely affect the exponential decay of the normal modes. If f varies sufficiently rapidly compared with the base state, we can substitute in $f(r,t) = e^{i(kr-\omega t)}$ in the bulk, resulting in the "dispersion relation"

$$-i\omega + \frac{2\varepsilon B}{1+s} k^4 r^{-\frac{s}{1+s}} = 0, \tag{5.5}$$

where the decay rate of a normal mode with wave number k is

$$\lambda(r; k, s, \varepsilon) = \frac{2\varepsilon B}{1+s} k^4 r^{-\frac{s}{1+s}}. \tag{5.6}$$

Hence, the decay rate is proportional to ε, and depends on the local value of r, as well as the fourth power of the wavenumber. This crude model also predicts that far from the facet the perturbation f goes to zero exponentially in time, leaving behind the original algebraic shape $r_n = n^{1+s}$. This prediction is shown to be correct, at least qualitatively, by Figures B-40 and B-41, produced by direct integration of the step flow equations.

5.3.1 Initializing Perturbations in the Step Flow Model

Since the PDE (3.12) is written in terms of the step density, we need to set the initial conditions in the simulation so that the step density consists of an algebraic function of r added to a sinusoidal function of r. The step flow simulations are initialized by setting the value of the radius of each step, $r(n)$ for each step numbered $n = 1, 2, 3, \ldots$. We now introduce a perturbation onto an algebraic function $r(n)$ so that $r(n) = n^{1+s} + \delta \sin(kn^{1+s})$, for real numbers δ, k, with s controlling the convexity/concavity. The resulting profile for the step density distribution consists of the original unperturbed $F_0(r) \equiv \frac{1}{1+s} r^{-\frac{s}{1+s}}$ superimposed with a sinusoid (whose amplitude depends on r) providing the amplitude of the perturbation is much smaller than its wavelength ($\delta k \ll 1$):

$$
\begin{aligned}
r(n) &= n^{1+s} + \delta \sin(kn^{1+s}) && (5.7)\\
\Rightarrow r'(n) &= (1+s)n^s + \delta k(1+s)n^s \cos(kn^{1+s}) && (5.8)\\
\Rightarrow f(n) = \frac{1}{r'(n)} &\approx \frac{1}{(1+s)n^s} - \frac{\delta k}{(1+s)n^s}\cos(kn^{1+s}) && (5.9)\\
\Rightarrow f(r) &\approx F_0(r) - \delta k F_0(r)\cos(kr) && (5.10)\\
&= \underbrace{\frac{r^{-\frac{s}{1+s}}}{1+s}}_{\text{base state}} - \underbrace{\frac{\delta k r^{-\frac{s}{1+s}}}{1+s}\cos(kr)}_{r \text{ dependent perturbation}} && (5.11)
\end{aligned}
$$

In the case where $s < 0$ (convex shapes), the amplitude in the perturbation of $f_0(r)$ grows with r, which means that far enough down the structure, we expect nonlinear effects to be important. However, for the purposes of testing a linear theory, it is sufficient to take $|\delta k|$ small enough and consider sufficiently small values of r so that $|\delta k F_0(r)| \ll 1$.

5.4 Decay Dependence on Wave Number

Equation (5.6) predicts that the decay rate always scales as the fourth power of the wavenumber, even for initial shapes which are not necessarily linear in n. This is confirmed by numerical results in Figures B-42. In each case, the decay rate was

measured at a fixed value of r. Bonzel and Mullins [13] have quantified the decay of small perturbations on a vicinal surface, where the kinetics is dominated by surface diffusion. They report that the decay rate scales like the wavenumber to the fourth power. Both the linearized PDE (5.3) and the simulation results in B-42 confirm this behavior.

5.5 Decay Dependence on Step-Interaction Parameter

A decay rate dependence which is proportional to ε is confirmed by numerical experiments, the results of which are shown in Figure B-43. This result was also shown empirically by the step flow simulations of Sato and Uwaha [102] but in the absence of step line tension. These results suggest that ε acts like an effective diffusivity: the larger its value, the more rapidly the step density profile reaches its steady state.

5.6 Large Perturbations and Nonlinear Effects

In this section, we present results where perturbations greater than 1 in magnitude were superimposed onto an initial linear profile. The plots shown in Figure B-44 show the evolution of a 600 step nanostructure with initial step radii given by

$$r(n) = n + 5\sin(0.1n) \tag{5.12}$$

The corresponding profile $F(n) = \frac{1}{r'(n)} = \frac{1}{1+0.5\cos(0.1n)}$. The evolution of this initial profile is very complex in general but can be broken down into three main stages. At early times, the sharp peaks in (a) decay. At intermediate times, there is a cusping in the troughs of the profile, accompanied by a rapid decay in the magnitude of the peaks. At later times, the entire F profile translates downwards, and finally at *long* times, we see an exponential decay characteristic of small-amplitude perturbations. A quantitative explanation for this behaviour is left as future work.

THIS PAGE INTENTIONALLY LEFT BLANK

Chapter 6

Numerical Solution of the Step-Flow Equations

6.1 Chapter Overview

In this final chapter, we give details on the algorithm that was used to integrate the step flow equations first presented in Chapter 2. We use a specially designed algorithm because the step flow equations have some unusual properties which may pose difficulties for standard Ordinary Differential Equation (ODE) integrators. The first of these properties is the singular and rapid collapse of the inner most step in the crystal structure. These collapses occur sequentially and each collapse results in the number of equations in the system decreasing by one. The second property is *local stiffness* which arises when steps bunch together. Because the step bunching and the associated stiffness only occur for a subset of the steps in the system, we use a *multi-adaptive*, explicit numerical scheme to take large time steps for non-stiff components, and smaller time steps for step bunched components.

6.2 Individual Time Stepping and Multi-adaptivity

We use the term *individual time-stepping* to describe the method whereby individual components of the solution vector $v_i(t)$ are advanced using their own individual time

steps. This is in contrast to conventional integrators which use the same time-step for all components, regardless of the time-scales involved in each. *Multi-adaptive* was a term used by Logg [73] to describe methods where individual time-stepping was used for different components, with the time-step size and order of the method chosen adaptively.

It is perhaps a little surprising to learn that individual time-stepping and Multi-adaptivity for ODEs have received relatively little attention, considering the wide variety of methods which researchers have used to try to improve the performance and accuracy of integration codes. It is even more surprising, given that Adaptive Mesh Refinement (AMR) is a well developed paradigm, used by many researchers who work in the field of Hyperbolic PDEs [10, 43]. Logg [73] has presented a well-developed Multi-adaptive Galerkin methodology for ODEs, but in terms of applications, individual time-stepping has been used in very few fields. Some researchers have used individual time-stepping in N-body problems [75],[119], [42] but as Logg pointed out, a general methodology is lacking. Individual time stepping clearly has computational advantages when there is a clear separation in time scales for the solution components, which may explain why this method has been quite popular with the astronomy community [26]. An example would be our solar system: Pluto has a much longer year than the earth, and ideally, one would like to use a larger time step to track Pluto's orbit, and a smaller one for the earth's. Gear and Kevrikidis [35] present a method for problems which contain a 'gap' in the eigenvalue spectrum, so that the solution contains both a rapidly damped component, and a slowly varying one. Their *projective integration* methods do not involve individual time stepping, but it is interesting to see how they tackle the problem of separation in time scales, and to compare their method with ours. We discuss this further in Section 6.3.2.

The step-flow equations possess a number of peculiar properties which pose problems for standard integrators - for example, *local* stiffness and the singular collapse of $\rho_1(t)$. Both of these concepts will be explained subsequently. In this chapter, we present and discuss the details of a custom-designed code, and show how the code can be used to solve the step-flow equations in an efficient manner.

6.3 Properties of The Step-Flow Equations

Before going into the properties of the system (2.39)-(2.43), we first outline qualitatively how the steps behave. In our equations, every step in the structure is subject to two types of physical effect. The first is a step-line tension, which arises due to a Gibbs-Thomson Effect [82]: an isolated, circular step of radius $r(t)$, sitting on an infinite substrate, initially devoid of adatoms, will reduce its perimeter (and hence radius) by emitting adatoms according to the law $\dot{\rho} \propto 1/\rho$ [55]. Note that $1/\rho$ is the curvature of the step. The second effect is a repulsive interaction with neighboring steps, characterized by a potential function that is inversely proportional to the square of the distance between the steps [62]. Steps in the bulk of the structure, having a smaller curvature will tend to be less affected by step-line tension, in contrast to steps near the top. When diffusion dominates over attachment detachment (TDL), the base step acts ultimately as the sink for all adatoms and grows monotonically.

Now, we focus on two peculiar properties of the Step-Flow Equations which require special attention when the integration is being carried out. These properties pose problems for standard integrators – hence the need for a custom designed algorithm. We simply state the properties here, and defer our solutions to section 6.4.

6.3.1 Singular Collapse of Steps

Equations (2.39)-(2.43) have the property that $\rho_1 \rightarrow 0$ at some finite time: the top step always undergoes a monotonic collapse because it will behave in such a way so as to minimize its radius. Naturally, as the top step shrinks and emits adatoms, the radii of the second and subsequent steps will grow as these are absorbed. When the top step completely disappears, the number of layers in the structure reduces by one. As a result of the sequential collapse of the top steps, a macroscopically flat region called a *facet* will form and grow on the top of the structure. Provided the collapse of the top step is tracked accurately, and the topmost ρ_i is removed at each time of collapse, the growth of the facet is automatically accounted for.

When a collapse does occur, ρ_1 is removed from the system, the number of equa-

tions to be integrated reduces by one, and the motion of the new top two steps is now governed by (2.39) and (2.40). Furthermore, if t_0 satisfies $\rho_1(t_0) = 0$, it can be shown that

$$\rho_1 \sim \sqrt{2}(t_0 - t)^{1/2} + \frac{1}{3}(t_0 - t)\ln(t_0 - t) + O(t_0 - t) \tag{6.1}$$

as $\rho_1 \to 0$, and so derivatives of $\rho_1(t)$ are divergent at the time of collapse. The accuracy of high order integrators usually rely on the solution having bounded derivatives, and applied to (2.39)-(2.43) as they stand, many standard integrators will have difficulty in tracking the collapse of top steps accurately near the time of collapse, t_0. In particular, for $(t_0 - t) = m\Delta t$ (so the solution is m time steps away from the collapse time), a method which has a truncation error of $O(\Delta t^p \frac{d^p y}{dt^p})$ for smooth solutions $y(t)$ and time step Δt will have its error greatly increased to

$$O(m^{-p+1/2}\Delta t^{1/2}) \tag{6.2}$$

when $y(t)$ has a square root singularity. It is also worth mentioning here that some adpative integration codes use Embedded Runge-Kutta Formulae which give estimates of local truncation errors. These codes typically scale their time steps assuming smooth solutions, and will update the step size using a formula like

$$\Delta t_{new} = \Delta t_{old}\left(\frac{desired\ error}{estimated\ error}\right)^{1/(\alpha+1)} \tag{6.3}$$

Here, α is the order of the integrator (e.g. $\alpha = 1$ for Simple Euler). Formulae like (6.3) break down near singularities, because there, the error does *not* scale like $\Delta t^{\alpha+1}$. The resulting behavior near singularities is somewhat unpredictable: adaptive integrators may take a huge number of tiny steps (making them inefficient), or may simply abort stating that the user-specified tolerance for the *desired error* was not achievable. Furthermore, even if the integrator manages to successfully step 'through' the singularity, it will probably output an error or produce complex solutions once it has stepped past the singularity.

6.3.2 Local Stiffness

An ODE is said to be stiff when its solutions are strongly stable, in the sense that small perturbations to the solutions decay very rapidly relative to the time scale of evolution. We say that an ODE is *locally stiff* when only perturbations to a few of the components in the solution decay in this way. In equations (2.39)-(2.43), this local stiffness has a clear physical interpretation: because of the nature of the step interactions discussed in Section 6.3, steps are strongly repelling when they get close to one another. Suppose we initialize the integration so that some of the steps in the bulk are tightly bunched together, but most of the other steps are widely spaced apart. In this case, a step in the middle of the bunch would be strongly stable because small perturbations in its trajectory would be opposed by strong interactions from the neighboring steps above and below. The same applies to any step inside the bunch. Solution components for the widely spaced steps do not experience this problem, and large time steps could be taken using an explicit integrator. Standard explicit integrators would not differentiate between local and global stiffness: if only a few of the solution components require a small time step, then this time step will be used for *all* of the components. Using implicit methods would, of course, work in principle, but it is questionable whether inverting a large $N \times N$ matrix is the best use of computational resources when only a small number of the N components are stiff. Of course, it could also happen that *all* the steps are very closely packed together, in which case all the components require small time steps, resulting in *global stiffness.* In this case, one would probably have to resort to implicit methods.

It is worth mentioning here some of the literature which deals with classes of problems involving disparate time scales. The work by Gear and Kevrikidis [35] involves so-called 'projective integration' methods which are used to integrate systems of ODEs which have a 'gap' in their eigenvalue spectrum. The solutions of the equations they study have a rapidly damped component, and a slowly varying one. However, their equations are *not*, in general, locally stiff (although having a gap in the spectrum is a necessary consequence of local stiffness): in their class of problems,

the fast time scales can potentially appear in every component of the solution. We emphasize again that local stiffness occurs when only a few of the components are rapidly damped when perturbed. In projective integration methods, it is assumed that the user has at his or her disposal an 'inner' and an 'outer' integrator. The idea is to take many small steps with every component of the solution using the inner integrator, so that the fast components are damped out, and then take a large *projective* step with the outer integrator. In our method, we also utilize two integrators (see Section 6.4.1), but we essentially use these integrators on different components of our solution. Our 'inner' integrator takes small steps only for the components with the fast time scales, and our 'outer' integrator takes large steps for those components with the slow time scales. Hence, projective integration methods use the inner/outer time steppers sequentially, whereas in our method, we use them simultaneously, taking advantage of the fact that the eigenvectors of the Jacobian corresponding to the large eigenvalues are *sparse*. There is also a large body of work (for example, [31], [44]) which uses Krylov methods to approximate the subspace spanned by the Jacobian, by using eigenvectors corresponding to the largest eigenvalues.

For our equations, stiffness will arise whenever a *step bunching instability* [50],[58], [63] occurs. Step bunching is a phenomenon well known to many researchers in the field of thin film epitaxy and crystal growth, and has potential applications in nanotemplates for quantum wires [72] and biological antifreeze agents [87]. Israeli and Kandel observed that step bunching occurred in ADL systems with initial unit step spacing whenever $\varepsilon \ll 1$, and our results from integration of (2.39)-(2.43) show that step bunching can occur in mixed systems also.

An analysis of stiffness usually requires computing the eigenvalues of the Jacobian matrix and showing that there is a large spread in the spectrum. The Jacobian of the equations (2.39)-(2.43) can be computed analytically by linearizing at a fixed $(\rho_1, \rho_2, ..., \rho_{N-1}, \rho_N)$, but the expressions involved are very complicated and do not give insight as to why the equations should be stiff. Instead, we present here a less rigorous approach and try to obtain approximations to the eigenvalues for a particular step configuration: that of equally spaced steps.

Let $\rho_i = \bar{\rho} + (i-1)\delta$ for $i = 1, 2, ..., N$ for some r, where δ is the step spacing. Then for $\delta \ll 1$ and $\bar{\rho} = O(1)$, the $N \times N$ pentadiagonal Jacobian Matrix defined by

$$J(i,j) = \partial_{\rho_j} F(\rho_{i-2}, \rho_{i-1}, \rho_i, \rho_{i+1}, \rho_{i+2}), \tag{6.4}$$

is

$$-\frac{3}{2}\frac{\varepsilon}{\delta^4}\begin{pmatrix} 2 & -3 & 1 & 0 & . & . & . & . & . & . \\ -3 & 6 & -4 & 1 & 0 & . & . & . & . & . \\ 1 & -4 & 6 & -4 & 1 & 0 & . & . & . & . \\ 0 & 1 & -4 & 6 & -4 & 1 & 0. & . & . & . \\ & . & . & . & . & . & . & . & . & . \\ & . & . & 1 & -4 & 6 & -4 & 1 & 0 & . \\ & & & . & . & . & & & & \\ & & & & & 0 & 1 & -4 & 6 & -3 \\ & & & & & & 0 & 1 & -3 & 2 \end{pmatrix}. \tag{6.5}$$

We recognize this matrix as being the finite dimensional approximation to a fourth derivative operator. To be more precise, if the eigenvalue problem

$$-\frac{3\varepsilon}{2}\frac{d^4}{dx^4}v(x) = \lambda x, \qquad 0 < x < L \tag{6.6}$$

such that $v'(0) = v'''(0) = v'(L) = v'''(L) = 0$ is solved by discretizing $v(x)$ and writing $\frac{d}{dx}$ as a second order differentiation matrix with a mesh width δ (so that $L = N\delta$), then the matrix $-\frac{3\varepsilon}{2}\frac{d^4}{dx^4}$ would be precisely (6.5), and the N eigenvectors and eigenvalues would be well approximated by

$$v_n(x_i) = \cos\left(\frac{n\pi x_i}{L}\right) = \cos\left(\frac{n\pi x_i}{N\delta}\right), \tag{6.7}$$

$$\lambda_n = -\frac{3}{2}\varepsilon\left(\frac{n\pi}{L}\right)^4 = -\frac{3}{2}\varepsilon\left(\frac{n\pi}{N\delta}\right)^4, \tag{6.8}$$

for $n = 0, 1, ..., N-1$ (note that 0 is always an eigenvalue of (6.5) with corresponding eigenvector $(1, 1, 1..., 1)^T$), where $x_i = (i-1)\delta$ for $i = 1, ..., N$.

These approximations to the eigenvectors and eigenvalues become exact in the limit of $\delta \to 0$ or $N \to \infty$. The smallest eigenvalue in magnitude is 0, and the largest $= O(\frac{\epsilon}{\delta^4})$. Therefore as the spacing, δ between all the steps becomes smaller, the system (2.39)-(2.43) becomes stiff very rapidly.

This argument can also be applied to clusters of steps - all that changes is that N, the total number of steps is replaced by N_i, say - the number of steps in the cluster. We can define a 'local' jacobian using N_i in much the same say, and a local step spacing δ_i by taking advantage of the fact that (2.39)-(2.43) is only locally coupled - so essentially, steps in one region can evolve without immediately affecting other steps which are far away. Hence, it is possible to have relatively large[1] local jacobians for some steps, but moderate local jacobians everywhere else.

6.4 Code Details

6.4.1 The Algorithm

Here, we explain how the algorithm works. Pseudocode with detailed information on the mechanics of the code is given in the Appendix.

As a reminder, the goal of the algorithm is to efficiently solve a system of locally coupled ODEs where only a few of the components are stiff. A standard explicit integrator would take small time steps for all components of the solution. Our method involves using individual timestepping to take large steps for non-stiff components, and small steps for the stiff ones.

The algorithm starts by taking an explicit, global time step, from t_n to t_{n+1}, say. Use of an Embedded Formula (see 6.4.2) yields estimates for the Local Truncation Error (LTE) for each component of the solution. Some of the LTEs may be very large, because some of the components may be stiff, while others will be acceptably small. We wish to keep the solutions which have small LTEs, but correct those which have large LTEs by performing a second integration. The second integration will

[1] Jacobians with large eigenvalues

basically be done only for the stiff components, and many small time steps will need to be taken in the interval $[t_n, t_{n+1}]$ to ensure stability (see 6.4.3 for details on how our code performs this second phase of integration). Although this second round of integration takes a large number of small time steps, it only needs to be done for a small subset of the total number of components. When the second integration is done, we must be able to generate dense output from the locally coupled non-stiff components between t_n and t_{n+1} in order to re-integrate the stiff components – see Figure B, and the most natural way to do this is through interpolation. The way that one interpolates to obtain the dense output is key to (non-trivially) generalizing the method to higher order time steppers – see Section 6.5.1. Our method uses the simplest type of interpolation – linear interpolation between t_n and t_{n+1}, meaning that the time stepper we use in the second round of integration should not be more accurate than 1st order.

When deciding which LTEs are 'large' and which are 'small', we adopt the following procedure: first, find the median, μ, of all the LTEs, which we will call e_i. Then, for some positive integer k, flag all components whose LTEs are greater than $10^k\mu$ (our code uses $k = 2$) as being unacceptably large. Let tol_i be the tolerance for solution component i. Make sure that the unflagged solution components satisfy tolerance requirements, i.e. $maxratio \equiv Max(|e_i/tol_i|) < 1$ where $Max()$ is taken over all all unflagged components only. If this is not satisfied, the global step size is reduced according to a formula like (6.3) using the value of α corresponding to the order of the Embedded Runge Kutta Formula and $maxratio$ as the ratio of errors. If the tolerance requirements are satisfied, then the step size is increased using the formula (6.3) using the same value of α and $errmax$.

Once solution components have been flagged as requiring re-integration, the local coupling means that some of the non-stiff components may also have to be re-integrated. To flag the solution components, the algorithm simply sweeps through all N components in $O(N)$ operations using the `makepairs` algorithm detailed in Appendix C. Because (2.39)-(2.43) is a pentadiagonal system of equations, if only $r_m(t)$ and $r_{m+2}(t)$ are stiff components with large LTEs, then all three of the components

$r_m(t), r_{m+1}(t)$ and $r_{m+2}(t)$ must be re-integrated as a set, using the dense output from $r_{m-2}(t)$, $r_{m-1}(t)$, $r_{m+3}(t)$ and $r_{m+4}(t)$ as 'boundary conditions'. Hence, the algorithm is slightly wasteful in that although $r_{m+1}(t)$ was deemed accurate enough, it still had to be integrated for a second time.

For the rest of this paper, we will call the first time stepper I_1 (used to generate the LTEs in the first place), and the second time stepper I_2 (used to re-integate stiff components with large LTEs). In general, I_1 and I_2 do not have to be the same method, or of the same order, but I_1 has to be able to generate estimates of the Local Truncation Error. In our code, I_1 is a Cash-Karp Runge-Kutta Formula and I_2 is a Simple Euler routine which adjusts its step size by step doubling. We refer to [96] for technical details of the Cash-Karp Embedded Formula.

6.4.2 Embedded Runge-Kutta Formulae

Embedded Runge-Kutta formulae contain two Runge-Kutta Formulae of different orders. As in all Runge Kutta Methods, between t_n and t_{n+1}, samples of $\mathbf{F}(\mathbf{y}, t)$ are taken. In a conventional Runge-Kutta Formula, these samplings of $\mathbf{F}$ are weighted and summed in order to advance the solution to t_{n+1}. In an Embedded Formula, however, more samplings are taken than for a normal Formula, with the benefit that now the samplings can be weighted in two different ways, before being summed – and these different weightings correspond to RK Formulae of different orders. In the case of the Cash-Karp pair, 6 samplings are taken, with the result that the Embedded Formula contains both a 4th and 5th order time stepper. The difference in the solutions obtained by advancing with each of these integrators gives a measure of the Local Truncation Error (LTE) committed by advancing from t_n to t_{n+1}. Adaptive Integrators use this information to monitor the quality of the solution and adjust their time steps accordingly.

Our algorithm uses the LTE in a different way: instead of immediately scaling the time step if the smallest LTE is greater than the tolerance level, we make a note of *which* solutions had the largest LTEs. The philosophy behind this is that it might not be efficient to re-take the time step for every trajectory, if only a few of them

are inaccurate. The largest LTEs [2] are discarded, and then, the time step scaled according to the largest of the *remaining* errors. This way, we get a larger time step for a majority of the solution components, and the way that this time step is adjusted throughout the course of the integration is not affected by the presence of a few rapidly varying or stiff components.

6.4.3 Re-integration of Step Bunches with Simple Euler

As mentioned already, step bunching instabilities can arise when integrating the step flow equations, resulting in local stiffness. The trajectories of these step bunches are integrated with an explicit Simple Euler Method. Although many small steps must be taken because of the stiffness, the overall procedure is not too costly providing the step bunching is restricted to only a small fraction of the total number of steps.

As a reminder for this section, we assume that we have two integrators at our disposal, which we call I_1 and I_2. I_1 takes large time steps for most of the slowly varying components, whereas I_2 takes relatively small steps for a few rapidly changing components. When I_1 takes a step from t_n to t_{n+1}, the algorithm uses a very crude interpolation – linear interpolation – to produce dense output for non-stiff components in the solution. Using a higher order method for I_2 would require an interpolation which is consistent with the method. For example, if we take I_2 to be second order Runge Kutta, quadratic interpolation would be required. Quadratic interpolation would require 3 data points (for Lagrange Interpolation), or would have to make use of derivative information at t_n as well as the values at t_n and t_{n+1} (Hermite interpolation). We have only partially explored the possibility of using higher order interpolants for the slowly varying component, but preliminary results seem to show that (i) the accuracy of the stiff components depends crucially upon the quality of the interpolation, and (ii) generating high quality interpolants as the algorithm is running ('during run time') is non-trivial. In any case, since our routine uses linear interpolation, using a time stepper I_2 which is of second order (say) is wasteful because large $O((t_{n+1} - t_n)^2)$ errors propagate into the stiff components at every time step,

[2] The largest LTS are a few orders of magnitude larger than the median LTE, as stated in 6.4.1.

when LTEs for I_2 are $O(\Delta t^3)$ for a time step Δt.

Step Doubling is a very crude way of adjusting the time step and these methods have long been superseded by Embedded Runge Kutta Formulae [96]. However, when (6.3) breaks down, using Step Doubling to monitor the quality of the solution is reasonable, and (6.3) breaks down when the top step collapses in a singular fashion. Details of the Step Doubling algorithm are given in Appendix C.

Note that there are two possibilities which can arise when performing the re-integration with I_2 on (2.39)-(2.43):

1. The re-integration involves solution components which includes ρ_1.

2. The re-integration does not involve the top-most layer.

The reason to distinguish between these two cases is that 1. will involve integration of a singular trajectory (see 6.3.1), but in general, 2. will not. Hence, in 1., using Simple Euler is the 'best' that one can do, whereas in 2., there is the potential for using higher order time steppers – but this generalization is not obvious because of the interpolation issues (see 6.5.1).

6.4.4 Treatment of Singular Collapse of Top Step

Solving for $\rho_1^2, \rho_2, ...\rho_N$ instead of $\rho_1, \rho_2, ..., \rho_N$ improves the performance I_2 because now ρ_1^2 satisfies

$$\rho_1^2(t) \sim C_3(t_0 - t) + C_4(t_0 - t)^{3/2} \ln(t_0 - t) \tag{6.9}$$

as $\rho_1^2 \to 0$ for some constants C_3 and C_4, which means that ρ_1^2 does have exactly one derivative at t_0. However, taking square roots to recover ρ_1 will result in a drastic loss in accuracy near t_0: at time t, consider taking a time step of size Δt with component ρ_1^2 using Simple Euler. Let $\rho_{exact}^2(t + \Delta t)$ be the result of taking this time step using a 'perfect' integrator, producing the exact solution at $t + \Delta t$, given $\rho_1^2(t)$. Then

$$
\begin{aligned}
|\rho_1^2(t+\Delta t) - \rho_{exact}^2(t+\Delta t)| &= O(\Delta t^{3/2}\ln\Delta t) && (6.10)\\
\Rightarrow \rho_1 &= (\rho_{exact}^2 + O(\Delta t^{3/2}\ln\Delta t))^{1/2} && (6.11)\\
&= \rho_{exact}\left(1 + \frac{O(\Delta t^{3/2}\ln\Delta t))}{\rho_{exact}^2}\right)^{1/2} && (6.12)
\end{aligned}
$$

Therefore, if $\rho_{exact}^2 \gg O(\Delta t^{3/2}\ln\Delta t)$, i.e. we are sufficiently far away from the singularity, then the LTE for ρ_1, $|\rho_1 - \rho_{exact}|$, is $O(\Delta t^{3/2}\ln\Delta t)$. However, if $\rho_{exact} \ll O(\Delta t^{3/2}\ln\Delta t)$, and we are close to t_0, then the LTE for ρ_1 is $O(\Delta t^{3/4}(\ln\Delta t)^{1/2})$, which is not really a big improvement over (6.2). Again, these order-of-magnitude estimates for the LTE are independent of the order of I_2. The main reason for solving for ρ_1^2 instead of ρ_1 is not to improve accuracy, but rather to enable the algorithm to 'step through' the singularity at $t = t_0$, and use linear interpolation to obtain t_0, the time of collapse of the top step. When I_2 has 'overstepped' t_0 and $\rho_1^2(t_m) > 0$ and $\rho_1^2(t_{m+1}) < 0$ for some integer m, then we set

$$
t_0 = \frac{\rho_1^2(t_{m+1})t_{m+1}}{\rho_1^2(t_m) - \rho_1^2(t_{m+1})} - \frac{\rho_1^2(t_{m+1})t_m}{\rho_1^2(t_m) - \rho_1^2(t_{m+1})} \qquad (6.13)
$$

as an approximation to the collapse time. Once ρ_1 is deemed to have vanished at t_0, it is removed from the system (2.39)-(2.43), the number of equations drops by one, and $\rho_2^2(t)$ replaces $\rho_1^2(t)$ as the new top step.

6.5 Implementation and Validation

Figure B-46 shows the results of applying the multi-adaptive integration algorithm to a TDL system. The algorithm takes small time steps for rapidly moving steps near the facet, but larger time steps for those in the bulk. Hence, in the TDL case, most of the work done by the algorithm is in re-integrating a few of the inner most steps: the efficiency of the algorithm increases if there are many uniformly spaced steps in the bulk.

6.5.1 Interpolation issues

We wish to stress here that the main reason why our method for individual time stepping is successful is because we use a *low order* integrator for I_2, which means that interpolation from solution data generated by I_1 can also be of a low order. In particular, if I_2 is a Simple Euler Routine, then only linear interpolation needs to be done to maintain consistency in the order of the I_2 method. If we use an I_2 which has order p, then the local truncation error for I_2 is $O(\Delta t^{p+1})$ and so the error committed when interpolating the end points generated by I_1 must also be $O(\Delta t^{p+1})$. For example, if we use Fourth Order Runge-Kutta as I_1 to step from t_n to t_{n+1}, and Second Order Runge Kutta as I_2, then we need some way of generating dense solution output between t_n and t_{n+1} which has error at most $O((t_{n+1}-t_n)^3)$ during run-time, so in this case simple linear interpolation would be inadequate. Possible solutions are to use previous data points like t_{n-1}, say, and use quadratic interpolation, or to make use of our knowledge of the derivatives at t_n and t_{n-1} to perform some kind of Hermite interpolation. Ultimately, one would like the orders of I_1 and I_2 to be equal, and this we leave for future work.

6.5.2 Validation

The code can be used to solve some model problems which have analytic solutions. Obtaining accurate collapse times $t_i, i = 1, 2, ...$ for these model problems necessarily follows from having a code which accurately solves for $\rho_i(t)$. Consider the following uncoupled system

$$\dot{r}_i = -1/r_i \tag{6.14}$$

for $i = 1, 2, ..., N$ with initial condition $r_i(0) = i$.

The solution to this set of ODEs is $r_i(t) = \sqrt{i^2 - 2t}$. Note in particular that the solution has the same asymptotic singular behavior at the collapse times $t_i = i^2/2$. In this case, r_1^2 is simply linear in time, and can therefore be integrated *exactly* by

Simple Euler. A second model problem is

$$\dot{r}_i = -1/r_i^2 \tag{6.15}$$

with the same initial condition. In this case, r_1^2 is no longer linear. The collapse times in this system take the form $t_i = i^3/3$ because the exact solutions are

$$r_i(t) = (i^3 - 3t)^{1/3}. \tag{6.16}$$

Table A.8 shows the results of integrating both of these model systems.

As well as studying model problems, whose solutions are known, we can also check the accuracy of our numerical scheme in the following way: a standard, fixed time step ($\Delta t = 10^{-6}$) Simple Euler routine was used to integrate (2.39)-(2.43), and linear interpolation on ρ_1^2 was used to obtain the collapse times (see Table A.9). Since the value of Δt used was very small, we took these collapse times as being the "exact" values, and used them as a reference for the multi-adaptive scheme. The multi-adaptive scheme takes much larger, variable sized time steps, but manages to reproduce the times of collapse to about 4 or 5 digits of accuracy.

THIS PAGE INTENTIONALLY LEFT BLANK

Appendix A

Tables

Quantity	Description	Value	Units	Source	Comments
g_1	Free energy per unit length and height to create an isolated step	~ 0.001	$eV/\mathring{A}^2$	Ising Model[1]	-
g_3	Step interaction energy per unit length and height	0.04–0.06	$eV/\mathring{A}^2$	[55] Table 7	Si(111) at 900^o
$c_s D_s$	Diffusion Coefficient on terraces	10^8	s^{-1}	[94]	-
D_s	Surface Diffusivity	10^{11}	$\mathring{A}^2/s$	[68]	Monte Carlo Simulations of Si(111) using $k_B T \sim 0.1eV$
$c_s \tilde{\beta} k_d$	Adatom detachment parameter	4.7×10^{-3}	$eV/\mathring{A}^2 s$	[48]	Island decay of Si(111) at 465^o C
$\tilde{\beta}$	Step Stiffness	0.03	$eV/\mathring{A}$	[55] Table 8	at 950^o C

Table A.1: Numerical values of main constants used in the axisymmetric Step Flow Model (2.20) and (2.21)–(2.24).

[1] $g_1 = \frac{\beta}{h} = \frac{\varepsilon_k}{a^2} - \frac{k_B T}{a^2} \ln\left(\coth \frac{\varepsilon_k}{2k_B T}\right)$ where β is the energy per unit length required to create an isolated step, h is the step height and $\varepsilon_k \sim 0.1eV$ is the kink energy. $a = h \sim 5\mathring{A}$ is taken as the lattice constant $k_B T \sim 0.1eV$

s	τ_s	a_{num} (σ_a)	$a_L(s)$	$a_S(s)$
-0.20	10	660 (23)	588	667
-0.15	10	472 (24)	423	462
-0.10	10	285 (1)	270	286
-0.05	10	133 (0)	130	133
0.00	10	000 (0)	000	000
0.05	10	-117 (0)	-120	-118
0.10	10	-223 (0)	-233	-222
0.15	10	-321 (3)	-337	-316
0.18	60	-371 (1)	-396	-367
0.20	60	-404 (2)	-435	-400
0.25	60	-492 (6)	-526	-476

Table A.2: Numerical and theoretical exponents for the exponent a in the relation (4.11). The step-step interaction parameter $g = 10$. Quantities in parentheses indicate the standard deviation, σ_a, of the distribution of a_{num}, and give an indication of the error. The exponents a_L and a_S are competing theoretical predictions for a_{num} (see (4.23) and (4.26)). Step Flow Simulations were initialized with $\rho_m = m^{1+s}$ and τ_s is the first sampling time (see Section 4.3.5). For convenience, values a_{num}, σ_a, a_L and a_S have all been multiplied by 10^4.

s	τ_s	b_{num} (σ_b)	$b_L(s)$	$b_S(s)$
-0.20	10	264 (6)	235	267
-0.15	10	263 (7)	239	262
-0.10	10	256 (0)	243	257
-0.05	10	252 (0)	247	253
0.00	10	249 (0)	250	250
0.05	10	246 (1)	253	247
0.10	10	246 (0)	256	244
0.15	10	247 (2)	258	242
0.18	60	244 (1)	260	241
0.20	60	243 (1)	261	240
0.25	60	247 (3)	263	238

Table A.3: Same as Table A.2 for $g = 10$, but for the exponent b. The values b_{num}, σ_b, b_L and b_S have all been multiplied by 10^3.

s	τ_s	γ_{num}	$\gamma_L(s)$	$\gamma_S(s)$
-0.20	10	303	340	300
-0.15	10	329	355	325
-0.10	10	353	370	350
-0.05	10	373	385	375
0.00	10	392	400	400
0.05	10	414	415	425
0.10	10	432	430	450
0.15	10	446	445	475
0.18	60	457	454	490
0.20	60	464	460	500
0.25	60	477	475	525

Table A.4: Theoretical and simulation values for the exponent γ, when $g = 10$, where the collapse times $\tau_n \sim n^{\gamma(s)}$ for large n. The exponents $\gamma_L(s)$ and $\gamma_S(s)$ are defined in (4.39) and (4.40). Simulation conditions are the same as in Tables A.2 and A.3, and γ_{num}, γ_L and γ_S have been multiplied by 10^2.

s	τ_s	a_{num} (σ_a)	$a_L(s)$	$a_S(s)$
-0.20	4×10^3	620 (17)	588	667
-0.15	10^4	416 (6)	423	462
-0.10	10^5	283 (3)	270	286
-0.05	4.5×10^4	130 (1)	130	133
0.00	10^5	000 (0)	000	000
0.05	1.9×10^6	-112 (1)	-120	-118
0.10	1.7×10^6	-222 (0)	-233	-222
0.15	2×10^6	-321 (0)	-337	-316
0.18	1.5×10^6	-378 (0)	-396	-367
0.20	1.8×10^6	-404 (2)	-435	-400
0.25	1.2×10^6	-484 (2)	-526	-476

Table A.5: Same as Table A.2 but with $g = 0.01$.

s	τ_s	b_{num} (σ_b)	$b_L(s)$	$b_S(s)$
-0.20	4×10^3	244 (60)	235	267
-0.15	10^4	238 (33)	239	262
-0.10	10^5	249 (3)	243	257
-0.05	4.5×10^4	242 (2)	247	253
0.00	10^5	252 (1)	250	250
0.05	1.9×10^6	252 (1)	253	247
0.10	1.7×10^6	253 (1)	256	244
0.15	2×10^6	255 (1)	258	242
0.18	1.5×10^6	256 (1)	260	241
0.20	1.8×10^6	254 (2)	261	240
0.25	1.2×10^6	253 (6)	263	238

Table A.6: Same as Table A.3 but with $g = 0.01$.

s	τ_s	γ_{num}	$\gamma_L(s)$	$\gamma_S(s)$
-0.20	4×10^3	340	340	300
-0.15	10^4	352	355	325
-0.10	10^5	364	370	350
-0.05	4.5×10^4	377	385	375
0.00	10^5	393	400	400
0.05	1.9×10^6	411	415	425
0.10	1.7×10^6	425	430	450
0.15	2×10^6	440	445	475
0.18	1.5×10^6	449	454	490
0.20	1.8×10^6	453	460	500
0.25	1.2×10^6	467	475	525

Table A.7: Same as Table A.4 but with $g = 0.01$.

eqn (6.14) *(numerical)*	*eqn* (6.14) *(exact)*	*eqn* (6.15) *(numerical)*	*eqn* (6.15) *(exact)*
0.500 000 000 000	0.500 000 000 000	**0.333** 347 109 507	0.333 333 333 333
2.000 020 070 412	2.000 000 000 000	**2.666** 738 664 937	2.666 666 666 667
4.500 068 682 565	4.500 000 000 000	**9.000** 204 981 678	9.000 000 000 000
8.000 133 885 813	8.000 000 000 000	**21.333** 765 043 031	21.333 333 333 333
12.500 213 330 475	12.500 000 000 000	**41.667** 438 341 838	41.666 666 666 667

Table A.8: Collapse times, computed with the multi-adaptive algorithm, for model systems (6.14) and (6.15).

fixed step SE	Multi-adaptive
0.540 289 230 794	**0.540** 305 641 980
5.100 219 762 927	**5.100** 284 674 837
21.036 583 847 637	**21.036** 757 035 271
59.481 455 149 416	**59.481** 830 949 331
135.366 866 973 862	**135.367** 562 952 919

Table A.9: First five collapse times shown for a TDL system, with $\varepsilon = 0.01$. These collapse times were computed in two different ways: with a fixed step ($\Delta t = 10^{-6}$) Simple Euler Integrator, and with the Multi-adaptive Algorithm detailed in Chapter 6. The initial condition was a 15-terraced conical profile with unit spacing.

THIS PAGE INTENTIONALLY LEFT BLANK

Appendix B

Figures

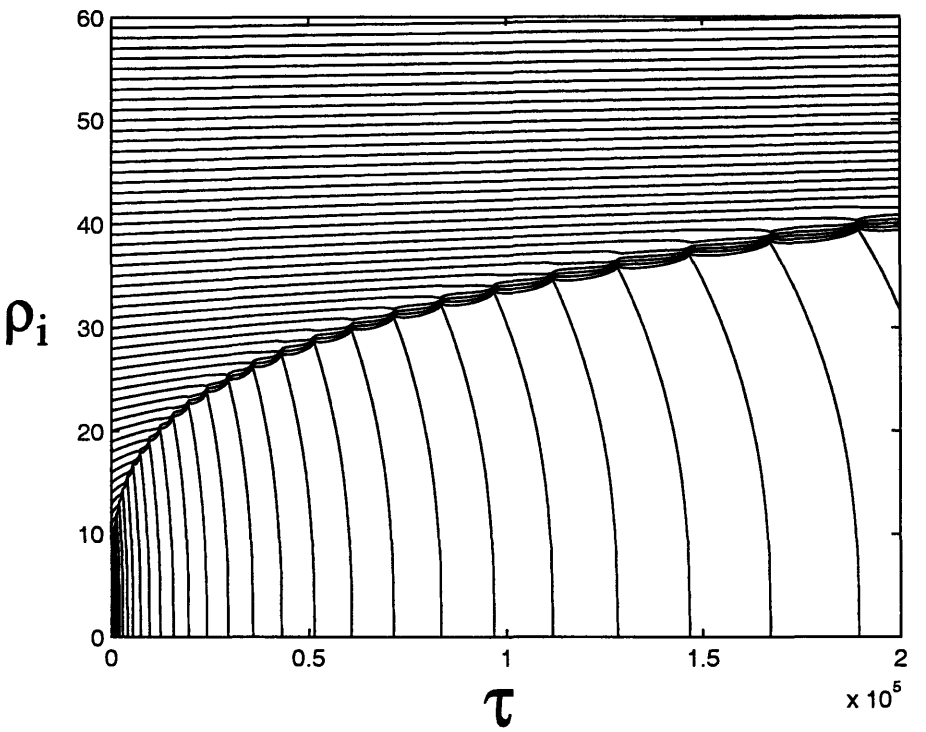

Figure B-1: Results from integration of the step flow equations when diffusion across terraces is the rate limiting process. The radii of each of the steps are plotted as a function of time. The step interaction parameter $g = 10^{-6}$ and an initial step spacing of unity was used. Note the rapid and regular collapse of the inner most step.

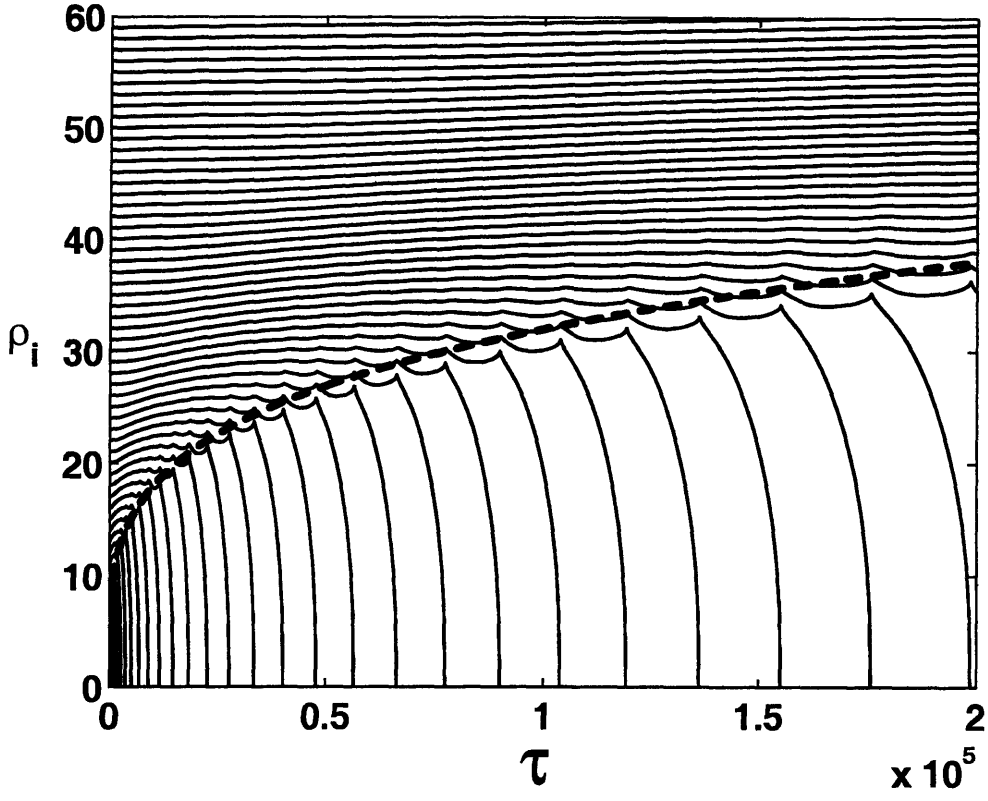

Figure B-2: Results from integration of the step flow equations in the Terrace Diffusion Limited (TDL) case, when the step interaction parameter $g = 10^{-2}$. Following Israeli and Kandel [50], the dotted line indicates the $t^{1/4}$ envelope which approximates the location of the facet.

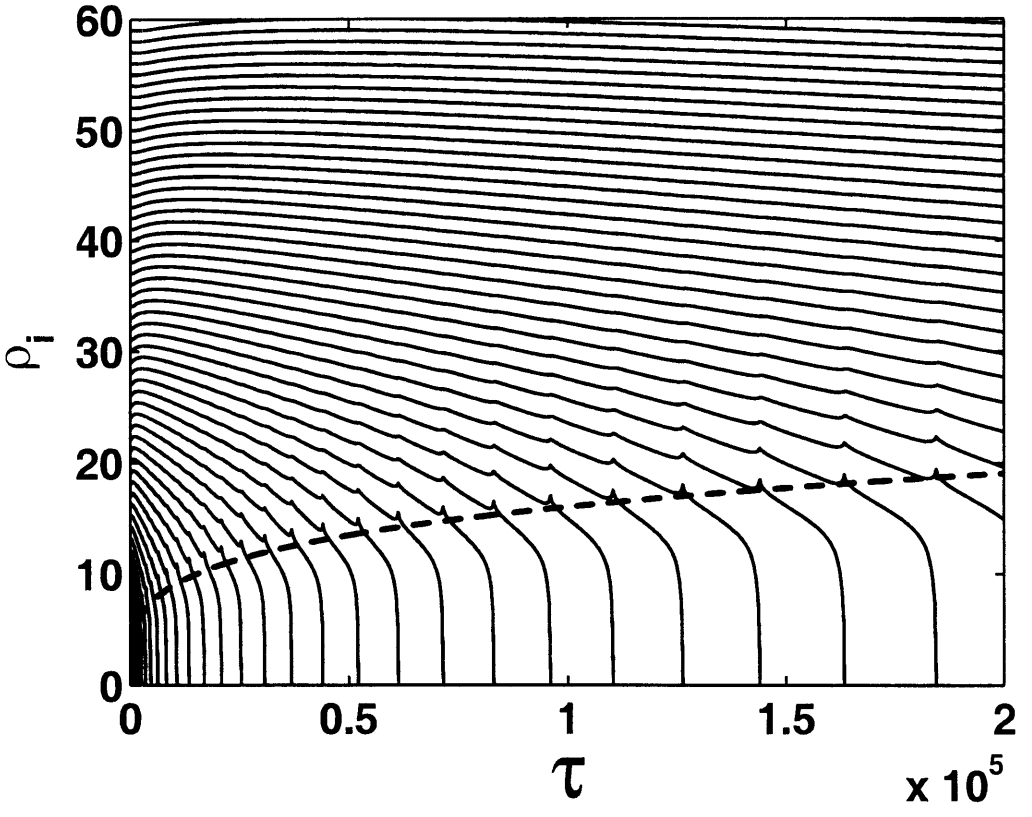

Figure B-3: Results from integration of the step flow equations in the Terrace Diffusion Limited (TDL) case, when the step interaction parameter $g = 1$. Compared to B-2 at a fixed time, the facet radius is a lot smaller.

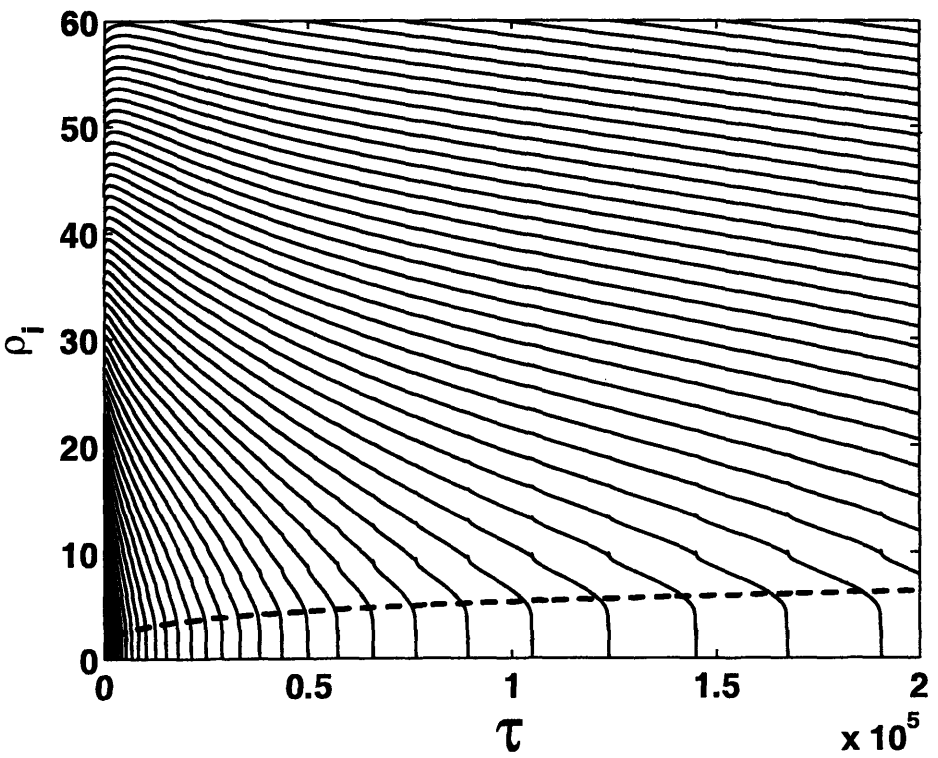

Figure B-4: Results from integration of the step flow equations in the Terrace Diffusion Limited (TDL) case, when the step interaction parameter $g = 10$. The facet radius is smaller still, compared to B-3 and B-2 at this value of g.

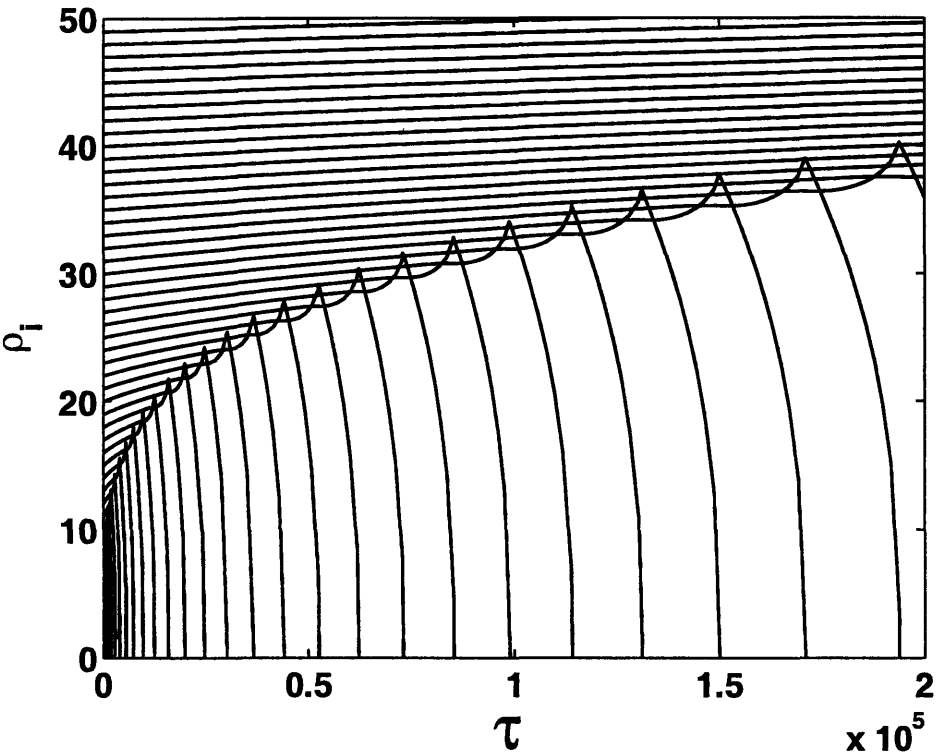

Figure B-5: Results from integration of the step flow equations in the Terrace Diffusion Limited (TDL) case, when step interactions are completely switched off ($g = 0$), resulting in steps crossing, which is unphysical. When steps first cross, the equations of motion are no longer valid.

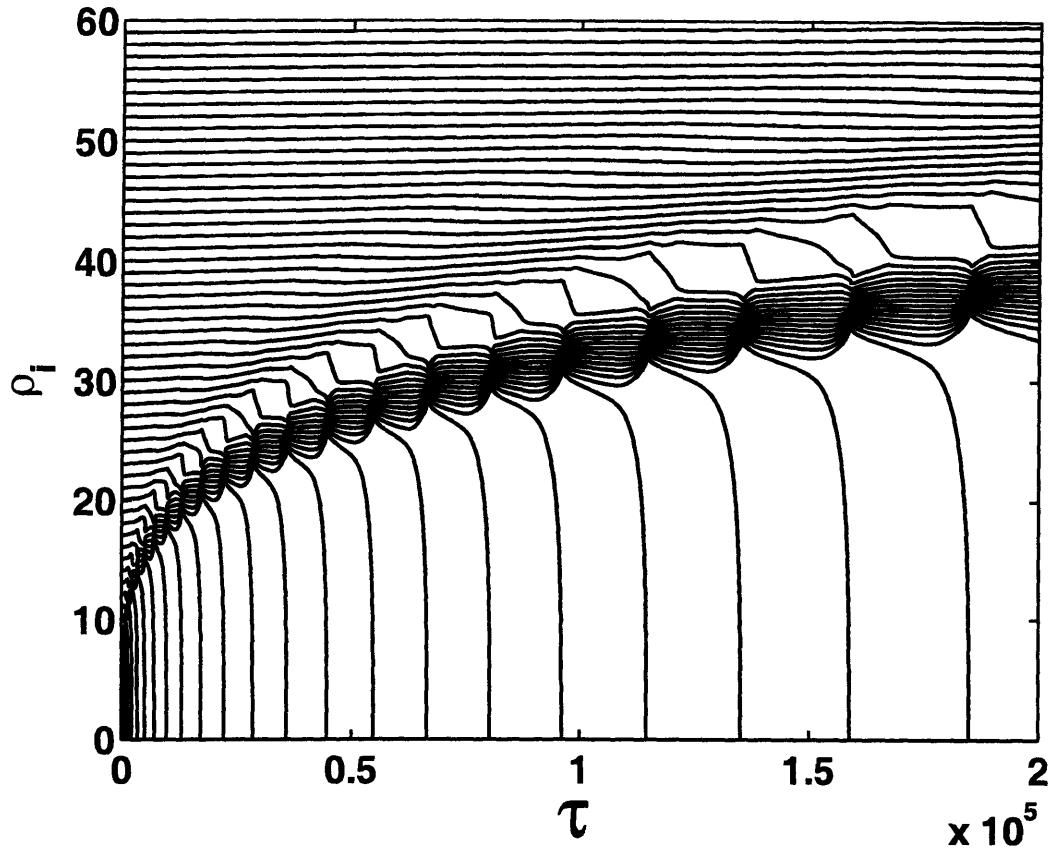

Figure B-6: Results from integration of the step flow equations when attachment-detachment at steps edges is the rate limiting process, for $g = 5 \times 10^{-4}$ and an initial step spacing of unity.

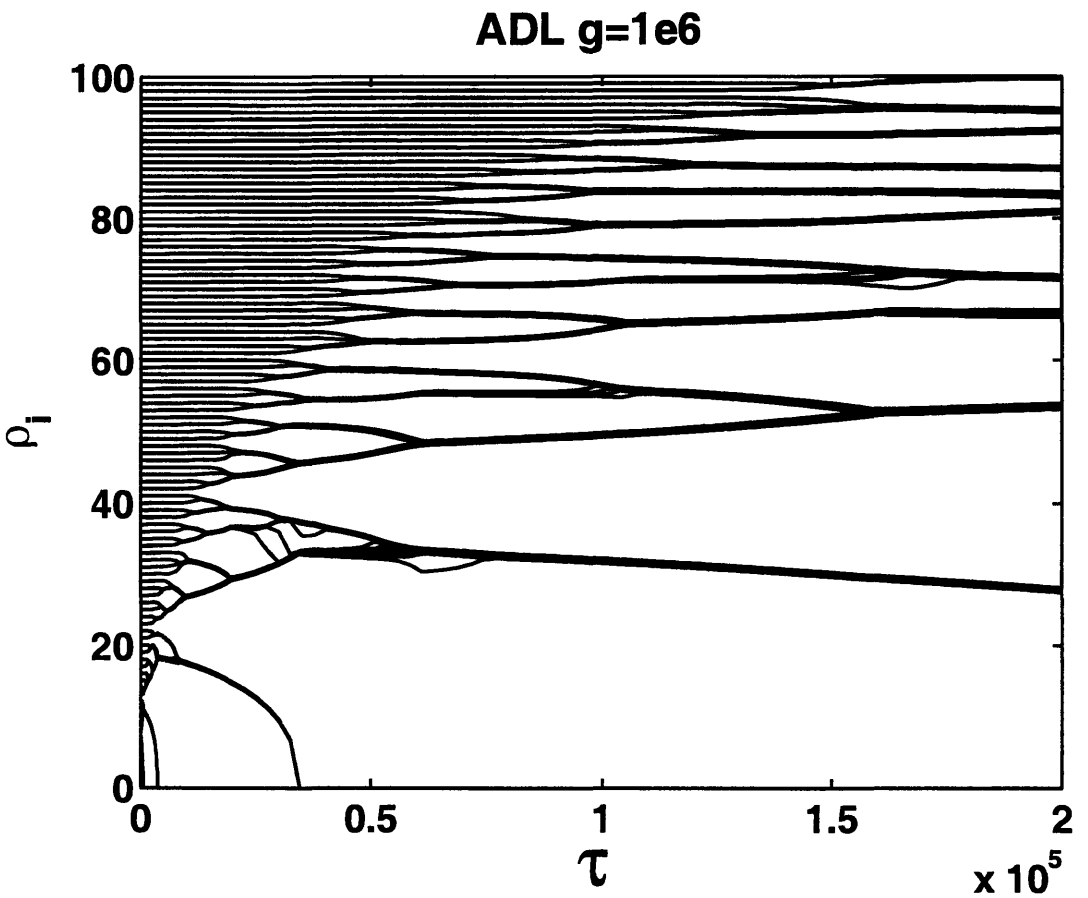

Figure B-7: ADL kinetics, with an initial step spacing of unity and $g = 10^{-6}$. Step bunching is very well developed for this small value of g, and the step bunches (as opposed to individual steps) are now the main dynamical entities in the system.

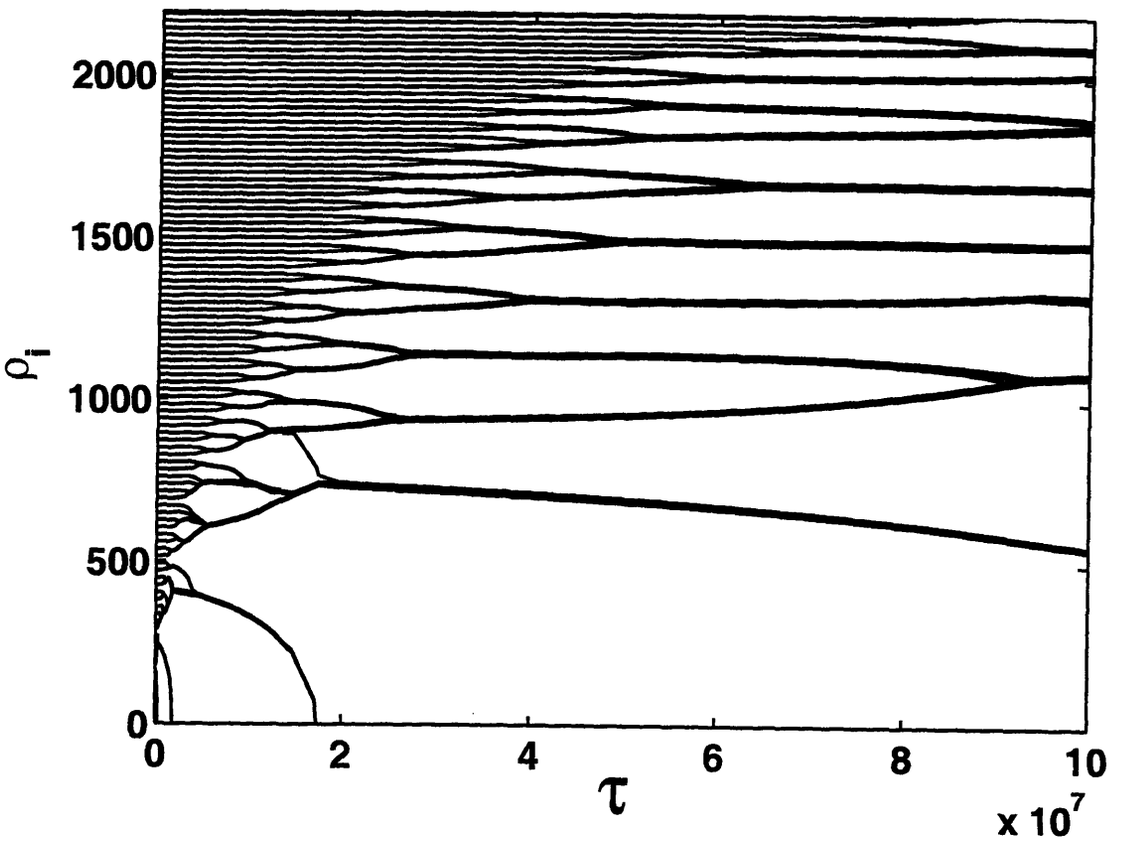

Figure B-8: The value of g in B-6 is used here, but the step simulation is initialized with a uniform spacing of $\sqrt{500}$. Step bunching is well developed, similar to B-7, but note the change in the vertical axis.

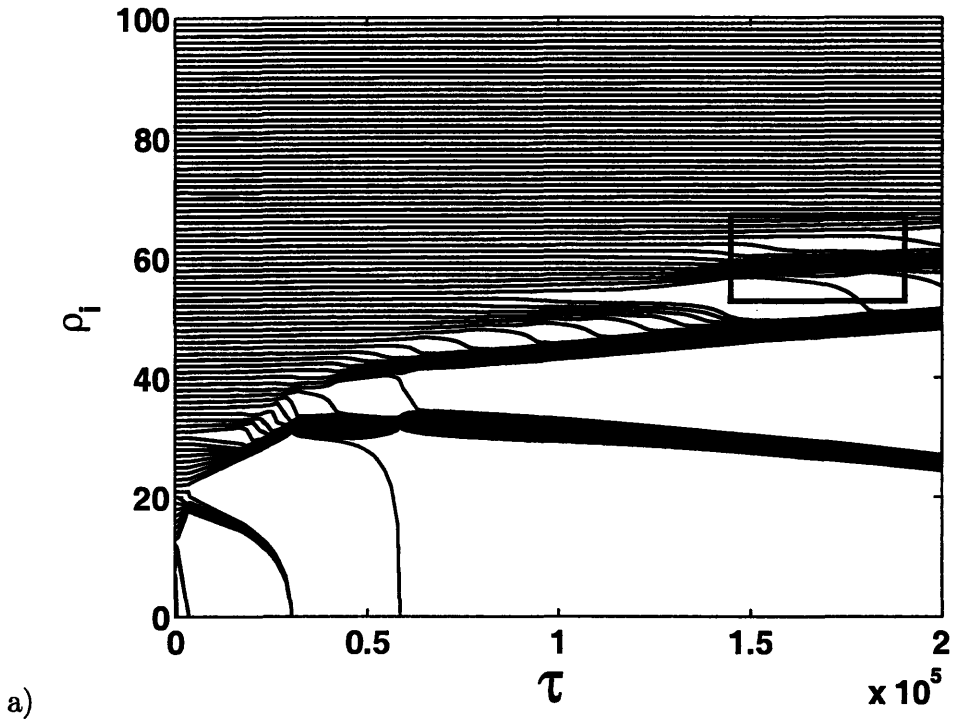

a)

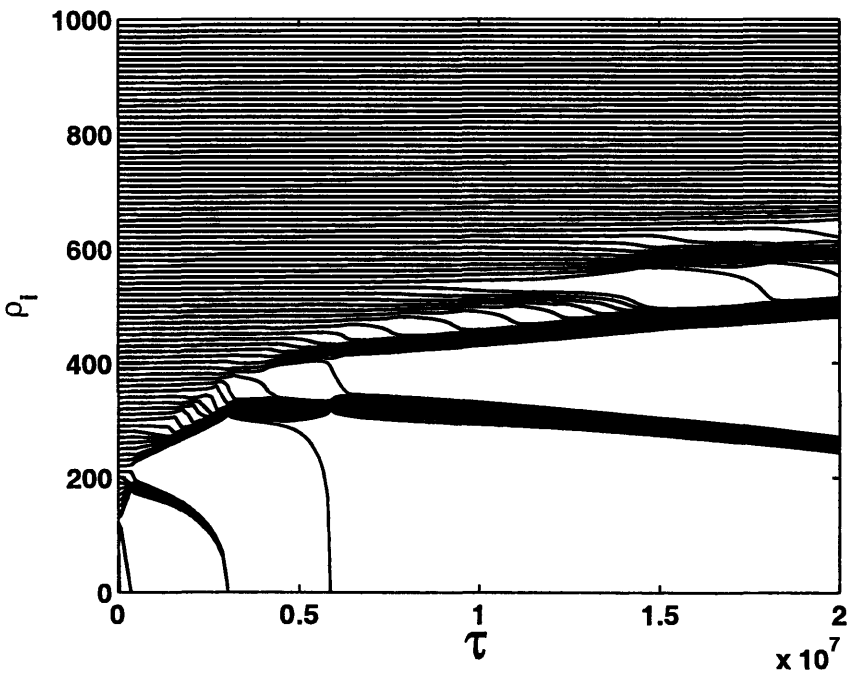

b)

Figure B-9: ADL systems with identical values of $g/(\text{step-spacing})^2$. Plot a) has $g = 10^{-4}$, and an initial step spacing of unity. Plot b) has $g = 10^{-2}$ and an initial step spacing of 10. The box in a) shows a region where step bunching is only starting to develop. Note the scales on the horizontal and vertical axes of each plot.

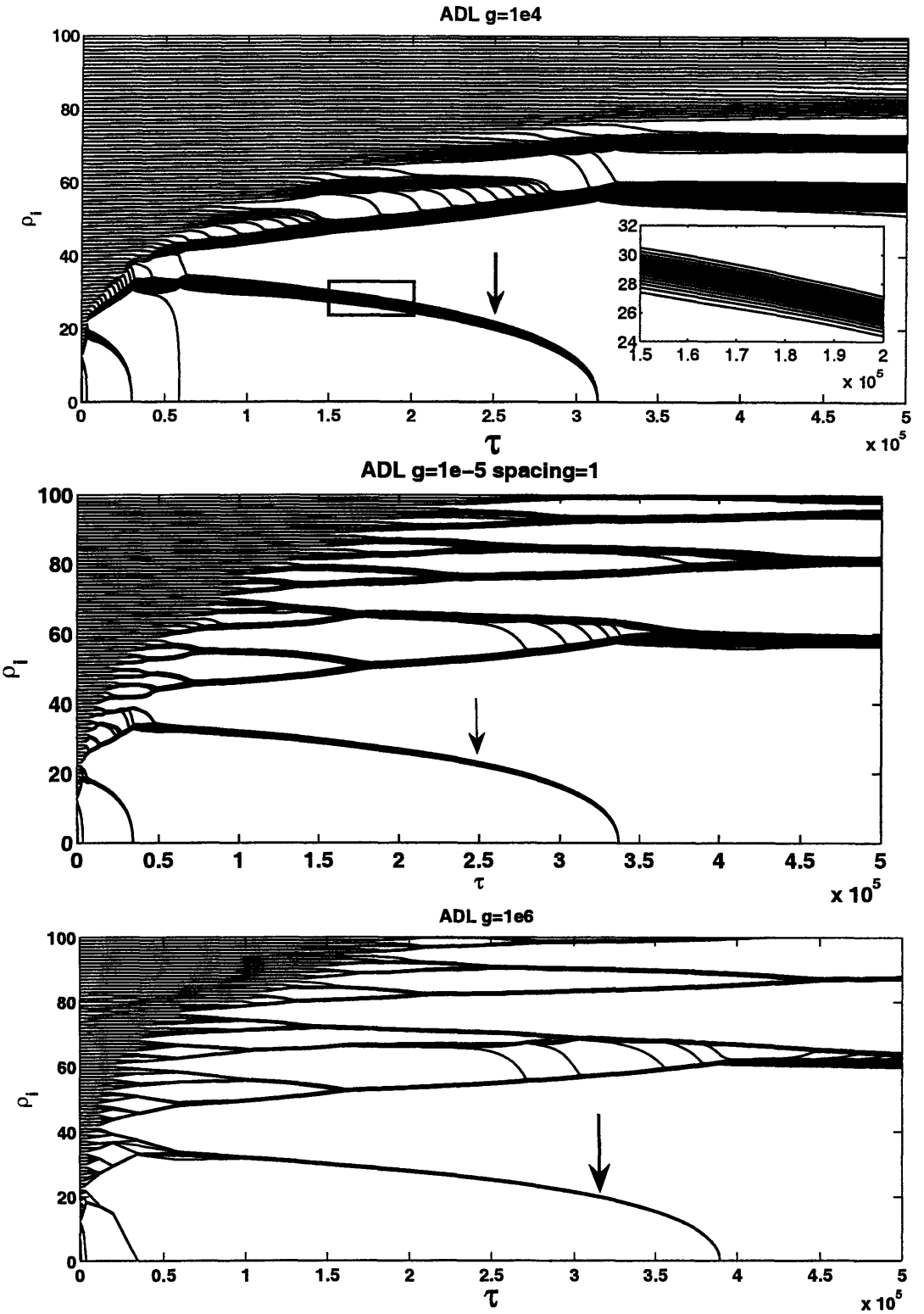

Figure B-10: ADL systems for $g = 10^{-4}, 10^{-5}$ and 10^{-6}, initialized with unit step spacing. Arrows indicate the step bunches which are analyzed in Section 2.4.3. The inset shows a close up of a particular step bunch.

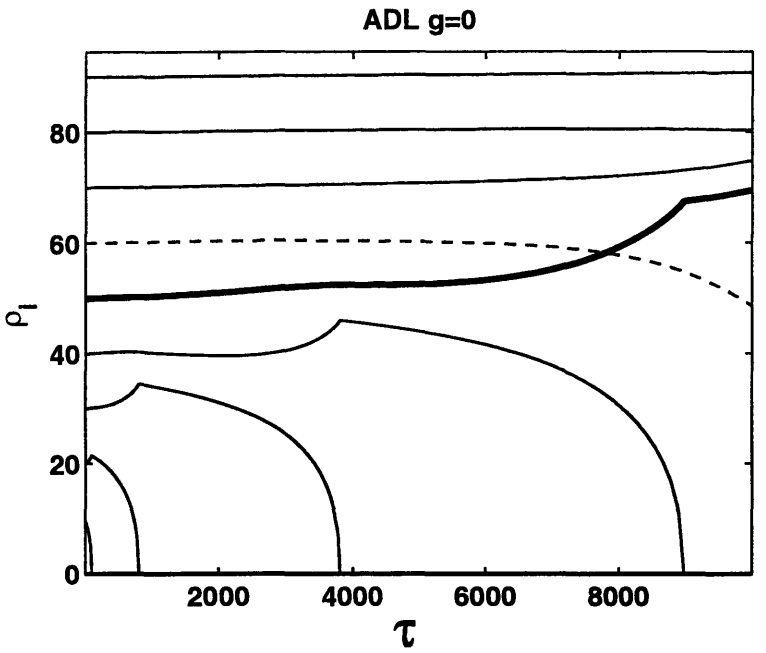

Figure B-11: ADL system with $g = 0$. With step interactions switched off, the step flow code predicts that steps can pass through each other, as shown by the solid and dotted trajectories. The step flow equations break down when steps first cross.

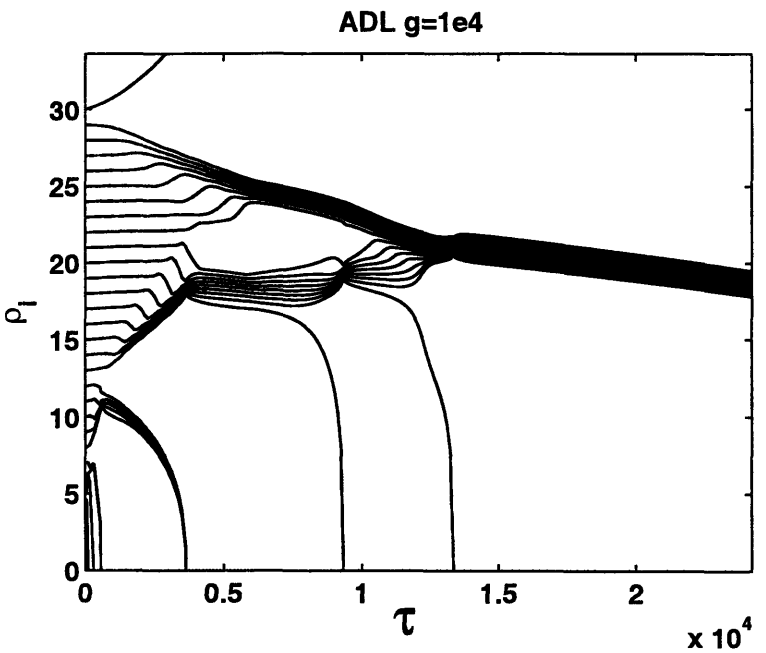

Figure B-12: ADL system with $g = 10^{-4}$, starting with only 30 steps. Note that the step which started with radius 30 has expanded and the radius of the step immediately inside decreases monotonically.

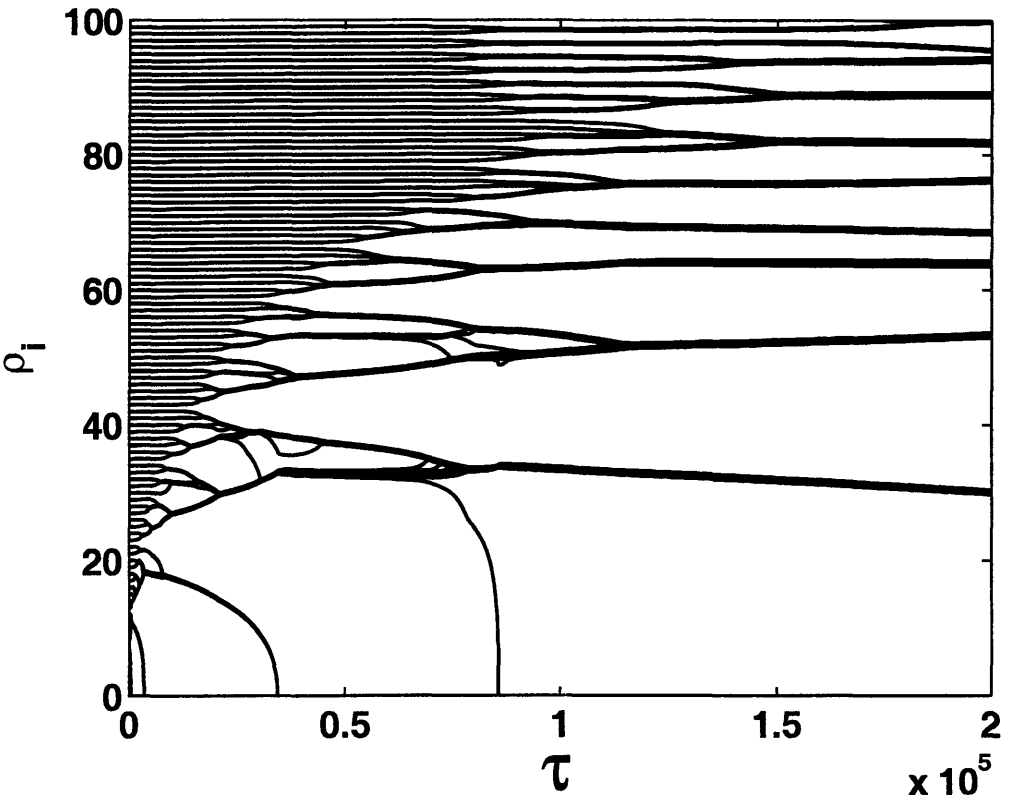

Figure B-13: ADL system with $g = 10^{-6}$. The simulation was started with an initial condition $\rho_n = n + \delta\rho_n$, where $\delta\rho_n = 10^{-4}\sin(200n)$ This small change in the initial condition has produced significant differences in the resulting step bunching instability, compared to Figure B-7. However, the two plots retain many similar qualitative features.

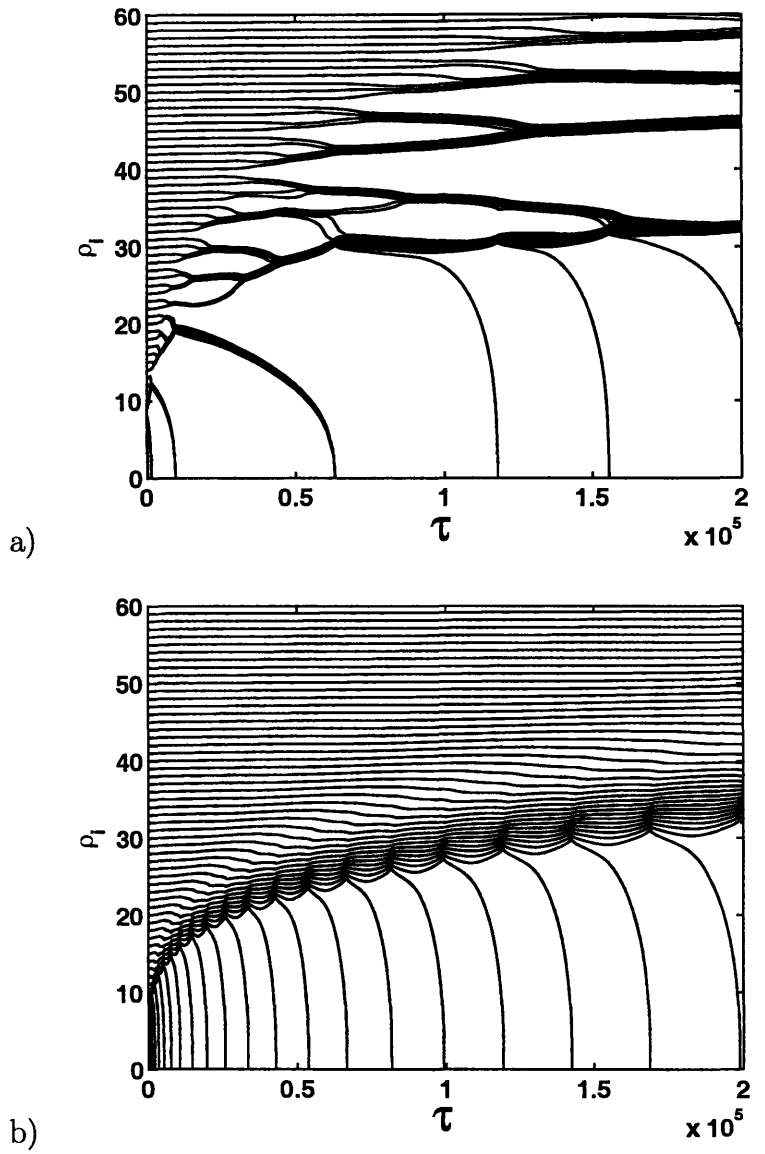

Figure B-14: Results from integration of the step-flow equations when both attachment-detachment and diffusion are comparable to one another so that $\frac{D_s}{kL} = m = O(1)$ in (2.24). In a) $g = 10^{-5}$ and in b) $g = 10^{-3}$. Step bunching is more developed for the smaller value of g.

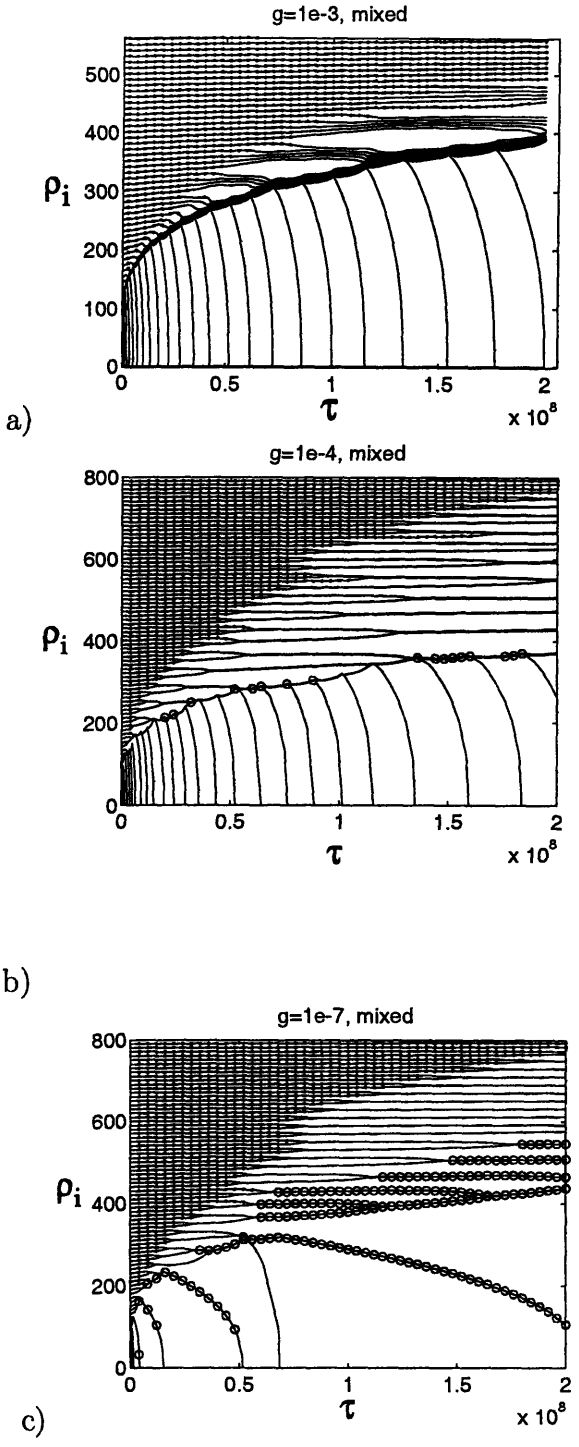

Figure B-15: Step trajectories for mixed kinetics: a) $g = 10^{-3}$, b) $g = 10^{-4}$ c) $g = 10^{-7}$. Trajectories highlighted with a dot indicate that diffusion across terraces is slower than attachment-detachment at step edges (TDL). An empty circle indicates that attachment-detachment is slower than diffusion (ADL). An initial step spacing of 10 was used in each case.

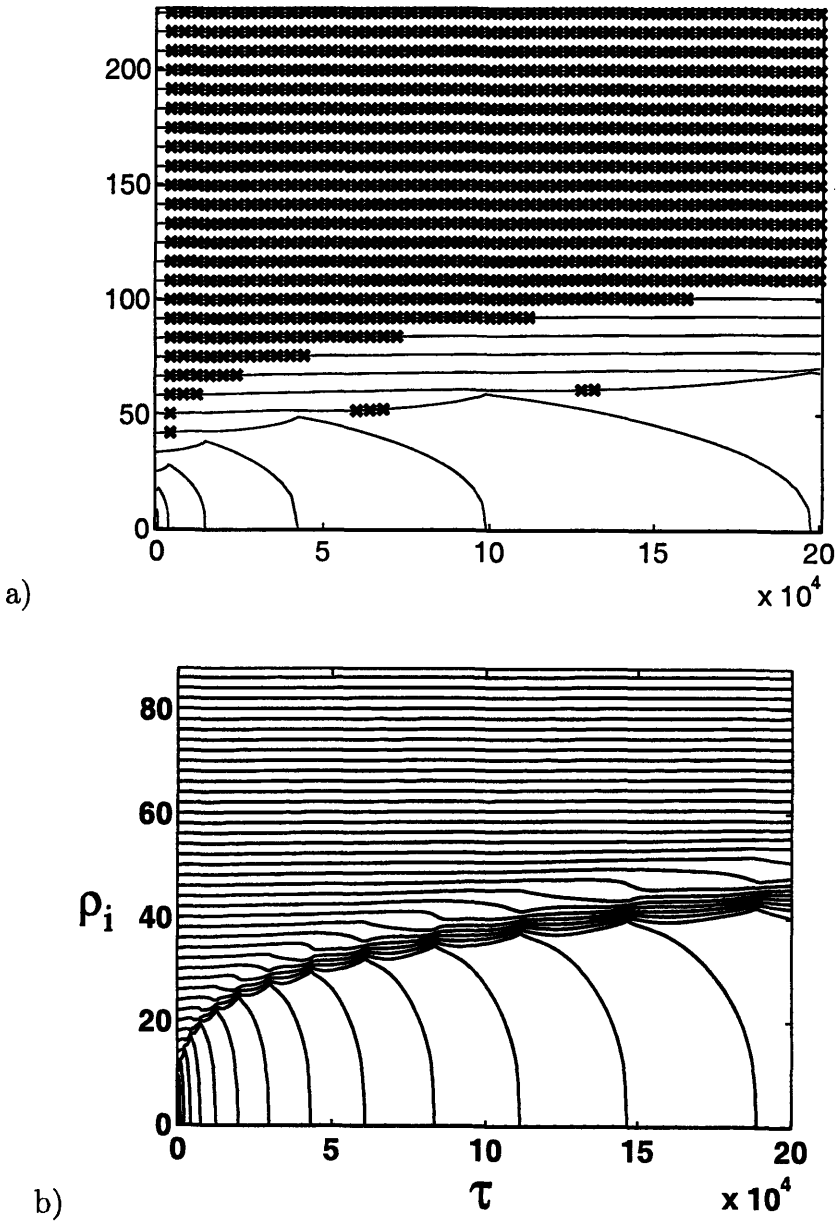

Figure B-16: Step trajectories for mixed kinetics, initialized with step spacings of a) 8.3, b) 2.0. Regions highlighted with a cross indicate that diffusion across terraces is slower than attachment-detachment at step edges (TDL), and an empty circle indicates that attachment-detachment is slower than diffusion (ADL). Unmarked regions correspond to diffusion and attachment-detachment being comparable. A value of $g = 10^{-3}$ was used in each case.

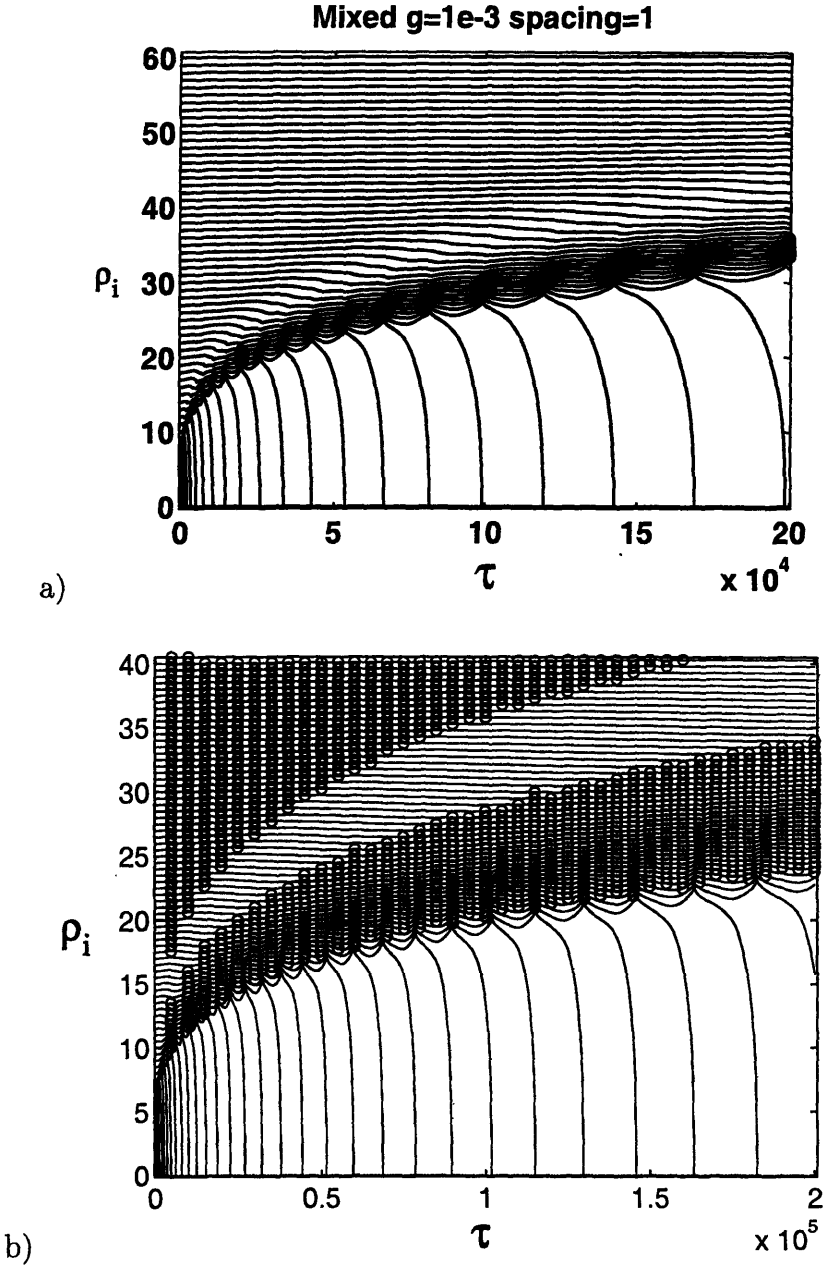

Figure B-17: Step trajectories for mixed kinetics, initialized with step spacings of a) 1.0, b) 0.5. Regions highlighted with a cross indicate that diffusion across terraces is slower than attachment-detachment at step edges (TDL), and an empty circle indicates that attachment-detachment is slower than diffusion (ADL). Unmarked regions correspond to diffusion and attachment-detachment being comparable. A value of $g = 10^{-3}$ was used in each case.

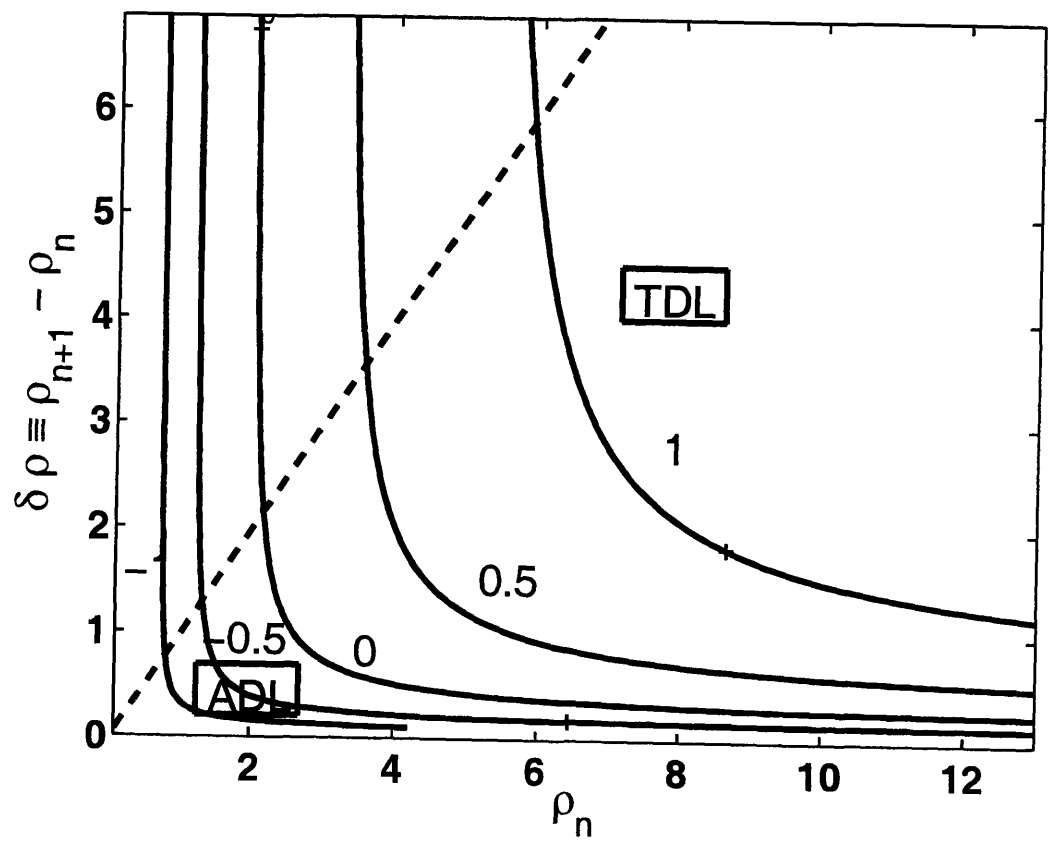

Figure B-18: The level curves of $F(\rho_n, \delta\rho) \equiv \log\left(\frac{\log(1+\delta\rho/\rho_n)}{\frac{1}{\rho_n}+\frac{1}{\rho_n+\delta\rho}}\right)$ where $\delta\rho \equiv \rho_{n+1} - \rho_n$. Regions where $F > 0$ correspond roughly to TDL kinetics, and regions where $F < 0$ correspond to ADL kinetics. When classifying the jth step from the top, where $j > 1$, we must have $\delta\rho < \rho_n$, so only the region to the right of the dashed line is considered in this case.

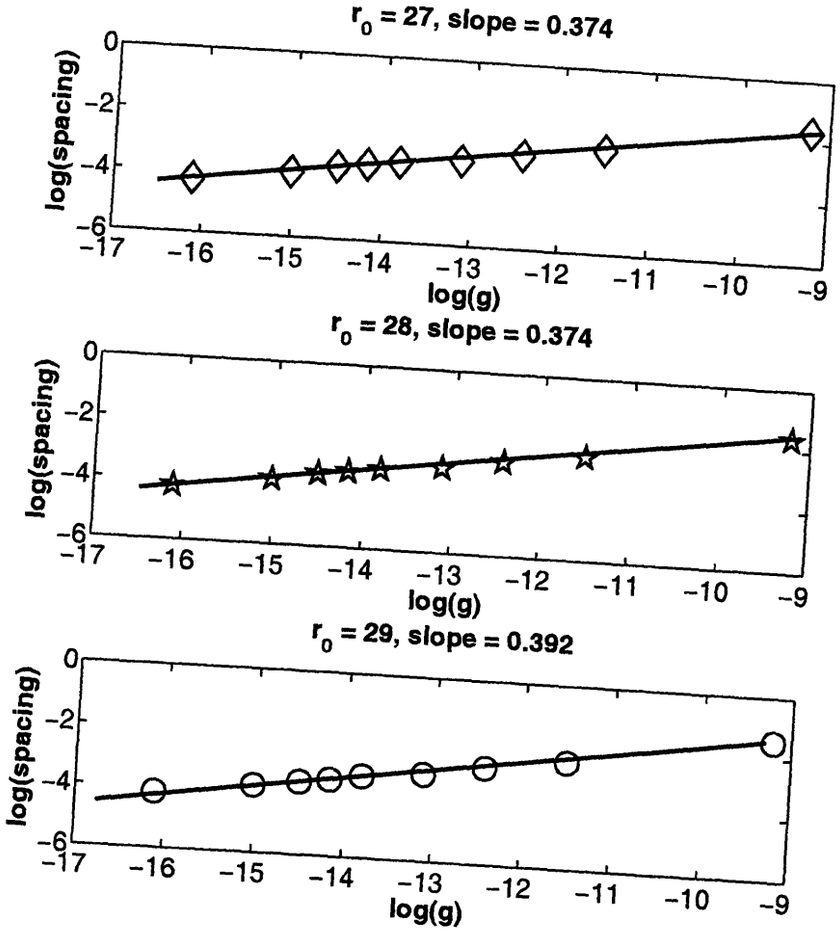

Figure B-19: Log-log plots of the average step spacing within the bunch against g, for three different values of r_0 under ADL kinetics. Values for (g, N) where $N =$ number of steps in bunch, are $(10^{-7}, 21)$,$(3 \times 10^{-7}, 21)$, $(7 \times 10^{-7}, 19)$, $(5 \times 10^{-7}, 19)$, $(10^{-6}, 19)$, $(2 \times 10^{-6}, 20)$, $(4 \times 10^{-6}, 18)$, $(10^{-5}, 17)$ and $(10^{-4}, 16)$.

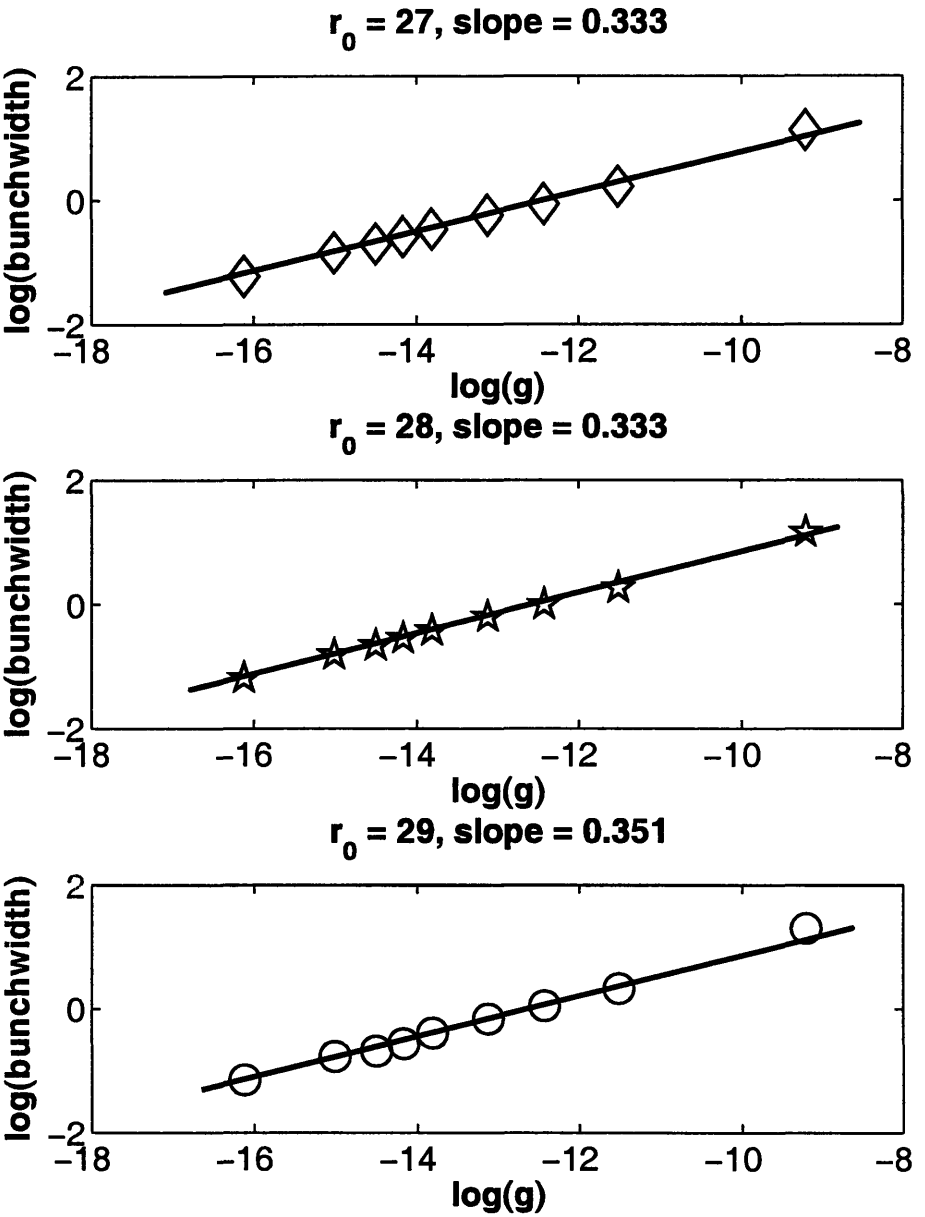

Figure B-20: Log-log plots of the total bunch width against g, for three different values of r_0 under ADL kinetics. The bunches measured are the same as those in Figure B-19.

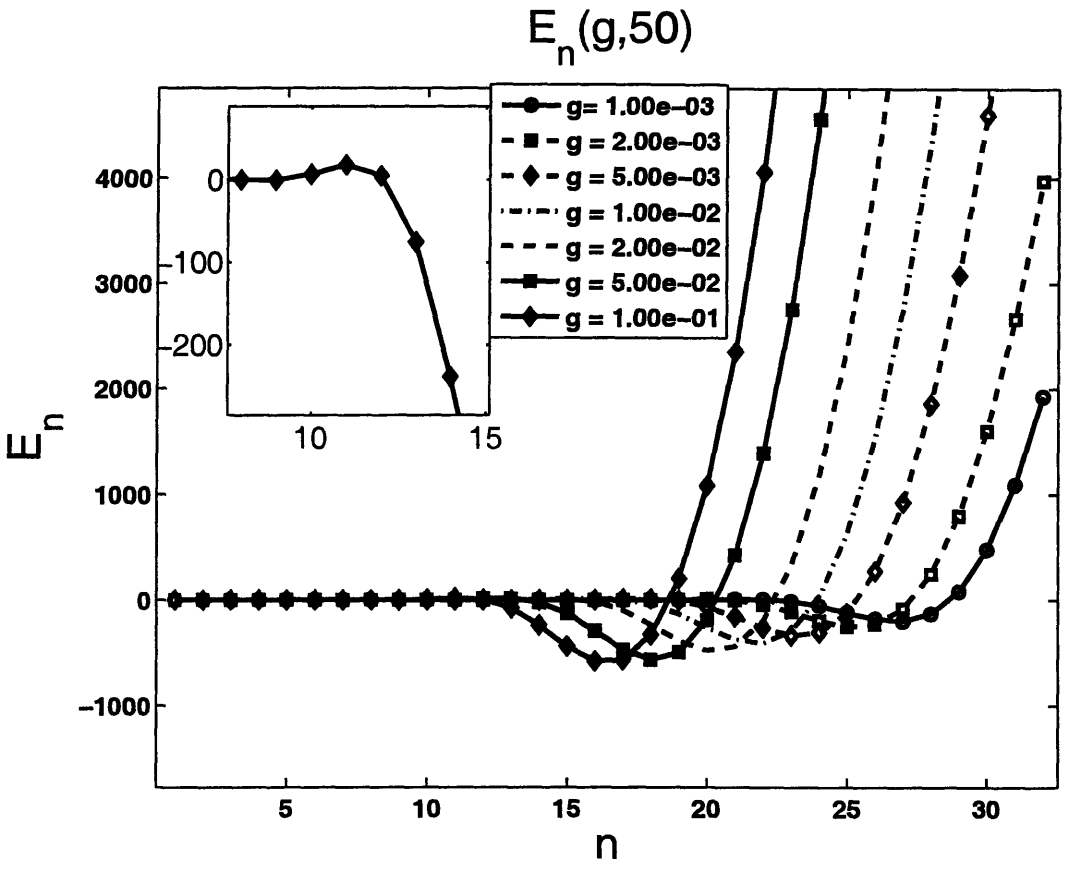

Figure B-21: Plots of $E_n(g, 50)$ for different g. The inset plot shows a close up of a representative E_n (for $g = 0.1$), indicating the presence of a local maximum.

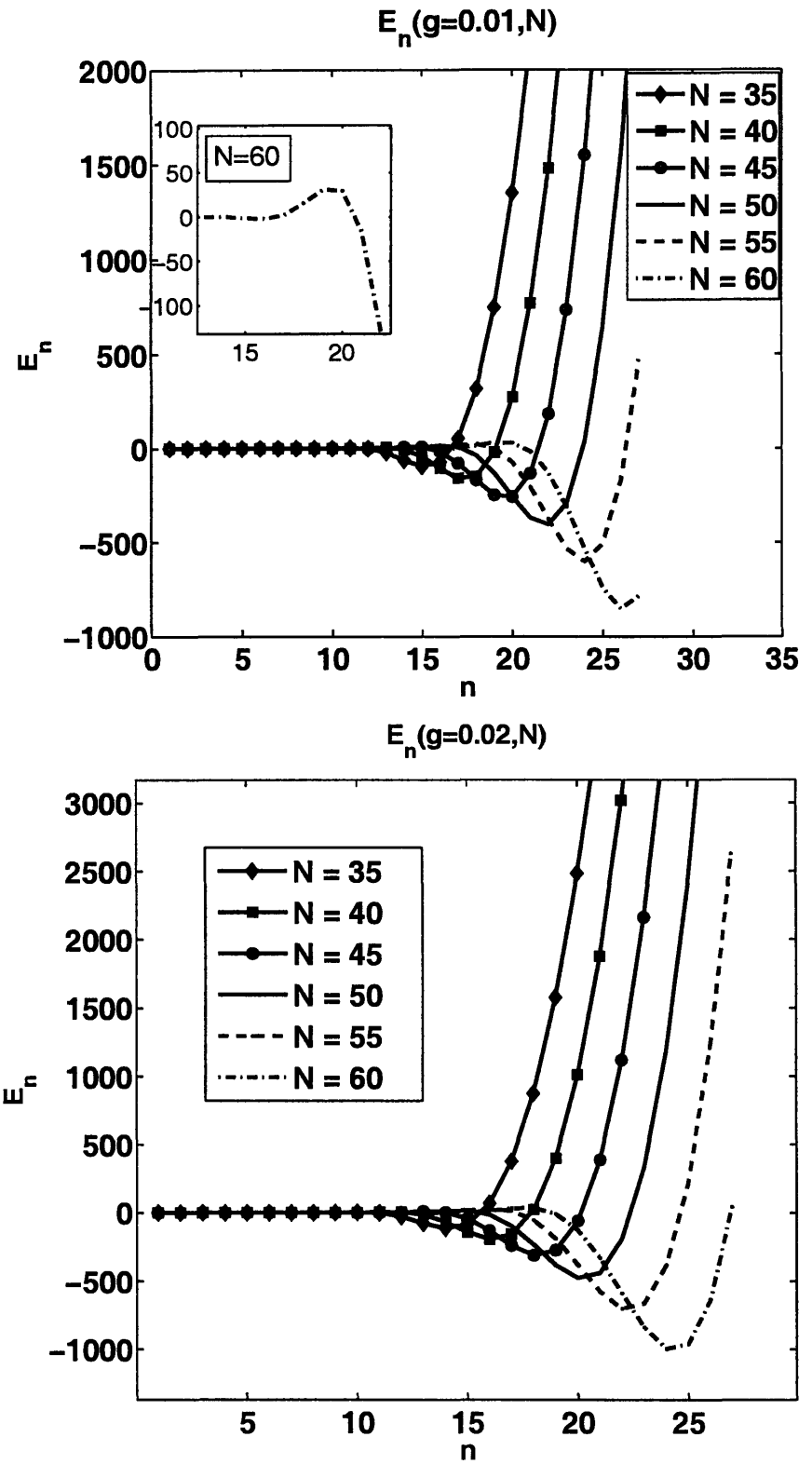

Figure B-22: Plots of $E_n(0.01, N)$ and $E_n(0.02, N)$ for different N. The inset in the top figure shows a close up of a representative E_n.

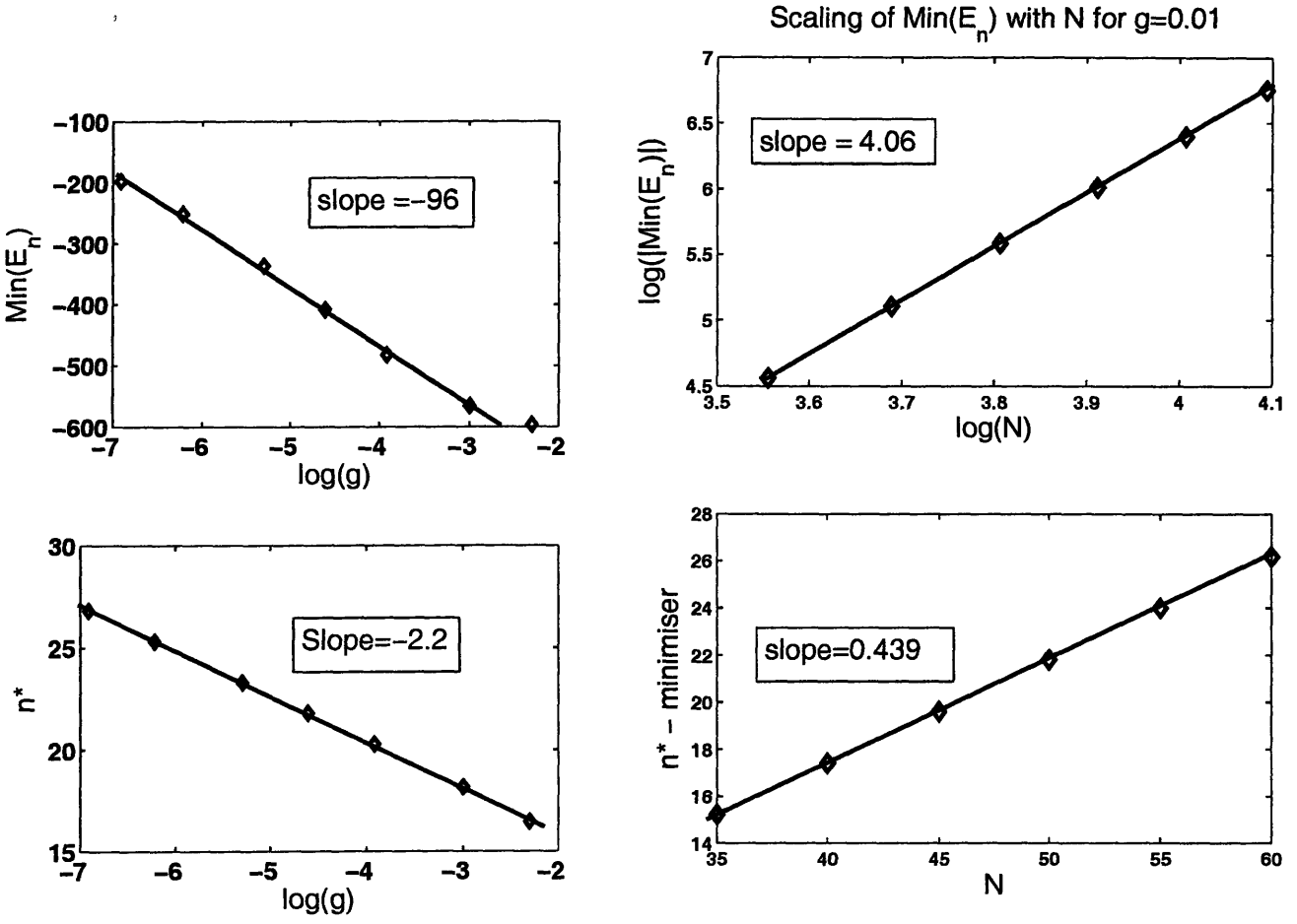

Figure B-23: These four plots illustrate possible scalings for E_n, providing quantification of Finite Height Effects (see Section 2.56): top left and bottom left plots show a possible $E_n \sim \log(\frac{1}{g})$ and $n^* \sim \log(\frac{1}{g})$ scaling; top right and bottom right plots suggest that $n^* \sim N$ and $\text{Min}(E_n) \sim N^4$.

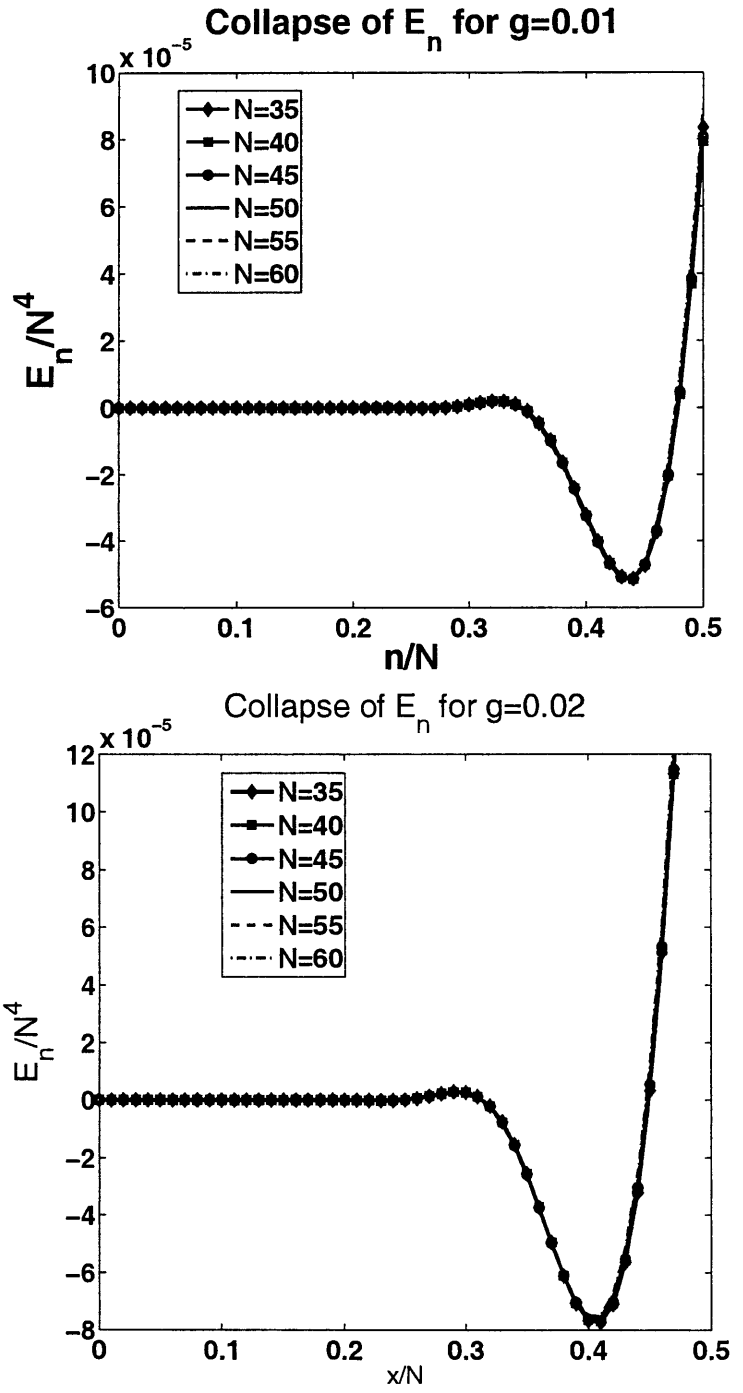

Figure B-24: Using the scaling results from B-23, the similarity form for $E_n = N^4 G(n/N)$, for some function G, is obtained empirically through a data collapse of the results from Figure B-22.

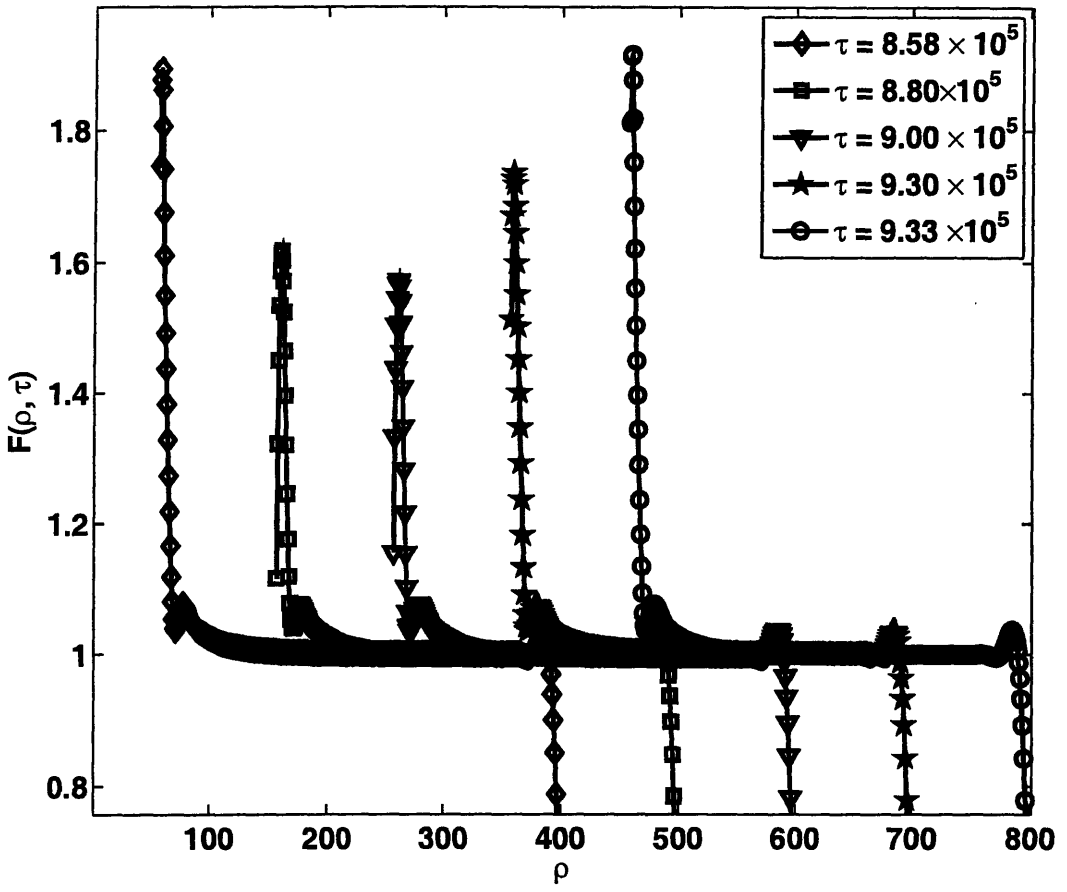

Figure B-25: Step density profiles under TDL kinetics, sampled between collapse times $t_{47} = 8.58 \times 10^5$ and $t_{48} = 9.33 \times 10^5$ for $\varepsilon = 1.7 \times 10^{-4}$. Each profile has been shifted to the right by 0,100,200,...,400 for convenience.

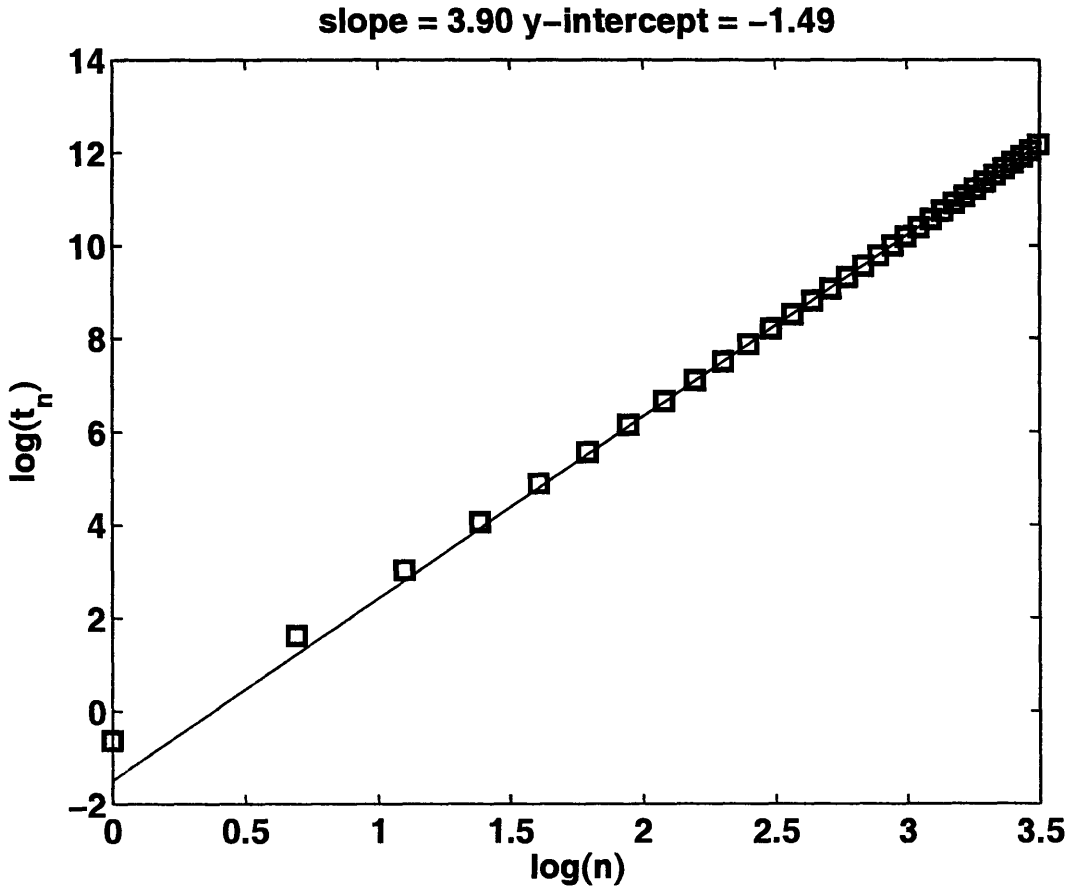

Figure B-26: Collapse times (TDL kinetics) for an initial linear (conical) profile follow the asymptotic relation $\tau_n \sim n^4$ – see Remark 2.3.1. A value of $g = 0.01$ was used.

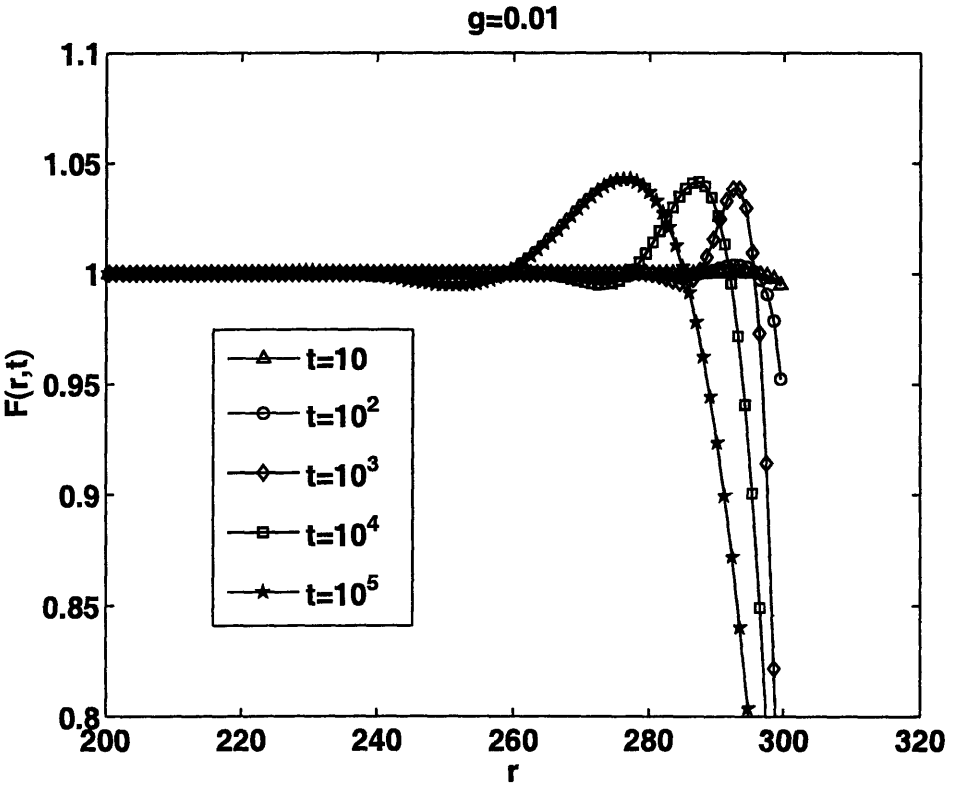

Figure B-27: Effect of finite height on the Step Density Function, for a finite linear profile. A value of $g = 10^{-2}$ was used. For a linear profile, the oscillations seem to propagate into the bulk logarithmically in time.

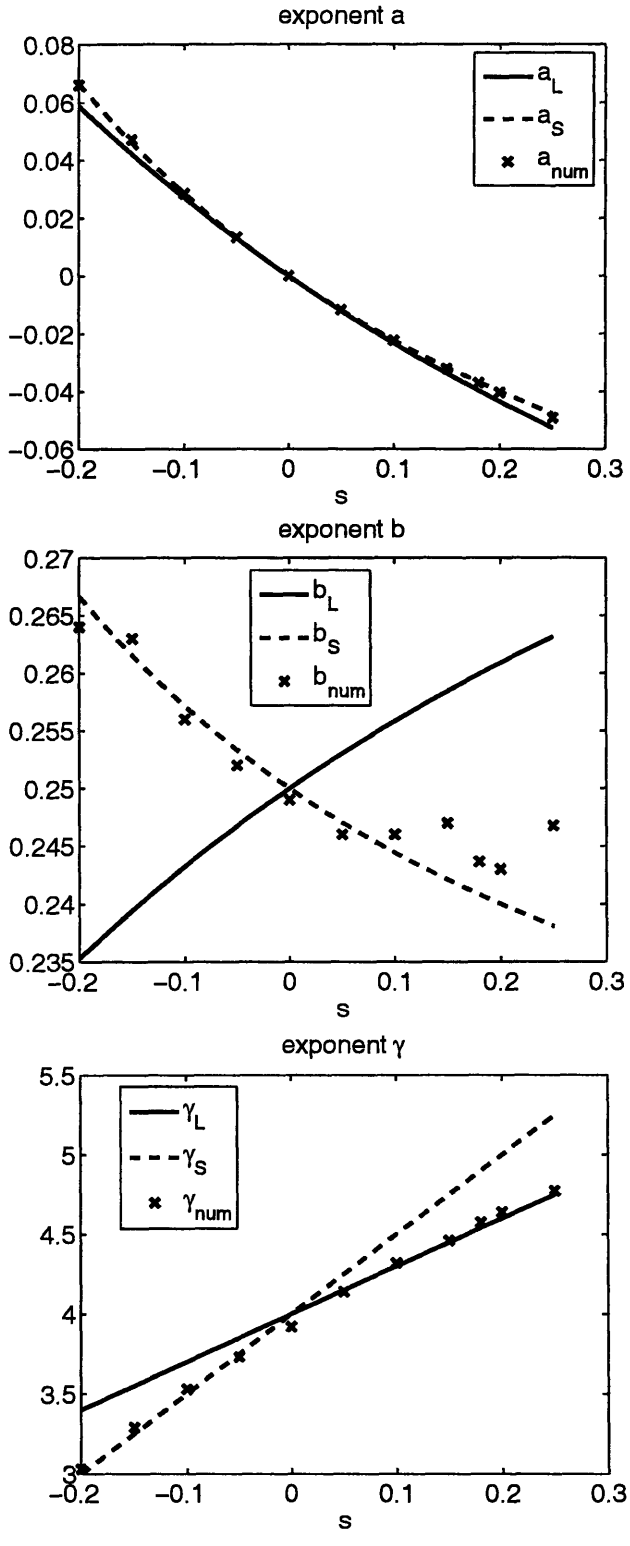

Figure B-28: Theoretical and numerical exponents for a, b and γ, from Tables A.2, A.3 and A.4. These exponents are used for similarity solutions in (4.43) in conjunction with (4.47) and (4.48), or (4.49) and (4.50). A value of $g = 10$ was used on all runs, for a range of algebraic profiles $\rho_n = n^{1+s}$. The exponent γ is defined through (4.6).

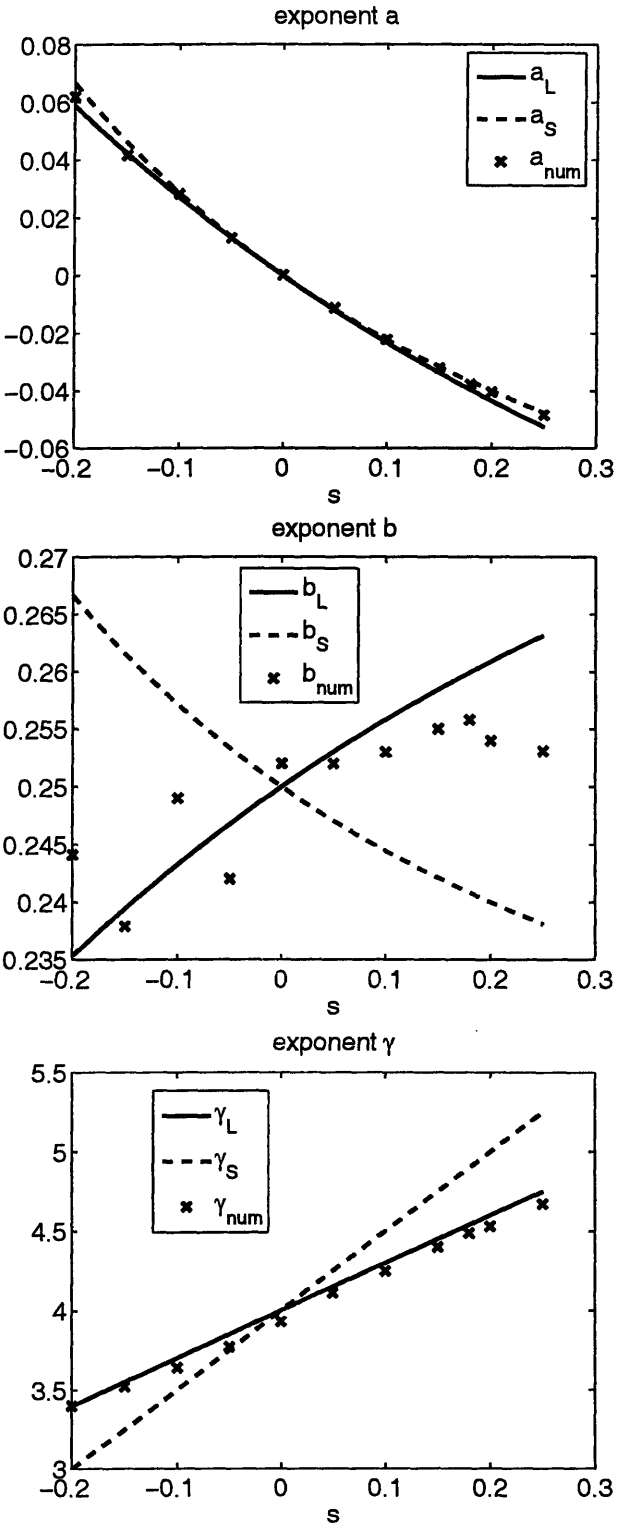

Figure B-29: Theoretical and numerical exponents for a, b and γ, from Tables A.5, A.6 and A.7. These exponents are used for similarity solutions in (4.43) in conjunction with (4.47) and (4.48), or (4.49) and (4.50). A value of $g = 0.01$ was used on all runs, for a range of algebraic profiles $\rho_n = n^{1+s}$. The exponent γ is defined through (4.6).

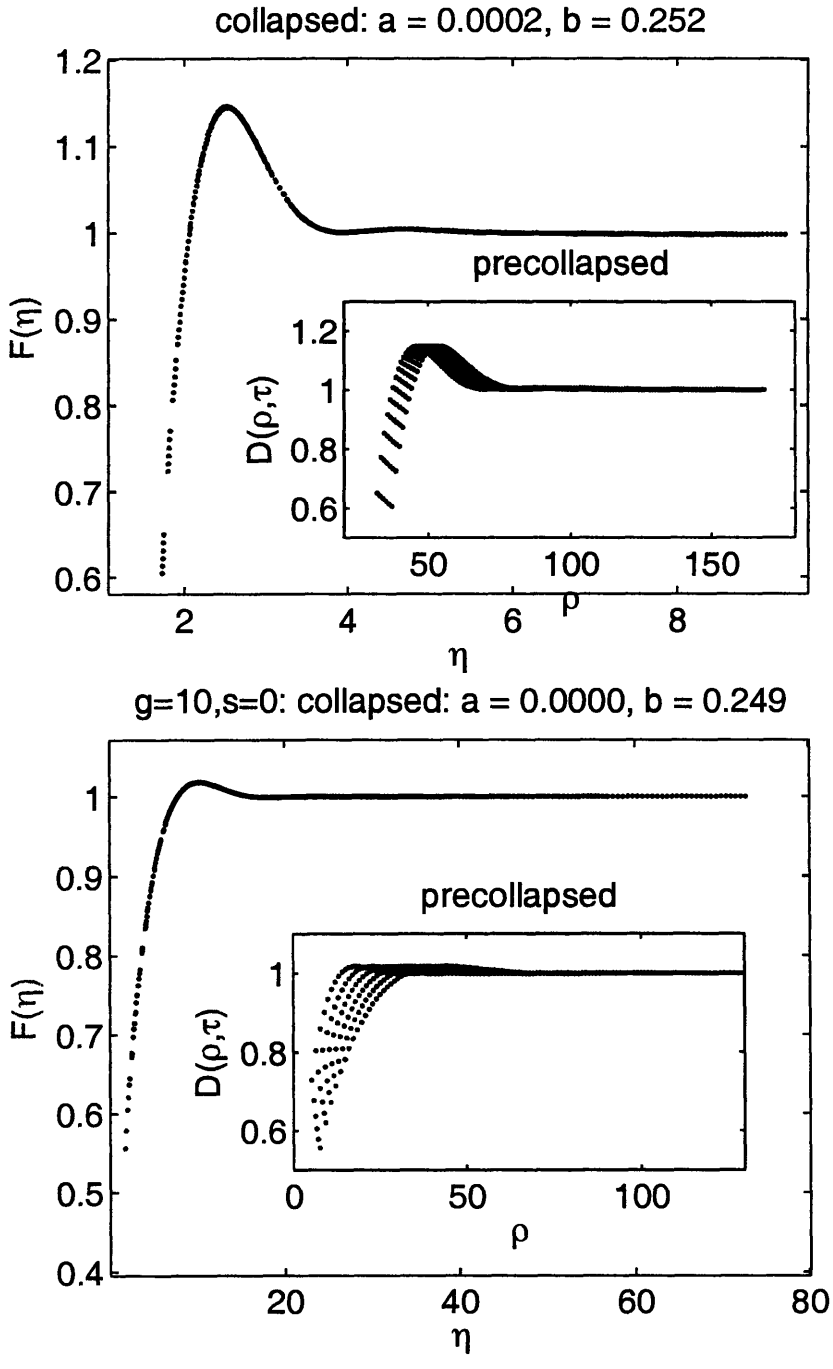

Figure B-30: Collapsed data sets for the numerical step density function, for algebraic profiles, with shape parameter $s = 0$ (see 4.1) and step-step interaction parameters $g = 0.01$ (top) and $g = 10$ (bottom). Inset shows pre-collapsed data sets.

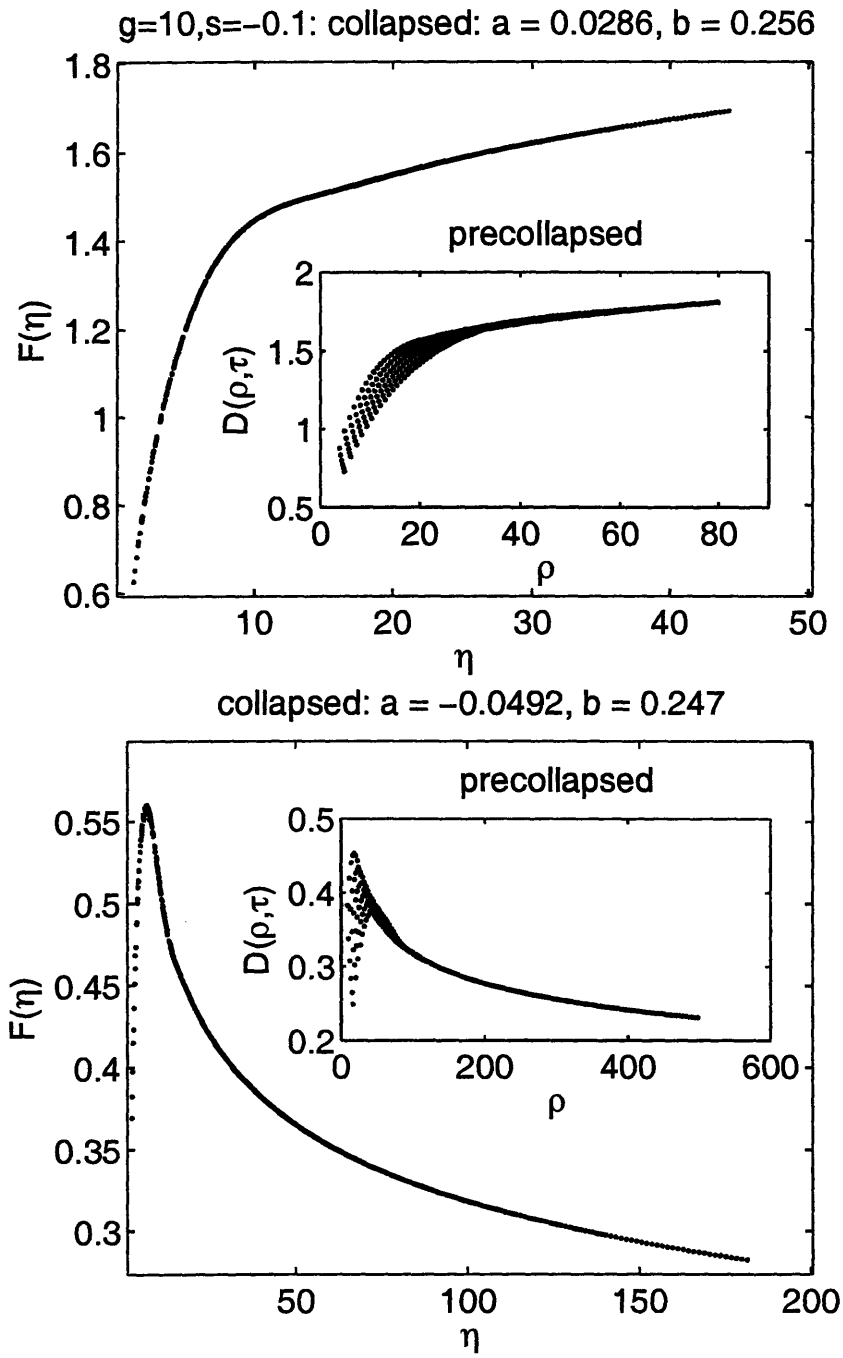

Figure B-31: Collapsed data sets for the numerical step density function, for algebraic profiles with shape parameters $s = -0.1$ and $s = 0.25$, and step-step interaction parameter $g = 10$. Insets show pre-collapsed data.

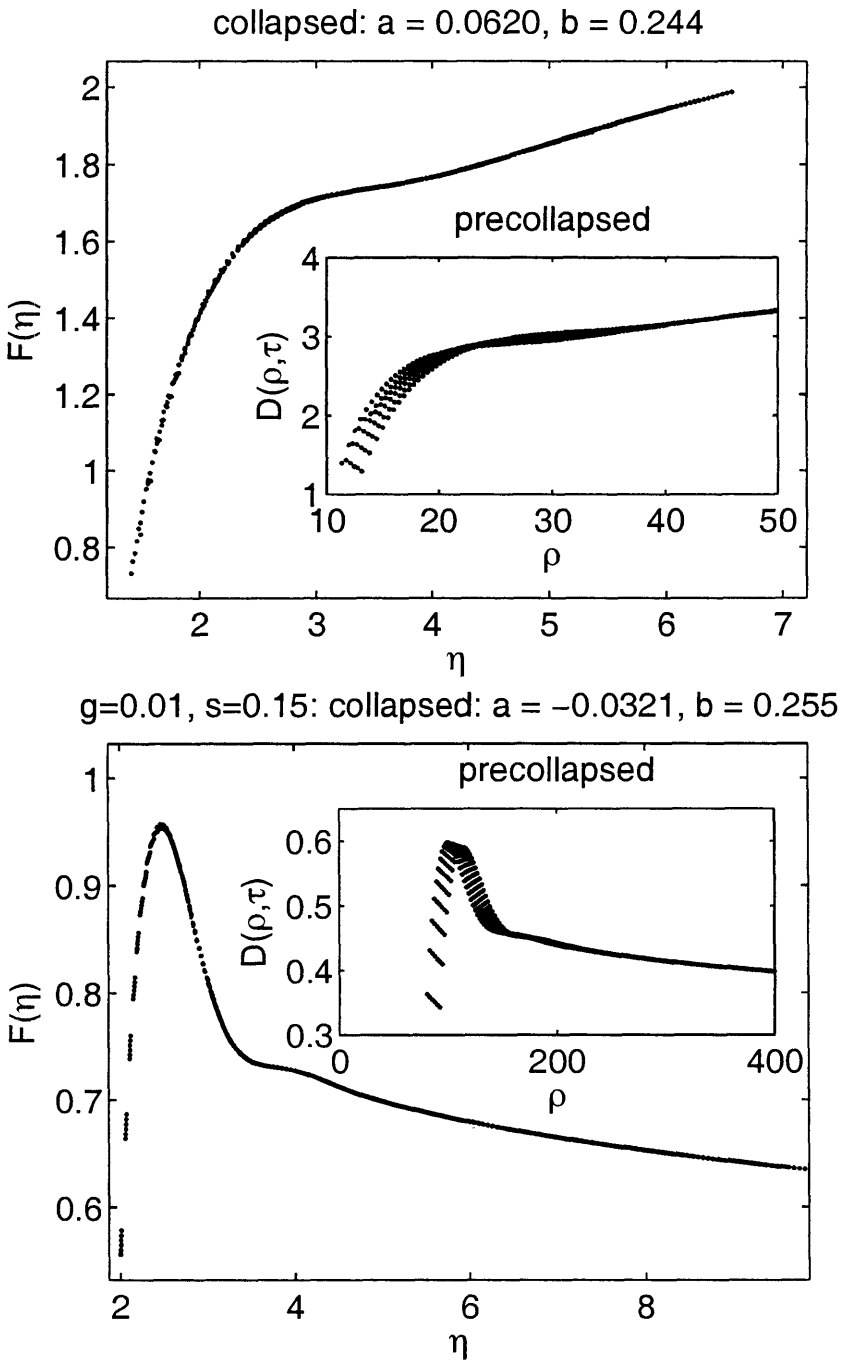

Figure B-32: Collapsed data sets for the numerical step density function, for algebraic profiles with shape parameter $s = -0.2$ and $s = 0.15$, and step-step interaction parameter $g = 0.01$. Insets show pre-collapsed data.

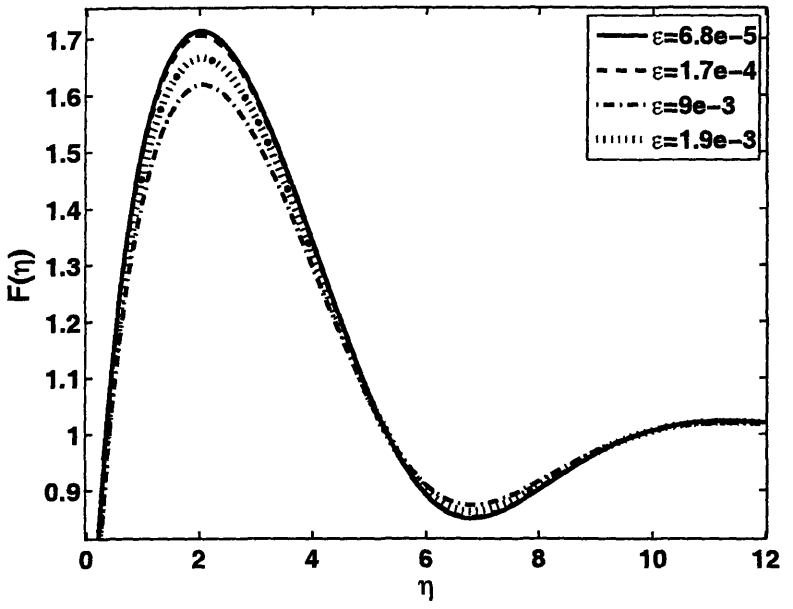

(a)

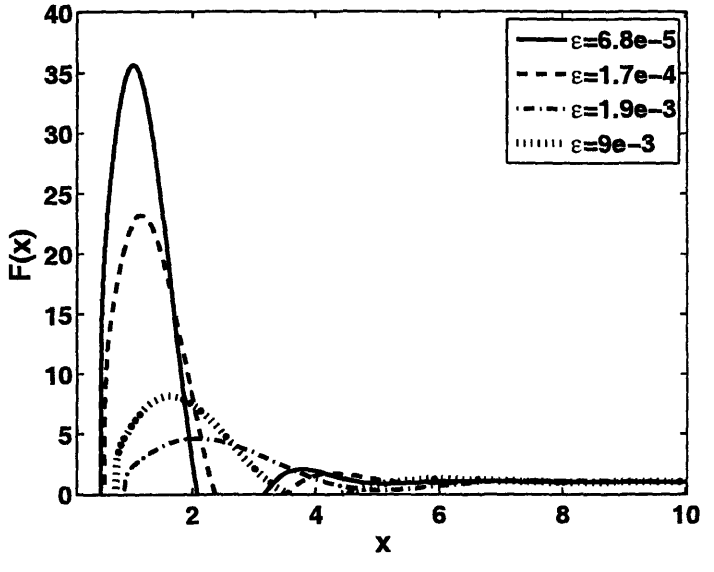

(b)

Figure B-33: Plot a) Solutions to the Universal ODE (3.40), $f_0(\eta)$. These curves correspond to $(c_1, c_3) = (1.67, -0.22)$, $(1.73, -0.23)$,$(1.78, -0.24)$, and $(1.79, -0.25)$ for $\varepsilon = 9 \times 10^{-3}$,$1.9 \times 10^{-3}$, 1.7×10^{-4} and 6.8×10^{-5}. Plot b) shows the actual step density profiles, F, constructed from taking $f_0(\eta)$, applying stretches, shifts and adding an outer solution: see (3.51) for the composite formula for F.

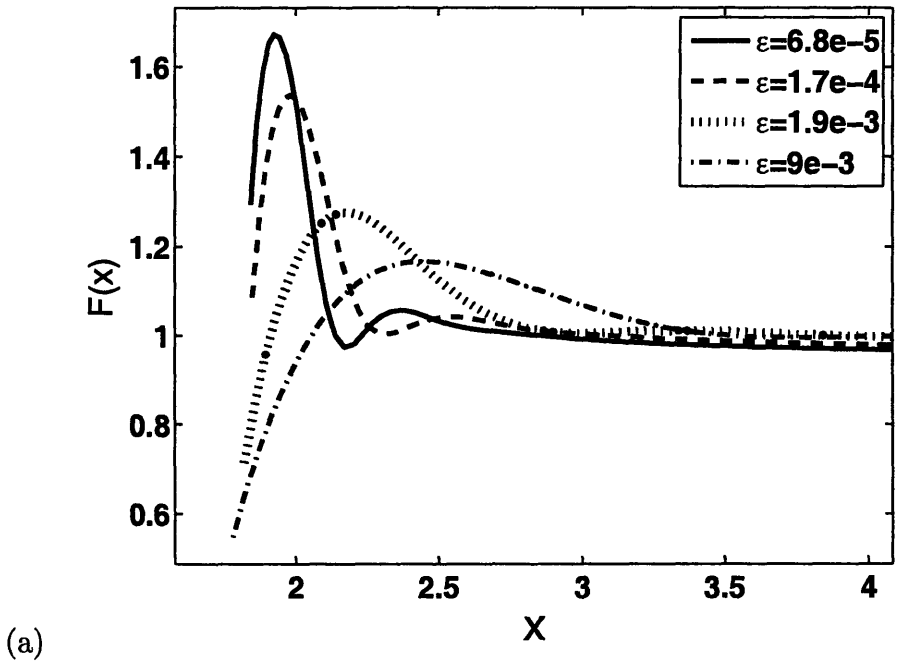

(a)

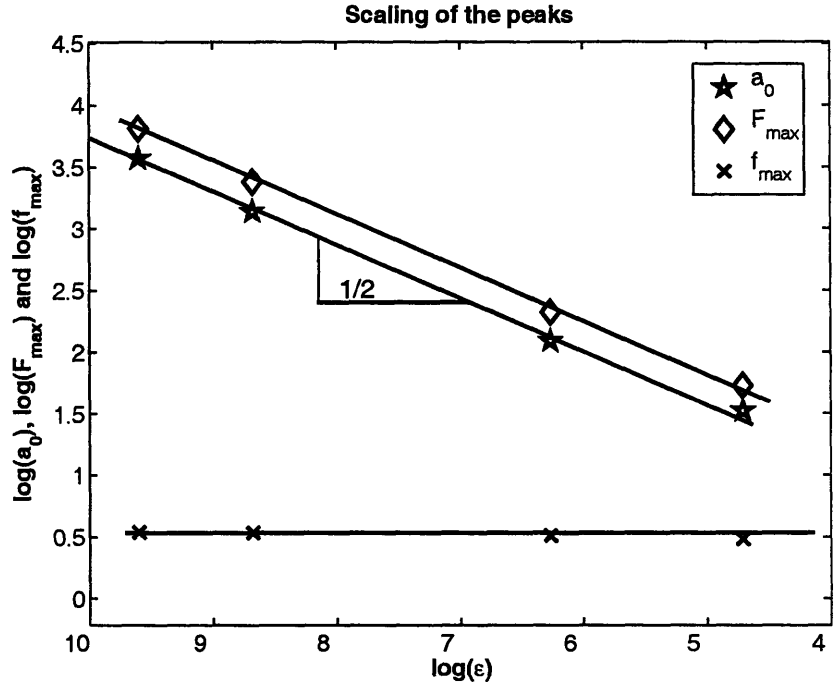

(b)

Figure B-34: Plot a) shows step density profiles generated from simulations. Plot (b) shows the scaling of the step density peaks f_{max} and F_{max} from Figures B-33 a) and b) respectively, as well as the dependence of $a_0 = O(\varepsilon^{-1/2})$ for (3.60).

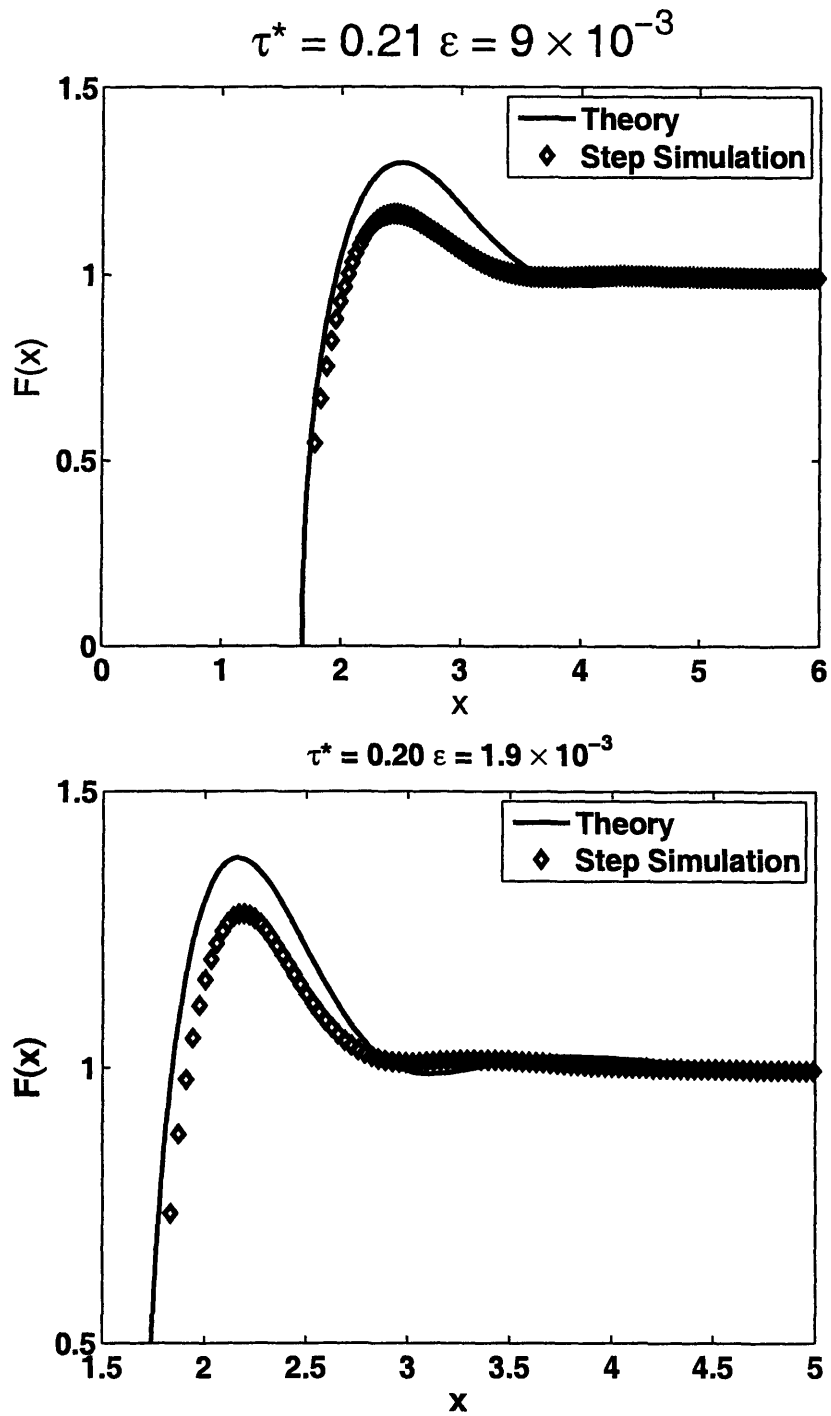

Figure B-35: Plots showing similarity solutions to the MAS PDE implemented with the step drop boundary condition (3.81) for $\varepsilon = 9 \times 10^{-3}$ and 1.9×10^{-3}. The final integration time for both simulations was $t = 1 \times 10^6$. Values of (c_1, c_3) were $(0.94, 0.003)$ and $(1.00, -0.019)$

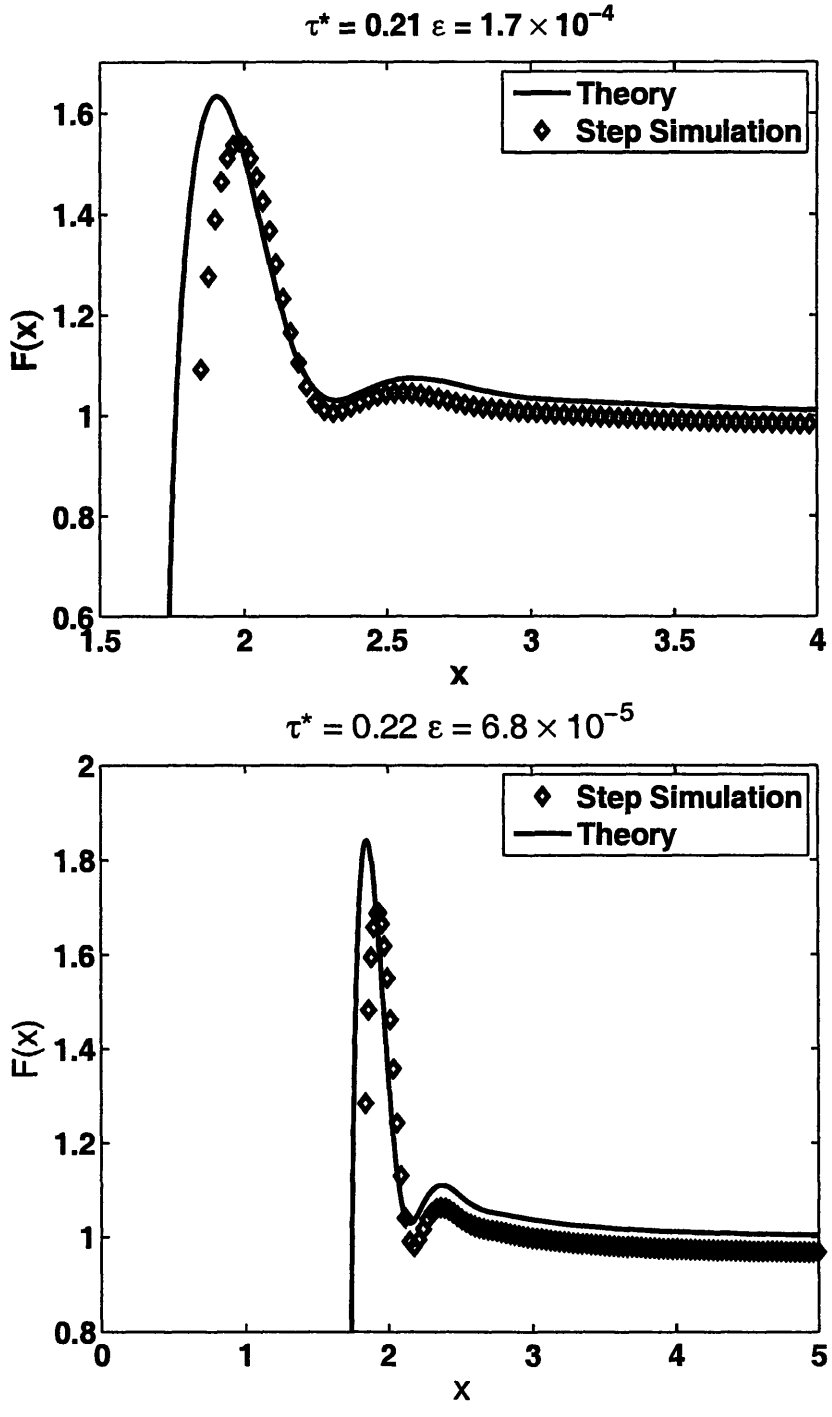

Figure B-36: Plots showing similarity solutions to the MAS PDE implemented with the step drop condition (3.81) for $\varepsilon = 1.7 \times 10^{-3}$ and 6.8×10^{-3}. The final integration time for both simulations was $t = 1 \times 10^6$. Values of (c_1, c_3) were $(1.12, -0.103)$ and $(1.44, -0.162)$.

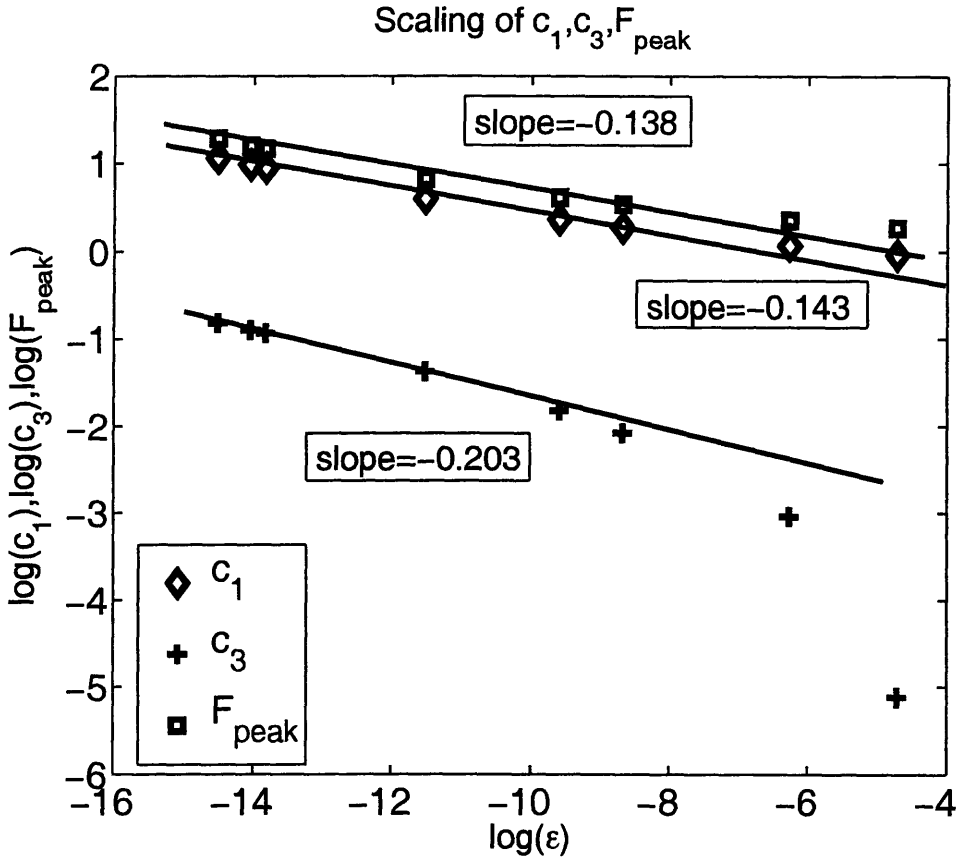

Figure B-37: This plot shows the scaling of c_1, c_3 and F_{peak} with ε, with the step drop condition (3.81) implemented. The coefficients c_1 and c_3 come from the expansion of $f_0(\eta)$ in (3.44), and F_{peak} is the maximum value of F in the composite formula (3.51). Slopes were calculated using the 5 leftmost data points. The theoretical scaling for c_1, c_3 and F_{peak} is $= O(\varepsilon^{-1/6})$.

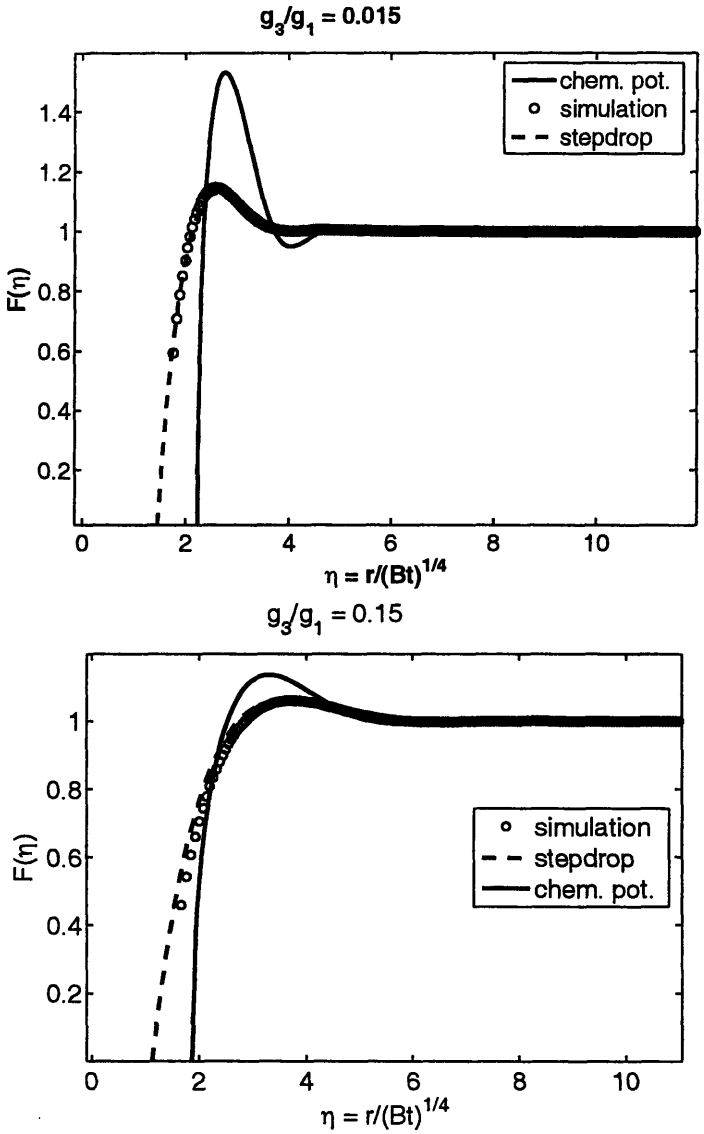

Figure B-38: Similarity solutions to (3.88) for $\varepsilon = 0.015$ and $\varepsilon = 0.15$. The dashed curves are for solutions using the step drop boundary condition (3.106), the solid curves use continuity of chemical potential at the facet (3.105), and the circles represent data taken from the step-flow model.

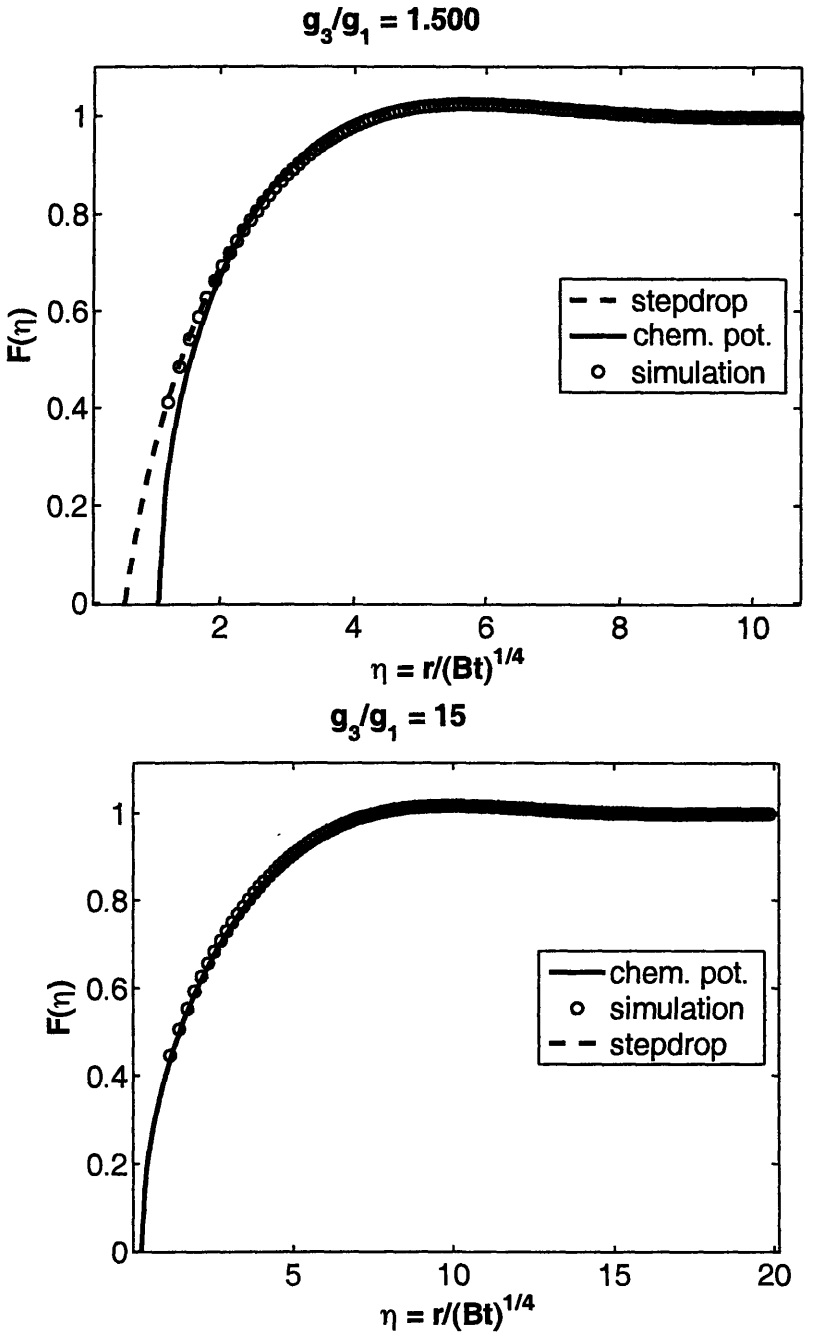

Figure B-39: Similarity solutions to (3.88) for $\varepsilon = 1.5$ and $\varepsilon = 15$. The dashed curves are for solutions using the step drop boundary condition (3.106), the solid curves use continuity of chemical potential at the facet (3.105), and the circles represent data taken from the step-flow model.

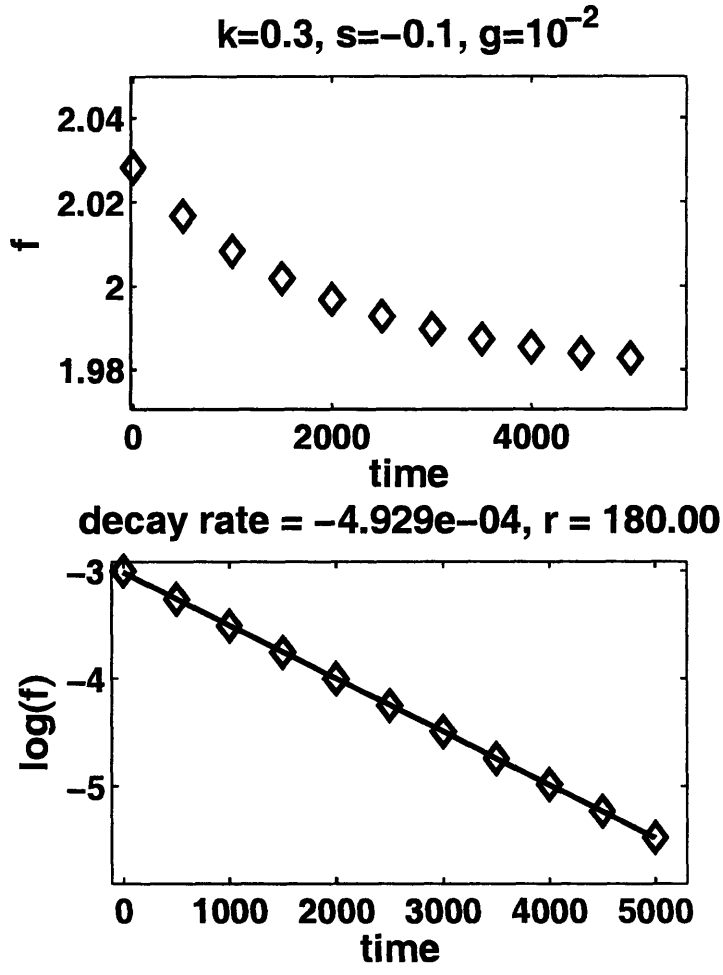

Figure B-40: These two plots show the exponential decay of small perturbation, f in time, (see 5.4) for a particular value of r.

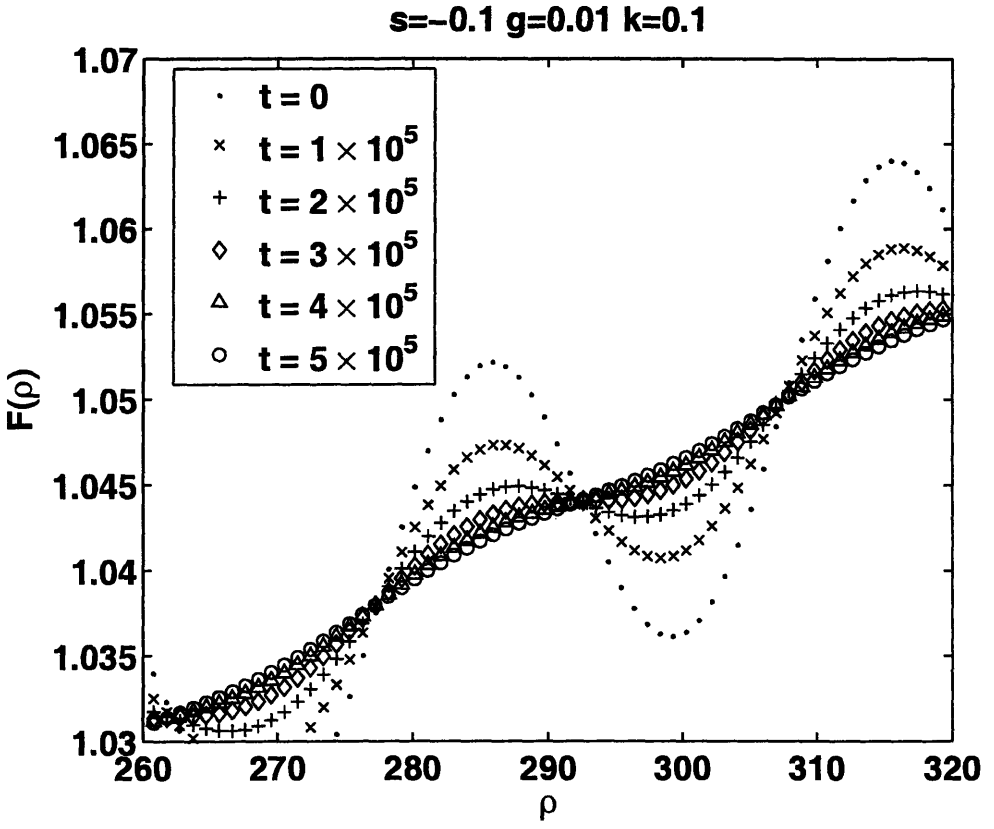

Figure B-41: Decay of perturbations in the Step Density Function. The shape parameter $s = -0.1$ where s is defined through (4.1).

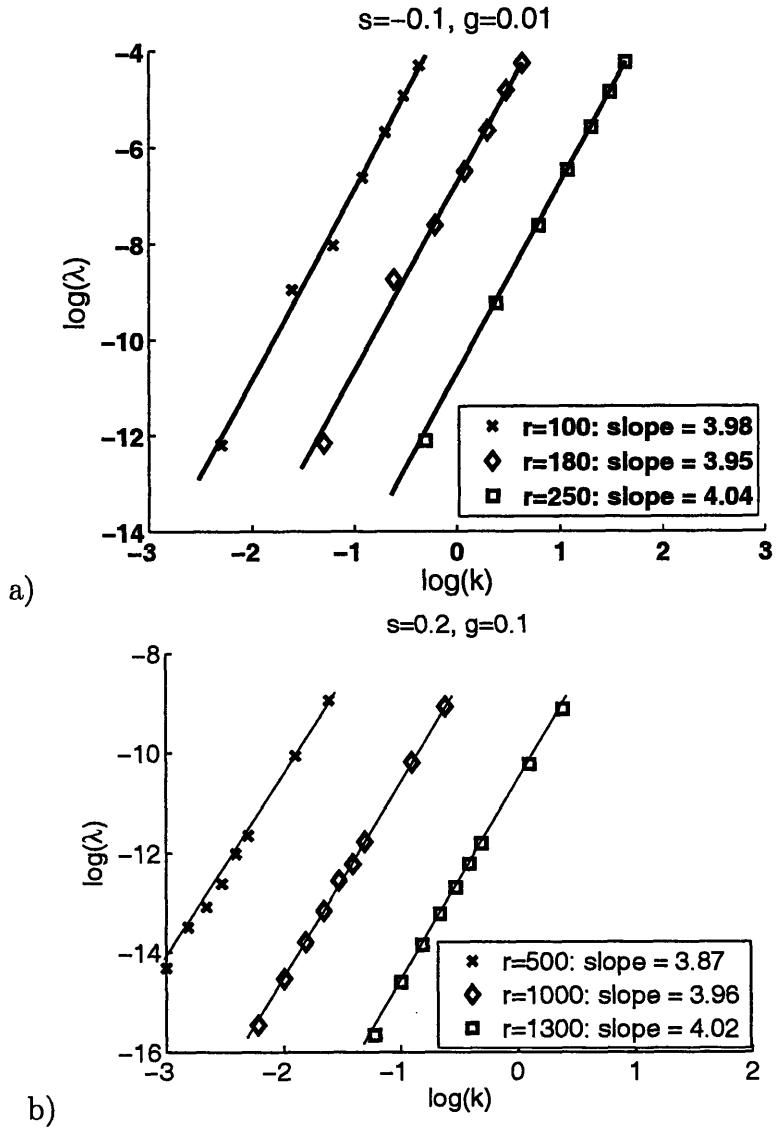

Figure B-42: Data from step simulations showing that the decay rate, λ, (defined in (5.6)) of sinusoidal perturbations is proportional to the fourth power of the wavenumber, for different values of r. The shape parameters used were $s = -0.1$ and $s = 0.2$ and the values of g used were 0.01 and 0.1. For clarity, in top plot, the two sets of data for $r = 180$ and $r = 250$ have been shifted to the right by $\log k = 1$ and $\log k = 2$ respectively. A similar translation was done on the bottom plot.

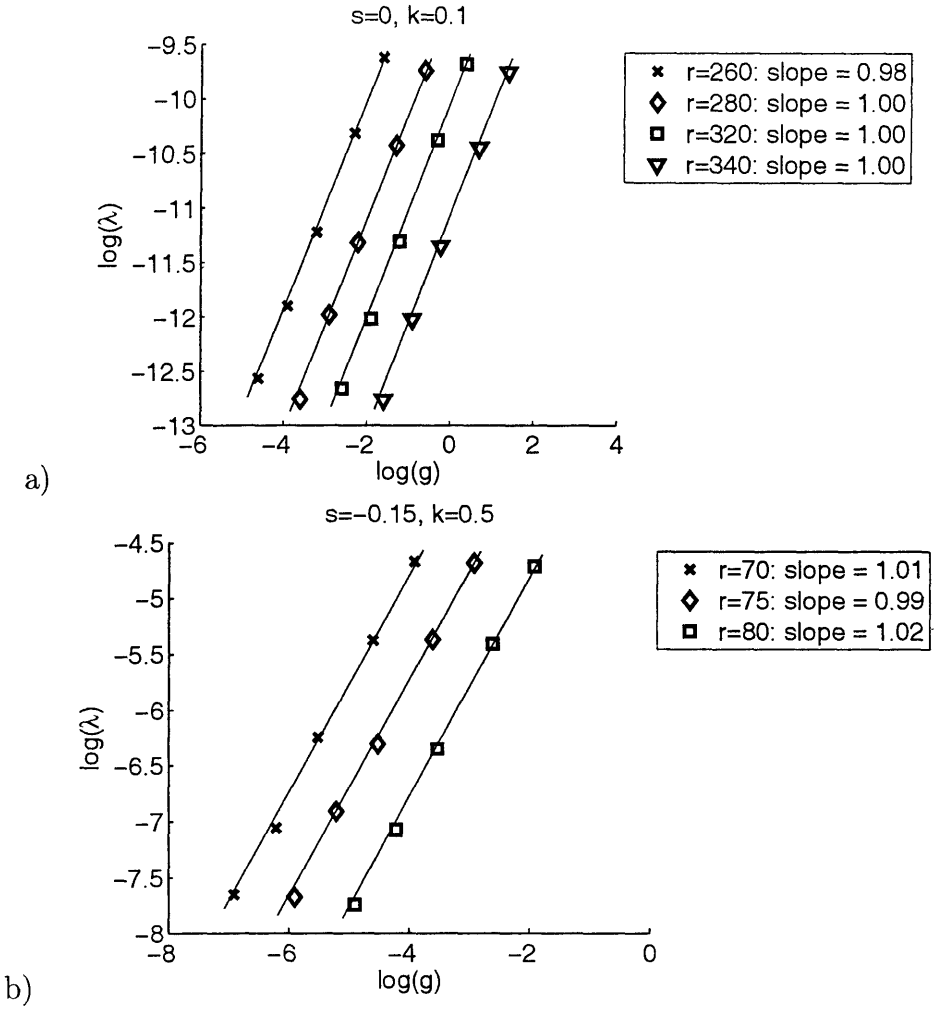

Figure B-43: Data from step simulations showing that the decay rate of small perturbations scales linearly with $g = \frac{2}{3}\varepsilon$, confirming (5.6). The top plot is for a conical profile, $s = 0$. The bottom is for $s = -0.15$. The wavenumbers for the perturbations were $k = 0.1$ and $k = 0.5$. The three sets of data for for $r = 280, 320$ and 340 have been shifted to the right by $\log g = 1, 2$ and 3. The data for $r = 75$ and 80 have also been shifted in a similar way.

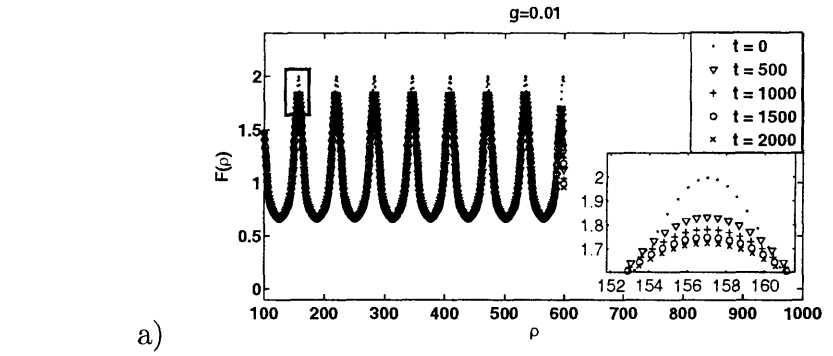

a)

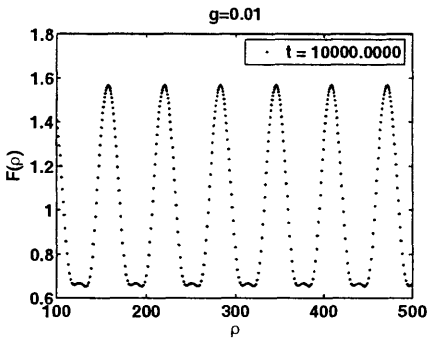

b)

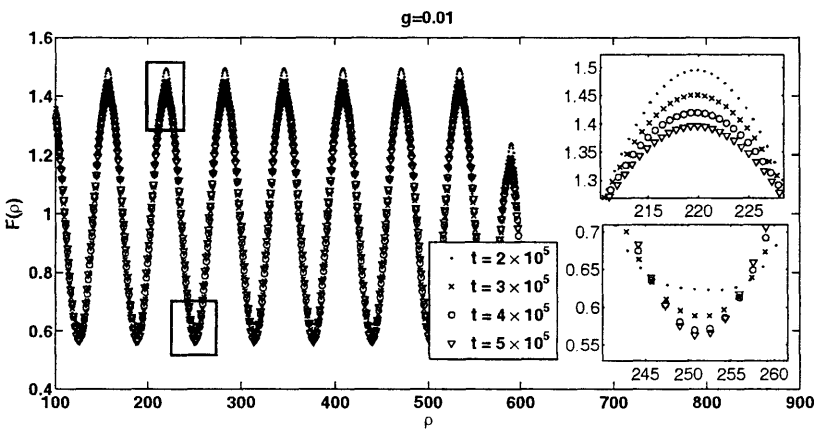

c)

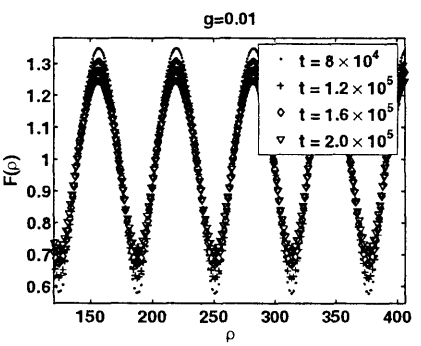

d)

Figure B-44: Plots showing the nonlinear evolution and eventual decay of the step density function. The initial form $F(r,0)$ was $\frac{1}{1+0.5\cos(0.1r)}$. a) shows the initial rapid decay of the maxima of $F(r,t)$, b) shows a cusping in the troughs for early-intermediate times, c) shows a vertical translation of the whole profile and in d) we observe a uniform decay throughout the whole of F.

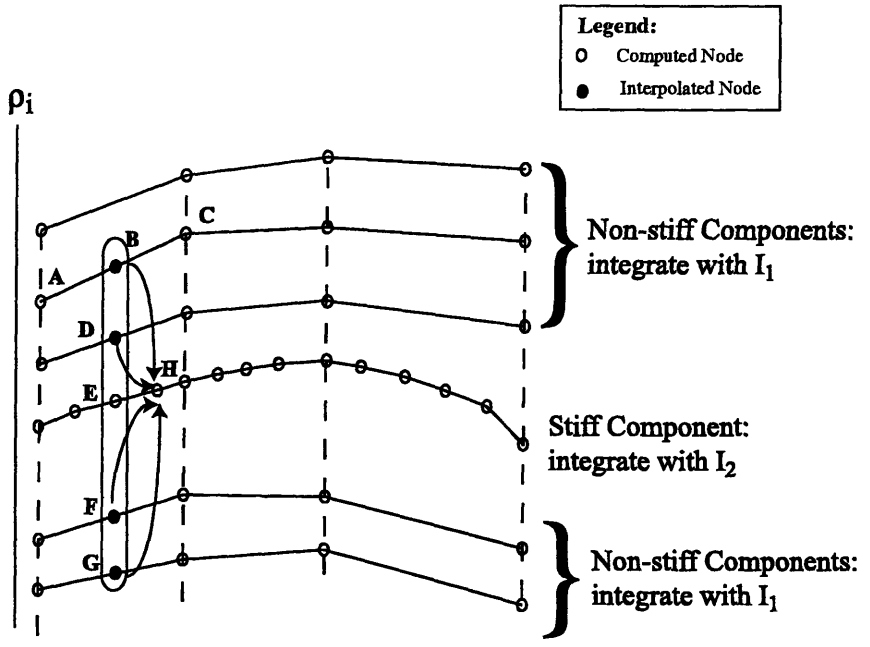

Figure B-45: Schematic showing the two phases of integration with timesteppers I_1 and I_2. Smaller time steps are taken for stiff components using a low order method, while larger sized steps are used in the slowly varying bulk. In the illustration, point B is interpolated from points A and C, and because equations (2.39)-(2.43) are pentadiagonal, points B,D,E,F and G must be used to compute point H. In practice, there would be more than one stiff component, because stiffness would arise from step bunching.

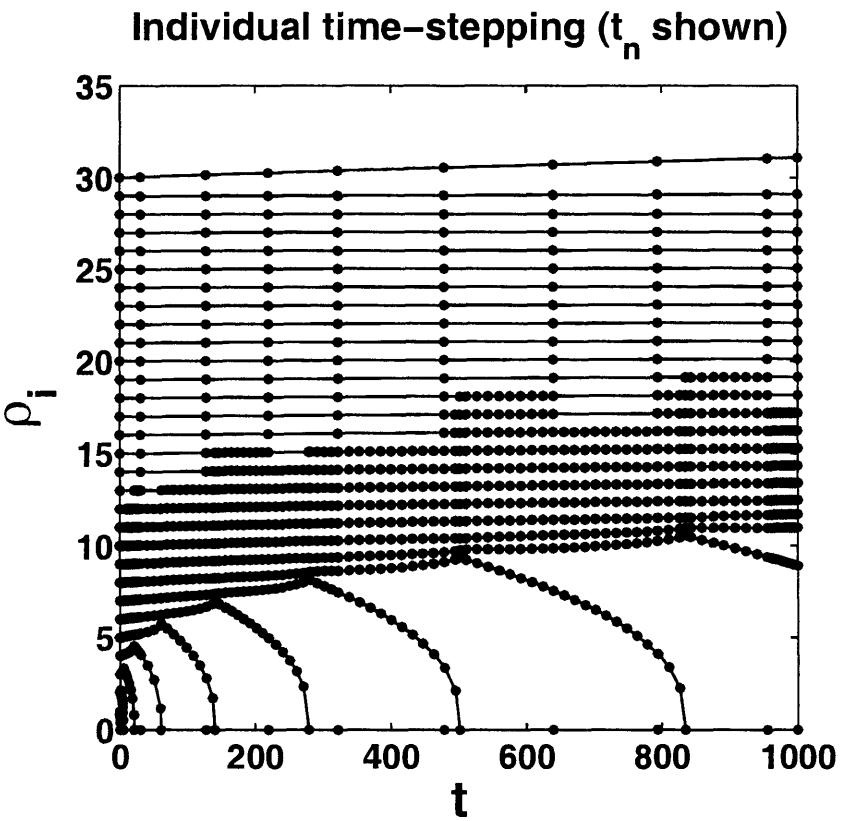

Figure B-46: Multi-adaptive integration of step flow equations using individual time stepping.

THIS PAGE INTENTIONALLY LEFT BLANK

Appendix C

Numerical Methods

C.1 Similarity Solutions of MAS PDE, for $\varepsilon \ll 1$

C.1.1 Solution of Universal ODE

Here we give details on how to numerically solve the Universal ODE (3.40)

$$\frac{d^3 f_0^2}{d\eta^3} - f_0 + 1 = 0 \tag{C.1}$$

which describes the step density f_0 inside the boundary layer near the facet located at $\eta = 0$. see . Our procedure is essentially a Newton iteration, but we approximate function derivatives using dense Pseudospectral Differentiation matrices based on Rational Chebyshev Functions. (see [117] for details).

Since the actual domain of solution is infinite, we use a change of variables

$$\eta = \frac{L(1+y)}{(1-y)}, \tag{C.2}$$

to map the semi-infinite domain $\eta \in (0, \infty)$ onto $y \in (-1, 1)$. The input parameter L controls the the mesh spacing[1] in the infinite domain and must be chosen so that the boundary layer near $\eta = 0$ is well resolved.

[1]For Chebyshev grids, the mesh spacing is non-uniform and cluster together more at the end points -1 and 1.

Furthermore, solving for $g \equiv f_0^2$ is preferable to solving for f_0 directly, due to g being more regular at $\eta = 0$, by (3.44). Recast in terms of g, equation (C.1) becomes:

$$\left(\frac{(1-y)^2}{2L}\frac{d}{dy}\right)^3 g - \sqrt{g} + 1 = 0, \tag{C.3}$$

with boundary conditions

$$g(-1) = 0, \tag{C.4}$$

$$g(1) = 1, \tag{C.5}$$

$$g'(-1) = \alpha, \tag{C.6}$$

where $\alpha \equiv c_1^2$ is the first coefficient in the expansion of $f_0^2(\eta)$ (see (3.44)). The ODE (C.3) with boundary conditions (C.4)-(C.6) is solved in the following way: let `D_y` be the differentiation matrix for the Chebyshev grid (see [117] for a definition), `y` the vector of n Chebyshev points

$$y_k = \cos\left(\frac{k\pi}{n-1}\right), \quad k = 0, 1, 2, ..., n-1, \tag{C.7}$$

and define the following matrices:

```
D = (0.5/L) * (1-y).^2  * D_y,
D3 = D^3,
D3_int = D3(2:end-1,2:end-1).
```

Here, we are using 'MATLAB notation', so that a dot between the vector and the carat means that the power-operation should be performed on each component of the vector, the submatrix `M(1:3,1:4)` refers to the first three rows and first four columns of the matrix `M`, and `v(end)` refers to the last component of the vector `v`.

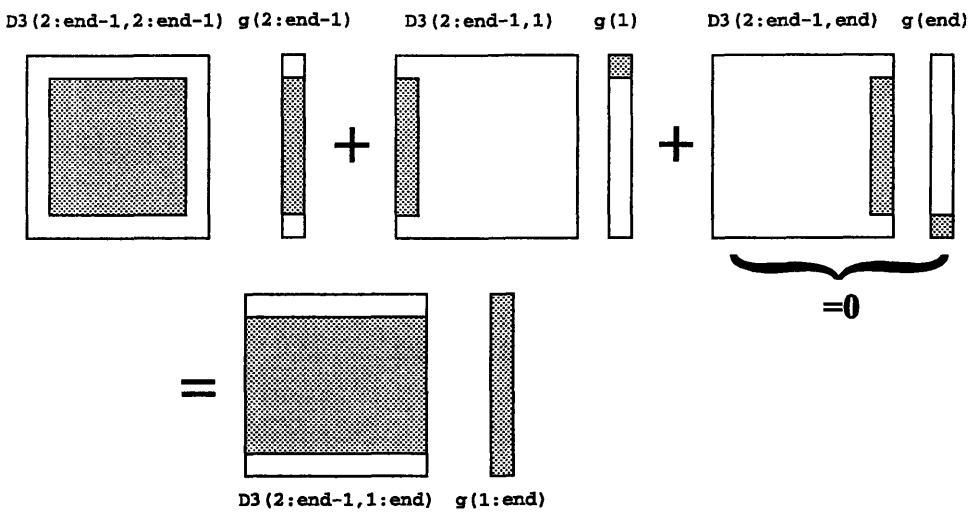

Figure C-1: Block diagram for constructing part of the residual vector corresponding to the first term in (C.3).

Furthermore, let g be the solution vector with n components such that

$$\texttt{g(end)} = g(-1) = 0 \tag{C.8}$$

$$\texttt{g(1)} = g(+1) = 1 \tag{C.9}$$

$$\texttt{g\_int} = \texttt{g(2:end-1)} \tag{C.10}$$

Note that the entries of g must be reversed because the Chebyshev points in (C.7) are also reversed, and form a *decreasing* sequence in k. We now define the $(n-2)$-component residual vector

```
Res =
D3_int * g_int + D3(2:end-1,1) * g(1) - sqrt(g_int) + 1.
```

Note that `g(end)` and `g(1)` are *not* variables. The boundary condition (C.6) is incorporated into the iteration by overwriting the first component of `Res` (which corresponds to $\eta \gg 1$):

```
Res(1) =
D(end,2:end-1) * g_int + D(end,1) * g(1) - alpha
```

```
% (last component of D*g) = alpha
```

Solving (C.3) has now been reduced to a root-finding problem: we must solve `Res = 0` in $(n-2)$ variables, and these variables consist of the components of `g_int`. The root-finding is done using a Newton iteration:

```
g_int_new = g_int_old - J^(-1) * Res
```

where `J` is the Jacobian of `Res` and takes the form

```
J = D^3 - (1/2) * diag(g.^(-1/2))
J(1,:) = D(end,2:end-1)   % overwrite first row of J
```

The entries of the matrix `diag(v)` are all zero, except for its leading diagonal, which consists of the entries of the vector `v`.

C.1.2 Construction of the Composite Solution

Solution with Continuity of Chemical Potential

Here, we give details on how to solve for the constants c_1,c_3,a_0,A and x_0 in the composite formula (3.51), by imposing continuity of chemical potential at the facet.

The 5 boundary conditions [78] discussed in Chapter 3, (3.53)- (3.57) are:

$$a_0^2 x_0 A(3\varepsilon^{2/3}c_1^2 + (x_0 A)^2) = 3 \tag{C.11}$$

$$a_0^2 \varepsilon^{1/3} x_0 A(3\varepsilon^{1/3}c_1^2 - 4x_0 A c_1 c_3) = 3, \quad \text{(cont. chem. pot.)} \tag{C.12}$$

$$4a_0 A^3 = x_0, \tag{C.13}$$

$$a_0 = \frac{3}{x_0^4} + 1, \tag{C.14}$$

$$c_1 = S(c_3). \tag{C.15}$$

The constants (c_1, c_3) parameterize the solution to the Universal ODE (3.40), and determine $f_0(\eta)$. This section outlines the steps taken in [78] to reduce the system (C.11)-(C.14) to a single equation in c_1 and c_3, by eliminating a_0, A and x_0, and then solving numerically for (c_1, c_3) with (C.15).

It is convenient now to switch back to the notation used in MAS, write $\tilde{w} = x_0 A$, and reduce equations (C.11)–(C.14) to

$$a_0^2 \tilde{w}(3\varepsilon^{2/3} c_1^2 + \tilde{w}^2) = 3, \tag{C.16}$$

$$a_0^2 \varepsilon^{1/3} \tilde{w}(3\varepsilon^{1/3} c_1^2 - 4\tilde{w} c_1 c_3) = 3, \quad \text{(cont. chem. pot.)} \tag{C.17}$$

$$a_0^2 - a_0 - \frac{3}{4\tilde{w}^3} = 0. \tag{C.18}$$

Equation (C.18) comes from (C.13) and (C.14). Now, λ is introduced through the relation

$$\tilde{w}^3 a_0^2 \lambda^2 = 3. \tag{C.19}$$

Equations (C.16), (C.18) and (C.19) imply

$$c_1(\lambda) = \varepsilon^{-1/3} 3^{-1/2} \left[\frac{3}{16} \frac{(4-\lambda^2)^2}{\lambda^2} \right]^{1/3} \sqrt{\lambda^2 - 1}, \tag{C.20}$$

and (C.16), (C.17), (C.18) and (C.19) imply

$$c_3(\lambda) = -\frac{\sqrt{3}}{4} (\lambda^2 - 1)^{-1/2}. \tag{C.21}$$

Equations (C.20) and (C.21) parameterize a curve in (c_1, c_3) space in terms of λ. Upon eliminating λ, this curve takes the following form [78]:

$$c_1 \varepsilon^{1/3} = -\frac{3}{4c_3} \left[\frac{1}{16^2 c_3^2} \frac{(16c_3^2 - 1)^2}{(16c_3^2 + 3)} \right]^{1/3}. \tag{C.22}$$

Hence, for each value of λ, there corresponds a pair (c_1, c_3).

Remark C.1.1 *It should be noted that the derivation of (C.21) and (C.22) uses Continuity of Chemical Potential at the facet, but (C.20) does not. The reason for making this distinction is that later on, when we replace Continuity of Chemical Potential with the Step Drop Condition, we will be reusing equation (C.20).*

The intersection points in (c_1, c_3) space of (C.22) and $c_1 = S(c_3)$ are now solved numerically to yield (ideally) exactly *one* pair, (c_1^*, c_3^*), corresponding to one value of

$\lambda = \lambda^*$. The pair (c_1^*, c_3^*) specifies $f_0(\eta)$ uniquely. The three other constants $a_0, \tilde{w}$ and x_0 all follow, if λ^* is known [78]:

$$a_0 = \frac{|4 - \lambda^{*2}| + (4 + \lambda^{*2})}{2|4 - \lambda^{*2}|}, \tag{C.23}$$

$$\tilde{w} = \left[\frac{3}{16}\frac{(4 - \lambda^{*2})^2}{\lambda^{*2}}\right]^{1/3}, \tag{C.24}$$

$$x_0 = \left\{\frac{3}{8}\frac{[|4 - \lambda^{*2}| + (4 + \lambda^{*2})]|4 - \lambda^{*2}|}{\lambda^{*2}}\right\}^{1/4}. \tag{C.25}$$

These relations also are independent of the Chemical Potential Boundary Condition. Two plots taken from MAS are now shown in Figure C-2. The intersections in (a) show the pairs (c_1^*, c_3^*) for different values of ε. These pairs produce the solutions to $f_0(\eta)$, shown plot (b). It was later found out that the code which produced the $c_1 = S(c_3)$ curve contained a small programming error. With the error fixed, we have the results in Figure C-3. Figure C-3 shows the revised version of Figure C-2 a), and a close up. These results suggest that as $\varepsilon \to 0$, c_1^* and c_3^* are only weakly dependent on ε. Even as ε spans several orders of magnitude, c_1^* and c_3^* remain $O(1)$, and in fact $(c_1^*, c_3^*) \to (2, -0.25)$ as $\varepsilon \to 0$. In general, there appear to be three possible intersection points between the newly revised $c_1 = S(c_3)$ and equation (C.22). However for extremely small values of ε, the number of intersections reduces to two, and the corresponding values of (c_1^*, c_3^*) are very close to each other. The consequence of this is that for $\varepsilon \ll 1$, the ambiguity in (c_1^*, c_3^*) has no real effect on $f_0(\eta)$.

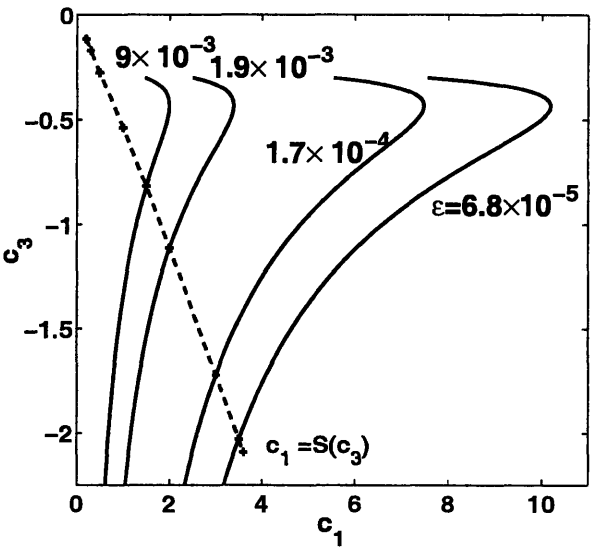

(a)

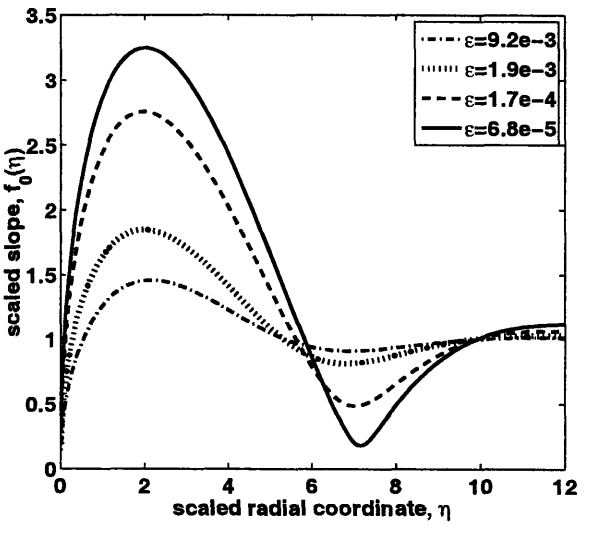

(b)

Figure C-2: Plots taken from the paper by MAS [78]. The intersections in (a) produce pairs (c_1^*, c_3^*) which uniquely determine $f_0(\eta)$, the solution to the Universal ODE (3.40): the $f_0(\eta)$ corresponding to each value of ε is shown in (b). The code which produced the curve $c_1 = S(c_3)$ in (a) contained a small programming error.

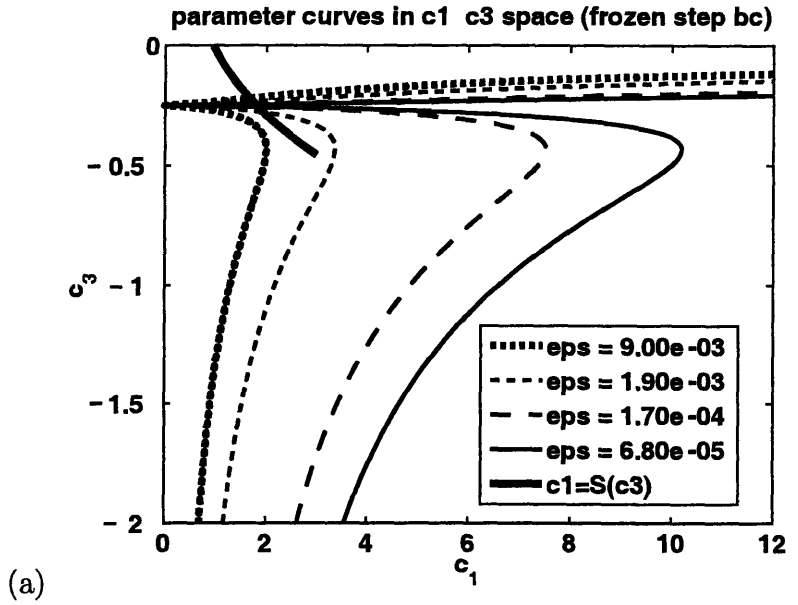

(a)

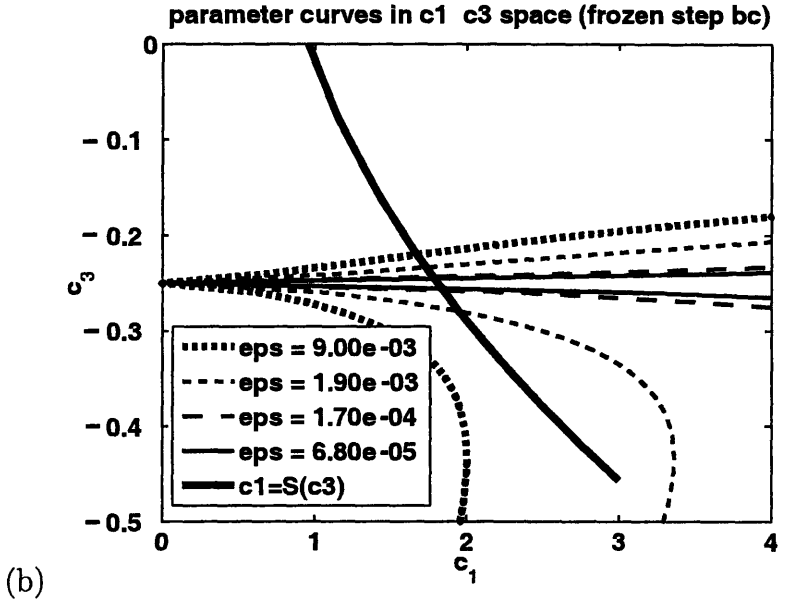

(b)

Figure C-3: Plots (a) and (b): intersections of the curve $c_1 = S(c_3)$, and the continuity of chemical potential boundary condition (C.22), with the programming error removed. In (a), $c_1 = S(c_3)$ was generated using the pseudo-spectral method outlined in Section C.1.1 . For values of c_1 greater than about 3, f_0^2 in (3.40) becomes negative, corresponding to unphysical solutions. The intersections shown here correspond to the solutions in Figure B-33 (b).

Remark C.1.2 *We can re-write equation (C.21), which does* not *assume continuity of chemical potential, as*

$$\lambda^2 - 1 - G\left[\frac{16}{3}\frac{\lambda^2}{(4-\lambda^2)^2}\right]^{2/3} = 0, \tag{C.26}$$

where $G = 3c_1^2\varepsilon^{2/3}$. *The roots of this equation are shown in figure C-4. For small* G,

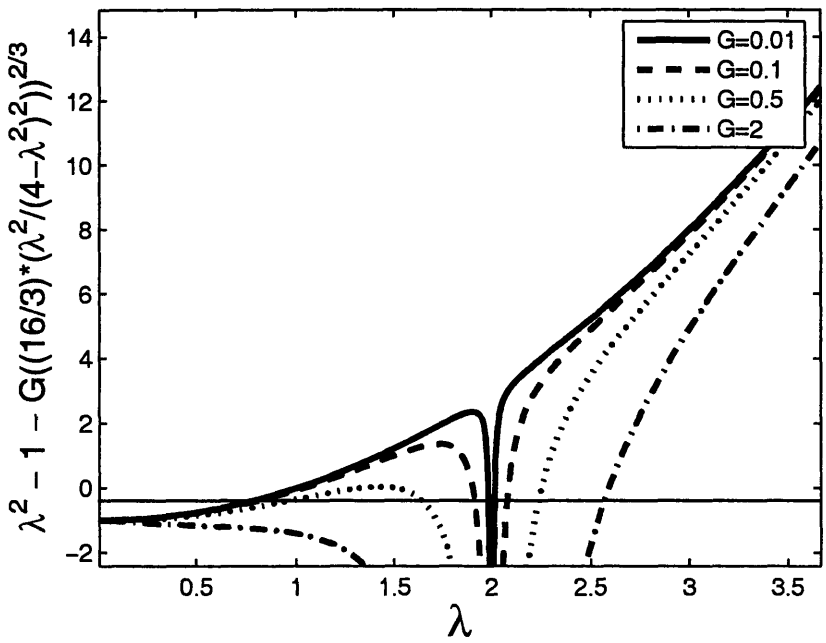

Figure C-4: Plots showing the roots of Equation (C.26) for different values of $G \equiv 3c_1^2\varepsilon^{2/3}$.

there are three possible roots for λ *which implies three possible intersections* (c_1^*, c_3^*)*: one close to* $\lambda = 1$ *and two close to* $\lambda = 2$. *For larger values of* G, *two roots vanish, leaving a unique solution,* $\lambda > 2$. *The unphysical scalings which are predicted by the condition of Chemical Potential Continuity correspond to one of the* $\lambda \approx 2$ *roots: for example, in order for* $a_0 = O(\varepsilon^{-1/2})$, *we must take the* $\lambda = 2 + O(\varepsilon^{1/2})$ *in (C.23).*

Solution with Step Drop Condition

The step drop condition (3.81) replaces equation (C.12) with

$$\left(\frac{x_0}{A^4}\right)(c_1 c_3 \varepsilon^{1/3}) - \frac{1}{x_0^3} + x_0 = \frac{1}{\tau^{*1/4}}. \tag{C.27}$$

In this equation, τ^* is an external parameter relating to the collapse of the inner most step, and comes from the discrete step flow simulations. We recall that a conversion from the parameters $(c_1, c_3) \to (\alpha, \beta)$ where $\alpha = c_1^2$ and $\beta = 4c_1c_3$ results in more stable numerical methods (see (3.45) and comments after).

The pseudospectral method in C.1.1 establishes a relation between α and β:

$$\beta = \tilde{S}(\alpha) \tag{C.28}$$

Analogous to the case of the chemical potential boundary condition, we use the remaining four equations (C.11), (C.13), (C.14) and (C.27) to obtain another relation between α and β, which we shall call

$$\beta = P(\alpha; \varepsilon). \tag{C.29}$$

For every value of α and input parameter ε, $P(\alpha, \varepsilon)$ is obtained using the following procedure:

1. For a particular value of τ^*, ε and α, calculate $G = 3\alpha\varepsilon^{2/3}$.
2. Find the root of (C.20), λ^*, which is closest to $\lambda \approx 1$ (the $\lambda \approx 2$ root, as we have seen, leads to unphysical solutions).
3. Compute a_0, $\tilde{w}$ and x_0 from (C.23), (C.24) and (C.25).
4. Compute $\beta \equiv 4c_1c_3$ from (C.27) using a Newton iteration (for example).

The curve $\beta = \tilde{S}(\alpha)$ and the *family* of curves $\beta = P(\alpha; \varepsilon)$ are shown in Figure C-5. For a particular value of ε, the intersections of $\tilde{S}$ and P produce a pair (α, β) which

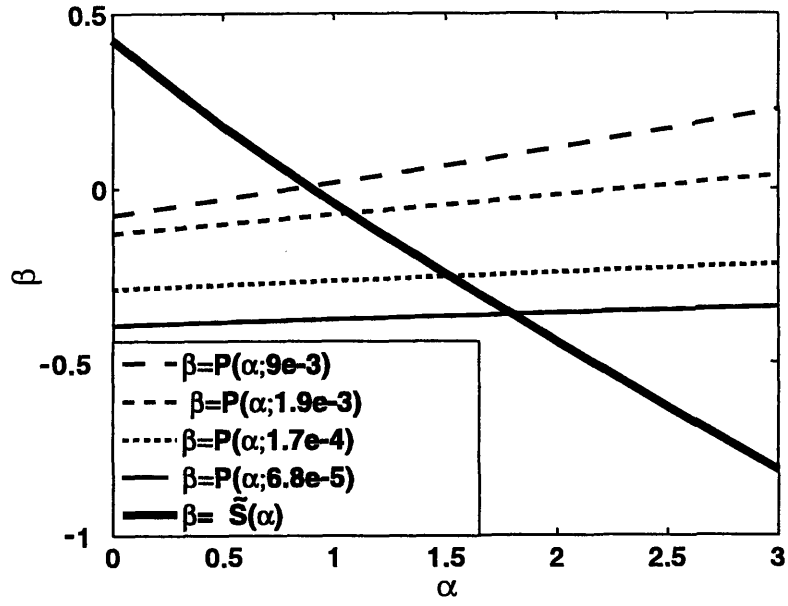

Figure C-5: Intersection of $\beta = \tilde{S}(\alpha)$ and $\beta = P(\alpha, \varepsilon)$ to generate solutions to the 3rd order MAS ODE (3.40) implemented with the step drop boundary condition.

fix the inner solution $f_0(\eta)$ in (3.40), and this pair corresponds to a particular value of $\lambda = \lambda^*$. The full solution F is obtained through using λ^* in equations (C.23), (C.24) and (C.25) to obtain the stretch factors and shift factors needed to construct the full solution. Some of these solutions are shown in Figures B-35 and B-36.

C.2 Similarity Solutions MAS PDE, arbitrary ε

C.2.1 Numerical Procedure

Here we give details on the numerical solution of the ODE (3.88) with boundary conditions (3.89)-(3.93) and either (3.94) or (3.95). MATLAB's `bvp4c` program [5] was used as the solver for this boundary value problem. The domain of solution is $[\xi_0, E]$ where $E \gg 1$ will approximate the point at infinity. The code `bvp4c` is a fourth order collocation method [7] which is fairly flexible in terms of being able to tackle singular problems and allowing implementation of numerical continuation (see later). We first make a linear change of variable $s = \xi - \xi_0$ to map $[\xi_0, E]$ onto $[0, E']$ where $E' = E - \xi_0$ The ODE, written as a system of 1st order equations for

$\varepsilon \equiv g_3/g_1$	τ^*	ϕ	x_{0SD}	x_{0CP}
0.015	0.22	0.08	1.44	2.24
0.15	0.21	0.18	1.13	1.87
1.5	0.18	0.45	0.59	1.11
7.5	0.12	0.90	0.49	0.49
15	0.07	1.33	0.31	0.31

Table C.1: Tabulated values of ϕ, τ^* and facet widths $x_0 \equiv \varepsilon^{1/8}\xi_0$ for different values of ε. x_{0SD} and x_{0CP} are the facet widths obtained when applying boundary conditions (C.39) and (C.40) respectively.

$\left(G_1 = f^2, G_2 = \frac{df^2}{ds}, G_3 = \frac{d^2f^2}{ds^2}, G_4 = \frac{d^3f^2}{ds^3}\right)$ to be solved on $s = [0, E']$ becomes

$$G_1' = G_2, \tag{C.30}$$

$$G_2' = G_3, \tag{C.31}$$

$$G_3' = G_4, \tag{C.32}$$

$$G_4' = -\frac{2}{s+\xi_0}G_4 + \frac{3}{(s+\xi_0)^2}G_3 - \frac{3}{(s+\xi_0)^3}G_2 \tag{C.33}$$

$$+ \frac{3}{(s+\xi_0)^4}G_1 + \frac{\alpha_0(s+\xi_0)}{8}G_1^{-1/2}G_2 + \frac{3}{(s+\xi_0)^4}, \tag{C.34}$$

and the 5 boundary conditions are

$$G_1(0) = 0 \tag{C.35}$$

$$3\xi_0 G_2(0) - \xi_0^3 G_4(0) = 3 \tag{C.36}$$

$$G_1(E') = k^2 g \tag{C.37}$$

$$G_2(E') = 0 \tag{C.38}$$

and **EITHER**
$$3\xi_0 G_2(0) - \xi_0^2 G_3(0) = 3 \tag{C.39}$$

OR
$$\frac{1}{\xi_0^3} + G_4(0) + \frac{2}{\xi_0}G_3(0) - \frac{1}{\xi_0^2}G_2(0) = -\phi \tag{C.40}$$

where

$$\phi = \frac{\varepsilon^{3/8}}{4\tau^{*1/4}} = O(\varepsilon^{3/8}) \tag{C.41}$$

Values for ϕ are shown in Table C.1. The solution of (C.30)-(C.34) would now be

relatively simple if it were not for the fact that $G_4'(s)$ is divergent at $s = 0$. In fact, we show below that $G_4'(s) \sim s^{-1/2}$ by considering the Taylor Series expansion for f^2. The solver `bvp4c` *does* evaluate (C.30)-(C.34) on both endpoints of the domain, and a naive implementation would result in erroneous output due primarily to singular Jacobians. One way to avoid this problem is to solve the ODE on $[s_0, E']$ as opposed to $[0, E']$ where $s_0 > 0$. Providing s_0 is chosen to be large enough, $G_4'(s_0) \sim s_0^{-1/2}$ can be made small enough so that the iterations in `bvp4c` converge to give a unique solution for (G_1, G_2, G_3, G_4). We therefore need to supplement equations (C.35)-(C.40) with extra conditions for the values of $G_1(s_0), G_2(s_0), G_3(s_0)$ and $G_4(s_0)$, which are all obtained through considering their series expansions. Hence, s_0 must be chosen such that it is large enough to avoid large Jacobians for (C.30)-(C.34), but small enough so that $G_i(s_0)$ are represented accurately with a reasonable number of terms. Taking more terms in the series expansions for the G_i allows a greater value of s_0 to be chosen. Section C.2.6 in this appendix gives the form of these expansions for reference.

The expansion for f is

$$f = c_1 s^{1/2} + c_3 s^{3/2} + c_5 s^{5/2} + \ldots \tag{C.42}$$

$$\Rightarrow f^2 = \underbrace{c_1^2}_{A} s + 2\underbrace{c_1 c_3}_{B} s^2 + \underbrace{(2c_1 c_5 + c_3^2)}_{C} s^3 + \ldots \tag{C.43}$$

$$\Rightarrow G_1(s = 0) = 0, \tag{C.44}$$

$$G_2(s = 0) = A, \tag{C.45}$$

$$G_3(s = 0) = 4B, \tag{C.46}$$

$$G_4(s = 0) = 6C, \tag{C.47}$$

and c_j for $j > 5$ can be written in terms of c_1, c_3 and c_5 simply by substituting (C.42) into the ODE (3.88) and equating coefficients. Section C.2.6 shows the form of the c_j explicitly. In particular, when $\alpha_0 \neq 0$, $c_6 \neq 0$ and so the fourth derivative of $f^2(s)$ diverges as $s^{-1/2}$ as $s \to 0$. For $\alpha_0 = 0$, the expansion of f only contains terms of the form $s^{m/2}$ where m is odd, and so in this case, f has infinitely many derivatives at

$s = 0$.

The boundary conditions for the ODE now consist of 8 equations because (c_1, c_3, c_5) (or A, B and C) are included as unknown parameters in the problem. In particular, (C.35) is replaced with a series representation for $G_1(s_0)$, (C.36),(C.39) and (C.40) are re-written in terms of A, B and C using (C.44)-(C.47), and three other equations specify the values of $G_2(s_0), G_3(s_0)$ and $G_4(s_0)$ through their asymptotic series. Hence, (C.35)-(C.40) become

$$G_1(s_0) - S_1^m(s_0) = 0 \quad \text{(C.48)}$$

$$G_2(s_0) - S_2^m(s_0) = 0 \quad \text{(C.49)}$$

$$G_3(s_0) - S_3^m(s_0) = 0 \quad \text{(C.50)}$$

$$G_4(s_0) - S_4^m(s_0) = 0 \quad \text{(C.51)}$$

$$G_1(E') - k^2 g = 0 \quad \text{(C.52)}$$

$$G_2(E') = 0 \quad \text{(C.53)}$$

$$\xi_0 A - 2\xi_0^3 C - 1 = 0 \quad \text{(C.54)}$$

and **EITHER**
$$3\xi_0 A - 4\xi_0^2 B - 3 = 0 \quad \text{(C.55)}$$

OR
$$1 + 6C\xi_0^3 + 8B\xi_0^2 - A\xi_0 + \phi\xi_0^3 = 0 \quad \text{(C.56)}$$

where $S_j^m(s_0)$ is a series representation of $G_j(s_0)$ up to the term $s_0^{m/2}$. A solution to the boundary value problem now consists of the four functions (G_1, G_2, G_3, G_4), and the four parameters (A, B, C, ξ_0).

C.2.2 Initial Guess for $G_i(s)$

This was set to:

$$G_1(s) = ase^{-s} + k^2 g \tanh s, \quad \text{(C.57)}$$

$$G_2(s) = a(1-s)e^{-s} + k^2 g \operatorname{sech}^2 s, \quad \text{(C.58)}$$

$$G_3(s) = a(s-2)e^{-s} - 2k^2 g \operatorname{sech}^2 s \tanh s, \quad \text{(C.59)}$$

$$G_4(s) = a(3-s)e^{-s} - 2k^2 g \operatorname{sech}^4 s + 4k^2 g \operatorname{sech}^2 s \tanh^2 s, \quad \text{(C.60)}$$

for some constant a so that $G_1(0) = 0$ and $G_1(s) \sim gk^2$ as $s \to \infty$. Iterations were generally found to be convergent when a was taken to be about 0.05.

C.2.3 Validation of Code

As well as checking that numerical solutions match the exact ones when $\alpha_0 = 0$, in the fully nonlinear case (see C.2.5), we can also check the validity of the expansions $S_j^m(s_0)$ by doing a convergence study of ξ_0. As m is increased, so should the accuracy of ξ_0. Although we do not have an analytic form for ξ_0 when $\alpha_0 = 1$, we can still check convergence by taking s_0 sufficiently small to get an approximation to the 'exact' ξ_0, ξ_{0e} say, and then plotting $|\xi_0(s_0) - \xi_{0e}|$ vs s_0 for larger s_0. Figure C-6 shows the results of these convergence studies in the linear and nonlinear cases.

C.2.4 Numerical Continuation

The code `bvp4c` requires the user to input starting values for the functions $G_i(s)$ and the parameters (A, B, C, ξ_0). Convergence to the true solution is contingent upon the quality of the initial guess, and a good initial guess is not always known a priori. In our case, however, we can solve the problem exactly when $\alpha_0 = 0$ and E is finite. To solve for the fully nonlinear case ($\alpha_0 = 1$), we start with the solution to the linear problem – let us denote this by $\mathcal{P}(g, \alpha_0 = 0, E)$, to indicate dependence on the problem parameters g, α_0 and E - and use the solution to this problem as the initial condition to $\mathcal{P}(g, d\alpha_0, E)$ where $d\alpha_0 \ll 1$. Likewise, once this has been solved, we use that solution as the initial guess to $\mathcal{P}(g, 2d\alpha_0, E)$ etc. until we obtain the solution to $\mathcal{P}(g, \alpha_0 = 1, E)$. A similar "bootstrapping" procedure can be done to reach particular values of g, E and ϕ (for the step drop condition) when the solution does not converge from the initial condition (C.57)-(C.60). In particular, for the step drop problem, it was very difficult to converge onto the solution using the initial guess (C.57)-(C.60) and $\alpha_0 = 1$ when g was less than about 0.1. Numerical continuation was essential to obtaining any kind of solution in this case. More details on Continuation can be found in [7].

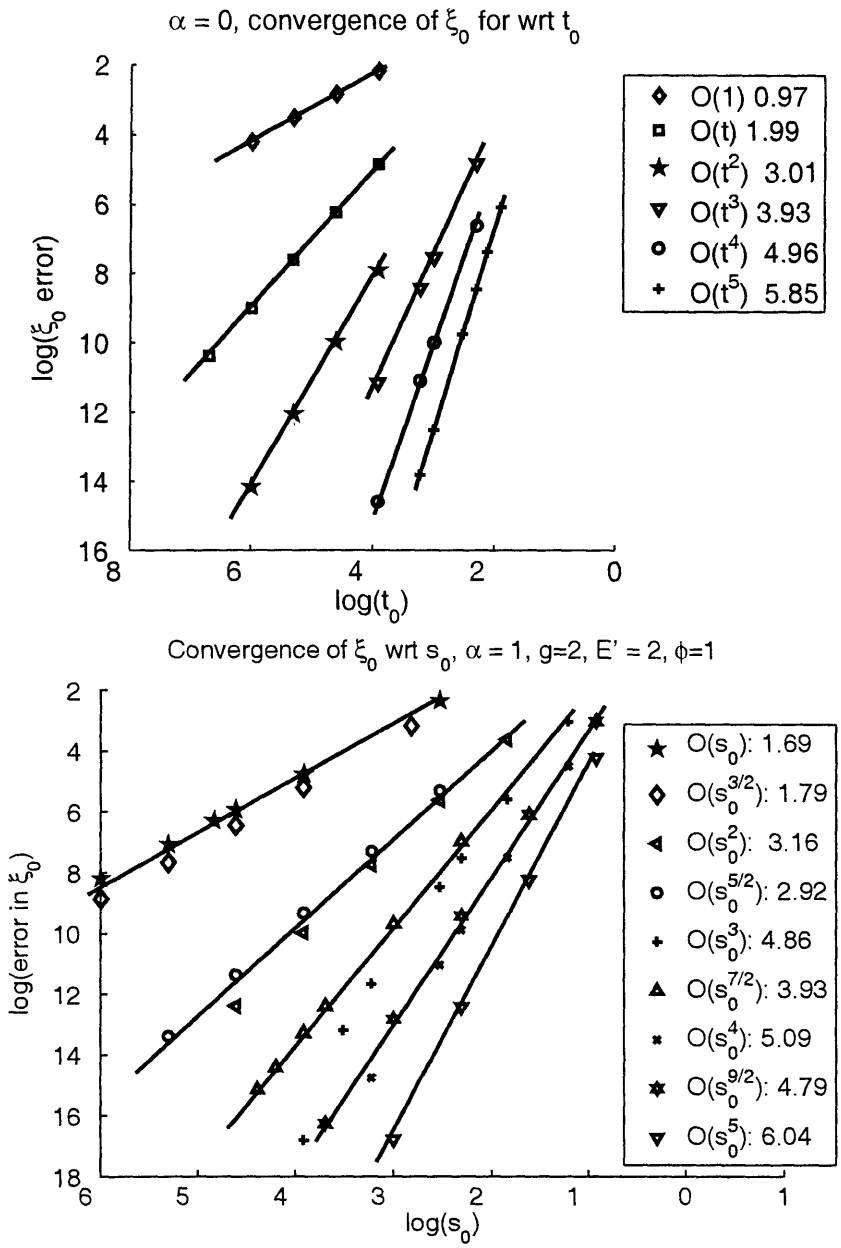

Figure C-6: Convergence of ξ_0 as s_0 is decreased in linear ($\alpha_0 = 0$) and nonlinear ($\alpha_0 = 1$) cases, when solving (3.88). The order of convergence is indicated in the legend, and varies depending on the number of terms taken in the expansions of S_i^m in (C.48)-(C.51).

C.2.5 Exact Solutions when $\alpha_0 = 0$

For reference, exact solutions are provided in the linear case when $\alpha_0 = 0$, and the domain of solution is *finite* (on $[\xi_0, E]$). Equation (3.88), and the boundary conditions are then linear in f^2 and the solution, along with ξ_0 can be solved for exactly because (3.88) is an inhomogeneous, equidimensional ODE which has the solution

$$f^2(\xi) = \frac{A_1}{\xi} + A_2\xi^3 + A_3\xi + A_4\xi\ln\xi - 1 \tag{C.61}$$

We now compute values for A_1, A_2, A_3, A_4 and ξ_0 for the case where:
(i) Continuity of chemical potential is enforced at the facet, and
(ii) The step drop condition is enforced at the facet.

Exact Solutions with Continuity of Chemical potential

We obtain a nonlinear algebraic system of equations for $(A_1, A_2, A_3, A_4, \xi_0)$ by imposing boundary conditions (C.35)-(C.40) at $\xi = \xi_0$ and $\xi = E$:

$$\frac{A_1}{\xi_0} + A_2\xi_0^3 + A_3\xi_0 + A_4\xi_0\ln\xi_0 = 1 \tag{C.62}$$

$$\frac{3A_1}{\xi_0} + 3A_2\xi_0^3 + 3\xi_0A_3 + 4\xi_0A_4 + 3A_4\xi_0\ln\xi_0 = 3 \tag{C.63}$$

$$\frac{A_1}{E} + A_2E^3 + A_3E + A_4E\ln E = C_0 \tag{C.64}$$

$$-\frac{A_1}{E} + 3A_2E^3 + A_3E + A_4E + A_4E\ln E = 0 \tag{C.65}$$

$$-\frac{5A_1}{\xi_0} + 3A_2\xi_0^3 + 3A_3\xi_0 + 2A_4\xi_0 + 3A_4\xi_0\ln\xi_0 = 3 \tag{C.66}$$

where $C_0 = gk^2 + 1$. This system can be solved exactly for (A_1, A_2, A_3, A_4), and a cubic equation is obtained for ξ_0:

$$\begin{aligned} A_1 &= 0, && \text{(C.67)} \\ A_2 &= -\frac{C_0}{2E^3}, && \text{(C.68)} \\ A_3 &= \frac{3C_0}{2E}, && \text{(C.69)} \\ A_4 &= 0, && \text{(C.70)} \\ \xi_0^3 - 3E^2\xi_0 + \frac{2E^3}{C_0} &= 0. && \text{(C.71)} \end{aligned}$$

The $\alpha_0 = 0$ solution is therefore

$$f(\xi) = \left(\frac{C_0}{2}\left[3\left(\frac{\xi}{E}\right) - \left(\frac{\xi}{E}\right)^3\right] - 1\right)^{1/2} \qquad \text{(C.72)}$$

where $\xi_0 \leq \xi \leq E$.

Exact Solutions with Step Drop boundary condition

The algebraic system to solve here is exactly the same as (C.62)-(C.66) but with (C.66) replaced by

$$-\frac{A_1}{\xi_0} + 15A_2\xi_0^3 - A_3\xi_0 - A_4\xi_0 \ln \xi_0 + \phi\xi_0^3 = -1. \qquad \text{(C.73)}$$

Now the coefficients and scaled facet location are given by

$$\begin{aligned} A_1 &= -\frac{E^4\phi}{16} + \frac{E}{2} + \frac{E(C_0 - 1)}{2}, && \text{(C.74)} \\ A_2 &= -\frac{\phi}{16}, && \text{(C.75)} \\ A_3 &= \frac{1}{2E} + \frac{C_0 - 1}{2E} + \frac{E^2\phi}{8}, && \text{(C.76)} \\ A_4 &= 0, && \text{(C.77)} \\ & && \text{(C.78)} \end{aligned}$$

and ξ_0 satisfies the quartic polynomial

$$A_2\xi_0^4 + A_3\xi_0^2 - \xi_0 - A_1 = 0 \tag{C.79}$$

C.2.6 Series Expansions

Here, we give the series expansions for S_j^m with $m = 10$: these expansions are used in the boundary conditions (C.48)-(C.51).

$$\begin{aligned}
S_1^{10}(s_0) &= c_1^2 s_0 + 2c_1c_3 s_0^2 + (c_3^2 + 2c_1c_5)s_0^3 + 2c_1c_6 s_0^{7/2} + 2(c_3c_5 + c_1c_7)s_0^4 \\
&\quad +2(c_3c_6 + c_1c_8)s_0^{9/2} + (c_5^2 + 2c_3c_7 + 2c_1c_9)s_0^5 \\
S_2^{10}(s_0) &= c_1^2 + 4c_1c_3 s_0 + 3(c_3^2 + 2c_1c_5)s_0^2 + 7c_1c_6 s_0^{5/2} + 8(c_3c_5 + c_1c_7)s_0^3 \\
&\quad +9(c_3c_6 + c_1c_8)s_0^{7/2} + 5(c_5^2 + 2c_3c_7 + 2c_1c_9)s_0^4 \\
&\quad +11(c_5c_6 + c_3c_8 + c_1c_{10})s_0^{9/2} + 6(c_6^2 + 2(c_5c_7 + c_3c_9 + c_1c_{11}))s_0^5 \\
S_3^{10}(s_0) &= 4c_1c_3 + 6(c_3^2 + 2c_1c_5)s_0 + \frac{35}{2}c_1c_6 s_0^{3/2} + 24(c_3c_5 + c_1c_7)s_0^2 + \frac{63}{2}(c_3c_6 + c_1c_8)s_0^{5/2} \\
&\quad +20(c_5^2 + 2c_3c_7 + 2c_1c_9)s_0^3 + \frac{99}{2}(c_5c_6 + c_3c_8 + c_1c_{10})s_0^{7/2} \\
&\quad +30(c_6^2 + 2(c_5c_7 + c_3c_9 + c_1c_{11}))s_0^4 + \frac{143}{2}(c_6c_7 + c_5c_8 + c_3c_{10} + c_1c_{12})s_0^{9/2} \\
&\quad +42(c_7^2 + 2(c_6c_8 + c_5c_9 + c_3c_{11} + c_1c_{13}))s_0^5 \\
S_4^{10}(s_0) &= 6(c_3^2 + 2c_1c_5) + \frac{105}{4}c_1c_6 s_0^{1/2} + 48(c_3c_5 + c_1c_7)s_0 + \frac{315}{4}(c_3c_6 + c_1c_8)s_0^{3/2} \\
&\quad +60(c_5^2 + 2c_3c_7 + 2c_1c_9)s_0^2 + \frac{693}{4}(c_5c_6 + c_3c_8 + c_1c_{10})s_0^{5/2} \\
&\quad +120(c_6^2 + 2(c_5c_7 + c_3c_9 + c_1c_{11}))s_0^3 + \frac{1287}{4}(c_6c_7 + c_5c_8 + c_3c_{10} + c_1c_{12})s_0^{7/2} \\
&\quad +210(c_7^2 + 2(c_6c_8 + c_5c_9 + c_3c_{11} + c_1c_{13}))s_0^4 \\
&\quad +\frac{2145}{4}(c_7c_8 + c_6c_9 + c_5c_{10} + c_3c_{12} + c_1c_{14})s_0^{9/2} \\
&\quad +336(c_8^2 + 2(c_7c_9 + c_6c_{10} + c_5c_{11} + c_3c_{13} + c_1c_{15}))s_0^5
\end{aligned}$$

where

$$
\begin{aligned}
c_6 &= \frac{\alpha_0\xi_0}{105} \\
c_7 &= \frac{1}{16\xi_0^4 c_1} - \frac{c_1}{16\xi_0^3} + \frac{c_3}{4\xi_0^2} - \frac{c_3^2}{4\xi_0 c_1} - \frac{c_5}{2\xi_0} - \frac{c_3 c_5}{c_1} \\
c_8 &= -\frac{8}{945c_1}\left(-\frac{\alpha_0 c_1}{8} + \frac{945}{8}c_3c_6 + \frac{105}{2}\frac{c_1c_6}{\xi_0} - \frac{3}{8}\alpha_0 c_3\xi_0\right) \\
c_9 &= -\frac{c_5^2}{2c_1} - \frac{c_3c_7}{c_1} - \frac{1}{20c_1\xi_0^5} + \frac{c_1}{20\xi_0^4} - \frac{3c_3}{20\xi_0^3} + \frac{c_3^2}{8c_1\xi_0^2} + \frac{c_5}{4\xi_0^2} - \frac{2c_3c_5}{5c_1\xi_0} - \frac{2c_7}{5\xi_0} \\
c_{10} &= -\frac{c_5c_6 + c_3c_8}{c_1} + \frac{8}{33}\frac{c_6}{\xi_0^2} - \frac{4}{11}\frac{c_3c_6}{\xi_0 c_1} - \frac{4}{11}\frac{c_8}{\xi_0} + \frac{\alpha_0 c_3}{1155c_1} + \frac{\alpha_0 c_5\xi_0}{693c_1} \\
c_{11} &= -\frac{1}{720c_1}\left(360c_6^2 + 720(c_5c_7 + c_3c_9) - \frac{30}{\xi_0^6} + \frac{30c_1^2}{\xi_0^5} - \frac{78c_1c_3}{\xi_0^4} + \frac{57c_3^2}{\xi_0^3}\right. \\
&\quad \left. + \frac{114c_1c_5}{\xi_0^3} - \frac{168c_3c_5}{\xi_0^2} - \frac{168c_1c_7}{\xi_0^2} + \frac{120c_5^2}{\xi_0} + \frac{240c_3c_7}{\xi_0} + \frac{240c_1c_9}{\xi_0} - \frac{3\alpha_0c_6\xi_0}{4}\right) \\
c_{12} &= -\frac{8}{9009c_1}\left(-\frac{5}{8}\alpha_0c_5 + \frac{9009}{8}(c_6c_7 + c_5c_8 + c_3c_{10}) + \frac{357}{2}\frac{c_1c_6}{\xi_0^3}\right. \\
&\quad \left. - \frac{252}{\xi_0^2}(c_3c_6 + c_1c_8) + \frac{693}{2\xi_0}(c_5c_6 + c_3c_8 + c_1c_{10}) - \frac{7c_7}{8}\alpha_0\xi_0\right) \\
c_{13} &= -\frac{1}{1680c_1}\left(-\frac{3\alpha_0c_6}{4} + 840c_7^2 + 1680(c_6c_8 + c_5c_9 + c_3c_{11}) + \frac{60}{\xi_0^7}\right. \\
&\quad -\frac{60c_1^2}{\xi_0^6} + \frac{144c_1c_3}{\xi_0^5} - \frac{96c_3^2}{\xi_0^4} - \frac{192c_1c_5}{\xi_0^4} + \frac{264}{\xi_0^3}(c_3c_5 + c_1c_7) \\
&\quad \left. - \frac{180c_5^2}{\xi_0^2} - \frac{360}{\xi_0^2}(c_3c_7 + c_1c_9) + \frac{240}{\xi_0}c_6^2 + \frac{480}{\xi_0}(c_5c_7 + c_3c_9 + c_1c_{11}) - \alpha_0c_8\xi_0\right) \\
c_{14} &= -\frac{8}{19305c_1}\left(-\frac{7\alpha_0c_7}{8} + \frac{19305}{8}(c_7c_8 + c_6c_9 + c_5c_{10} + c_3c_{12}) - \frac{279c_1c_6}{\xi_0^4}\right. \\
&\quad + \frac{747}{2\xi_0^3}(c_3c_6 + c_1c_8) - \frac{495}{\xi_0^2}(c_5c_6 + c_3c_8 + c_1c_{10}) \\
&\quad \left. + \frac{1287}{2\xi_0}(c_6c_7 + c_5c_8 + c_3c_{10} + c_1c_{12}) - \frac{9}{8}\alpha_0c_9\xi_0\right) \\
c_{15} &= -\frac{1}{3360c_1}\left(-\alpha_0c_8 + 1680c_8^2 + 3360(c_7c_9 + c_6c_{10} + c_5c_{11} + c_3c_{13}) - \frac{105}{\xi_0^8} + \frac{105c_1^2}{\xi_0^7}\right. \\
&\quad -\frac{240c_1c_3}{\xi_0^6} + \frac{150c_3^2}{\xi_0^5} + \frac{300c_1c_5}{\xi_0^5} - \frac{390}{\xi_0^4}(c_3c_5 + c_1c_7) + \frac{255}{\xi_0^3}c_5^2 + \frac{510}{\xi_0^3}(c_3c_7 + c_1c_9) - \frac{330}{\xi_0^2}c_6^2 \\
&\quad -\frac{660}{\xi_0^2}(c_5c_7 + c_3c_9 + c_1c_{11}) + \frac{420}{\xi_0}c_7^2 + \frac{840}{\xi_0}(c_6c_8 + c_5c_9 + c_3c_{11} + c_1c_{13}) \\
&\quad \left. - \frac{5}{4}\alpha_0c_{10}\xi_0\right)
\end{aligned}
$$

C.3 Subroutines for Multi-adaptive Algorithm

C.3.1 Primary Integrator (for non-stiff components)

Variables in the Algorithm:

- integer N: number of atomic layers in the structure
- double array $\rho_i, i = 1, 2, ..., N$: trajectories of the solution
- double array $e_i, i = 1, 2, ..., N$: Local Truncation Errors of ρ_i
- double t_n: current time
- double t_{end}: time to integrate to
- double μ: median of the Local Truncation Errors
- double *errmax*
- integer array $flag_i$: vector array of 1s and 0s. 1s correspond to steps which require re-integration
- integer arrays a_j and b_j

Algorithm:

1. Initialize step radii $\rho_i, i = 1, 2, ..., N$
2. Let $n = 0$ and $t = 0$
3. Choose a time step[2]
4. While $t < t_{end}$
   (a) Advance $\rho_i(t)$ using I_1, with a step size Δt. This produces (unsigned) local truncation errors for each solution, $E \equiv \{e_i : i = 1, 2, ..., N\}$ where $error(\rho_i) \equiv e_i$

[2]This was done arbitrarily, but there are ways of choosing an optimal initial step size based on the form of **F**: see [25].

(b) Compute $\mu \equiv \text{median}(e_i)$. Partition the errors into $E = U \cup V$ such that $e_i \in V \Rightarrow e_i > 10^k \mu$, and $U \doteq E \setminus V$. Let $flag_i = 1 \Leftrightarrow e_i \in V$

(c) Flag ρ_i such that $error(\rho_i) \in V$.

(d) Compute $\left|\frac{e_i}{tol_i}\right|$ for $e_i \in U$

(e) Is $errmax \equiv Max\left\{\frac{e_i}{tol_i} : e_i \in U\right\} < 1$?

If YES: goto (4f)

If NO: goto (4g)

(f) Successful I_1 step:

i. Let $\Delta t \leftarrow Min(safety \times errmax^{-1/5}, pgrow) \times \Delta t$

ii. If $t + \Delta t > t_{end}$, take $\Delta t \leftarrow (t_{end} - t)$.

iii. Apply the *makepairs* algorithm to $flag_i$. This produces pairs (a_j, b_j)

iv. Re-integrate the steps $(\rho_{a_j}, \rho_{a_j+1}, ..., \rho_{b_j})$ with I_2 over the time interval $[t, t + \Delta t]$ for each pair (a_j, b_j)

(g) Failed I_1 step:

i. Take $\Delta t \leftarrow Max(safety \times errmax^{-1/5}, pshrnk) \times \Delta t$

C.3.2 'Makepairs' algorithm

After the first integration, steps are flagged either with '0' which means that the error committed by the first integration was within tolerance level, or with a '1' which means that these trajectories in the solution need to be integrated again because the first integration gave a local truncation error that was too large. The `makepairs` algorithm takes as input a string of 0s and 1s and outputs pairs of indices (a_i, b_i) such that groups of trajectories $\rho_{a_i}, \rho_{a_i+1}, ..., \rho_{b_i}$ for each i can be passed onto another timestepper which will re-integrate these steps with sufficient accuracy.

Before we give details of the algorithm, we introduce some notation for convenience. Let X be a 'wild' character - i.e. either a 1 or a 0. Let M be a string of characters (it could be the empty string) which does not contain two consecutive 0s. Let Q be a string that starts and ends with a 1, and does not contain two consecutive

0s. $Q = 1$ is allowed. Let s_1 be all strings of the form $1XM100$ or $X1M100$. Let s_2 be all strings of the form $001MX1$ or $001M1X$.

Given an input binary string, S, of length n, initialize integer variables $START$ and END.

1. Check for the string s_1 at the beginning of S. If this string exists, note the start and end indices as being a pair (a_i, b_i) which needs to be re-integrated, and let $START =$ (index of the penultimate zero in s_1). If the beginning of S does not match s_1, let $START = 1$ (the index of the first character in S)

2. Check for the string s_2 at the end of S. If this string exists, note the start and end indices as being a pair (a_i, b_i), and let $END =$ (index of second zero in s_2). Otherwise, if the end of S does not match s_2, let $END = n$ (index of final character in S)

3. Scan from $START$ to END, looking for strings of the form $00Q00$. Every time one of these types of strings is found, note the indices of the first and last 0s, and record these as being a_i and b_i respectively.

As an example, let's say that we integrated a structure consisting of 15 steps, and that upon performing the first phase of integration, we obtained $S = 111000100010011$, a binary string of 15 characters. The first three steps near the facet, the two base steps and intermediate steps 7 and 11 require a re-integration. Because the first two and final two characters are both 1s, $s_1 = 11100 \Rightarrow START = 4$, $s_2 = 0010011$ (because $|s_2| \geq 5) \Rightarrow END = 10$. We automatically have $(a_1, b_1) = (1, 5)$ and $(a_2, b_2) = (9, 15)$. Then, in part (3) of the algorithm, we scan from position 4 to position 10, searching for patterns of 1s which have two zeros on both ends of the string. We note that $S(5 : 9) = 00100$, so $(a_3, b_3) = (5, 9)$. The 'makepairs' algorithm will output three pairs of $(a_1, b_1) = (1, 5), (a_2, b_2) = (9, 15)$ and $(a_3, b_3) = (5, 9)$. In this (artificial) example, the number of steps we had to re-integrate exceeded the original number of steps, so the multi-adaptive algorithm was very inefficient. We would have been better off just using Simple Euler from the very beginning. The algorithm improves

its efficiency when only a few steps require re-integration. When $\varepsilon \ll 1$ and $|S|$ is very large, say $\sim 10^2$, a typical S will contain a few 1s near the beginning and the end, with the majority of the bulk steps unflagged.

C.3.3 Simple Euler with Step Doubling (for stiff components)

The following algorithm takes one step (whose size is determined by the algorithm) of Simple Euler so that every component of $\mathbf{q}_n$ has a truncation error less than a user specified tolerance. As well as accepting as input $\mathbf{q}_n$, $\mathbf{f}$ and the usual parameters, the routine also requires as an argument the vector $\mathbf{R} = [\rho_{Q-1}(T_1), \rho_{Q-1}(T_2), \rho_Q(T_1), \rho_Q(T_2)]$ and t, the current time, satisfying $T_1 \leq t \leq T_2$. We introduce the solution vector $\mathbf{q}_n = [\rho_P(t_n), ..., \rho_{Q-3}(t_n), \rho_{Q-2}(t_n)]$, and the augmented solution vector $\tilde{\mathbf{q}}_n = [\rho_P(t_n), ..., \rho_{Q-1}(t_n), \rho_Q(t_n)]$

$$[\mathbf{q}_{n+1}, t_{n+1}] = \mathit{OneStepSESD}(\mathbf{q}_n, \mathbf{f}(), \mathbf{R}, t, \Delta t, \mathit{Tol}_i)$$

1. Obtain $\rho_{Q-1}(t)$ and $\rho_Q(t)$ by performing linear interpolation of $[\mathbf{R}(1), \mathbf{R}(2)]$ and $[\mathbf{R}(3), \mathbf{R}(4)]$ respectively and form the augmented vector $\tilde{\mathbf{q}}_n$

2. Advance $\tilde{\mathbf{q}}_n$ by Δt using Simple Euler:
   $\tilde{\mathbf{q}}_{n+1} = \tilde{\mathbf{q}}_n + \Delta t \mathbf{f}(\tilde{\mathbf{q}}_n, t)$

3. Advance $\mathbf{q}_n$ by using two steps of size $\Delta t/2$ with Simple Euler:
   $\tilde{\mathbf{q}}_{n+1/2} = \tilde{\mathbf{q}}_n + (\Delta t/2)\mathbf{f}(\tilde{\mathbf{q}}_n, t)$
   Interpolate $[\mathbf{R}(1), \mathbf{R}(2)]$ and $[\mathbf{R}(3), \mathbf{R}(4)]$ to obtain $\rho_{Q-1}(t_{n+1/2})$ and $\rho_Q(t_{n+1/2})$
   Replace the last two entries of $\tilde{\mathbf{q}}_{n+1/2}$ with $\rho_{Q-1}(t_{n+1/2})$ and $\rho_Q(t_{n+1/2})$
   $\tilde{\mathbf{q}}^*_{n+1} = \tilde{\mathbf{q}}_n + (\Delta t/2)\mathbf{f}(\tilde{\mathbf{q}}_{n+1/2}, t_{n+1/2})$

4. Drop the last two entries of $\tilde{\mathbf{q}}_{n+1}$,$\tilde{\mathbf{q}}_{n+1/2}$ and $\tilde{\mathbf{q}}^*_{n+1}$ to recover $\mathbf{q}_{n+1}$,$\mathbf{q}_{n+1/2}$ and $\mathbf{q}^*_{n+1}$

5. Calculate unsigned local truncation errors from $\mathbf{e} = \mathbf{q}_{n+1} - \mathbf{q}^*_{n+1}$

6. If $Max(e_i/Tol_i) < 1$,

   take $t_{n+1} = t + \Delta t$

   $\Delta t \leftarrow 3\Delta t/2$

   Exit

7. Else $\Delta t \leftarrow \Delta t/2$

   $\tilde{\mathbf{q}}_{n+1} \leftarrow \tilde{\mathbf{q}}_{n+1/2}$

   Goto (3)

Interpolation in steps (1) and (3) are done using Neville's Algorithm, which is detailed in [96]. Integration from $[t_n, t_{n+1}]$ is then done through successive calls to *OneStepSESD*, for example

1. /* Initialize Tol_i and Δt_0 */

2. $t = t_n$

3. While $t < t_{n+1}$

4. $[\mathbf{q}, t] = OneStepSESD(\mathbf{q}, \mathbf{f}(), \mathbf{R}, t, \Delta t_0, Tol_i)$

THIS PAGE INTENTIONALLY LEFT BLANK

Appendix D

Constants and Variables used

D.1 Primitive Quantities in Step Flow Equations

- D_s: Diffusivity on terraces (length^2/time)
- k: attachment-dettachment rate coefficient at step edge (length/time)
- k_u: attachment-detachment rate coefficient at step edge from below (length/time)
- k_d: attachment-detachment rate coefficient at step edge from above (length/time)
- a: Step height (length)
- $\Omega = O(a^3)$: Atomic volume (length^3)
- g_1: Step-line tension free energy (energy/length^2)
- g_3: Step-step interaction energy (energy/length^2)
- k_B: Boltzmann constant (energy/temperature)
- c_s: Equilibrium adatom density at straight step edge (length^{-2})
- C_i^{eq}: Equilibrium adatom density at circular step edge (length^{-2})
- T: Temperature in Kelvin (temperature)

- $r_i(t)$: Physical radius of i^{th} step (length)
- μ_i: Step Chemical Potential at i^{th} step (energy)
- $V(r_i, r_{i+1})$: Local interaction potential between steps i and $i+1$ (energy)
- t: Physical time (time)
- L: Characteristic initial step separation (length)
- U: Characteristic step velocity (length/time)

D.2 Derived Quantities in Step Flow Equations

- $m \equiv \frac{D_s}{kL}$: Kinetic parameter – see (2.34) and (2.35).
- α: Schwoebel parameter
- $g \equiv \frac{2}{3}\frac{g_3}{g_1}\left(\frac{a}{L}\right)^2 \equiv \frac{2}{3}\varepsilon\left(\frac{a}{L}\right)^2$: Ratio of step-step interaction strength to step line tension
- $\Omega_s \equiv \frac{\Omega}{a}$: Atomic surface area $= O(a^2)$.
- $\rho_i \equiv \frac{r_i}{L}$: Non-dimensionalized radius (r_i: radius of ith step)
- $\tau \equiv \frac{t}{L/U}$: Non-dimensionalized "Step-Flow" time
- τ_n: The n^{th} non-dimensionalized collapse time, and $\tau_n \sim n^\gamma$ as $n \to \infty$, where γ is the collapse exponent.
- $\Phi \equiv \frac{\Omega_s^2 g_1 c_s}{k_B T}\left(\frac{aD_s}{L^2 U}\right)$: Dimensionless material parameter
- $z \equiv \frac{\rho}{\tau^{1/4}}$: Similarity variable used in data collapse
- D_i: step density at step i
- E_n: Measure of finite height effect

D.3 Quantities used in the MAS Model

- r: Physical radial distance from axis of symmetry
- t: Physical time
- $h(r,t)$: Height profile
- $w(t)$: Facet radius
- $\varepsilon \equiv \frac{g_3}{g_1}$: Ratio of step line tension to step-step interaction
- $B \equiv \frac{c_s D_s \Omega^2 g_1}{k_B T}$: Material parameter
- $x \equiv \frac{r}{(Bt)^{1/4}}$: Similarity variable
- $x_0 \equiv \frac{w}{(Bt)^{1/4}}$: Scaled facet width
- $F(r,t)$: Magnitude of slope of nanostructure
- $f_0(\eta)$: Inner solution for step density when $\varepsilon \ll 1$
- $\eta = \frac{A(x-x_0)}{\varepsilon^{1/3}}$: Inner similarity variable, A is defined in (3.39)

D.4 Conversion of Parameters

D.4.1 Step Densities

$$D \sim \frac{1}{\rho} = \frac{L}{r} = \left(\frac{L}{a}\right)\left(\frac{a}{r}\right) = \frac{1}{C}F$$

- D: Slope of profile from step simulations. Note: in practice, a second order finite difference formula is used to calculate the slope: $D_i = \frac{2}{\rho_{i+1}-\rho_{i-1}}$ (see (4.13)).
- F: Continuum slope profile from MAS [78].

- $C \equiv \frac{a}{L}$: Ratio of the step height to the characteristic step separation, is dimensionless. Its value is obtained by equating the slopes of the simulation data and the continuum theory in the far field, for an infinite cone $\Rightarrow C = 1$.

D.4.2 Material Parameters

$$\Phi \equiv \frac{\Omega_s^2 c_s g_1}{k_B T}\left(\frac{aD_s}{L^2 U}\right) \tag{D.1}$$

$$= \frac{c_s \Omega_s^2 g_1}{k_B T}\left(\frac{D_s}{aU}\right) C^2 \tag{D.2}$$

$$= \frac{c_s \Omega^2 g_1 D_s}{k_B T}\left(\frac{1}{a^3 U}\right) C^2 \quad \text{since } \Omega_s a = \Omega \tag{D.3}$$

$$= \frac{B}{a^3 U} C^2 \quad \text{from definition of } B \tag{D.4}$$

$$\Rightarrow B = \frac{\Phi a^3 U}{C^2} \tag{D.5}$$

D.4.3 Step-step Interaction Parameter

$$g = \frac{2g_3}{3g_1}\left(\frac{a}{L}\right)^2 \tag{D.6}$$

$$= \frac{2}{3}\varepsilon C^2 \tag{D.7}$$

D.4.4 Similarity variables

$$
\begin{aligned}
z \equiv \frac{\rho}{\tau^{1/4}} &= \left(\frac{r}{L}\right)\left(\frac{t}{L/U}\right)^{-1/4} && \text{(D.8)}\\
&= \frac{r}{t^{1/4}}\frac{1}{L^{3/4}U^{1/4}} && \text{(D.9)}\\
&= \frac{r}{(Bt)^{1/4}}\frac{B^{1/4}}{L^{3/4}U^{1/4}} && \text{(D.10)}\\
&= x\left(\frac{\Phi a^3 U}{C^2}\right)^{1/4}\frac{1}{L^{3/4}U^{1/4}} \quad \text{using (D.5)} && \text{(D.11)}\\
&= x\Phi^{1/4}\left(\frac{a}{L}\right)^{3/4}C^{-1/2} && \text{(D.12)}\\
&= C^{1/4}\Phi^{1/4}x && \text{(D.13)}\\
\Rightarrow z &= (C\Phi)^{1/4}x && \text{(D.14)}
\end{aligned}
$$

so when $\Phi = C = 1$, $z = x$, and the similarity variables from MAS [78] and the step flow data are identical.

D.4.5 Step Drop Parameters

For a profile which is initially a cone, the collapse times obey:

$$
\begin{aligned}
t_n &= t^* n^4 \quad \text{(in physical time)} && \text{(D.15)}\\
\tau_n &= \tau^* n^4 \quad \text{(in "step flow" time)} && \text{(D.16)}
\end{aligned}
$$

In this section, we show how to obtain (3.107) from (3.106).

$$
\begin{aligned}
\frac{a}{(Bt^*)^{1/4}} &= \left(\frac{a}{L}\right)\frac{L}{(Bt^*)^{1/4}} && \text{(D.17)}\\
&= C\left(\frac{\Phi a^3 U}{C^2}\right)^{-1/4}\frac{L}{t^{*1/4}} \quad \text{using (D.5)} && \text{(D.18)}\\
&= C^{3/4}\Phi^{-1/4}\frac{L^{1/4}}{U^{1/4}}\frac{1}{t^{*1/4}} && \text{(D.19)}\\
&= C^{3/4}\Phi^{-1/4}\frac{1}{\tau^{*1/4}} && \text{(D.20)}
\end{aligned}
$$

With $C = \Phi = 1$, we have that $\frac{a}{(Bt^*)^{1/4}} = \frac{1}{\tau^{*1/4}}$.

Bibliography

[1] http://qt.tn.tudelft.nl/research/nanowires/.

[2] http://qt.tn.tudelft.nl/research/qdots/.

[3] http://www.findarticles.com/p/articles/mi_m1200/is_v130/ai_4563858.

[4] http://www.llnl.gov/nif/project/pdf/nif_optics.pdf.

[5] http://www.mathworks.com/bvp_tutorial.

[6] http://www.sandia.gov/surface_science/stm/.

[7] U.M. Ascher and L.R. Petzold. *Computer Methods for Ordinary Differential Equations and Differential-Algebraic Equations.* SIAM, 1998.

[8] G.S. Bales and Zangwill A. Morphological instability of a terrace edge during step-flow growth. *Phys. Rev. B*, 41(9):5500–5508, 1990.

[9] E. Bänsch, F. Hausser, O. Lakkis, and A. Voigt. Finite element method for epitaxial growth with attachment-detachment kinetics. *J. Comp. Phys.*, 194:409–434, 2004.

[10] M.J. Berger and J. Oliger. Adaptive mesh refinement for hyperbolic partial differential equations. *J. Comp. Phys.*, 53(3):484–512, 1984.

[11] G.A. Bird. Recent advances and current challenges for DSMC. *Computers and Mathematics with Applications*, 35(1):1–14, 1998.

[12] R.B. Bird, C.F. Curtiss, R.C. Armstrong, and O. Hassager. *Dynamics of Polymeric Liquids, Volume 2: Kinetic Theory.* Wiley, New York, 1987.

[13] H.P. Bonzel and W.W. Mullins. Smoothing of perturbed vicinal surfaces. *Surf. Sci.*, 350:285–300, 1996.

[14] H.P. Bonzel and E. Preuss. Morphology of periodic surface profiles below the roughening temperatures: aspects of continuum theory. *Surf. Sci.*, 336:209–224, 1995.

[15] H.P. Bonzel, E. Preuss, and B. Steffen. The dynamical behavior of periodic surface profiles on metals under the influence of anisotropic surface energy. *Appl. Phys. A*, 35(1):1–8, 1984.

[16] Born.M. and R. Oppenheimer. Zur quantentheorie der molekeln. *Ann. Phys. (Leipzig)*, 80(20):457 – 484, 1927.

[17] W.K. Burton, N. Cabrera, and F.C. Frank. The growth of crystals and the equilibrium structure of their surfaces. *Philos. Trans. R. Soc. London, Ser. A*, 243(299):299–358, 1951.

[18] R.E. Caflisch, W. E, M.F. Gyure, B. Merriman, and C. Ratsch. Kinetic model for a step edge in epitaxial growth. *Phys. Rev. B*, 59(6):6879 – 6887, 1999.

[19] R.E. Caflish and B. Li. Analysis of island dynamics in epitaxial growth of thin films. *Multiscale Model. Simul.*, 1(1):150–171, 2003.

[20] R. Car and M. Parrinello. Unified approach for molecular dynamics and density functional theory. *Phys. Rev. Lett.*, 55(22):2471–2474, 1985.

[21] A. Chame, S. Rousset, H.P. Bonzel, and J. Villain. Slow dynamics of stepped surfaces. *Bulgarian Chem. Commun.*, 29:398–434, 1996–1997.

[22] S. Chen, B. Merriman, S. Osher, and P. Smereka. A simple level set method for solving Stefan problems. *J. Comp. Phys.*, 135:8–29, 1997.

[23] S.T. Chui and J.D. Weeks. Phase transition in the two-dimensional Coulomb gas, and the interfacial roughening transition. *Phys. Rev. B*, 14(11):4978–4982, 2001.

[24] C.V. Ciobanu, D.T. Tambe, V.B. Shenoy, C.Z. Wang, and K.H. Ho. Atomic-scale perspective on the origin on attractive step interactions on Si(113). *Phys. Rev. B*, 68(201302), 2003.

[25] A.R. Curtis. The FACSIMILE numerical integrator for stiff initial value problems. In *Computational Techniques for Ordinary Differential Equations, I. Gladwell and D.K. Sayers, eds.*, pages 47–82. Academic Press, London, 1980.

[26] R. Davé, J. Dubinski, and L. Hernquist. Parallel TreeSPH. *New Astronomy*, 2:277–297, 1997.

[27] M. Degawa, F. Szalma, and E.D. Williams. Nano-scale equilibrium in crystal shapes. *Surf. Sci.*, 583:126–138, 2005.

[28] J.J. DeYoreo, L.A. Land, and B. Dair. Growth morphology of vicinal hillocks on the (101) face of KH_2PO_4: From step-flow to layer-by-layer growth. *Phys. Rev. Lett.*, 73(6):838–841, 1994.

[29] D.B. Dougherty, K. Thürmer, M. Degawa, and W.G. Cullen. Triggered fast relaxation of metastable Pb crystallites. *Surface Science*, 554:233 – 244, 2004.

[30] W. E and B. Engquist. Multiscale modeling and compuation. *Notices of the AMS*, 50(9):1062–1070, 2003.

[31] W.S. Edwards, L.S. Tuckerman, R.A. Friesner, and D.C. Sorensen. Krylov methods for the incompressible Navier-Stokes equations. *J. Comp. Phys.*, 110:82–102, 1994.

[32] G. Ehrlich and F.G. Hudda. Atomic view of surface self diffusion: Tungsten on tungsten. *J. Chem. Phys.*, 44(3):1039–49, 1966.

[33] J.D. Erlebacher, M.J. Aziz, E. Chason, M.B. Sinclair, and J.A. Floro. Spontaneous pattern formation on ion bombarded Si(001). *Phys. Rev. Lett.*, 82(11):2330–2333, 1999.

[34] J.D. Erlebacher, M.J. Aziz, E. Chason, M.B. Sinclair, and J.A. Floro. Nonclassical smoothening of nanoscale surface corrugations. *Phys. Rev. Lett.*, 84(25):5800–5803, 2000.

[35] C.W. Gear and I.G. Kevrikidis. Projective methods for stiff differential equations: Problems with gaps in their eigenvalue spectrum. *SIAM J. Sci. Comput.*, 24(4):1091–1106, 2003.

[36] W.M. Gelbart and A. Ben-Shaul. The "new" science of "complex fluids". *J. Phys. Chem.*, 100:13169 - 13189, 1996.

[37] F. Gibou and R. Fedkiw. A fourth order accurate discretization for the Laplace and heat equations on arbitrary domains with applications to the Stefan problem. *J. Comp. Phys.*, 202:577–601, 2005.

[38] L.A. Graham, Y.-C. Liou, V.K. Walker, and P.L. Davies. Hyperactive antifreeze protein from beetles. *Nature*, 388:727–728, 1997.

[39] E.E. Gruber and W.W. Mullins. On the theory of anisotropy of crystalline surface tension. *J. Phys. Chem. Solids*, 28(5):875–887, 1967.

[40] N.G. Hadjiconstantinou. Hybrid atomistic-continuum formulations and the moving contact-line problem. *J. Comp. Phys.*, 154:245–265, 1999.

[41] J. Hager and H. Spohn. Self-similar morphology and dynamics of periodic surface profiles below the roughening transition. *Surf. Sci.*, 324:365–372, 1995.

[42] D.J. Hardy, D.I. Okunbor, and R.D. Skeel. Symplectic variable step size integration for n-body problems. *Applied Numerical Mathematics*, 29:19–30, 1999.

[43] W.D. Henshaw and D.W. Schwendeman. An adaptive numerical scheme for high-speed reactive flow on overlapping grids. *J. Comp. Phys.*, 191(3):420–447, 1984.

[44] M. Hochbruck and C. Lubich. On Krylov subspace approximations to the matrix exponential operator. *SIAM J. Numer. Anal.*, 34(5):1911–1925, 1997.

[45] Y. Homma, H. Hibino, T. Ogino, and N. Aizawa. Sublimation of a heavily boron-doped Si(111) surface. *Phys. Rev. B*, 58:13146–13150, 1998.

[46] W. Hong, H.N. Lee, M. Yoon, H.M. Christen, D.H. Lowndes, Z. Suo, and Z. Zhang. Persistent step-flow growth of strained films on vicinal surfaces. *Phys. Rev. Lett.*, 95(095501), 2005.

[47] A. Ichimiya, K. Hayashi, E.D. Williams, T.L. Einstein, M. Uwaha, and K. Watanabe. Decay of silicon mounds: Scaling laws and description with continuum step parameters. *Phys. Rev. Lett.*, 84(16):3662–3665, 2000.

[48] A. Ichimiya, Y. Tanaka, and K. Ishiyama. Quantitative measurements of thermal relaxation of isolated silicon hillocks and craters on the Si(111)-(7x7) surface by scanning tunneling microscopy. *Phys. Rev. Lett.*, 76(25):4721–4724, 1996.

[49] N. Israeli, H.C. Jeong, D. Kandel, and J.D. Weeks. Dynamics and scaling of one-dimensional surface structures. *Phys. Rev. B*, 61(8):5698–5706, 2000.

[50] N. Israeli and D. Kandel. Profile of a decaying crystalline cone. *Phys. Rev. B*, 60(8):5946–5962, 1999.

[51] N. Israeli and D. Kandel. Decay of one-dimensional surface modulations. *Phys. Rev. B*, 62(20):13707–13717, 2000.

[52] N. Israeli and D. Kandel. Novel continuum modeling of crystal surface evolution. *Phys. Rev. Lett.*, 88(11):116103, 2002.

[53] C. Jayaprakash, C. Rottman, and W.F. Saam. Simple model for crystal shapes: Step-step interactions and facet edges. *Phys. Rev. B*, 30(11):6549–6554, 1984.

[54] H-C. Jeong and J.D. Weeks. Effects of step-step interactions on the fluctuations of an individual step on a vicinal surface and its wavelenth dependence. *Surface Science*, 432:101 – 114, 1999.

[55] H-C. Jeong and E.D. Williams. Steps on surfaces: experiment and theory. *Surface Science Reports*, 34:171–294, 1999.

[56] D. Kandel and E. Kaxiras. Microscopic theory of electromigration on semiconductor surfaces. *Phys. Rev. Lett.*, 76(7):1114–1117, 1996.

[57] D. Kandel and J. Weeks. Step bunching as a chaotic pattern formation process. *Phys. Rev. Lett.*, 69(26):3758–3761, 1992.

[58] D. Kandel and J. Weeks. Simultaneous bunching and debunching of surface steps: Theory and relation to experiments. *Phys. Rev. Lett.*, 74(18):3632–3635, 1995.

[59] M. E. Keefe, C.C. Umbach, and J.M. Blakely. Surface self-diffusion on Si from the evolution of periodic atomic step arrays. *J. Phys. Chem. Solids*, 55(10):965–973, 1994.

[60] M. Kitamura, M. Nishioka, J. Oshinowo, and Y. Arakawa. In situ fabrication of self-aligned InGaAs quantum dots on GaAs multiatomic steps by metalorganic chemical vapor deposition. *Appl. Phys. Lett.*, 66(26):3663–3665, 1995.

[61] D. Kouris, A. Peralta, and K. Sieradzki. Elastic interaction of defects on crystal surfaces. *Journal of Engineering Materials and Technology (Transactions of the ASME) (USA)*, 121(2):129–135, 1999.

[62] J. Krug. Introduction to step dynamics and step instabilities. *International Series of Numerical Mathematics*, 149:69–95, 2005.

[63] J. Krug, V. Tonchev, S. Stoyanov, and A. Pimpinelli. Scaling properties of step bunches induced by sublimation and related mechanisms. *Phys. Rev. B*, 71:045412, 2005.

[64] R.V. Kukta and K. Bhattacharya. A micromechanical model of surface steps. *J. Mech. Phys. Solids*, 50:615–649, 2002.

[65] R.V. Kukta, A. Peralta, and D. Kouris. Elastic interaction of surface steps: Effect of atomic-scale roughness. *Phys. Rev. Lett.*, 88(18):186102, 2002.

[66] R.V. Kukta, A. Peralta, and D. Kouris. Surface steps: From atomistics to continuum. *Journal of Applied Mechanics*, 69(4):443–450, 2002.

[67] Y. Kuramoto and T. Tsuzuki. Persistent propagation of concentration waves in dissipative media far from thermal equilibrium. *Progress of Theoretical Physics*, 55(2):356–369, 1976.

[68] I. Kwon, R. Biswas, G.S. Grest, and C.M. Soukoulis. Molecular-dynamics simulation of amorphous and epitaxial Si film growth on Si(111). *Phys. Rev. B*, 41(6):3678–3687, 1990.

[69] A. Latyshev, A. Aseev, A. Krasilnikov, and S. Stenin. Transformations on clean Si (111) stepped surface during sublimation. *Surf. Sci.*, 213:157–169, 1989.

[70] J. Lee and J.M. Kosterlitz. Finite-size scaling and Monte Carlo simulations of first-order phase transitions. *Phys. Rev. B*, 43(4):3265–3277, 1991.

[71] D.J. Liu and J.D. Weeks. Quantitative theory of current-induced step bunching on Si(111). *Phys. Rev. B*, 57(23):14891–14900, 1998.

[72] F. Liu, J. Tersoff, and M.G. Lagally. Self-organization of steps in growth of strained films on vicinal substrates. *Phys. Rev. Lett.*, 80(6):1268–1271, 1998.

[73] A. Logg. Multi-adaptive time integration. *Appl. Numer. Math.*, 48:339–354, 2004.

[74] D.H. Lowndes, D.B. Geohegan, A.A. Puretzky, D.P. Norton, and C.M. Rouleau. Synthesis of novel thin-film materials by pulsed laser deposition. *Science*, 273(5277):898–903, 1996.

[75] J. Makino and S. Aarseth. On a Hermite integrator with Ahmad-Cohen scheme for gravitational many-body problems. *Publ. Astron. Soc. Japan*, 44:141–151, 1992.

[76] V.I. Marchenko and A.Y. Parshin. Elastic properties of crystal surfaces. *Sov. Phys. JETP*, 52:129–131, 1980.

[77] D. Margetis. Unified continuum approach to crystal surface morphological relaxation. *Phys. Rev. Lett. (submitted).*

[78] D. Margetis, M. Aziz, and H.A. Stone. Continuum approach to profile scaling in nanostructure decay. *Phys.Rev.B*, 71:165432, 2005.

[79] D. Margetis, P.W. Fok, H.A. Stone, and M.J. Aziz. Continuum theory of evolving crystal surfaces: Study of boundary conditions at a circular facet. *In Preparation.*

[80] D. Margetis and R.V. Kohn. Continuum theory of interacting steps on crystal surfaces in 2+1 dimensions. *Submitted to SIAM Journal of Multiscale Modeling and Simulation.*

[81] D. Margetis and R.R. Rosales. Continuum description of crystal surface morphological evolution by Lagrangian coordinates. *In Preparation.*

[82] J.G. McLean, B. Krishnamachari, D.R. Peale, E. Chason, J.P. Sethna, and B.H. Cooper. Decay of isolated features driven by the Gibbs-Thomson effect in an analytic model and a simulation. *Physical Review B*, 55(3):1811–1823, 1997.

[83] P. Müller and R. Kern. Equilibrium nano-shape changes induced by epitaxial stress (generalised Wulf-Kaishew theorem). *Surf. Sci.*, 457:229–253, 2000.

[84] W.W. Mullins. Theory of thermal grooving. *J. Appl. Phys.*, 28(3):333–339, 1957.

[85] W.W. Mullins. Flattening of a nearly plane solid surface due to capillarity. *J. Appl. Phys.*, 30(1):77–83, 1959.

[86] P. Nozières. On the motion of steps on a vicinal surface. *J. Phys.*, 48:1605–1608, 1987.

[87] C.A. Orme. *Private Communication.*

[88] P.L. O'Sullivan, F.H. Baumann, G.H. Gilmer, J. Dalla Torre, C.S. Shin, I. Petrov, and T.Y. Lee. Continuum model of thin film deposition incorporating finite atomic length scales. *J. Appl. Phys.*, 92(7):3487–3494, 2002.

[89] M. Ozdemir and Zangwill A. Morphological equilibration of a facetted crystal. *Phys. Rev. B*, 45(7):3718–3729, 1992.

[90] W.W. Pai, J.S. Ozcomert, N.C. Bartelt, and T.L. Einstein. Terrace-width distributions on vicinal Ag(110): evidence of oscillatory interactions. *Surf. Sci.*, 307–309:747–754, 1994.

[91] L. Pedemonte, G. Bracco, C. Boragno, F. Buatier de Mongeot, and U. Valbusa. Smoothing of nanoscale surface ripples studied by he atom scattering. *Phys. Rev. B*, 68(115431), 2003.

[92] I. Peterson. Fish antifreeze with an electrical twist. *Science News*, 133:325, 1988.

[93] R. Phillips. *Crystals, Defects and Microstructures.* Cambridge University Press, 2001.

[94] A. Pimpinelli, J. Villain, D.E. Wolf, J.J. Metois, J.C. Heyraud, I. Elkinani, and G. Uimin. Equilibrium step dynamics on vicinal surfaces. *Surf. Sci.*, 295:143–153, 1993.

[95] A. Prasad and P.B. Weichman. Layering transitions, disordered flat phases, reconstruction, and roughening. *Phys. Rev. B*, 57(8):4900–4938, 1998.

[96] W.H. Press, S.A. Teukolsky, W.V. Vetterling, and B.P. Flannery. *Numerical Recipes in C: The Art of Scientific Computing.* Cambridge University Press, second edition, 1992.

[97] M.V. Ramana Murty. Morphological stability of nanostructures. *Phys. Rev. B*, 62(24):17004–17011, 2000.

[98] C. Ratsch, M.F. Gyure, R.E. Caflisch, F. Gibou, M. Petersen, M. Kang, J. Garcia, and D.D. Vvedensky. Level-set method for island dynamics in epitaxial growth. *Phys. Rev. B*, 65(195403), 2002.

[99] A. Rettori and J. Villain. Flattening of grooves on a crystal surface: A method of investigation of surface roughness. *J. Phys. (France)*, 49(2):257–267, 1988.

[100] J.M. Rickman and D.J. Srolovitz. Defect interactions on solid surfaces. *Surf. Sci.*, 284:211 – 221, 1993.

[101] Y. Saito, H. Uemura, and M. Uwaha. Two-dimensional elastic lattice model with spontaneous stress. *Phys. Rev. B*, 63(045422), 2001.

[102] M. Sato and M. Uwaha. Growth of step bunches formed by the drift of adatoms. *Surf. Sci.*, 442:318 – 328, 1999.

[103] M. Sato and M. Uwaha. Growth law of step bunches induced by the Ehrlich-Schwoebel effect in growth. *Surf. Sci.*, 493:494 – 498, 2001.

[104] R.L. Schwoebel. Step motion on crystal surfaces II. *J. Appl. Phys.*, 40(2):614–618, 1969.

[105] R.L. Schwoebel and E.J. Shipsey. Step motion on crystal surfaces. *J. Appl. Phys.*, 37(10):3682–3686, 1966.

[106] V.B. Shenoy, A. Ramasubramaniam, H. Ramanarayan, D.T. Tambe, W.L. Chan, and E. Chason. Influence of step-edge barriers on the morphological relaxation of nanoscale ripples on crystal surfaces. *Phys. Rev. Lett.*, 92(25):256101, 2004.

[107] G.I. Sivashinsky. Nonlinear analysis of hydrodynamic instability in laminar flames. I - derivation of basic equations. *Acta Astronautica*, 4:1177–1206, 1977.

[108] K.M. Smith and V. Yakhot. Finite-size effects in forced two-dimensional turbulence. *J. Fluid Mech.*, 274:11129–11132, 1994.

[109] H. Spohn. Surface dynamics below the roughening transition. *J. Phys. I France*, 3(69):69–81, 1993.

[110] S. Stoyanov. Electromigration induced step bunching on si surfaces - how does it depend on the temperature and heating current direction? *Jpn. J. Appl. Phys.*, 30(1), 1991.

[111] S. Stoyanov and V. Tonchev. Properties and dynamic interaction of step density waves at a crystal surface during electromigration and affected sublimation. *Phys. Rev. B*, 58(3):1590–1600, 1998.

[112] E.B. Tadmor, M. Ortiz, and R. Phillips. Quasicontinuum analysis of defects in solids. *Philosophical Magazine A (Physics of Condensed Matter: Structure, Defects and Mechanical Properties)*, 73:1529–1593, 1996.

[113] E.B. Tadmor, R. Phillips, and M. Ortiz. Hierarchical modeling in the mechanics of materials. *Internationl Journal of Solids and Structures*, 37:379–389, 2000.

[114] S. Tanaka, N.C. Bartelt, C.C. Umbach, R.M. Tromp, and J.M. Blakely. Step permeability and the relaxation of biperiodic gratings on Si(001). *Phys. Rev. Lett.*, 78(17):3342–3345, 1997.

[115] J. Tersoff, M.D. Johnson, and B.G. Orr. Adatom densities on GaAs: Evidence for near-equilibrium growth. *Phys. Rev. Lett.*, 78(2), 1997.

[116] K. Thürmer, J.E. Reutt-Robey, E.D. Williams, M. Uwaha, A. Edmundts, and H.P. Bonzel. Step dynamics in 3D crystal shape relaxation. *Phys. Rev. Lett.*, 87(18):282–285, 2001.

[117] L.N. Trefethen. *Spectral Methods in MATLAB*. SIAM, 2001.

[118] J. Villain, D.R. Grempel, and J. Lapujoulade. Roughening transition of high-index crystal faces: the case of copper. *J. Phys. F: Met. Phys.*, 15:809–834, 1985.

[119] J. Waltz, G.L. Page, S.D. Milder, J. Wallin, and A. Antunes. A performance comparison of tree data structures for N-body simulation. *J. Comp. Phys.*, 178:1–14, 2002.

[120] M. Wortis. *Fundamental Problems in Statistical Mechanics VI.* North-Holland, Amsterdam, 1985.

[121] K. Yagi, H. Minoda, and M. Degawa. Step bunching, step wandering and faceting: self-organization at Si surfaces. *Surf. Sci. Rep.*, 43:45–126, 2001.

[122] K. Yamashita, H.P. Bonzel, and H. Ibach. Steady state shapes of periodic profiles on (110), (100), and (111) surfaces of nickel. *Applied Physics A*, 25(3):231 – 238, 1981.

[123] H.M. Zbib and T. Diaz de la Rubia. A multiscale model of plasticity. *International Journal of Plasticity*, 18:1133 – 1163, 2002.

[124] L.A. Zepeda-Ruiz, G.H. Gilmer, T.N. Thomas, T. Land, and J.J. DeYoreo. Effect of Fe on the growth of KDP. *Journal of Crystal Growth, submitted.*